Stabilité et érosion du manteau lithosphérique subcontinental : Relations entre déformation, hydratation et percolation de fluides et magmas sous le craton du Kaapvaal et le Rift Est-Africain

Virginie Baptiste

Collège Doctoral du Languedoc-Roussillon

THÈSE

Pour obtenir le grade de

Docteur

Délivré par **UNIVERSITE MONTPELLIER 2**

Préparée au sein de l'école doctorale SIBAGHE
Et de l'unité de recherche Géosciences Montpellier

Spécialité : **Structure et évolution de la Terre et des autres planètes**

Présentée par **Virginie Baptiste**

Stabilité et érosion du manteau lithosphérique subcontinental : Relations entre déformation, hydratation et percolation de fluides et magmas sous le craton du Kaapvaal et le Rift Est-Africain

Soutenue le 14/11/2014 devant le jury composé de

Jérôme BASCOU, MC, Univ. de St Etienne	Rapporteur
Anne-Marie BOULLIER, DR1, IST Terre Grenoble	Rapporteur
Sylvie DEMOUCHY, CR1, Géosciences Montpellier	Co-directrice
Fabrice GAILLARD, CR1, IST Orléans	Examinateur
Marguerite GODARD, DR2, Géosciences Montpellier	Examinatrice
Andréa TOMMASI, DR1, Géosciences Montpellier	Co-directrice

UNIVERSITÉ MONTPELLIER 2
SCIENCES ET TECHNIQUES

Remerciements

Après trois années riches de rencontres, de découvertes, d'épreuves et d'apprentissages, voici enfin venu le temps des remerciements. A toutes les personnes qui ont croisé ma route le temps de quelques jours, quelques mois ou années durant cette période si transformatrice de ma vie, voici une tentative, peut-être un peu vaine, d'exprimer ma gratitude.

Pour avoir cru en les capacités d'une étudiante de master fraichement débarquée de Suède, je tiens tout d'abord à remercier **Andréa Tommasi**. Un immense merci pour ta grande disponibilité, ton soutien constant, ta compréhension pendant ces quatre années mouvementées. Merci pour toutes ces corrections extrêmement appliquées (les quelques touffes de cheveux arrachées ont depuis repoussé) !

Pour m'avoir initié aux joies de l'hydrogène dans le manteau et de l'expérimentation, et m'avoir encadrée depuis quatre ans, je souhaite ensuite remercier **Sylvie Demouchy**. Un grand merci pour ta patience et ton soutien face à cette étudiante un brin maladroite qui ne savait même pas tenir une pince coupante ou se servir d'un chalumeau correctement (mes nombreuses blessures de guerre en témoignent !).

Pour m'avoir donné le goût de l'étude des microstructures et des orientations préférentielles de réseau lors des ses cours de première année de master, je tiens à remercier **Alain Vauchez**. Un grand merci pour ta patience face à cette étudiante (alias malédiction n°2) qui s'obstinait à débarquer dans ton bureau pour te demander de l'aide ou des explications. Et bien sûr, merci pour ton humour et avoir mis de l'animation dans ce couloir 4ème gauche parfois un peu trop silencieux.

Merci à **Jérôme Bascou**, **Anne-Marie Boullier**, **Fabrice Gaillard**, **Marguerite Godard** et **Michel Grégoire** d'avoir accepté d'être mes examinateurs ou rapporteurs, et d'avoir pris le temps de s'intéresser à mes travaux de thèse.

Merci à **Nathalie Bolfan-Casanova**, **Roberta Rudnick**, **Shantanu Keshav et Fleurice Parat** pour leur collaboration. Merci à **Dave Mainprice** pour m'avoir dépannée à plusieurs reprises quand j'avais un problème avec un de ses programmes.

Un grand merci à l'ensemble de **l'équipe Manteau et Interfaces** qui m'a permis, du master à la thèse, de travailler dans un contexte agréable et dynamique.

Merci à **Fabrice Barou**, **Claude Merlet** et **Bernard Boyer** pour leur assistance lors de mes excursions à l'EBSD ou à la microsonde électronique. Merci à **Christophe Nevado** et **Doriane Delmas** pour toutes ces magnifiques lames minces toujours réalisées dans les temps. Merci à **Marie-France** pour son immense gentillesse et son dévouement.

Il n'est pas de mots assez forts pour remercier ma mère, **Marie-Claude**, pour m'avoir toujours épaulée et accompagnée dans toutes mes aventures, qu'elles soient petites ou grandes, dans notre jardin ou à l'autre bout de la planète. Un grand merci pour les nombreuses tablettes de chocolat, gâteaux et autres friandises sans lesquelles je n'aurais certainement pas survécu au rush de fin de thèse. Merci à mon père, **Alain**, pour son soutien indéfectible et pour les nombreux voyages en voiture (promis, tu ne devras pas me chercher à Stockholm une deuxième fois !) que je lui ai fait faire ces dernières années. Merci à mes deux grands frères, **Nicolas** et **Sébastien** pour m'avoir toujours supportée dans mes choix (ou supportée tout court) et avoir toujours veillé sur moi.

Un immense merci aux membres du CSC **Julie**, **Fatna** et **Stéphanie** pour tous les moments partagés ensemble ces trois dernières années et tous ceux à venir ! Une dissertation entière ne suffirait pas à vous dire tout ce que j'ai à vous dire les filles. Vous êtes de ses amies qui vous font grandir et que l'on souhaite garder toute une vie.

Merci à mon amie, ma sœur de cœur, **Olivia**, pour m'avoir aidée à cheminer et m'avoir toujours écoutée avec la bienveillance qui te caractérise.

Merci à **Valérie** pour tous ces supers moments passés ensembles à Montpellier ou à Lyon. Prépare-toi, je vais bientôt avoir plus de temps pour venir d'embêter.

Merci à **Céline** pour avoir toujours gardé un œil sur moi, même si je ne donnais pas souvent de nouvelles.

Merci aux membres successifs du bureau 411. **Ana**, pour ta grande gentillesse et ta bonne. **Gustavo** pour toutes nos conversations. Le club des femmes à chats : **Claudia** pour ton immense gentillesse et ton sourire, **Nathalie** car tu es aussi de ces amies que je souhaite conserver toute ma vie, **Laura-May** et **Adelaïde** (qui venait si fréquemment qu'elle faisait presque partie de notre bureau) pour ces nombreux fous rires. Merci à **Carolina** (alias malédiction n°3) pour m'avoir relayé quand je ne pouvais pas embêter Alain et pour toutes ses supers soirées au Barberousse.

Enfin, merci à tous les thésards de GM pour ces bons moments passés ensemble : **Laure**, **Anaïs**, **Kate**, **Roberto**, **Erwin**, **Antoine**, **Yannick**, **Manon**, **Romain**, **René**, **Théo**, **Robin**… et tous ceux que j'ai sûrement oublié.

Résumé :

Les travaux réalisés durant cette thèse apportent de nouvelles contraintes sur les relations entre déformation, hydratation et percolation de fluides et/ou de magmas dans le manteau subcontinental sous un craton et sous un rift, et leurs implications sur son comportement rhéologique. Il repose sur l'analyse des microstructures, des OPRs et des teneurs en hydrogène de xénolites mantelliques du craton du Kaapvaal, et sur deux séries de xénolites provenant de différentes localités le long du rift Est-Africain (Divergence Nord Tanzanienne et SE de l'Ethiopie).

Les microstructures granulaires à gros grains et les OPRs bien définies des péridotites du craton du Kaapvaal sont cohérentes avec un épisode de déformation suivi d'une longue période de quiescence. Les OPRs de l'olivine sont majoritairement à symétrie orthorhombique, mais des symmétries axiale-[100] et axiale-[010] sont aussi mesurées. Les péridotites cratoniques enregistrent de multiples épisodes métasomatiques, ayant entraîné une hétérogénéité de compositions à petite échelle ne pouvant être détectée par les études sismiques. Les teneurs en hydrogène mesurées dans l'olivine sont variables, mais ont tendance à augmenter jusqu'à 150 km de profondeur, atteignant alors jusqu'à 50 ppm wt. H_2O. En dessous de cette profondeur, les échantillons montrent des teneurs en hydrogène très faibles. Les expériences réalisées en piston-cylindre sur la diffusion de l'hydrogène issue d'un liquide kimberlitique vers de la forstérite suggèrent que la fugacité en eau pourrait fortement être diminuée par la présence de CO_2, empêchant l'hydratation de l'olivine durant extraction des xénolites par les kimberlites. Ces résultats expérimentaux suggèrent que les teneurs en hydrogène dans l'olivine des péridotites du craton du Kaapvaal ont été acquises durant un épisode métasomatique en profondeur et non pendant leur extraction par les kimberlites. Ces teneurs n'ont toutefois pas à ce jour entraîné de remobilisation de la racine cratonique. Enfin, le calcul des propriétés sismiques des péridotites cratoniques révèle que les anisotropies générées par les OPRs de ces échantillons sont suffisantes pour expliquer les anisotropies mesurées par les ondes SKS et les ondes de surface.

Les xénolites de la Divergence Nord-Tanzanienne, montrent des variations significatives de microstructures et d'OPR de l'olivine entre les péridotites des localités dans l'axe du rift et celles de la chaîne volcanique transverse (Lashaine et Olmani). A Lashaine, les microstructures granulaires à gros grains et les OPRs de type orthorhombique et axial-[010] peuvent être expliquée par une déformation en transpression liée à la formation de la chaîne Mozambique ou par la présence d'une relique d'un domaine cratonique à l'intérieur de la chaîne Mozambique. Dans l'axe du rift, les microstructures porphyroclastiques à mylonitiques suggèrent une déformation plus récente, accompagnée de réactions magma-roche sous des conditions proches du solidus, suivie d'un recuit variable. L'hétérogénéité des microstructures enregistrées par les échantillons du rift suggère de multiples épisodes de déformation localisée, probablement liés à l'injection percolation épisodique de magmas, espacés de périodes d'accalmie. Les OPRs de l'olivine de type axial-[100] et l'orientation des directions de polarisation des ondes SKS suggère que le rift s'est formé en régime de transtension

Les péridotites du Sud-Est de l'Ethiopie présentent des microstructures porphyroclastiques à gros grains moins recristallisées qu'en Tanzanie. Les microstructures et les OPRs principalement de type orthorhombique suggèrent une déformation syn- à post-métasomatisme. Les anisotropies de polarisation des ondes S calculées pour ces échantillons sont insuffisantes pour expliquer à elles seules les déphasages des ondes SKS dans cette partie du rift.

MOTS CLÉS : Péridotite, déformation, OPR, teneurs en hydrogène, craton, rift, propriétés sismiques, percolation réactive.

Abstract :

This study provides additional constraints on the relations between deformation, hydration and percolation of fluids and melts in the subcontinental lithospheric mantle beneath a craton and a rift, as well as their implication on its geodynamical behaviour. I have analysed the microstructures, the CPOs, and the hydrogen content of mantle xenoliths from the Kaapvaal craton, and two sets of xenoliths from different localities along the East African Rift (North Tanzanian Divergence and SE Ethiopia).

The coarse-granular microstructures and the well-defined CPOs in Kaapvaal peridotites suggest a deformation followed by a long quiescence time. Orthorhombic olivine CPOs predominates, but axial-[100] and axial-[010] are also measured. Cratonic peridotites record multiple metasomatic episodes, leading to a significant compositional heterogeneity, which cannot be imaged by seismic studies. Olivine hydrogen contents are variable, but tend to increase until 150 km depth, reaching up to 50 ppm wt. H_2O. The deeper samples are almost dry. Piston-cylinder experiments on hydrogen diffusion between a volatile-rich kimberlitic melt and forsterite suggest that the presence of CO_2 in the system could significantly decrease water fugacity and thus forsterite hydration. These experimental results indicate that the hydrogen contents measured in olivine were acquired during a metasomatic event rather than during xenolith extraction by kimberlites. However, this metasomatism was not followed by remobilization of the cratonic root.

In the North Tanzanian Divergence, localities within the rift axis and the volcanic transverse belt (Lashaine and Olmani) show significant differences in microstructures and olivine CPO patterns. In Lashaine, coarse-granular microstructures and orthorhombic to axial-[100] CPO patterns in olivine can be explained by transpressional deformation during the formation of the Mozambique belt, or by the occurrence of a remnant of a cratonic domain embedded within the Mozambique belt. Within the rift axis, porphyroclastic to mylonitic microstructures suggest a recent rift-related deformation accompanied by syn-kinematic melt-rock reactions, and followed by variable annealing. The strong heterogeneity in microstructures and olivine CPO suggests that this deformation was acquired during multiple tectonic events probably linked to episodic magma percolation, separated by quiescence episodes. The axial-[100] patterns in olivine and the oblique fast directions reported by SKS studies are coherent with transtensional deformation within the lithospheric mantle beneath the rift.

The peridotites from SE Ethiopia are less recrystallized than the rift-axis Tanzanian peridotites, displaying coarse-porphyroclastic microstructures. Microstructures and orthorhombic CPOs in olivine suggest syn- to post-metasomatic deformation. S-waves polarization anisotropies calculated for these samples cannot explain alone the delay times reported by SKS studies in this part of the East-African Rift.

KEYWORDS: Peridotite, deformation, CPO, hydrogen contents, craton, rift, seismic properties, reactive percolation.

« Dans les sciences, le chemin est plus important que le but. Les sciences n'ont pas de fin. »
Erwin Chargaff

À ma grand-mère, Cécile, et à mon parrain, Guy.

Table des matières

Chapitre 1 : Introduction

1.1. Le manteau lithosphérique subcontinental

1.1.1. Caractéristiques du manteau lithosphérique subcontinental

Le manteau subcontinental représente plus de 60% des plaques continentales, lui conférant un rôle déterminant sur le devenir de la lithosphère continentale au cours des temps géologiques. La structure et la composition de cette enveloppe varient significativement d'une région à une autre. L'épaisseur du manteau subcontinental passe ainsi de quelques dizaines de kilomètres sous les rifts, à plus de 250 km sous certains cratons archéens (Figure 1.1). Ces changements d'épaisseur sont généralement couplés à une variation de la structure thermique, comme le suggèrent les tomographies sismiques ainsi que les données thermobarométriques sur des xénolites mantelliques. Les cratons sont ainsi caractérisés par des géothermes froids, comme en témoignent par exemple les vitesses anormalement élevées des ondes de volume révélées par la tomographie sismique (Figure 1.2). A contrario, au niveau des rifts continentaux, les géothermes chauds se traduisent par des vitesses sismiques plus lentes que la moyenne (Figure 1.2).

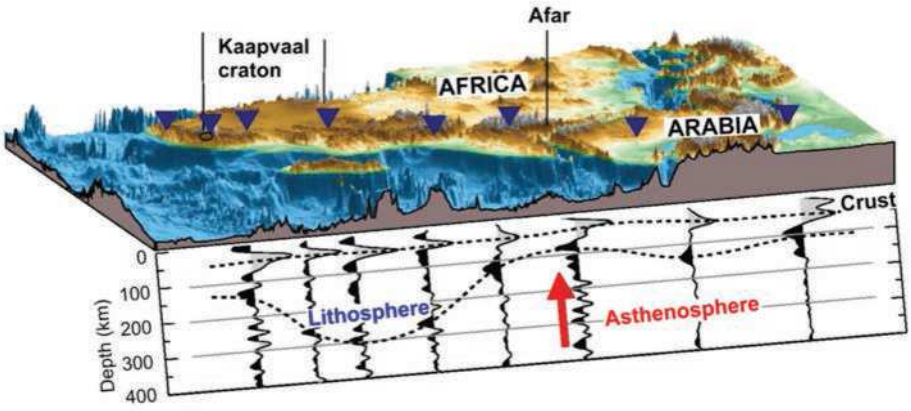

Figure 1.1 Coupe sismique sous l'Afrique construite à partir des fonctions récepteurs S, montrant la variation d'épaisseur de la lithosphère entre le craton archéen du Kaapvaal et le rift Est Africain (Eaton et al., 2009). Les triangles correspondent aux stations sismiques. Les amplitudes positives sont ombrées en gris et les amplitudes négatives sont ombrées en noir.

Le manteau lithosphérique subcontinental est d'une manière générale composé de roches ultramafiques. Sa composition varie, selon l'enrichissement en olivine, de la lherzolite, à l'harzburgite, en passant par la dunite. Ces variations lithologiques sont généralement interprétées comme étant liées à des épisodes de fusion partielle ou des épisodes métasomatiques (percolations réactionnelles de magmas ou fluides) (e.g. Griffin et al., 2009).

Les études sur les xénolites mantelliques révèlent aussi une variation systématique de la composition du manteau lithosphérique subcontinental. Les compositions les plus appauvries sont ainsi mesurées au niveau des cratons archéens, tandis que les chaînes mobiles protérozoïques et phanérozoïques montrent un appauvrissement modéré (e.g. Griffin et al., 2009).

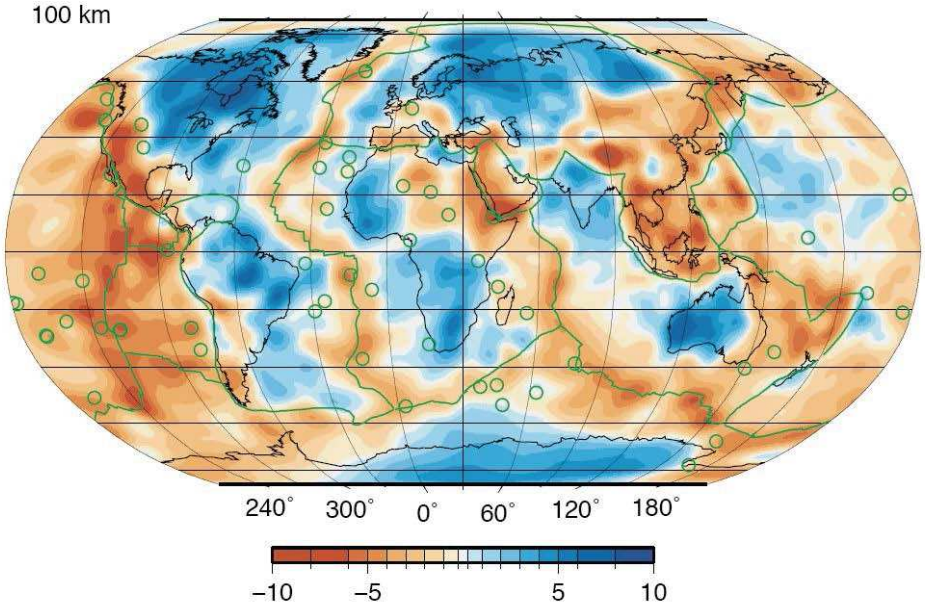

Figure 1.2 : Carte des anomalies de la vitesse des ondes SV au sommet du manteau (à 100 km de profondeur) (Debayle et al., 2005).

Ces variations des caractéristiques du manteau lithosphérique subcontinental sont liées à des contextes géodynamiques bien différents tels que les cratons, stables pour la plupart depuis leur formation durant l'Archéen et au Protérozoïque inférieur (e.g. Griffin et al., 2003a; Pearson et al., 1995) et les rifts, où la lithosphère est déstabilisée au profit de la création d'une nouvelle frontière de plaque. Or, de tels changements d'épaisseur, de structure thermique et de composition peuvent être reliés à des processus affectant directement la rhéologie du manteau. Etudier ces processus est donc primordial pour comprendre le comportement géodynamique des continents.

1.1.2. Outils d'étude du manteau lithosphérique subcontinental

De multiples outils sont aujourd'hui à la disposition des géologues afin d'étudier la structure, la composition et le comportement du manteau lithosphérique subcontinental. Les méthodes d'observation indirecte, telles que celles utilisées par les sismologues, donnent accès à la structure globale du manteau. La tomographie sismique offre par exemple la

possibilité de détecter des anomalies de vitesse dans une région donnée. Selon le contexte étudié, ces anomalies peuvent être reliées à des modifications du géotherme, des variations de composition, ou encore à la présence de fluides ou de magmas dans le manteau. L'interprétation de ces données en terme de composition ou de pourcentage de magma reste toutefois délicate et requiert des contraintes telles que celles apportées par les études sur les xénolites mantelliques ou par les études expérimentales. Les fonctions récepteurs (Vinnik, 1977) sont aussi communément employées afin de détecter des discontinuités sismiques dans le manteau supérieur. L'étude de l'anisotropie sismique permet quant à elle de détecter l'orientation des flux mantelliques ainsi que la déformation du manteau supérieur. L'analyse du déphasage des ondes SKS permet ainsi d'identifier la présence d'une ou plusieurs couches anisotropes et offre une bonne résolution latérale. L'utilisation des ondes de surfaces offre quant à elle une meilleure résolution verticale (e.g. Eaton et al., 2009). Enfin, les études magnétotelluriques rendent possible la détection de limites structurales verticales ou latérales (Evans et al., 2011), mais aussi de corréler des variations de conductivité à des variations de température et de composition.

Les possibilités d'observation directes du manteau continental restent plus rares. Elles ne peuvent se faire qu'au travers de l'étude de fragments remontés à la surface par des processus tectoniques ou magmatiques que sont les massifs péridotitiques ou les xénolites. Ces fragments n'offrent ainsi qu'une vision locale, et donc parcellaire, du manteau lithosphérique. L'étude de ces roches permet toutefois d'obtenir des informations précieuses sur les processus physiques et chimiques affectant le manteau lithosphérique. En effet, par l'étude de la composition minéralogique et chimique de ces roches, il est possible de retracer leur évolution thermique et d'identifier le ou les épisode(s) métasomatique(s) auxquels elles ont été soumises. Les conditions et l'historique de déformation peuvent être aussi obtenus à partir de l'analyse des microstructures de déformation et des orientations préférentielles de réseau (OPR) des minéraux. Par l'analyse conjointe des compositions et de la déformation de ces échantillons, le rôle de la percolation de magmas et de fluides et de l'hydratation sur la déformation peut être étudié. Enfin, les propriétés sismiques d'une roche peuvent être calculées à partir des OPRs des minéraux la constituant, de la composition modale, de la densité et des constantes élastiques des minéraux (Mainprice, 1990; Mainprice et al., 2000; Mainprice and Humbert, 1994). Ces valeurs peuvent ensuite être comparées aux déphasages mesurés par les ondes SKS, afin de mieux comprendre la source de l'anisotropie mesurée, et si elle peut être lithosphérique, de faire des hypothèses sur l'orientation de la foliation fossilisée par le manteau lithosphérique (Figure 1.3 ; Mainprice and Silver, 1993; Nicolas and

Christensen, 1987).

Enfin, l'expérimentation et les modélisations numériques et analogiques apportent des informations supplémentaires sur le comportement du manteau supérieur, en tentant de reproduire et de caractériser les processus qui s'y tiennent place. L'ensemble de ces outils apporte donc des informations précieuses et complémentaires. Les considérer dans leur ensemble offre ainsi les contraintes importantes nécessaires à l'établissement d'interprétations solides.

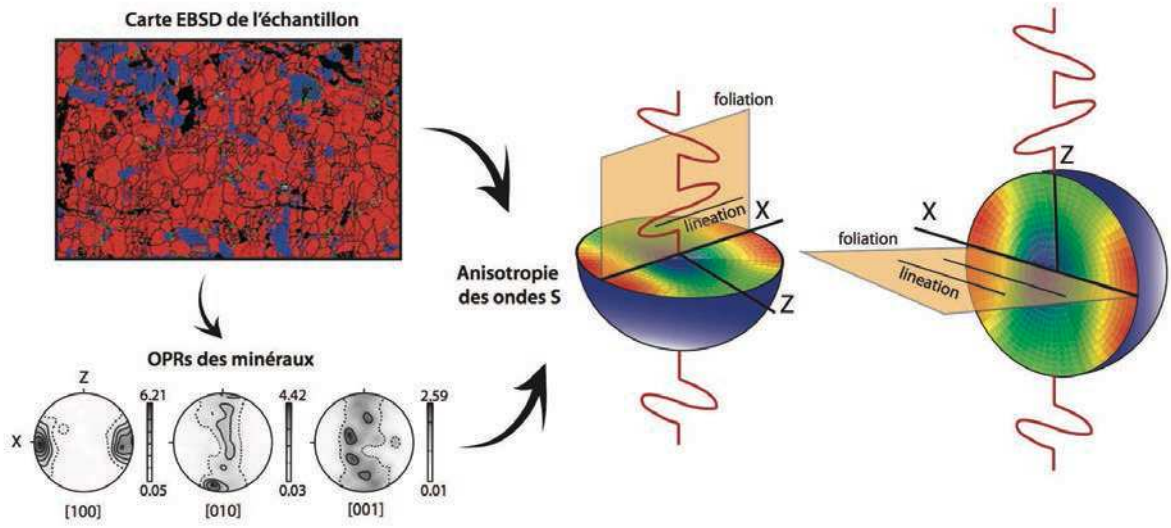

Figure 1.3 : Schéma présentant l'anisotropie de polarisation des ondes S échantillonnée par les ondes SKS pour un échantillon donné et pour différentes orientations de foliation et linéation. La couleur rouge indique les valeurs les plus faibles tandis que la couleur bleue indique les valeurs les plus fortes.

1.1.3. Les cratons

1.1.3.1. Modèles de formation

Les cratons sont des domaines continentaux lithosphériques épais dont la formation et l'origine reste controversée. Plusieurs modèles sont encore débattus dans la littérature pour expliquer leur formation.

Un premier modèle explique la formation de la lithosphère cratonique comme le résultat de la fusion au sein d'un panache mantellique où les hautes températures génèreraient les forts taux de fusion nécessaires à la formation d'une racine appauvrie en fer et sèche (Figure 1.4) (Arndt et al., 2009; Griffin and O'Reilly, 2007; Griffin et al., 2003a; Lee et al., 2011). Un tel modèle prévoit une stratification de la lithosphère d'une composition appauvrie (forts taux de fusion et Mg# de l'olivine élevés) à une composition fertile (faibles taux de fusion et Mg# de l'olivine faibles ; voir Figure 1.4 a ; Lee et al., 2011). Les réflecteurs horizontaux détectés par

les fonctions récepteurs des ondes S au niveau du craton du Kaapvaal et du craton Nord Américain pourraient, entre autre, être expliqués par une telle stratification (Savage and Silver, 2008; Wittlinger and Farra, 2007; Yuan and Romanowicz, 2010). Si ce changement de composition est en effet observé dans les xénolites de plusieurs cratons, il n'est toutefois pas systématique (Lee et al., 2011).

Un second modèle propose que la racine se forme par injection épisodique de petits diapirs (100-200 km) (de Smet et al., 1998, 1999, 2000). Un tel processus permet en effet la formation rapide d'une racine de composition distincte, faite de péridotite appauvrie en fer, telle que le suggère les xénolites cratoniques. Toutefois, ces deux modèles ne parviennent pas à expliquer la présence d'éclogites parmi les xénolites cratoniques.

Dans un troisième modèle, la lithosphère cratonique se forme par le sous-plaquage ou l'imbrication successive de plaques plongeantes (Figure 1.4 b) (Lee et al., 2011; Pearson and Wittig, 2008; Simon et al., 2007). Un contexte de subduction pourrait expliquer les fluides en Si responsables de l'enrichissement en orthopyroxène mesuré dans les xénolites du craton du Kaapvaal (Simon et al., 2007). L'accrétion de lithosphère océanique est également suggérée par les signatures éclogitiques mesurées dans les inclusions de sulfides dans des diamants de ce même craton (Richardson et al., 2001). Ce modèle explique aussi la présence d'éclogite parmi les xénolites mantelliques cratoniques, mais la quantité d'éclogites attendue à la base du craton devrait être bien supérieure à celle présente sur les continents (Lee et al., 2011; Schulze, 1989). De plus, les différences de distribution des éclogites dans les kimberlites de groupe I et II du craton du Kaapvaal implique la subduction d'éclogites sous le craton il y a 100-115 Ma, en désaccord avec les reconstructions des mouvements tectoniques dans la région durant cette période (Griffin and O'Reilly, 2007). Cette imbrication semble aussi peu probable compte tenu de la flottabilité négative des plaques océaniques plongeantes qui devraient plutôt entrer en subduction (Arndt et al., 2009). De plus, l'imbrication de ces plaques plongeantes créerait des failles ou des zones de faiblesse de grande échelle qui devrait être cicatrisées pour pouvoir expliquer la stabilité à long terme des cratons (Lee et al., 2011).

Un quatrième modèle suggère que la formation du manteau cratonique pourrait être liée à l'accrétion et l'épaississement d'arcs continentaux (Figure 1.4 c ; Lee et al., 2011). Si ce modèle, comme le précédent, peut expliquer les teneurs élevées en orthopyroxène dans les péridotites du craton du Kaapvaal, un tel contexte devrait générer la production de laves andésitiques, qui ne sont pas observées au niveau des cratons.

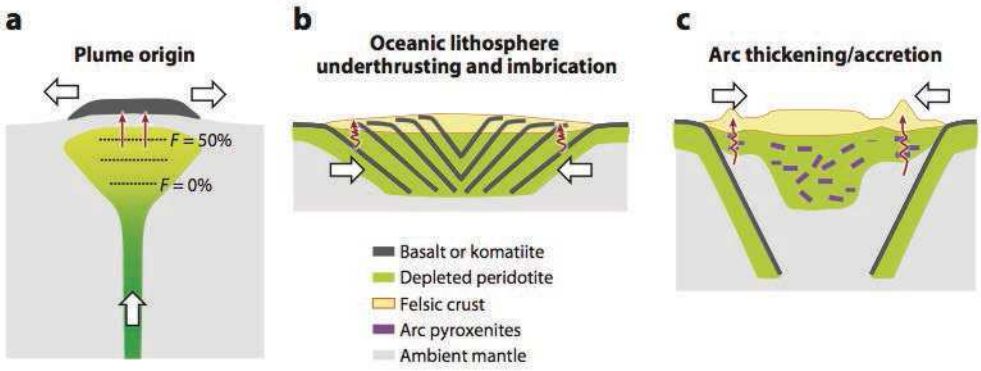

Figure 1.4 : Schéma présentant les différents modèles de formation du manteau subcratonique (Lee et al., 2011) : (a) formation associée à un panache mantellique, (b) formation par sous-plaquage et imbrication successive de plusieurs plaques subduites, et (c) formation par épaississement/accrétion d'arcs volcaniques.

1.1.3.2. Stabilité

La stabilité et la longévité de certains cratons ont fait l'objet de nombreux débats et de nombreuses études depuis plusieurs décennies, mais restent aujourd'hui encore une question géodynamique majeure. Les compositions très appauvries en fer des péridotites cratoniques ont tout d'abord conduit Jordan (1978) à proposer que la composition réfractaire, et donc moins dense de la racine cratonique, compensait l'élévation de densité lié au géotherme froid du craton. Ces compositions devaient ainsi résulter en une flottabilité neutre de la lithosphère par rapport à l'asthénosphère. Or, des modèles numériques ont démontré que la diminution de densité liée à une composition appauvrie ne suffirait pas pour expliquer la stabilité des racines cratoniques sur plusieurs milliards d'années (Doin et al., 1997; Lenardic and Moresi, 1999). D'autres modèles suggèrent que la stabilité de ces racines pourrait être favorisée par la présence de matériel peu résistant autour du craton, telles que des chaines collisionnelles Neoproterozoïques ou plus récentes, qui localiserait la déformation (Lenardic et al., 2003). Plusieurs études suggèrent également qu'un fort contraste de viscosité entre la racine cratonique et l'asthénosphère pourrait être à l'origine de leur longévité (Doin et al., 1997; Pollack, 1986). Toutefois, les géothermes cratoniques, même s'ils sont froids, ne peuvent pas générer les 2-3 ordres de grandeur de contraste de viscosité nécessaires à la stabilité des cratons (Doin et al., 1997; Lenardic and Moresi, 1999). Assumant que l'épisode de fusion partielle responsable des compositions très réfractaires des péridotites cratoniques (Boyd and Mertzman, 1987) avait dû produire une déshydratation générale de la racine, puisque l'hydrogène se comporte comme un élément incompatible durant la fusion partielle (Bolfan-Casanova, 2005; Dixon et al., 2002; Hirschmann et al., 2005), des études ont suggéré qu'un

tel contraste de viscosité pouvait être lié à de très faibles teneurs en hydrogène dans l'olivine (Doin et al., 1997; Pollack, 1986). En effet, des expériences suggèrent que la présence d'hydrogène dans les roches mantelliques modifie significativement leur viscosité (voir section 1.2.4). Cette question sera abordée plus en détails dans le chapitre 2 de ce manuscrit.

1.1.3.3. Déstabilisation

Bien que la plupart des cratons tels que le craton du Kaapvaal ou encore le craton tanzanien aient survécu à la tectonique des plaques et à la convection mantellique durant plusieurs milliards d'années, d'autres cratons tels que le craton Nord Chinois et celui du Wyoming ont vu leur racine partiellement détruite (e.g. Carlson et al., 2004; Chen et al., 2008; Eggler and Furlong, 1991; Gao et al., 2002; Menzies et al., 1993). Les processus à l'origine de leur déstabilisation sont encore vivement débattus au sein de la communauté scientifique, donnant lieu à la publication de nombreux modèles (Figure 1.5) parmi lesquels trois modèles principaux rappelés ci-dessous.

Tout d'abord, la racine peut être déstabilisée par des courants convectifs où l'enlèvement est induit par des forces de flottabilité (Figure 1.5 a). Des contrastes latéraux ou verticaux de densité ou de température peuvent ainsi créer de petites instabilités convectives favorisant l'érosion à la base ou sur les côté de la lithosphère cratonique (Morency et al., 2002). Un second mécanisme consiste à modifier la rhéologie de la base de la racine avec des magmas riches en eau ou des fluides relâchés par une plaque subduite (Figure 1.5 c).

Dans un troisième modèle, la déstabilisation de la racine cratonique passe par un processus d'érosion pétro-thermomécanique, durant lequel des épisodes magmatiques vont successivement refertiliser la racine, entraînant une migration de la limite lithosphère-asthénosphère (e.g. Foley, 2008). Les observations pétrologiques sur les xénolites mantelliques cratoniques montrent fréquemment un ré-enrichissement qui se traduit par la cristallisation de clinopyroxene et de grenat, causant la lherzolitisation des harzburgites appauvries (Simon et al., 2003; Tang et al., 2008). L'efficacité d'un tel processus repose sur le fait qu'il ré-enrichit localement plutôt que de manière homogène la base de la lithosphère (Foley, 2008). La génération de magmas, nécessaire à ce processus, est favorisée par des contextes de points chauds ou d'instabilités convectives (Lee et al. 2011). Cependant, un tel processus n'est pas possible sous les continents épais si ce n'est par l'intervention d'un panache mantellique ou d'une production de chaleur radiogénique anormale pour augmenter localement la température (Lee et al., 2011). De plus, la production de telles quantités de magma basaltiques est difficile à plus de 200 km compte-tenu des pressions impliquées.

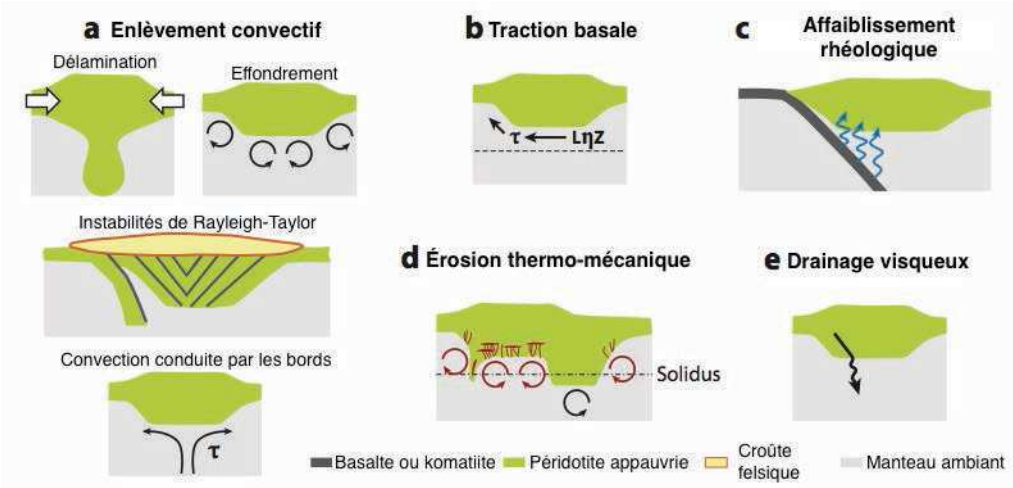

Figure 1.5 : Schéma représentant les différents modèles de destruction ou de recyclage de la lithosphère cratonique (Lee et al., 2011) : (a) Déstabilisation par des courants convectifs où l'enlèvement est induit par des forces de flottabilité (thermiques ou chimiques) . Ces processus incluent la délamination, l'effondrement, les instabilités de Rayleigh-Taylor, et la convection conduite par les bords; (b) Déstabilisation par traction basale, où un cisaillement à la base de la racine entraîne une déformation. Cette traction est liée à la présence d'une zone plus mince de faible viscosité à la base des continents. Les pointillés représentent la zone de faible viscosité ; (c) Déstabilisation facilitée par une diminution de la rhéologie de la lithosphère cratonique, facilitant alors la délamination de la racine par les courants convectifs ; (d) Erosion thermo-magmatique par des magmas à la base de la lithosphère modifiant localement la densité et la température du manteau, (e) Drainage visqueux durant lequel des pyroxénites (de faible viscosité) glisse le long d'un plan incliné au cours des temps géologiques.

1.1.4. Les rifts : modèles d'extension

Les rifts continentaux sont les manifestations physiques de la rupture continentale. La grande diversité de morphologies a donné lieu à la publication de plusieurs modèles d'extension, désireux d'expliquer les processus à l'origine de la déstabilisation d'un continent.

Il existe des rifts larges, tels que le « Basin and Range » aux Etats-Unis, s'étendant sur plusieurs centaines de kilomètres et des rifts étroits, dont l'expression en surface ne dépasse généralement pas 100 km, tels que le rift Est-Africain et le rift Baïkal. McKenzie, (1978) proposa d'abord un modèle de rift large où la lithosphère s'amincit et s'étire de manière homogène en réponse à des contraintes extensives éloignées. Afin d'expliquer les observations du « Basin and Range », Wernicke (1981, 1985) proposa ensuite un modèle d'extension asymétrique dans lequel la majeure partie de la déformation est accommodée par un long détachement affectant l'ensemble de la lithosphère. Un modèle de rift étroit, dans lequel le rifting se produit via la rupture lithosphérique et la remontée d'un coin mantellique, fut ensuite proposé par Nicolas et al. (1994). Ce modèle fut ensuite repris par Vauchez et al., (1997) et Tommasi and Vauchez (2001) qui suggérèrent que l'extension continentale se

produit sous un régime de déformation en transtension produit par la réactivation d'ancienne OPR de l'olivine préservée dans la lithosphère (voir section 1.2.6). D'autres études suggèrent que la présence d'hétérogénéités rhéologiques a également un rôle important dans la localisation de la déformation (Dunbar and Sawyer, 1989; Vauchez et al., 1997).

Rifts passifs et rifts actifs ont aussi longtemps été opposés dans la littérature. Dans le cas d'un rift passif, l'amincissement est le résultat de contraintes extensives en limite de plaque, qui entraîne une remontée passive de l'asthénosphère par décompression adiabatique (McKenzie, 1978; Wernicke, 1981, 1985). A contrario, la formation d'un rift actif est attribuée à l'impact d'un panache mantellique à la base de la lithosphère provoquant son érosion et son amincissement. Des modèles plus récents proposent une combinaison de ces deux processus (Huismans et al., 2001; Petit and Déverchère, 2006). En effet, les données fournies par les études sismiques suggèrent qu'en plus d'être soumise à des contraintes extensives, la lithosphère serait soumise à la percolation de magmas, notamment sous la forme de filons pouvant faciliter la localisation de la déformation (Buck, 2006).

Si ces modèles sont complémentaires et basés sur des observations géomorphologiques, sismiques et géochimiques, les observations directes sur de la manière dont la déformation se localise et est accommodée par le manteau lithosphérique durant le rifting sont rares dans la littérature.

1.2. Rhéologie du manteau lithosphérique

1.2.1. Effet des variations de contraintes et de température

Le comportement rhéologique d'un agrégat cristallin est classiquement décrit sous la forme d'une loi de puissance semi-empirique où la vitesse de déformation ($\dot{\varepsilon}$) est directement proportionnel à la contrainte différentielle (σ) élevée à une puissance n (e.g. Nicolas and Poirier, 1976). L'expression exacte de cette loi ainsi que la valeur des différents paramètres dépend des conditions ainsi que des mécanismes étudiés (Tableaux 1 et 2). L'une de ces expressions possibles est (Hirth and Kohlstedt, 2003):

$$\dot{\varepsilon} = A\sigma^n d^{-p} f_{H_2O}^r \exp(\alpha\phi) \exp\left(-\frac{E^*+PV^*}{RT}\right) \quad (1)$$

où A est une constante du matériel considéré, n l'exposant de la contrainte, d la taille de grain moyenne, P la pression, fH$_2$O la fugacité en eau pure, α une constante, r l'exposant de la fugacité en eau, ϕ la fraction de magma, E^* l'énergie d'activation, V^* le volume d'activation, R la constante des gaz parfaits, et T la température absolue (en K). Le manteau supérieur étant

majoritairement composé de péridotite, dont l'olivine la phase cristalline majeure (>60%), une telle loi peut-être utilisée pour décrire son comportement rhéologique. Selon cette équation, une baisse de résistance est attendue si la contrainte (pour n≥1), la température, la fugacité en eau, ou la fraction de magma augmente ou si la pression ou la taille de grains diminue (Figure 1.6). Des modèles numériques montrent ainsi qu'à plus grande échelle, une variation latérale du géotherme peut produire des contrastes de résistances significatifs au sein d'une plaque lithosphérique et promouvoir la localisation de la déformation en contexte intraplaque (Neves et al., 2008; Tommasi et al., 1995).

Tableau 1: Paramètres rhéologiques pour l'équation 1 (D'après Hirth et Kohlstedt, 2003)

	A	n	p	r	α	E* (kJ/mol)	V* (10^{-6} m^3/mol)
Diffusion anhydre	$1,5x10^9$	1	3	-	30	375 ± 50	2-10
Diffusion hydratée	$2,5x10^7$	1	3	0,7-1,0	30	375 ± 50	0-10
Diffusion hydratée (C_{OH} constante)	$1,0x10^6$	1	3	1	30	375 ± 50	4
Dislocation anhydre	$1,1x10^5$	3,5 ± 0,3	0	-	30-45	530 ± 4	(voir tableau 2)
Dislocation hydratée	1600	3,5 ± 0,3	0	1,2 ± 0,4	30-45	520 ± 40	22 ± 11
Dislocation hydratée (C_{OH} constante)	90	3,5 ± 0,3	0	1.2	30-45	480 ± 40	11
GBS anhydre, T>1250°C	$4,7x10^{10}$	3.5	2	-	30-45	600	(voir tableau 2)
GBS anhydre, T<1250°C	6500	3.5	2	-	30-45	400	(voir tableau 2)

Tableau 2: Détermination des volumes d'activation (D'après Hirth et Kohlstedt, 2003)

Technique	V* (10^{-6} m^3/mol)	Gamme de P (GPa)	Référence
Déformation	23	0,2-0,4	Wang et al. (2010)
Déformation	13,4 (18)	0,5-1,5	Ross et al. (1979)
Déformation	14 (18)	0,3-2	Karato and Jung (2003)
Déformation	14	0,3-15	Karato and Rubie (1997)
Déformation	27	0,6-2,0	Borch and Green II (1989)
Restauration	19	10^{-4}-0,5	Kohlstedt et al. (1980)
Restauration	14	10^{-4}-2,0	Karato and Ogawa (1982)
Restauration	6	10^{-4}-10	Karato et al. (1993)
Diffusion (Si)	-2	5-10	Béjina et al. (1999)

Les trois principaux mécanismes de déformation ductile dans les roches sont le fluage-dislocation, le glissement aux joints de grains accommodé par le mouvement des dislocations, le glissement aux joints de grain accommodé par diffusion. Durant la déformation, ces mécanismes sont activés simultanément. Selon les conditions de déformation, l'un de ces mécanismes va dominer et contrôler la résistance de la roche. Bien que la déformation uniquement par diffusion soit théoriquement possible, ce mécanisme est probablement trop

lent pour être dominant. Une variation de température ou de contrainte peut entraîner une transition d'un mécanisme à un autre et considérablement modifier la microstructure d'une roche, et donc sa résistance (voir section 1.2.2). En effet, alors que la migration et l'accumulation de dislocations au sein de la structure cristalline promeut la recristallisation dynamique par rotation des sous-grains et tend à entraîner une réduction de la taille de grains ; la diffusion de défauts ponctuels ou d'atomes associée au régime de fluage diffusion entraîne généralement une augmentation de la taille de grains.

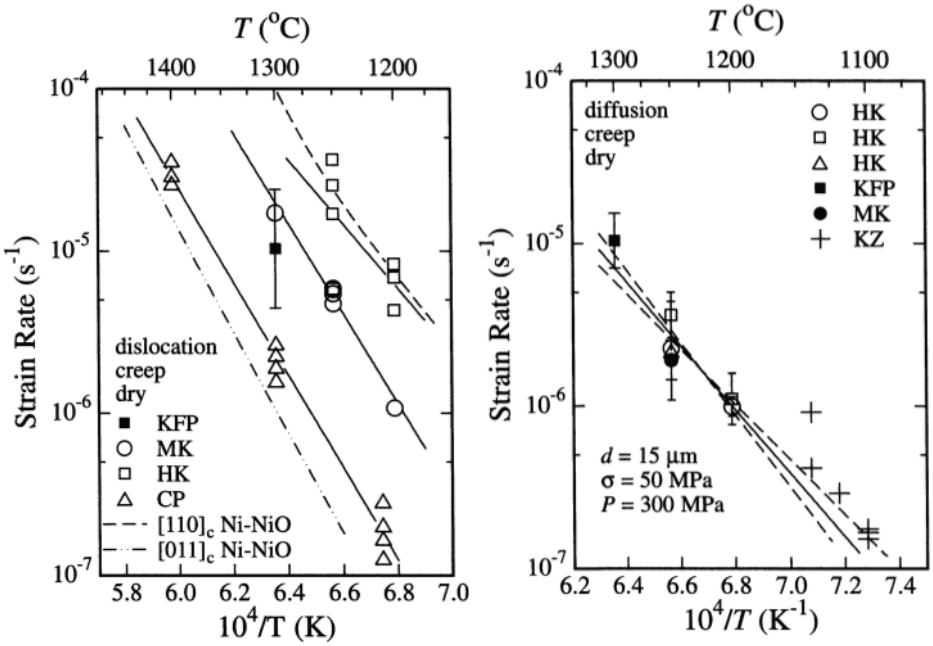

Figure 1.6 : Diagramme d'Arrhenius montrant le taux de déformation en fonction de 1/T pour des agrégats d'olivine se déformant par fluage dislocation et par fluage diffusion (Hirth et Kohlstedt, 2003). Les lignes pleines et en pointillées montrent les relations d'Arrhenius pour E*=530±40 et E*=550±20 kJ/mol et n=3.5 (gauche) et pour E*=375±50 kJ/mol (droite) et n=1. Les différents symboles correspondent aux données expérimentales de diverses études (HK : Hirth and Kohlstedt (1995a, b) ; KFP : Karato et al. (1986); MK : Mei and Kohlstedt (2000a, b) ; KZ : Kohlstedt and Zimmerman (1996)).

1.2.2. Effet de la taille de grain

Parmi les autres paramètres pouvant considérablement affecter la viscosité du manteau se trouve la taille de grain. L'équation (1) prédit une diminution du taux de déformation à taille de grain croissante. Une variation de la taille de grains va également entraîner un changement de mécanisme de déformation. A température constante, une roche se déformant par fluage dislocation voit sa taille de grains moyenne par recristallisation dynamique et donc sa viscosité diminuer. Ce changement peut entraîner un passage vers une déformation par fluage diffusion (Figure 1.7) (Rutter and Brodie, 1988). Il est aussi couramment admis qu'une diminution de la taille de grains par recristallisation dynamique peut favoriser la transition

d'une déformation par fluage dislocation à une déformation par fluage dépendant de la taille de grain (grain sensitive creep), sous lequel le glissement aux joints grains (grain boundary sliding) accommoderait la déformation (e.g. Boullier and Gueguen, 1975; Hirth and Kohlstedt, 2003; Hirth and Kohlstedt, 1995a, b; Langdon, 1994; Schmidt et al., 1977). La réduction de taille de grains liée à un tel régime a pour effet de diminuer considérablement la viscosité et pourrait favoriser une localisation de la déformation. Toutefois, les exemples de glissement aux joints de grains dans des échantillons naturels sont extrêmement rares et limités à des bandes d'ultra-mylonites de largeur millimétrique ou à des bandes de cisaillement composées d'orthopyroxène dans les mylonites du craton du Kaapvaal (e.g. Boullier and Gueguen, 1975; Vauchez et al., 2012 et références citées).

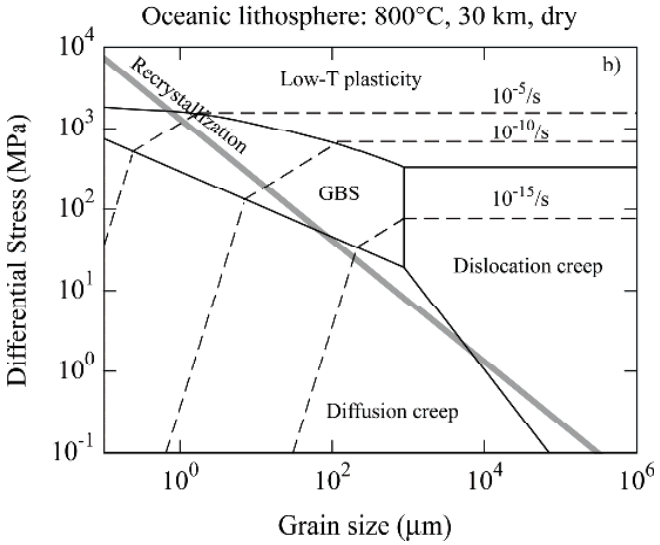

Figure 1.7 : Exemple de carte des mécanismes de déformation pour la lithosphère océanique à 800°C (Hirth et Karato, 2002).

1.2.3. Rôle de l'assemblage minéralogique

L'assemblage minéralogique a de nombreuses implications sur la rhéologie d'une roche. Dans la nature, les roches polyminérales subissant une déformation plastique tendent à voir les minéraux qui les composent se répartir en couches monominérales distinctes (e.g. Herwegh et al., 2008; Mehl and Hirth, 2008; Vauchez et al., 2012). S'il existe une différence de résistance entre les divers minéraux, cette microstructure engendre une anisotropie mécanique diminuant la résistance au cisaillement parallèle aux couches (Vauchez et al., 2012). De la même façon, la cristallisation de nouvelles phases moins résistantes lors de réactions durant la déformation peut également réduire la viscosité d'une roche (Rutter and Brodie, 1988).

Plusieurs autres études ont souligné les implications de la présence d'une seconde phase sur la taille de grains d'une roche (Farla et al., 2013; Hiraga et al., 2010; Solomatov et al., 2002). En effet, la croissance de grains peut être limitée par la présence d'une seconde phase en quantité suffisante sous l'effet d'un processus nommé épinglage de Zener (Zener pinning ; Figure 1.8 ; (Farla et al., 2013; Smith, 1948; Solomatov et al., 2002). Il a donc été proposé que le Zener pinning pourrait permettre de préserver des tailles de grain fines et donc une viscosité faible dans le manteau (e.g. Bercovici and Ricard, 2012; Farla et al., 2013).

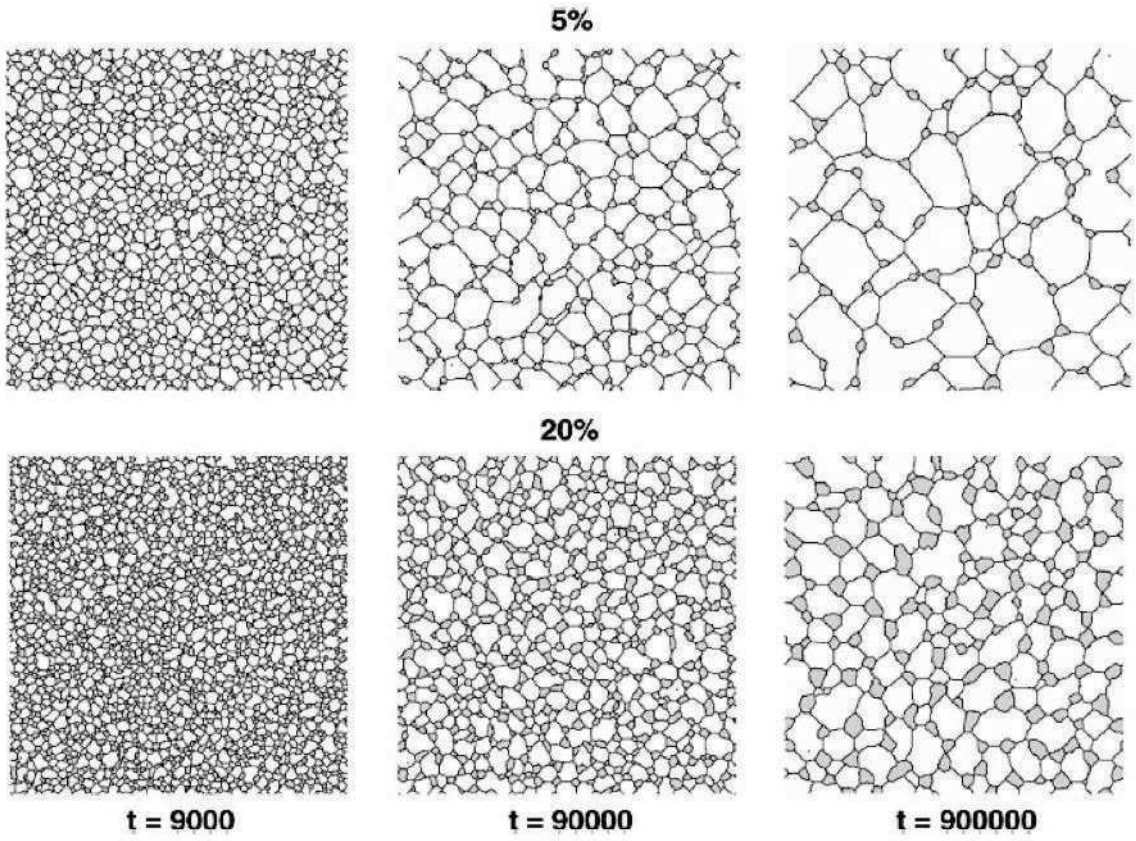

Figure 1.8 : Evolution microstructurale d'un système à deux phases cristalline, pour diverses fractions de la deuxième phase (modèle numérique de Solomatov et al., 2002). Chaque carré correspond à un test différent.

1.2.4. Effet de la teneur en hydrogène

Les roches du manteau supérieur sont principalement composées de minéraux nominalement anhydres (NAMs : Nominally Anhydrous Minerals) ne contenant pas d'H_2O, d'OH ou d'H dans leur dans leur formule structurale. Ces minéraux peuvent toutefois incorporer des atomes d'hydrogène associés à des défauts ponctuels au sein de leur structure (Beran and Putnis, 1983; Beran and Zemman, 1969; Miller et al., 1987). La solubilité de l'eau est ainsi principalement contrôlée par 3 types de défauts : (1) par substitution d'un site métallifère au sein d'un octaèdre (Mg^{2+}, Fe^{2+} ou Fe^{3+}), (2) par substitution d'un Si^{4+} au cœur

d'un tétraèdre, (3) dans un site interstitiel. La solubilité de l'hydrogène dans l'olivine (C_{OH}) peut être exprimée par une loi de puissance semi-empirique où la solubilité est directement proportionnelle à la fugacité en eau (f_{H2O}) (Férot and Bolfan-Casanova, 2012; Hirschmann et al., 2005; Kohlstedt et al., 1996; Zhao et al., 2004). Elle est également fonction de la pression (Férot and Bolfan-Casanova, 2012; Hirschmann et al., 2005; Kohlstedt et al., 1996), et de la teneur en Fe à basse pression (0,3 GPa ; Zhao et al., 2004). L'expression exacte de cette loi est fonction des conditions expérimentales et des paramètres étudiés.

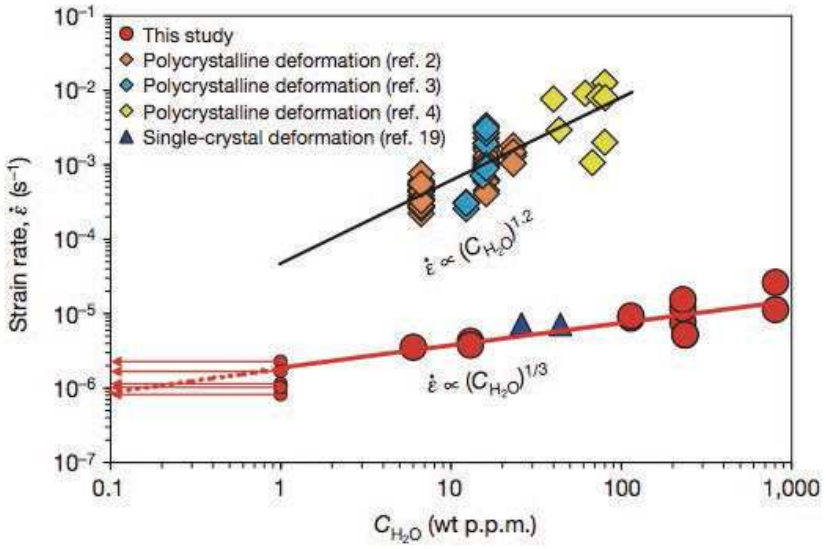

Figure 1.9 : Evolution du taux de déformation en fonction de la teneur en hydrogène (Fei et al., 2013).

La teneur en hydrogène figure parmi les paramètres souvent cités pour son effet sur la rhéologie du manteau (e.g. Hirth and Kohlstedt, 1996). Ainsi, l'équation (1) prédit une diminution de la résistance si la fugacité en eau dans le système augmente. Des expériences ont montré que l'incorporation d'hydrogène engendre une diminution de résistance mécanique des roches mantelliques et augmentent les taux de fluage dislocation et fluage diffusion (Figure 1.9) (e.g. Chopra and Paterson, 1984; Demouchy et al., 2012; Karato et al., 1986; Mackwell et al., 1985; Mei and Kohlstedt, 2000a, b). Toutefois, ces résultats ayant été obtenus sur des échantillons placés dans un milieu saturé en eau, et de l'eau libre pourrait avoir été présente aux joints de grains (Demouchy et al., 2012; Fei et al., 2013). En effet, des expériences récentes de détermination du coefficient de diffusion du Si dans la forstérite par Fei et al. (2013) suggèrent ainsi que l'effet de l'hydrogène sur la déformation de l'olivine pourrait être faible (Figure 1.7). Une reproductibilité de tels résultats est toutefois nécessaire afin de remettre en cause avec certitude l'effet de hydrogène sur la résistance des roches

mantelliques obtenus par de nombreuses études expérimentales précédentes.

1.2.5. Effet de la présence de magmas

La présence de faibles fractions de magma peut considérablement diminuer la résistance mécanique d'une roche du manteau supérieur (Daines and Kohlstedt, 1997; Mei et al., 2002; Zimmerman and Kohlstedt, 2004). La distribution de ces magmas revêt une grande importance sur le style de déformation auquel la roche pourra être soumise. En effet, alors qu'une distribution homogène dans un volume important tend à promouvoir une déformation homogène (e.g. Vauchez et al., 2007), la présence de magmas localisés dans un faible volume pourrait favoriser une localisation de la déformation (e.g. Holtzman et al., 2003a; Holtzman et al., 2003b; Vauchez et al., 2012). Par ailleurs, des expériences en cisaillement simple suggèrent que durant la déformation de roches partiellement fondues, le magma se concentre en bandes distinctes qui localisent la déformation (Holtzman et al., 2003a; Holtzman et al., 2003b). Enfin, l'étude des microstructures et des OPRs dans une section verticale de la zone de transition croûte-manteau des ophiolites d'Oman révèle un changement de l'OPR de l'olivine en présence de magma d'une symétrie axiale-[100] à une symétrie axiale-[010] (Higgie and Tommasi, 2012). A plus grande échelle, un tel changement pourrait donc créer une hétérogénéité au sein de la lithosphère.

Les conséquences possibles de l'injection de magmas sont multiples. En effet, si le liquide n'est pas à l'équilibre avec la roche encaissante, leur percolation peut engendrer un métasomatisme. Selon la composition du liquide, un tel métasomatisme peut lui-même résulter en la cristallisation de nouvelles phases ou en l'hydratation des minéraux présents et modifier la rhéologie de la roche percolée (voir sections 1.2.3 et 1.2.4). De même, l'injection de larges volumes de magmas peut entraîner une modification locale de la température (Kourim et al., 2014).

1.2.6. Rôle de l'anisotropie mécanique

Une roche se déformant par fluage dislocation développe une orientation préférentielle de réseau des cristaux (OPR) qui la composent. Le développement des ces OPRs à grande échelle dans des zones tectoniquement actives a pour effet de générer une anisotropie mécanique, mesurée par les études sismiques sur les déphasages des ondes SKS sur de larges distances. De cette anisotropie découle une diminution de la résistance aux contraintes imposées selon certaines directions par rapport à l'OPR existante. En effet, des modèles numériques montrent que la résistance du manteau devient alors plus faible à des

cisaillements parallèles à la foliation et à la linéation (Tommasi et al., 2009) ou à une extension ou une compression oblique à la fabrique préexistante (Tommasi et al., 2009; Tommasi and Vauchez, 2001) devient alors plus faible (Figure 1.10). Une variation de l'orientation et de l'intensité des OPRs au sein du manteau lithosphérique pourrait donc permettre une localisation de la déformation à grande échelle (Tommasi et al., 2009). Le parallélisme entre l'axe d'anciens orogènes et l'axe des rifts a ainsi conduit Vauchez et al. (1997) à proposer que d'anciennes OPRs fossilisées dans le manteau lithosphérique pourraient être réactivées lors de la formation d'un rift.

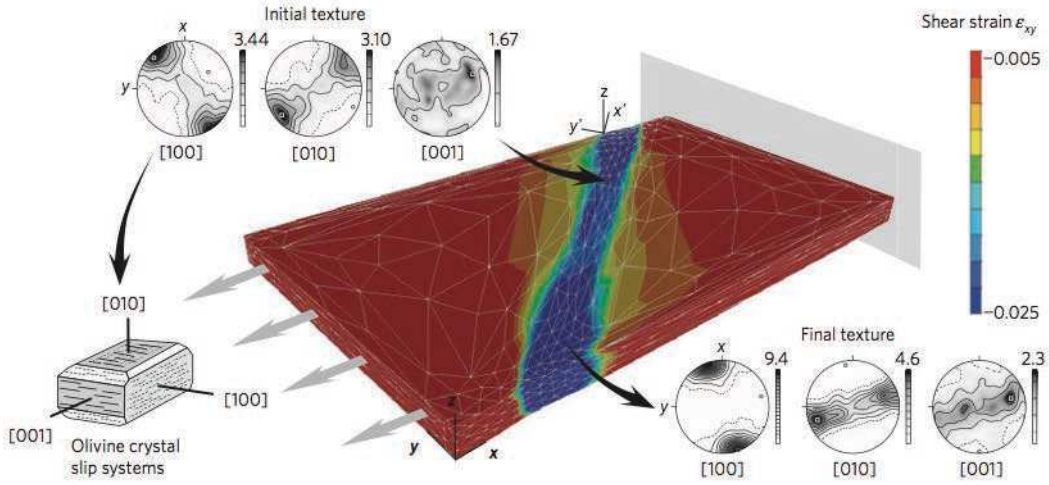

Figure 1.10 : Géométrie, conditions aux limites et distribution de la déformation cisaillante après un étirement total de 40% dans un modèle avec une zone de cisaillement héritée à 45° de la direction d'extension imposée (Tommasi et al., 2009).

1.3. Objectifs de la thèse et structure du mémoire : Le craton et le rift comme objet d'étude du comportement du manteau subcontinental

1.3.1. Le craton du Kaapvaal

Le craton du Kaapvaal fait partie des cratons ayant survécu à la tectonique des plaques et la convection mantellique depuis leur formation. Il est formé d'un assemblage de terrains Archéens composés principalement de gneiss et de granitoïdes, recouverts par des bassins sédimentaires datant de l'Archéen supérieur et du Protéroizoïque inférieur (Begg et al., 2009; de Wit et al., 1992). La formation de la croûte il y a ~3.7-3.1 Ga fut suivi par l'amalgamation et la stabilisation des différents blocs qui composent le craton il y a 3.1-2.6 Ga (de Wit et al.,

1992; Griffin et al., 2003b). Des analyses Re-Os sur les sulfides dans des inclusions dans des diamants et dans des xénolites mantelliques indiques que la formation de la racine cratonique serait antérieure à 3 Ga et donc contemporaine de la formation de la croûte (Griffin et al., 2003b; Shirey et al., 2002).

Le craton du Kaapvaal a été ensuite affectée par de multiples épisodes magmatiques. La mise en place du complexe du Bushveld il y a 2.05 Ga (e.g. Scoates and Friedman, 2008) est le premier et le plus important d'entre eux. Il fut suivi il y a 182 Ma par la mise en place de la province volcanique du Karoo associée à la rupture du Gondwana (Riley et al., 2005). Le craton du Kaapvaal fut ensuite affecté par de nombreuses éruptions kimberlitiques principalement à la fin du Jurassique et au Crétacé, mais aussi au Paléozoïque (530-255 Ma) et au Méso-Protérozoïque (1650-1200 Ma) (Allsopp et al., 1985; Kramers and Smith, 1983; Phillips et al., 1998). La répartition de ces diatrèmes kimberlitiques est large. Les kimberlites sont des laves remontées depuis la base de la lithosphère à très grande vitesse (Mitchell, 1986) en transportant de nombreux xénolites mantelliques provenant d'une large gamme de profondeurs (James et al., 2004). Ces xénolites font du craton du Kaapvaal un objet d'étude idéal pour tenter de comprendre le manteau lithosphérique subcontinental des racines cratoniques. Depuis plusieurs dizaines années, le craton du Kaapvaal a été l'objet de nombreuses publications qui apportent des contraintes précieuses à toute nouvelle étude visant à mieux comprendre sa structure ainsi que l'origine de sa stabilité (voir les chapitres 2 et 4 de ce manuscrit pour une revue plus complète de ces publications).

1.3.2. Le rift Est-Africain

Le rift Est Africain est un des rifts les plus actifs de la planète. Il s'étend sur plus de 4 000 km du point triple de l'Afar au golfe du Mozambique en suivant la direction d'anciens orogènes (e.g. Nyblade and Brazier, 2002; Vauchez et al., 1997). Les témoins les plus anciens du volcanisme lié au rift datent de 45 Ma et ont été trouvés au Kenya, au niveau de la dépression de Turkana, un système de bassins en extension de près de 300 km, au niveau duquel l'axe du rift se décale. La branche éthiopienne du rift Est-Africain ou rift Ethiopien commença à se propager au Sud de l'Ethiopie il y a 25-20 Ma (Hendrie et al., 1994; Morley et al., 1992) avant d'atteindre le Nord de l'Ethiopie il y a 11 Ma (Wolfenden et al., 2004). Le rift Est-Africain migra aussi vers le Sud et se subdivise en deux branches distinctes autour du craton tanzanien. Dans la branche Est du rift, le volcanisme et l'extension date atteignirent le Sud du Kenya il y a 8-5 Ma (Cerling and Powers, 1977; Crossley and Knight, 1981; Dawson, 1992). Dans la branche Ouest, les premières traces de volcanisme remontent à 12 Ma au

Nord, à 6 Ma près du Rwanda (Kampunzu et al., 1998).

Le rift Est Africain est associé à deux plateaux à la topographie élevée (le plateau Ethiopien et le plateau Est-Africain), dont l'existence pourrait être liée à la présence d'un ou plusieurs panaches mantelliques détectés dans plusieurs modèles de tomographie sismique (e.g. Adams et al., 2012; Benoit et al., 2006; Ritsema et al., 1998) et interprétés comme la continuation du super-panache africain, une large anomalie de vitesse lente détectée dans le manteau inférieur sous le craton sud-africain (e.g. Benoit et al., 2006; Ritsema and van Heijst, 2000).

En Ethiopie, au Kenya et en Tanzanie, des laves ont rapporté à la surface des xénolites mantelliques, qui représentent un objet d'étude idéal pour comprendre les processus affectant le manteau subcontinental à différents stades de rifting.

1.3.3. Objectifs de la thèse et structure du mémoire

L'objectif de ce travail est d'étudier le manteau lithosphérique subcontinental de deux objets aux caractéristiques et aux comportements géodynamiques opposés : le craton du Kaapvaal (Afrique du Sud) et le rift Est-Africain (Divergence Nord Tanzanienne et SE Ethiopie), afin de tenter de comprendre les processus permettant d'expliquer ces différences. L'étude de la déformation (microstructures et OPRs) et de l'hydratation de xénolites mantelliques du craton Kaapvaal apporte des contraintes sur le rôle de l'hydrogène sur la stabilité à long terme du manteau subcratonique. Ce travail a été complété par une série d'expériences visant à affiner notre interprétation sur l'origine des teneurs en hydrogène mesurées. Le calcul des propriétés sismiques de ces échantillons permet de enfin de caractériser la structure de la racine cratonique, en quantifiant l'impact des variations de composition lié au métasomatisme sur celles-ci, et en tentant de relier l'anisotropie sismique et l'orientation de la fabrique fossilisée. Enfin, l'étude du rift Est-Africain à deux stades de maturité différents et développé dans des régions présentant des héritages structuraux différents vise à contraindre le rôle de l'anisotropie mécanique, des hétérogénéités rhéologiques, et des interactions de fluides et de magmas sur le type et le régime de déformation d'un rift continental.

Ce mémoire est présenté sous la forme de 7 chapitres. Il comporte 2 articles publiés dans des revues internationales (*Lithos* et *Solid Earth*), un article soumis à *Tectonophysics*, un article soumis à *American Mineralogist* et un article en cours de préparation.

Le chapitre 2 « **Déformation et hydratation du manteau lithosphérique sous le**

craton du Kaapvaal » présente une étude sur 50 xénolites péridotitiques échantillonnés dans 9 diatrèmes kimberlitiques différents au sein du craton du Kaapvaal. Ce travail a été publié dans le journal *Lithos* (Baptiste et al., 2012) et repose sur l'analyse des microstructures, des OPRs, et sur les teneurs en hydrogène dans l'olivine de ces xénolites. Il a pour objectif de contraindre les relations entre déformation, hydratation et percolation de fluides ou magmas au sein d'une racine cratonique, et ainsi de mieux comprendre l'origine de sa longévité.

Le chapitre 3 « **Diffusion de l'hydrogène d'un liquide kimberlitique à la forstérite** » présente une étude expérimentale soumise en Septembre 2014 à la revue *American Mineralogist,* basée sur 5 expériences réalisées en piston-cylindre au laboratoire Magmas et Volcans de Clermont-Ferrand. Son but est de tester si l'incorporation d'hydrogène dans l'olivine par diffusion ionique à partir d'un liquide kimberlitique riche en volatiles (H_2O-CO_2) à haute pression est possible durant le transport de la péridotite vers la surface par le magma, et ainsi de mieux comprendre l'origine des fortes teneurs en hydrogène dans l'olivine des xénolites cratoniques.

Le chapitre 4 « **Contraintes pétrophysiques sur les propriétés sismiques du manteau lithosphérique sous le craton du Kaapvaal** » présente une étude publiée dans le journal *Solid Earth* (Baptiste et Tommasi, 2014) où les propriétés sismiques des 50 xénolites du craton du Kaapvaal sont calculées. Il a pour but de mieux comprendre les variations de vitesses et les anisotropies mesurées par les études sismiques et de mieux évaluer les structures qui en sont déduites, en les confrontant aux variations des propriétés sismiques liées à la composition, à la profondeur d'origine, et à un changement de l'orientation de la foliation dans les xénolites Sud-africain.

Le chapitre 5 « **Déformation, hydratation et anisotropie du manteau lithosphérique sous un rift actif** » est une étude sur 53 xénolites mantelliques provenant de 4 localités différentes au sein de la Divergence Nord Tanzanienne du Rift Est-Africain. Ce travail a été soumis au mois de Juillet 2014 au journal *Tectonophysics,* et est actuellement en cours d'évaluation. Il est basé sur la caractérisation des microstructures, des OPRs, des teneurs en hydrogène dans l'olivine des xénolites tanzaniens, ainsi que sur le calcul de leurs propriétés sismiques. Il vise à mieux comprendre les relations entre déformation et percolation de fluides et magmas au début du rifting ainsi que le régime de déformation mis en jeu.

Le chapitre 6 « **Déformation et anisotropie du manteau lithosphérique sous un rift mature**» est un article en cours de rédaction sur 25 xénolites mantelliques provenant de la région au Sud de Mega (Sud de l'Ethiopie, Rift Est Africain). Ce travail a pour objectif de comprendre les relations entre déformation et percolation de magmas au sein d'un rift mature

formé à l'aplomb d'un panache mantellique.

Le chapitre 7 « **Discussions, Conclusions et Perspectives** » présente une discussion et une synthèse générale sur le rôle de l'anisotropie mécanique, la percolation de fluides et magmas, l'hydratation et les hétérogénéités rhéologiques sur le comportement géodynamique du manteau subcontinental. Les nouvelles questions posées par les résultats obtenus dans cette étude et les approches possibles pour y répondre sont aussi exposées.

Chapitre 2: Déformation et hydratation du manteau lithosphérique sous le craton du Kaapvaal

Le craton du Kaapvaal est un domaine continental épais et froid resté stable depuis sa formation durant l'Archéen (Griffin et al., 2004; Pearson et al., 1995; Shirey et al., 2002). Les péridotites du Kaapvaal montrent des compositions appauvries en CaO et Al_2O_3 et des Mg# dans l'olivine élevés, suggérant qu'elles sont le résultat de forts taux de fusion partielle (Boyd and Mertzman, 1987). Pourtant, ces compositions appauvries et le géotherme froid caractéristiques des cratons ne suffisent pas à générer des contrastes de viscosité suffisamment élevés pour expliquer la stabilité et la longévité des cratons (Doin et al., 1997; Lenardic and Moresi, 1999). Partant de l'idée que l'épisode de fusion partielle ayant formé les cratons avait dû entrainer une déshydratation de la racine, plusieurs études ont ainsi proposé qu'un contraste de densité suffisant pouvait être lié à de très faibles teneurs en hydrogène dans l'olivine (Doin et al., 1997; Pollack, 1986). Pourtant, une étude récente de Peslier et al. (2010) révèle que des teneurs en hydrogène dans l'olivine de xénolites mantelliques du Kaapvaal sont souvent élevées (jusqu'à 100 wt. ppm H_2O), à l'exception des échantillons les plus profonds (<10 wt. ppm H_2O). De plus, de multiples épisodes métasomatiques ont été identifiés dans les péridotites du craton du Kaapvaal (e.g. Boyd and Mertzman, 1987; Griffin et al., 2003b; Kelemen et al., 1998; Nixon et al., 1981; Simon et al., 2007).

Le travail présenté dans ce chapitre se base sur l'étude de 50 xénolites péridotitiques échantillonnés dans 9 diatrèmes kimberlitiques différents au sein du craton du Kaapvaal. Ces péridotites présentent donc une large distribution latérale, mais aussi verticale. L'analyse des microstructures et des OPRs révèle que les échantillons granulaires à gros grains qui prédominent parmi les péridotites du Kaapvaal enregistrent une déformation par fluage dislocation, suivie par une longue période de recuit. Ces observations supportent un épisode de déformation ancien, probablement associé à la formation de la racine, suivie d'un refroidissement lent et d'une longue période de quiétude. Les textures et compositions révèlent également de multiples évènements métasomatiques à la répartition géographique hétérogène. L'analyse combinée des microstructures et des OPRs montre que les épisodes

métasomatiques à l'origine des fortes compositions modales en orthopyroxene sont pré- à post-cinématiques. Le métasomatisme causé par des fluides riches en K est quand à lui post-cinématique. L'analyse des textures et des OPRs des mylonites cratoniques suggèrent une déformation plus tardive et locale. Les teneurs en hydrogène sont variables, mais ont tendance à augmenter jusqu'à une profondeur d'environ 150 km (~150 wt. ppm H_2O, calibration de Bell et al. (2003)). Les échantillons les plus profonds sont quant à eux presque secs. L'absence de corrélation entre les teneurs en hydrogène et le Mg# de l'olivine suggèrent une réhydratation postérieure à la formation de la racine cratonique appauvrie, par métasomatisme lié à la percolation des fluides ou magmas riches en eau ou par contamination durant le transport des xénolites à la surface par les kimberlites. Or, une étude magnétotellurique récente montre que les données de conductivité (Evans et al., 2011) sont mieux expliquées par un modèle montrant une variation de la teneur en hydrogène dans l'olivine similaire à celle mesurée (Fullea et al., 2011), suggérant que ces données pourrait être représentatives de l'ensemble de la racine cratonique. Que cette réhydratation soit extensive ou plus hétérogène, elle n'a toutefois pas à ce jour entraîné une remobilisation de la racine d'après les textures très recuites des péridotites cratoniques.

Lithos 149 (2012) 31–50

Contents lists available at SciVerse ScienceDirect

Lithos

journal homepage: www.elsevier.com/locate/lithos

Deformation and hydration of the lithospheric mantle beneath the Kaapvaal craton, South Africa

Virginie Baptiste *, Andréa Tommasi, Sylvie Demouchy

Géosciences Montpellier, Université Montpellier 2 & CNRS, CC 60, Place E. Bataillon, 34095 Montpellier cedex 5, France

ARTICLE INFO

Article history:
Received 21 October 2011
Accepted 3 May 2012
Available online 12 May 2012

Keywords:
Craton
Kaapvaal
Peridotite
Deformation
Olivine crystal preferred orientations
Water contents

ABSTRACT

To constrain the relations between deformation and metasomatism in the subcratonic lithospheric mantle, we have analyzed the microstructures and crystal preferred orientations in 50 mantle xenoliths from the Kaapvaal craton. Water contents in olivine and pyroxenes were measured in 14 samples equilibrated at different depths. Coarse-granular microstructures recording deformation by dislocation creep followed by annealing predominate. Mylonitic (sheared) peridotites with partially or totally recrystallized microstructures are however common below 140 km. Refractory compositions predominate, but multiple metasomatic events resulted in orthopyroxene enrichment or secondary crystallization of clinopyroxene and phlogopite. Coherent orthopyroxene and olivine CPO in most coarse-grained peridotites implies in pre- to syn-kinematic orthopyroxene enrichment or epitaxial growth on primary orthopyroxene. Undeformed, interstitial orthopyroxene, clinopyroxene, and phlogopite with random orientations in coarse-grained peridotites record post-kinematic modal metasomatic events. Deformation of these phases in the sheared peridotites implies that mylonitization results from a later event, which affected locally the deep cratonic lithosphere. Olivine CPO recording dominant [100] glide predominate at all depths. Only two samples, equilibrated at ~3.3 GPa show olivine [001] and orthopyroxene [001] axes subparallel, suggesting dominant [001] glide. Water contents in olivine are maximum (150 wt. ppm H_2O) in peridotites equilibrated at ~160 km depth. Peridotites equilibrated below 180 km depth are, in contrast, almost dry. Lack of correlation between olivine mg# and water content indicates that the high water contents in olivine record re-hydration after the extensive partial melting, which produced the cratonic root. The vertical variation in water contents in olivine observed in the Kaapvaal peridotites may result from hydrogen addition or loss during extraction by the kimberlites. Comparison with magnetotelluric electrical conductivity data suggests, however, that the observed vertical variation of water contents in olivine may be representative of the present-day state of the Kaapvaal mantle, implying that extensive metasomatism resulted in hydration of the cratonic mantle at intermediate depths. The annealed microstructures of Kaapvaal peridotites indicate however that this metasomatism was not followed by remobilization of the cratonic root.

1. Introduction

Cratons are domains of thick lithosphere with cold geotherms (Boyd et al., 1985; Chevrot and Zhao, 2007; Evans et al., 2011; Jaupart and Mareschal, 1999), which have remained stable for long geologic periods since their formation in the Archean (Pearson et al., 1995). However, while the mantle roots of some cratons, such as the Kaapvaal in South Africa, survived from reworking by plate tectonics and mantle convection since the Archean, others, like the north China and Wyoming craton, were partially destroyed in more recent times (e.g., Eggler and Furlong, 1991; Menzies et al., 1993). The processes that result in the stability or destruction of the cratonic mantle roots are poorly constrained, and are a major open question in geodynamics.

Studies of kimberlite-embedded xenoliths reveal that most cratonic peridotites are depleted in CaO and Al_2O_3 and have olivine with high mg# (mg# = MgO/(MgO + FeO)), implying that they were formed by a high degree of partial melting (e.g., Boyd and Mertzman, 1987). These observations led Jordan (1978) to propose the isopycnic (equal density) hypothesis to explain the stability of craton roots: the more refractory composition of the sub-cratonic mantle compensates the increase in density linked to cooling, implying a neutral buoyancy with respect to the asthenosphere. However, numerical models show that buoyancy alone is unable to explain the stability of cratons over several Ga (Doin et al., 1997; Lenardic and Moresi, 1999). The most common explanation for cratonic root longevity is a high viscosity contrast with the surrounding mantle (Doin et al., 1997; Pollack, 1986). The stability of cratonic roots is also favored by higher yield stresses relative to the

* Corresponding author. Tel.: +33 467144912; fax: +33 467143603.
E-mail address: virginie.baptiste@gm.univ-montp2.fr (V. Baptiste).

0024-4937/$ – see front matter © 2012 Elsevier B.V. All rights reserved.
doi:10.1016/j.lithos.2012.05.001

surrounding lithosphere and by neighboring weak material, such as mobile belts, which may localize the deformation (Lenardic et al., 2003).

The stability of cratonic roots appears therefore to depend essentially on its rheological properties. As the dominant phase (≥50% in volume), olivine controls these properties. The strength of olivine-rich rocks under upper mantle conditions depends strongly on stress, temperature, grain size, and water fugacity (e.g., Demouchy et al., 2009; Hirth and Kohlstedt, 2003) and, on a lesser extent, on pressure, chemical composition, and oxygen fugacity (e.g., Keefner et al., 2011; Raterron et al., 2007). The relatively cold cratonic geotherm results in a viscosity increase of the cratonic root relatively to the surrounding convective mantle, but it cannot generate the 2–3 orders of magnitude viscosity contrast mantle required to ensure craton stability over Gy time spans (Doin et al., 1997; Lenardic and Moresi, 1999). Based on the assumption that the partial melting event responsible for the refractory compositions of cratonic xenoliths led to extensive devolatilization of the cratonic mantle, many models consider that the high viscosity of the cratonic mantle results from extremely low water concentrations in olivine (e.g., Doin et al., 1997; Pollack, 1986). However, water contents in olivine from the Kaapvaal mantle measured by Fourier transform infrared spectroscopy (FTIR) are often high (up to 100 wt. ppm H_2O), except for the deepest samples (below 180 km), which have <10 wt. ppm H_2O (Grant et al., 2007; Kurosawa et al., 1997; Peslier et al., 2010).

In the present study, we explore the relations between deformation, melt or fluid percolation, and hydration by jointly analyzing microstructures, crystallographic preferred orientations, and water contents in a new series of peridotite xenoliths of the Kaapvaal craton. Previous petrophysical studies carried out on cratonic xenoliths focused on either the relation between deformation and seismic anisotropy (Bascou et al., 2011; Ben Ismaïl et al., 2001) or on the water contents (Bell et al., 2004; Peslier et al., 2008, 2010; Yang et al., 2008). The association of two approaches results in additional constraints on the relative timing of deformation and hydration. For instance, experiments on olivine aggregates deformed under high water fugacities (>50 wt. ppm H_2O) produced olivine crystal preferred orientation patterns that differ significantly from those obtained under dry conditions; these results were interpreted as due to changes in the dominant olivine slip systems due to variations in the OH^- concentration in olivine (Jung et al., 2006).

2. Geological setting

The Kaapvaal craton (South Africa) is an assemblage of Archean terranes that extends over more than 12,000 km^2. It is mainly composed by granitoids and gneisses that enclose narrow greenstone belts, but Upper Archean and Lower Proterozoic basins cover most of it (Begg et al., 2009; de Wit et al., 1992). Crustal formation occurred essentially between ~3.7 and ~3.1 Ga, followed by terrane assembly and stabilization of the craton between 3.1 and 2.6 Ga (de Wit et al., 1992; Griffin et al., 2003).

Formation of the Kaapvaal mantle root as early as 3.3–3.5 Ga is indicated by Re–Os whole-rock data on peridotite xenoliths (Pearson et al., 1995) and on sulfides in diamond inclusions (Shirey et al., 2002). These conclusions were confirmed by Re–Os analyses of sulfide phases in peridotite xenoliths, which indicate that the Kaapvaal mantle root formed prior to 3 GPa, that is, previously to or simultaneously to the formation of the crust, implying that each terrane carried its own keel during the craton assembly (Griffin et al., 2004).

Recent electrical conductivity measurements suggest that the lithosphere beneath the central Kaapvaal craton is currently defined by a high resistivity layer 200–250 km thick (Evans et al., 2011). High seismic velocities imaged in body and Rayleigh wave tomography also indicate a 250 km thick root beneath most of the craton (Chevrot and Zhao, 2007; James et al., 2001). Body-wave data suggest however that the high-velocity cratonic root may locally attain depths of 300 km (James et al., 2001). A slightly thinner high-velocity layer, 175–250 km thick, was imaged recently using SH-waves (Begg et al., 2009). These lithospheric thicknesses estimated from geophysical data are slightly higher, but still consistent with the 185 to 215 km thick Kaapvaal lithosphere constrained by xenolith thermobarometry (Eaton et al., 2009).

Following its stabilization, the Kaapvaal craton was affected by several magmatic events. The most important is the Bushveld complex, which intruded the Kaapvaal craton at 2.05 Ga (Scoates and Friedman, 2008). Another major magmatic event was the extrusion of the Karoo large igneous province at 182 Ma (Riley et al., 2005), which is associated with the Gondwana breakup. The craton was also affected by numerous kimberlitic eruptions. Kimberlitic pipes were mostly emplaced between the Late Jurassic and the Cretaceous (Kramers and Smith, 1983), but also erupted between 1650 and 1200 Ma (Kramers and Smith, 1983) and between 530 and 255 Ma (Allsopp et al., 1985; Kramers and Smith, 1983; Phillips et al., 1998).

These kimberlitic pipes contain xenoliths of the cratonic mantle that have been extensively studied for their microstructures, petrology, and geochemistry. Kaapvaal mantle xenoliths may be classified in two groups: (1) coarse-grained peridotites, which have dominantly refractory compositions and (2) fine-grained sheared peridotites, which are equilibrated at high temperatures and pressures and have, on average, more fertile compositions (Boullier and Nicolas, 1975; Boyd and Mertzman, 1987; Boyd and Nixon, 1975; Nixon et al., 1981). Petrological and geochemical data on Kaapvaal coarse-grained nodules reveal that they represent a highly refractory lithospheric mantle residue, implying ~40% melt extraction, which was subsequently affected by several metasomatic episodes (e.g., Boyd and Mertzman, 1987; Griffin et al., 2003; Kelemen et al., 1998; Nixon et al., 1981; Simon et al., 2007). The high orthopyroxene/olivine ratio that characterizes many low-temperature Kaapvaal xenoliths, for instance, is usually attributed to Si-enrichment due to interaction with subduction-related fluids or intraplate hydrous melts (Bell et al., 2005; Kelemen et al., 1998; Simon et al., 2007; Wasch et al., 2009). Lu–Hf and Sm–Nd model ages on garnet and orthopyroxene clots in peridotite xenoliths from Kimberley suggest multiple, rather than a single Si-enrichment episode, ranging from 1.3 to 1.1 Ga to Neoproterozoic (Wasch et al., 2009). Kaapvaal xenoliths and xenocrysts also display geochemical evidence for refertilization, which added basaltic components like Fe, Ca and Al to a depleted protolith (Griffin et al., 2003). Crystallization of diopside, lherzolitic garnet, and phlogopite has been proposed to result from interactions with kimberlitic–carbonatitic fluids (Grégoire et al., 2003; Simon et al., 2007). Recent geochemical data indicate that diamonds and subcalcic garnets also result from interaction with reduced asthenosphere-derived fluids, corroborating the hypothesis that the cratonic mantle was originally essentially composed by highly refractory harzburgites and dunites (Malkovets et al., 2007). Melt-related metasomatism has also been identified in sheared peridotites, which may have acquired their fertile composition by interactions with asthenosphere-derived melts shortly before the kimberlitic eruption (O'Reilly and Griffin, 2010). In the present study, we will refer to all such changes in modal composition due to melt or fluid–rock interactions as modal metasomatism.

For the present study, we selected, from the >400 samples of the Kaapvaal mantle xenolith collection of Geosciences Montpellier (France), 50 peridotite xenoliths with varied microstructures and compositions. Study of samples from 9 pipes with ages ranging from 1.2 Ga to 87 Ma: Kimberley, Jagersfontein, Monastery, Lentseng, De Beers, Finsch, Kamfersdam, Premier, and Mothae (Fig. 1 and Table 1), allowed the sampling of possible lateral and temporal variations of deformation and composition in the Kaapvaal mantle. Analysis of a larger number of samples from Jagersfontein and Kimberley (18 samples for each locality) allowed studying vertical variations at these locations.

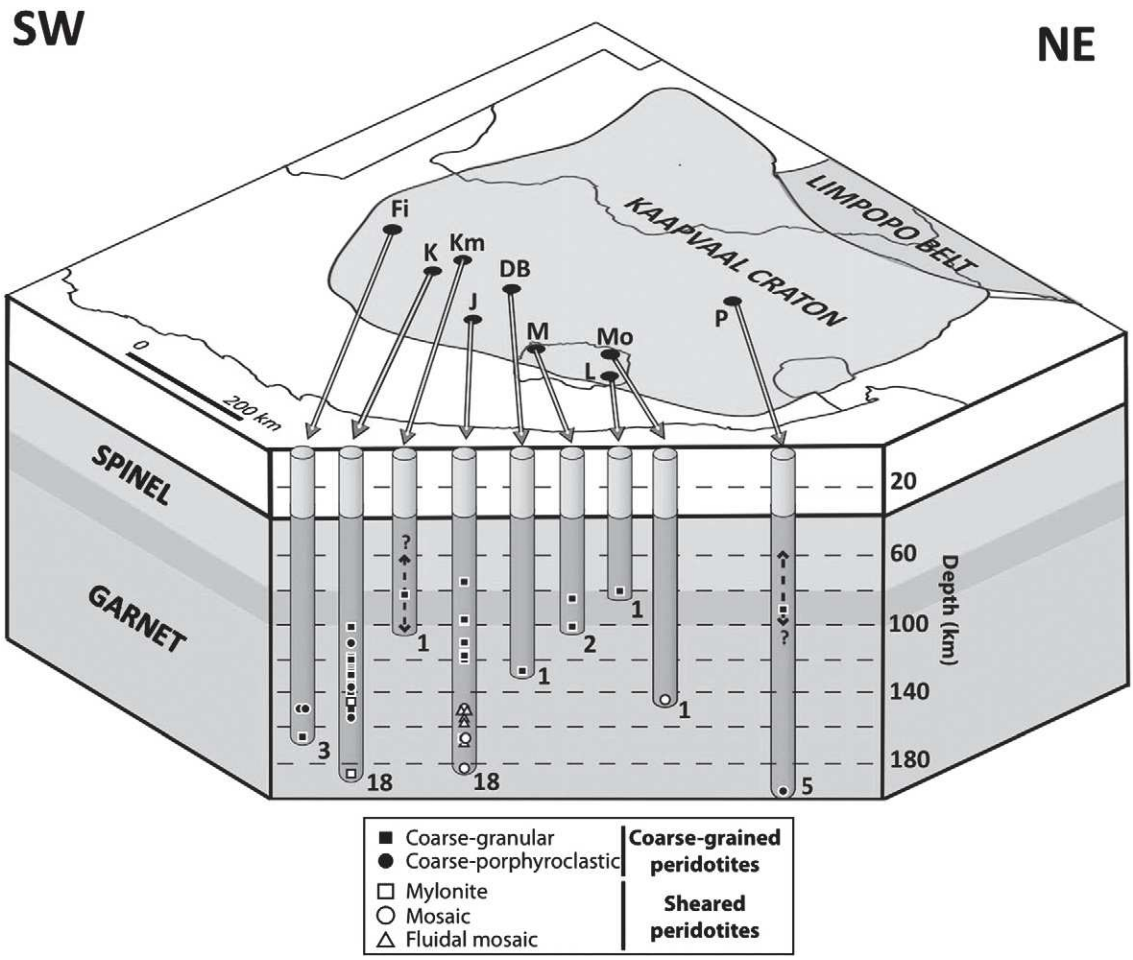

Fig. 1. Sketch of the Kaapvaal craton showing the location of the sampled kimberlite pipes (Fi: Finsch, K: Kimberley, Km: Kamfersdam, J: Jagersfontein, DB: De Beers, M: Monastery, Mo: Mothae, L: Lentseng, P: Premier) as well as the microstructure and calculated depth of provenance of the studied xenoliths. The number of xenoliths studied for each pipe is indicated at the bottom of the columns. Dark gray level indicates depths for which spinel- and garnet-bearing xenoliths are sampled.

3. Methods

3.1. Mineral compositions and pressure–temperature estimates

Chemical compositions of olivine, orthopyroxene, clinopyroxene, garnet and spinel were analyzed using a Cameca SX100 electron microprobe at Microsonde Sud facility, in Montpellier (France). Analysis conditions were a 20 kV accelerating voltage and a 10 nA probe current. Core and rim compositions were analyzed systematically. For each mineral phase, three to four grains were measured. The aim was to determine pressure and temperature equilibrium conditions of the selected peridotites to constrain their depth distribution. Equilibrium temperatures were calculated using the two pyroxenes Fe–Mg exchange geothermometer from Brey and Köhler (1990), which has an uncertainty of ±30 °C. In highly-depleted garnet harzburgites that contained no clinopyroxene, the geothermometer of O'Neill and Wood (1979), based on Fe–Mg partitioning between garnet and olivine, which has uncertainties around ±60 °C, was used. For garnet- and clinopyroxene-free harzburgites, we used the geothermometer Li et al. (1995), based on Fe–Mg exchange between olivine and spinel, which yield temperatures within ±50 °C. Equilibrium pressures were calculated using the orthopyroxene–garnet barometer of Nickel and Green (1985), which has uncertainties of ±0.2 GPa. For the spinel-bearing peridotites, pressures were estimated based on the equilibrium temperatures and the geotherm that best fits the equilibrium pressure and temperature data for the garnet-bearing samples.

Table 1
List of the studied kimberlitic pipes, the number of samples selected and their ages.

Kimberlite name	Number of samples	Age (Ma)	Reference
Kimberley	18	91	1
Jagersfontein	18	86	5
Monastery	2	90	1, 3
Lentseng	1	89	1, 4
Mothae	1	90	1
Kamfersdam	1	87	1
DeBeers	1	117,92	1, 2
Premier	5	1202	4
Finsch	3	120	5

1: Davis (1977).
2: Davis (1978).
3: McIntyre and Dawson (1976).
4: Kramers and Smith (1983).
5: Smith et al. (1985).

3.2. Electron-backscattered diffraction (EBSD)

Crystallographic preferred orientations (CPO) of olivine, pyroxenes, and garnet in all 50 samples were measured at the SEM-EBSD facility in Geosciences Montpellier by indexation of EBSD patterns produced by interaction between an electron beam with the crystals in thin sections tilted at 70° to the horizontal. Measurements were performed in a JEOL JSM 5600 scanning electron microscope using an acceleration voltage of 17 kV and a working distance of 23 mm. Maps covering almost entirely each thin section were performed

using sampling steps of 100, 40 or 30 μm, depending on grain size. Indexation rates range from 40 to 75% depending on the extent of fracturing and serpentinization in the xenolith. Phlogopite is usually poorly indexed. Indexation is also poor in very fine-grained layers in samples displaying mylonitic or fluidal mosaic textures. Orthopyroxene was rarely misindexed as clinopyroxene. Errors in the measurements were reduced by careful post-acquisition data treatment, controlled by comparison between EBSD maps and microscopic observations. Modal composition, grain sizes, and shape-preferred orientations were also obtained from EBSD maps.

Crystal-preferred orientation data is displayed in pole figures, presented as lower hemisphere stereographic projections. To avoid over-representation of large grains, data were plotted as one point per grain. When the foliation and lineation could be identified, the orientation of the main crystallographic directions: [100], [010] and [001] for olivine and pyroxenes, was plotted relatively to the principal axes of the deformation ellipsoid X, Y, and Z. However, in most coarse-grained samples, the identification of the foliation and lineation was not possible and thin sections were cut in random orientations. To allow easy comparison among different samples, we rotated the CPO of all samples into a common orientation, in which the maximum concentration of orthopyroxene [001] axes and of the olivine [010] axes are parallel to the E–W and the N–S directions of the pole figure, respectively. This choice was based on the observation that [001] is the only known glide direction in orthopyroxene; plastic deformation tends therefore to align this axis in the flow direction (cf. review in Frets et al., 2012). This choice allowed presenting the CPO without making an ad-hoc hypothesis on the dominant glide direction in olivine. When the orthopyroxene CPO was too dispersed, the maximum concentration of olivine [100] or [001] axes, depending on which had the strongest concentration, was placed in the E–W direction of the pole figure.

The strength of the fabric was quantified using the dimensionless J-index, which is the volume-averaged integral of squared orientation densities defined by:

$$J = f(g)^2 dg \quad (1)$$

where f(g) is the orientation distribution function (ODF) and $dg = d\varphi_1\ d\varphi\ d\varphi_2\ \sin\varphi\pi^2$, where φ_1, φ, and φ_2 are the Euler angles that define the rotations allowing for coincidence between the crystallographic and external reference frames. Olivine CPO in natural peridotites is characterized by J-indexes between 2 and 20, with a peak at 8–10 (Ben Ismaïl and Mainprice, 1998; Tommasi et al., 2000). The J-index for all samples was calculated based on the mean orientation of each grain using the SuperJctf program by D. Mainprice (ftp://www.gm.univ-montp2.fr/mainprice//CareWare_Unicef_Programs/) with a 10° Gaussian half-width, 1° cells, and truncation of the orientation distribution function (ODF) at 22°.

3.3. Fourier transform infrared spectroscopy (FTIR)

Fourteen doubly-polished thin sections were prepared for unpolarized FTIR analysis. Prior to analyses, all sections were immersed in pure acetone for at least 12 h to dissolve any intergranular CrystalBond glue. FTIR spectroscopy analyses were performed at the Laboratoire des Colloïdes, Verres, Nanomatériaux in Montpellier using a Bruker IFS66v coupled with a Bruker HYPERION microscope and a liquid nitrogen-cooled mercury–cadmium–telluride (MCT) detector. A Globar light source and a Ge-KBr beam splitter were used to generate unpolarized mid-infrared radiation. Measurements on olivine, orthopyroxene, clinopyroxene, garnet, and phlogopite crystals were performed with square aperture sizes ranging from 40 to 100 μm; for each measurement 200 scans were accumulated with a resolution of 4 cm^{-1}. They were preceded by a background measurement, followed by a baseline correction using the OPUS software, and, finally, normalized to a sample thickness of 1 cm. Fractures and inclusions were strictly avoided. The sample thickness was measured using a micrometer with a tolerance of ±1 μm and was always near 500 μm.

The calibration of Paterson (1982) was used to quantify the OH concentration in each mineral phase:

$$C_{OH} = \frac{X_i}{150\zeta} \int \frac{k(\bar{\nu})}{(3780-\bar{\nu})} d\bar{\nu} \quad (2)$$

where C_{OH} is the hydroxyl concentration (in mol H/l), ζ is an orientation factor (1/3 for unpolarized measurements), and $K(\bar{\nu})$ is the absorption coefficient in cm^{-1} for a given wavenumber $\bar{\nu}$. X_i is a density factor ($X_{i(ol)} = 2695$ ppm wt. H_2O; $X_{i(orthopyroxene)} = 2812$ ppm wt. H_2O; $X_{i(clinopyroxene)} = 2761$ ppm wt. H_2O). Estimated errors on the resulting water contents are ~30% (Kohlstedt et al., 1996). To compare the present data with previous studies where measurements were done using polarized infrared radiation and the Bell et al. (2003) calibration, OH concentrations for olivine have to be multiplied by a factor between 2 and 4 (Bell et al., 2003). Following Ferot (2011), a factor of 3 was used in the present study.

4. Microstructures

Kaapvaal xenoliths are generally highly fractured due to fast decompression during kimberlite eruption and have abundant alteration products, such as serpentine along grain boundaries and fractures. Original microstructures can however still be clearly observed. Five distinct microstructures were identified following the original classification of Boullier and Nicolas (1975). Among the 50 studied xenoliths, 78% are coarse-grained, displaying either coarse-granular (protogranular) or coarse-porphyroclastic microstructures, and 22% are fine-grained, high-temperature sheared peridotites, showing mylonitic, fluidal mosaic, or mosaic microstructures (Fig. 2).

4.1. Coarse-grained peridotites

Coarse-grained peridotites predominate in our xenolith suite; they are present in every studied pipe except Mothae (Fig. 1). They are characterized by plurimillimetric grain sizes (Fig. 2). Most are coarse-granular (CG) peridotites (32/50, 66%), with rare intracrystalline deformation features, but a few are coarse-porphyroclastic (6/50, 12%), exhibiting a well-defined foliation and lineation and frequent subgrain boundaries in olivine.

4.1.1. Coarse-granular peridotites

Coarse-granular peridotites correspond to the protogranular peridotites in the original Boullier and Nicolas (1975) classification, being characterized by large anhedral olivine and orthopyroxene crystals. The coarsest-grained peridotites from Jagersfontein have cm-wide crystals (Fig. 2a). Most coarse-granular xenoliths have, however, 5–8 mm wide crystals in average (Fig. 2b) and a few samples have slightly smaller grain sizes (1–2 mm in average, Fig. 2c).

In most coarse-granular peridotites, olivine and orthopyroxene crystals have irregular shapes with curvilinear boundaries, evolving locally to polygonal arrangements with 120° triple junctions (Fig. 2a–c). No foliation or lineation can be identified. However, some coarse-granular xenoliths from Kimberley have a weak foliation, highlighted by the elongation of olivine and orthopyroxene crystals (aspect ratios range from 1:2 to 1:4, Fig. 2b).

Olivine crystals are usually free of intracrystalline deformation, but subgrains and undulose extinctions are locally observed (white arrows in Fig. 2a–c). Orthopyroxene crystals sometimes display kinks (black arrows, Fig. 2b and c). Small interstitial orthopyroxenes are also observed; they are most often free of any intracrystalline deformation features, but may also display kinks (Fig. 3a). Clinopyroxene exsolution may or

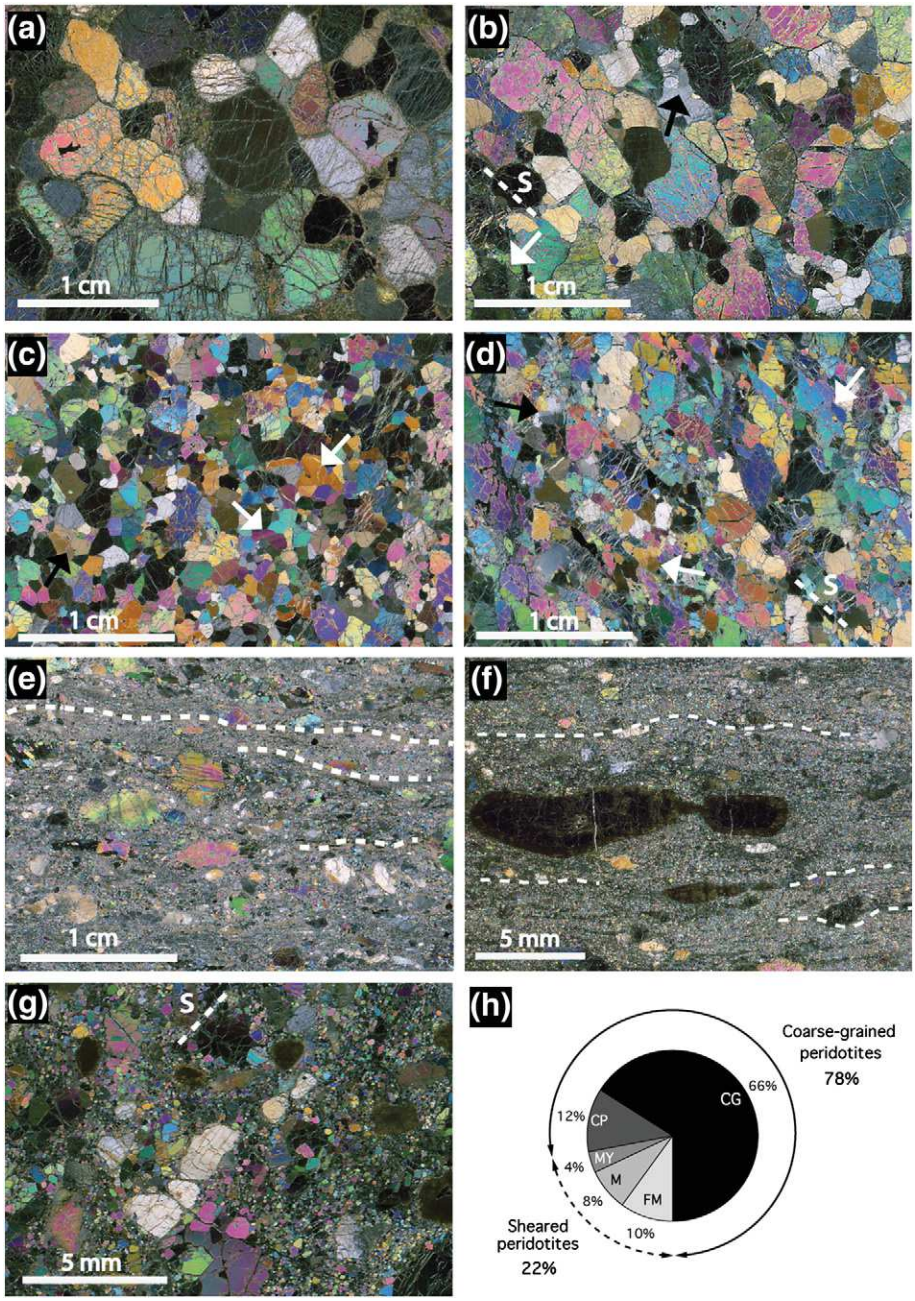

Fig. 2. Photomicrographs in cross-polarized light showing typical microstructures for the studied xenoliths. (a) Very coarse-granular gt-bearing J34 lherzolite from Jagersfontein, showing centimetric irregularly shaped grains with straight grain boundaries. (b) Coarse-granular texture in gt- and sp-bearing harzburgite KBBF16 from Kimberley, where elongation of olivine crystals marks a weak foliation (S). (c) Sp-harzburgite KBBF10 from Kimberley showing an equigranular, less coarse-grained microstructure. White arrows in (b) and (c) mark undulose extinctions and subgrain boundaries in olivine crystals. (d) Coarse-porphyroclastic spinel harzburgite KBBF8 exhibiting a foliation (S) marked by elongated olivine crystals with well-developed subgrain boundaries and undulose extinction (white arrows); orthopyroxene crystals have irregular shapes with embayments filled by olivine and display kinks locally (black arrow). (e) Mylonite KBBF11 showing strained orthopyroxene and olivine porphyroclasts surrounded by a fine-grained olivine–orthopyroxene matrix; dashed lines highlight very fine-grained orthopyroxene-rich domains. (f) Fluidal mosaic texture in lherzolite KBJ63 characterized by elongated garnet crystals enclosed in a matrix composed of polygonal olivine and very fine-grained orthopyroxene-rich domains, highlighted by dashed lines as in (e). (g) Mosaic texture in garnet–lherzolite J47 characterized by olivine and orthopyroxene porphyroclasts enclosed in an olivine-rich polygonal matrix. S marks the foliation trace deduced from crystallographic orientation data. (h) Pie-chart showing the representativity of the different microstructures among the 50 studied xenoliths.

not be present. Interpenetrating boundaries between orthopyroxene and olivine grains were identified in more than half of the studied samples (Fig. 2a and b). Rounded olivine crystals are occasionally included in orthopyroxene, but orthopyroxene inclusions in olivine are also observed. Large, often undeformed clinopyroxene crystals are observed in some samples. Most clinopyroxene occurs however as small dark green crystals along vein-like structures or as small interstitial crystals. It is often spatially related to phlogopite (Fig. 3b), spinel, and garnet.

When present, garnet forms large rounded 1 to 5 mm wide crystals (Fig. 2b). Garnet rimming orthopyroxene is however observed in lherzolite FRB1339 from Premier (Fig. 3c). Kelyphite rims with variable thickness (~0.06 to 1 mm) are almost always present. When present, spinel occurs as dark, irregularly shaped and mm-sized crystals, as small crystals in kelyphite rims, or as small interstitial crystals along fractures and grain boundaries. Spinel–pyroxene symplectites are observed in two harzburgites. Garnet- and spinel-bearing harzburgite J41 has

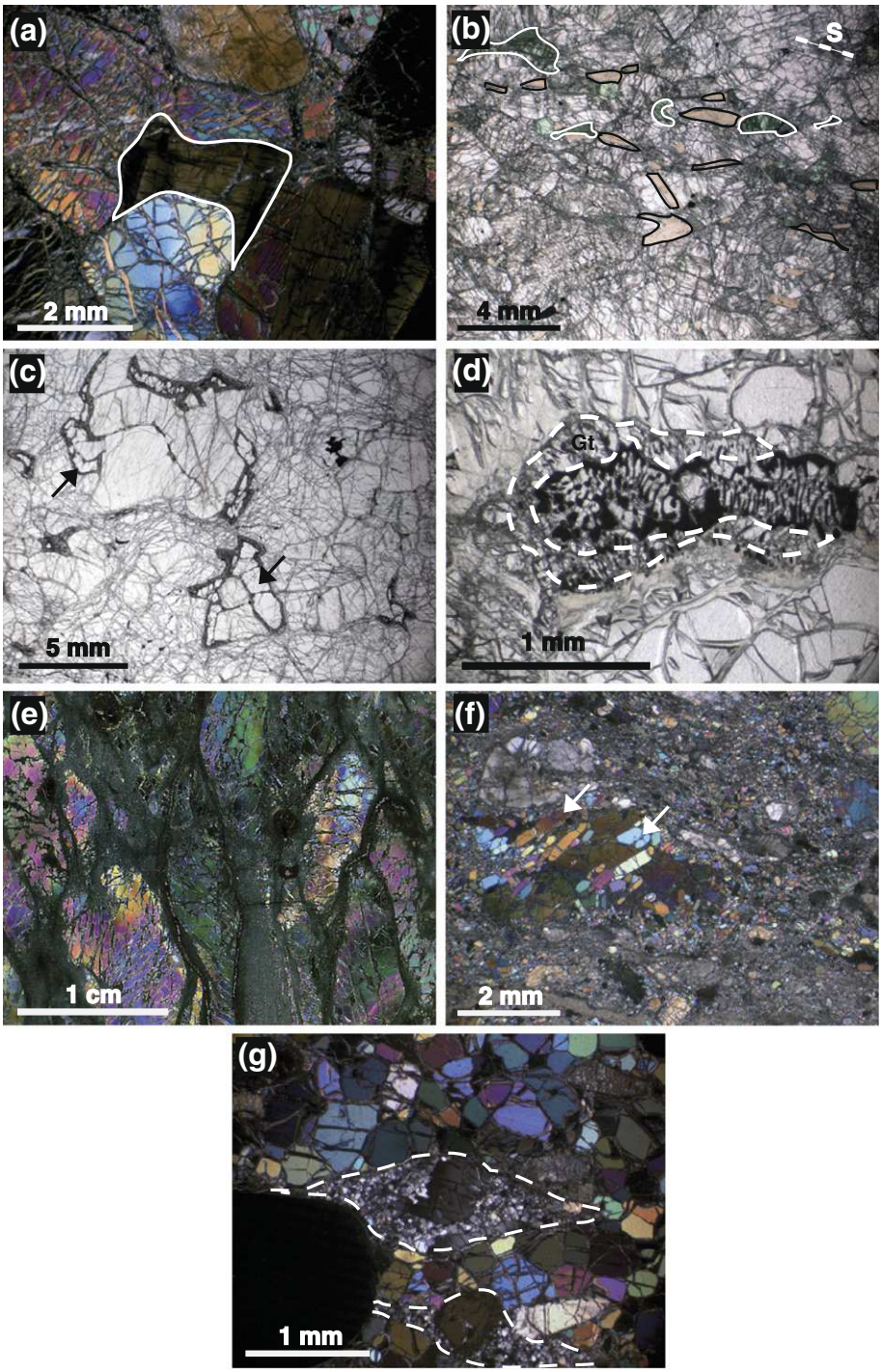

Fig. 3. Photomicrographs in plane-polarized (a, b, and c) and cross-polarized light (d, e, and f) of: (a) interstitial orthopyroxene showing subgrain boundaries in a coarse-grained peridotite; (b) interstitial dark green clinopyroxene and phlogopite aligned parallel to the foliation in coarse-porphyroclastic peridotite KBBF18; (c) interstitial garnet (black arrow) rimming orthopyroxene in coarse-grained harzburgite FRB1339; (d) a clinopyroxene–spinel symplectite rimmed by garnet in coarse-grained harzburgite J41; (e) coarse lens-shaped olivine porphyroclasts surrounded by a matrix composed of very fine-grained polygonal olivine almost entirely replaced by serpentine in porphyroclastic harzburgite PHN2760; (f) strain-free olivine tablets (white arrows) crystallized on an olivine porphyroclast in mylonite KBBF11; (g) core-and-mantle structure in a partially recrystallized orthopyroxene porphyroclast (delimited by the dashed lines) and coarser-grained polygonal strain-free olivine neoblasts in fluidal mosaic peridotite KBJ33.

spinel–clinopyroxene symplectites rimmed by garnet (Fig. 3d), whereas harzburgite KBBF10 has spinel–orthopyroxene symplectites.

Phlogopite crystallizes as reaction products in kelyphite rims, along fractures, or as small interstitial crystals along grain boundaries or triple junctions. Millimetric to plurimillimetric, subhedral phlogopite crystals are observed in two samples (KBJ59 and KBBF14, Table 2). Among these samples, garnet- and spinel-bearing lherzolite KBJ59 from Jagersfontein displays an extremely high phlogopite content (14%).

4.1.2. Coarse-porphyroclastic peridotites

Coarse-porphyroclastic microstructures are rarer, but they are observed in 6 harzburgites and lherzolites from the Kimberley, Finsch and Premier pipes, which display equilibrium temperatures ranging from 850 °C to 1464 °C (Table 2). These peridotites have plurimillimetric, lens-shaped olivine crystals (with aspect ratios up to 4:1) marking the foliation and the lineation (Fig. 2d). Olivine crystals usually exhibit undulose extinction and subgrains (white arrows

Table 2
Textures, equilibrium conditions, modal contents, olivine mg#, olivine CPO, olivine and opx J-indexes of the studied Kaapvaal peridotites.

Texture	Locality	Sample	Pressure (GPa)	Temperature (°C)	Ol mg# (%)	Reference for mg#, T, and P data	Modal compositions§						Olivine	Olivine	Opx
							ol	opx	cpx	gt	sp	phl	CPO	J-index	J-index
CG	Kimberley	KBBF6a	3.8[3]	926[1]	90.8	This study	74	13	4	9	0	0	Axial [100]	7.6	9.9
	Kimberley	KBBF6b	3.7[3]	908[1]	91.0	This study	82	8	4	6	0	0	Axial [100]	7.0	–
	Kimberley	KBBF9	4.7[3]	1102[1]	89.8	This study	67	16	9	8	0	0	Axial [010]	3.6	7.5
	Kimberley	KBBF10	–	948[1]	92.4	This study	72	27	1	0	0	0	Axial [010]	4.7	2.4
	Kimberley	KBBF14	–	996[1]	93.0	This study	82	16	1	0	0	1	Ortho	4.0	6.1
	Kimberley	KBBF15	4.3[3]	1067[1]	92.6	This study	65	31	0	4	0	0	Ortho	4.0	5.6
	Kimberley	KBBF16	4.0[3]	–	93.3	BI	71	26	0	3	0	0	Ortho	3.0	4.1
	Kimberley	KBBF20	–	800[1]	–	BI	65	35	0	0	0	0	Ortho	10.2	–
	Kimberley	FRB1404	4.4[2]	987[2]	93.5	J	59	36	1	4	0	0	Ortho	3.5	6.2
	Kimberley	FRB1422	4.4[2]	994[2]	93.5	J	65	31	0	4	0	0	Ortho	2.1	8.7
	Kimberley	FRB1423	3.8[1]	851[1]	91.8	J	68	18	4	10	0	0	Axial [100]	5.5	10.6
	Kimberley	FRB1447	4.2[2]	968[2]	93.4	J	73	23	1	3	0	0	Axial [010]	2.4	7.8
	Kimberley	FRB348	3.7[1]	938[1]	92.3	J	58	28	7	7	0	0	Ortho	4.7	8.2
	Jagersfontein	KBJ50	–	–	92.2	This study	76	0	16	1	1	6	Ortho	–	–
	Jagersfontein	KBJ52	–	900[4]	92.7	This study	75	25	0	0	0	0	Ortho	4.3	5.7
	Jagersfontein	KBJ54	3.8[3]	907[4]	92.3	This study	75	23	2	0	0	0	Axial [010]	8.7	7.0
	Jagersfontein	KBJ56	3.5[3]	895[2]	92.5	This study	65	28	0	7	0	0	Axial [010]	3.8	7.0
	Jagersfontein	KBJ59	–	898[1]	89.9	This study	66	16	4	0	0	14	Ortho	1.5	4.8
	Jagersfontein	KBJ62	3.1[3]	759[2]	92.6	This study	64	36	0	0	0	0	Ortho	10.6	10.4
	Jagersfontein	J34	2.4[3]	656[1]	92.0	This study	59	29	5	7	0	0	Axial [100]	–	–
	Jagersfontein	J41	3.7[3]	668[4]	92.4	This study	61	39	0	0	0	0	Ortho	5.8	7.9
	Jagersfontein	J57	3.1[3]	765[2]	92.4	This study	79	18	3	0	0	0	Axial [100]	8.5	8.2
	Monastery	R0M23	3.3[3]	910[1]	92.2	MO	66	28	4	1	0	1	Ortho	7.1	–
	Monastery	R0M69	2.6[3]	784[1]	92.2	MO	76	20	3	1	0	0	Ortho	–	–
	Lentseng	PHN4274	4.3[3]	1015[1]	93.1	BI	62	33	2	3	0	0	Ortho	6.1	7.0
	Kamfersdam	PHN5580	–	*	92.6	This study	72	27	0	0	0	1	Ortho	7.1	–
	De Beers	KBB2	4.0[3]	917[2]	93.3	This study	66	33	0	1	0	0	Ortho	6.5	9.2
	Premier	FRB1330	–	744[1]	91.3	This study	80	17	3	0	0	0	Axial [100]	4.7	2.6
	Premier	FRB1336	*	*	88.9	This study	70	30	0	0	0	0	Axial [010]	4.3	6.7
	Premier	FRB1339	*	*	91.7	This study	71	18	8	3	0	0	Axial [010]	10.4	–
	Premier	PHN5266	–	*	92.7	This study	70	26	4	0	0	0	Ortho	6.0	7.4
	Finsch	FRB1513	5.2[3]	1037[2]	92.6	This study	70	27	1	2	0	0	Ortho	7.0	–
CP	Kimberley	KBBF8	–	1029[4]	94.3	This study	81	19	0	0	0	0	Axial [010]	8.1	–
	Kimberley	KBBF18	–	850[1]	92.2	BI	75	17	6	0	0	2	Axial [100]	3.6	5.2
	Kimberley	PHN2760	4.9[3]	1053	93.2	BI	95	2	–	3	–	–	Ortho	–	–
	Premier	PHN5267	6.5[3]	1464[1]	91.3	This study	70	19	6	5	0	0	Ortho	2.3	–
	Finsch	FRB1501	4.6[3]	1030[2]	93.0	This study	70	22	0	8	0	0	Ortho	3.6	5.0
	Finsch	FRB1512	4.7[3]	1058[2]	92.0	This study	68	22	0	10	0	0	Ortho	3.5	6.9
FM	Jagersfontein	KBJ6	4.9[3]	1163[1]	90.7	This study	84	9	3	4	0	0	Bimodal	3.2	2.1
	Jagersfontein	KBJ8	–	1219[1]	90.9	This study	87	13	0	0	0	0	Ortho	4.6	2.4
	Jagersfontein	KBJ14	4.7[3]	1140[1]	91.3	This study	70	5	12	13	0	0	Ortho	2.9	4.7
	Jagersfontein	KBJ33	4.8[3]	1217[1]	89.3	This study	68	8	6	18	0	0	Ortho	4.1	1.6
	Jagersfontein	KBJ63	4.9[3]	1250[1]	91.3	This study	82	10	3	5	0	0	Bimodal	4.3	1.6
M	Jagersfontein	KBJ30	5.8[1]	1282[1]	89.4	G	63	11	11	15	0	0	Bimodal	2.3	4.8
	Jagersfontein	KBJ60	5.2[3]	1190[1]	91.5	This study	86	13	1	0	0	0	Bimodal	2.5	7.5
	Jagersfontein	J47	4.7[3]	1227[1]	90.7	This study	85	6	8	1	0	0	Bimodal	3.2	4.9
	Jagersfontein	J63	5.2[3]	1176[1]	87.7	This study	78	10	10	2	0	0	Bimodal	1.8	5.5
	Mothae	PHN1925	4.6[3]	1306[1]	89.9	This study	63	22	11	4	0	0	Bimodal	1.9	2.0
MY	Kimberley	KBBF11	5.9[2]	1159[2]	93.6	B&N	88	11	1	0	0	0	Ortho	2.7	1.6
	Kimberley	FRB1402	4.6[2]	1023[2]	93.2	J	83	9	0	8	0	0	Bimodal	2.2	2.9

[1]Brey and Köhler (1990) thermometry and barometry; [2]O'Neill and Wood (1979) thermometry; [3]Nickel and Green (1985) barometry; [4]Li et al. (1995) thermometry.
*Calculation was not possible because of compositional variability leading to large variations (>200° or >1 GPa) in P, T estimates within the sample.
§Modal compositions determined from EBSD maps.
References for P, T data: BI = Ben Ismaïl (1999); B&N = Boyd and Nixon (1978); G = Grant et al. (2007); J = James et al. (2004); MO = Moore (1986).
Texture: CG = Coarse-grained peridotite; CP: Coarse-porphyroclastic; E = Equigranular; FM = Fluidal mosaic; M = Mosaic; MY = Mylonite.
CPO types: ortho = orthorhombic, bimodal, axial [100] and axial [010] crystal-preferred orientations, see main text and Fig. 6 for details.
J indexes could not be calculated for samples in which less than 100 grains were measured.

in Fig. 2d) and have sinuous to polygonal grain boundaries (Fig. 2d). Orthopyroxene is coarse-grained and irregularly shaped. Kinks and undulose extinctions in orthopyroxene are locally observed (black arrows in Fig. 2d). Interpenetrating boundaries between orthopyroxene and olivine grains are common (Fig. 2d). As in coarse-granular peridotites, rounded olivine crystals are occasionally included in orthopyroxene, but orthopyroxene inclusions in olivine are also observed. Most coarse-porphyroclastic peridotites and harzburgites have no clinopyroxene, but lherzolite PHN5267 has anhedral clinopyroxenes, which show undulose extinctions. In contrast, spharzburgite KBBF18 displays an alignment of interstitial, undeformed phlogopite and clinopyroxene aggregates in the foliation (Fig. 3b). When present, spinel is elongated, marking the lineation. Garnet occurs as plurimillimetric rounded crystals.

Garnet-bearing harzburgite PHN2760 from Kimberley displays an unusual coarse, but highly strained texture. This rock has very large (>1 cm long) lens-shaped olivine crystals with well-developed undulose extinction (Fig. 3e), surrounded by a very fine-grained recrystallized olivine matrix (average grain size<25 μm). Olivine grains in the matrix have been largely replaced by low-temperature

serpentine, but they still preserve the original polygonal shapes. Orthopyroxene porphyroclasts are rare; they are strongly altered and generally show abundant clinopyroxene exsolutions.

4.2. Sheared peridotites

Sheared peridotites are characterized by a bimodal grain size distribution where rare porphyroclasts are enclosed in a fine-grained matrix (grain sizes range from tens to few hundreds of micrometers). They also usually display a well-developed foliation, but the later may be absent (mosaic microstructure). Two other microstructures: mylonitic and fluidal mosaic, may be discriminated based on the average grain size of the recrystallized matrix. In our sample set, mylonitic microstructures are only observed in two xenoliths from Kimberley, fluidal mosaic microstructures in five xenoliths from Jagersfontein, and mosaic microstructures in four samples from Jagersfontein and one from Mothae.

The *mylonites* display large asymmetric olivine and orthopyroxene porphyroclasts (1–5 mm long), with well-developed undulose extinctions, closely-spaced subgrain boundaries, and recrystallization tails enclosed in a fine-grained matrix composed of recrystallized olivine (30–100 μm wide) and very fine-grained (<25 μm) orthopyroxene-rich bands (Fig. 2e). Phlogopite often displays sigmoidal shapes and strong undulose extinction. Euhedral olivine crystals devoid of any internal deformation (tablets) commonly crystallize on olivine porphyroclasts and sometimes also on matrix crystals (Fig. 3f).

In *fluidal mosaic peridotites*, orthopyroxene and clinopyroxene porphyroclasts are also enclosed in a fine-grained matrix with a polygonal texture, but olivine grains in the matrix are larger (up to 0.5 mm wide; Fig. 2f). Olivine is usually entirely recrystallized, but rare porphyroclasts are preserved in gt- and sp-lherzolites KBJ8 and KBJ63. Orthopyroxene porphyroclasts are elongated and show asymmetric recrystallization tails composed of very fine-grained orthopyroxene with polygonal boundaries and undulose extinctions (Fig. 3g). These recrystallization tails evolve into mm-scale, orthopyroxene-rich bands within the olivine-rich matrix (Fig. 3g). Olivine crystals in the matrix are polygonal and free of any internal deformation features (Fig. 3g). Garnet forms large porphyroclasts, which may be elongated parallel to the foliation, as in mosaic fluidal peridotites KBJ63 and KBJ14 (Fig. 2f). It can also be rounded, as in samples KBJ30 and KBJ33, in which garnet is more abundant (>15%).

The four studied *mosaic peridotites* (sp-lherzolite J47, gt- and sp-lherzolites J63, KBJ30, KB60) are characterized by large olivine porphyroclasts with strong undulose extinctions and rare subgrain boundaries, and by irregularly-shaped orthopyroxene porphyroclasts enclosed in a polygonal olivine-rich matrix (Fig. 2g). Contrary to the previous textures, these samples show neither a clear foliation nor a compositional banding. Crystallization of olivine tablets on olivine porphyroclasts is frequent. Olivine crystals in the matrix are polygonal and free of any intracrystalline deformation features. Orthopyroxene porphyroclasts are usually surrounded by fine-grained orthopyroxene neoblasts (<25 μm).

4.3. Compositions and equilibrium conditions

Most coarse-grained peridotites are harzburgites or clinopyroxene-poor lherzolites with high modal contents of orthopyroxene (>20%, Fig. 4). Coarse-grained lherzolites are rarer. A single very coarse-grained peridotite from Jagersfontein has a wehrlitic composition that is accompanied by enrichment in phlogopite. In contrast, half of the analyzed sheared peridotites are lherzolites with fertile compositions. Garnet modal content is highly variable (0–18%, Table 2) and shows no correlation with olivine or clinopyroxene contents. Spinel, when present, is always a minor phase (≤1%).

The mineral compositions of the analyzed samples are presented in the online Supplementary Material Table 1. Olivine mg# varies between 87.7 and 94.3 (Table 2). Mg# tends to be higher in coarse-grained peridotites (average mg# 92.1) and lower in the sheared peridotites (average mg# 91.1). However, mylonites from Kimberley are harzburgites with refractory olivines (average mg# = 93.4) and one of the lowest mg# (88.9) pertain to olivine crystals from coarse-granular peridotite. Low mg# in olivine are sometimes, but not always, accompanied by modal metasomatism (enrichment in clinopyroxene or phlogopite).

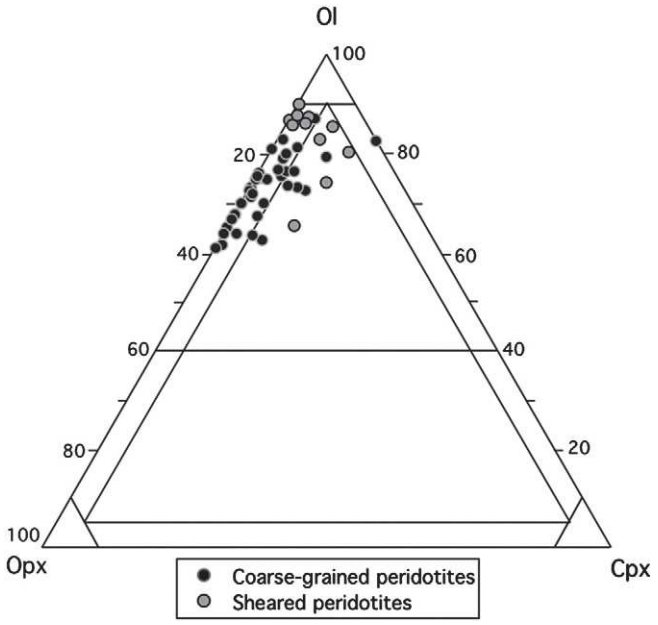

Fig. 4. Olivine:orthopyroxene:clinopyroxene modal ratios in the studied peridotites as a function of their texture. Garnet, spinel, phlogopite and serpentine were not considered for the construction of the ternary diagram; modal compositions derived from the EBSD maps were recalculated for a total of 100% of olivine + orthopyroxene + clinopyroxene.

Orthopyroxene is enstatite; it has very low Al_2O_3 contents (<1.10 wt.%), except for five samples (KBBF10, FRB1330, FRB1339, PHN1925, and PHN5266), where Al_2O_3 contents up to 2.76 wt.% are observed. Orthopyroxene has also Ti-poor compositions (<0.30 wt.%). Clinopyroxene is diopside in 11 samples and augite in 14 out of 25 samples. Garnet is always pyrope-rich and is Ca-saturated except in 4 samples (FRB1336, KBJ8, KBJ50 and KBJ56). Spinel is generally Cr-rich (cr# > 50, reaching 94 in harzburgite KBBF14). However, phlogopite-rich harzburgite KBJ59 has Al-rich spinels (cr# = 9).

Coarse-grained peridotites display the widest range of equilibrium temperatures, from 650 °C to 1464 °C, and pressures, from 2.4 to 6.5 GPa (Fig. 5). Equilibrium temperatures and pressures for sheared peridotites are comprised between 1023 and 1306 °C and 4.6–5.9 GPa. Pressure and temperature estimates for the coarse-grained xenoliths are consistent with a geotherm leading to a surface heat flux of 40 mW/m^2, which intersects the 1283 °C adiabat at 195 km of depth as illustrated in Fig. 5. Most sheared peridotites plot however slightly above this geotherm, in agreement with previous data for Kaapvaal sheared xenoliths (Finnerty and Boyd, 1987; Kennedy et al., 2002).

5. Crystal-preferred orientations

5.1. Coarse-granular and coarse-porphyroclastic peridotites

Coarse-granular and coarse-porphyroclastic peridotites show similar olivine CPO patterns, which range from orthorhombic to axial-[100] or axial-[010] (Fig. 6). Orthorhombic olivine CPO predominates (~60% of the coarse-grained peridotites). This CPO is characterized by point concentrations of the three crystallographic axes, with [100]

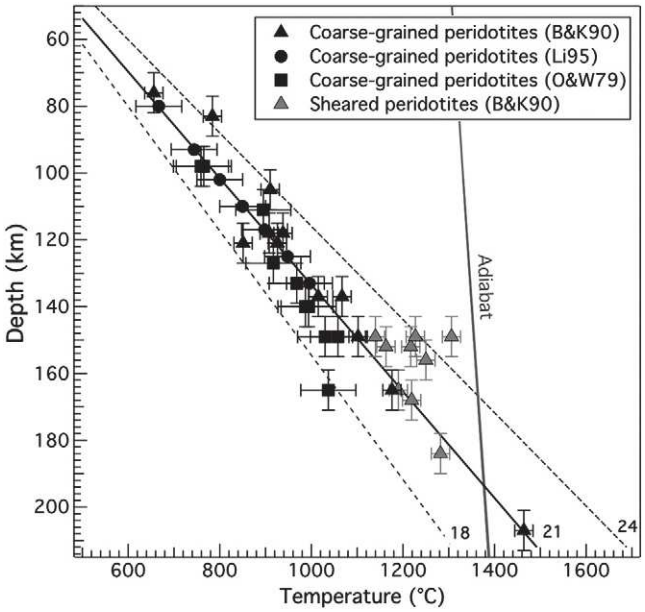

Fig. 5. Equilibrium pressures and temperatures of the studied coarse-grained and sheared peridotites (see text for details) plotted against geotherms calculated for reduced mantle heat flows of 18, 20, and 24 mW m^{-2}. T°O&W79, T°B&K90 and T°Li95 indicate data calculated using the O'Neill and Wood (1979), the Brey and Köhler (1990), and the Li et al. (1995) thermometers, respectively. Geotherms were calculated considering a crustal thickness of 35 km and a surface heat flow of 40 mW/m^2 following James et al. (2003) and Stachel et al. (2003), respectively.

axes exhibiting the strongest point concentration (Fig. 6). Seven coarse-grained harzburgites have axial-[100] CPO characterized by a strong concentration of [100] axes close to the lineation (when the latter could be determined) and a girdle distribution for [010] and [001] axes normal to the distribution of [100] axes (Fig. 6). Eight coarse-grained harzburgites have characteristic axial-[010] CPO, with a strong point concentration of [010] axes normal to the girdle distribution of [100] and [001] axes. Finally, two coarse-grained peridotites (spinel–harzburgite KBBF8, that has an axial-[010]; and garnet–harzburgite ROM 23, that has an orthorhombic olivine CPO), display a stronger concentration of [001] axes than of [100] axes (Fig. 6).

Olivine CPO intensities are highly variable. Calculated J-indexes are comprised between 1.5 and 10.6, which correspond to very weak and to rather strong fabric, respectively (Table 2). There is no clear correlation between CPO strength and microstructure (Fig. 7a); the lowest and the highest J-index values in the present study were obtained for coarse-grained peridotites with orthorhombic olivine CPO. There is also no correlation between the olivine CPO strength and pattern (Fig. 7b) or composition (Table 2). There is, however, a relation between the olivine CPO pattern and the equilibrium pressure (Fig. 7c). Orthorhombic olivine CPOs are observed over the whole pressure range, while axial-[100] CPOs tend to concentrate on the top of the column (2.4–3.8 GPa). Axial-[010] olivine CPO are observed in xenoliths equilibrated between 3.5 and 4.7 GPa, whereas bimodal CPOs are restricted to higher pressure xenoliths, between 4.6 and 5.8 GPa.

Orthopyroxene CPO is generally more dispersed, but it is usually correlated to the olivine CPO (i.e., the main dislocation glide directions and planes, which are [100] and (010) for olivine and [001] and (100) or (010) for pyroxenes, are aligned). Orthorhombic orthopyroxene CPO, characterized by weak point concentrations of the three main crystallographic axes, predominates. [001] axes always show the strongest concentration. In sixteen samples, [010] axes are aligned perpendicular to the plane that contain most [001] and [100] axes. In twelve other samples, [100] axes are normal to the plane containing the [001] and [010] axes. Two samples (KBBF9 and FRB1501) have, however, an axial-[001] pattern, characterized by [100] and [010] axes distributed in plane normal to the point concentration of [001] axes. Six coarse-grained harzburgites (KBBF18, FRB1404, FRB1422, FRB1423, KBJ52, J41 and J57) have an almost random orthopyroxene CPO. Three of these samples (J41, FRB1404, and FRB1422) are particularly enriched in orthopyroxene, with modal contents greater than 30%. In coarse-grained peridotites PHN2760 and KBJ50, the number of analyzed orthopyroxene crystals is too small to identify a CPO pattern.

5.2. Sheared peridotites

Mylonitic, fluidal mosaic, and mosaic peridotites show weak olivine CPO; J-indexes are comprised between 1.9 and 4.6 (Fig. 7a, Table 2). Olivine CPO patterns are nevertheless well-defined, with either an orthorhombic or an axial-[010] symmetry (Fig. 6). One mylonite (KBB11) and 3 fluidal mosaic lherzolites (KBJ8, KBJ14 and KBJ33) have typical orthorhombic olivine CPO with [100] axes aligned close to the lineation and [010] axes normal to the foliation. Seven garnet–lherzolites from Jagersfontein, Kimberley and Mothae show, however, a particular axial-[010] pattern characterized by a bimodal alignment of [100] and [001] axes in the foliation plane (Fig. 6). None of the maxima are parallel to the lineation, which is underlined by the elongation of the olivine crystals and the maximum concentration of orthopyroxene [001] axes. These bimodal olivine CPO samples have systematically weak CPO (Fig. 7b). There is also a clear depth distribution: bimodal olivine CPO are characteristic of sheared peridotites equilibrated at pressures > 4.5 GPa (Fig. 7c).

Orthopyroxene CPOs are weak, as indicated by J-indexes between 1.6 and 4.9. CPO patterns are nevertheless clear and correlated to the olivine CPO, although a small obliquity (<10°) between the CPO of the two minerals is observed for most samples. [001] is always aligned in the lineation. In six xenoliths (mosaic peridotites KBJ60 and J47, mylonite KBFF11, fluidal mosaic peridotites KBJ33, KB14 and KBJ63), [100] axes are concentrated normal to the foliation. In four other samples (mosaic lherzolite KBJ30, mylonite FRB1402, fluidal mosaic lherzolites KBJ6 and KBJ8), [010] axes are aligned normal to the foliation, whereas [100] axes are distributed in the foliation plane and perpendicular to the lineation. Clinopyroxene CPOs (presented in the online supplementary material) are weak, but correlated to the orthopyroxene CPO in all sheared peridotites, except in mylonite FRB1402.

6. FTIR spectroscopy and water contents

6.1. Olivine

The olivine spectra of xenoliths from Kimberley are heterogeneous and complex, often displaying more than six O–H absorption bands (Fig. 8a). This large number of absorption bands suggests H incorporation in a variety of point defects (e.g., Berry et al., 2007; Kovacs et al., 2010; Miller et al., 1987). A total of nine bands were identified in the studied xenoliths from Kimberley, but in most samples just a few of these bands are observed. Absorption bands can be divided into two groups: group I with absorptions between 3650 and 3450 cm^{-1} and group II between 3450 and 3200 cm^{-1} (Bai and Kohlstedt, 1993). The band at 3571 cm^{-1} exhibits the maximum O–H absorbance, in agreement with observations in many natural olivines (Miller et al., 1987). The intensity of other group I absorption bands is variable. The 3610, 3590 and 3525 cm^{-1} bands usually represent major peaks as observed for samples PHN2760 and KBBF16 spectra. Group II absorption bands have minor peaks except in sample KBBF16 where they appear to be the dominant defect sites for H^+ incorporation (Fig. 8a). O–H absorption bands at 3709, 3685 and 3645 cm^{-1} are attributed to hydrous minerals as serpentine, while

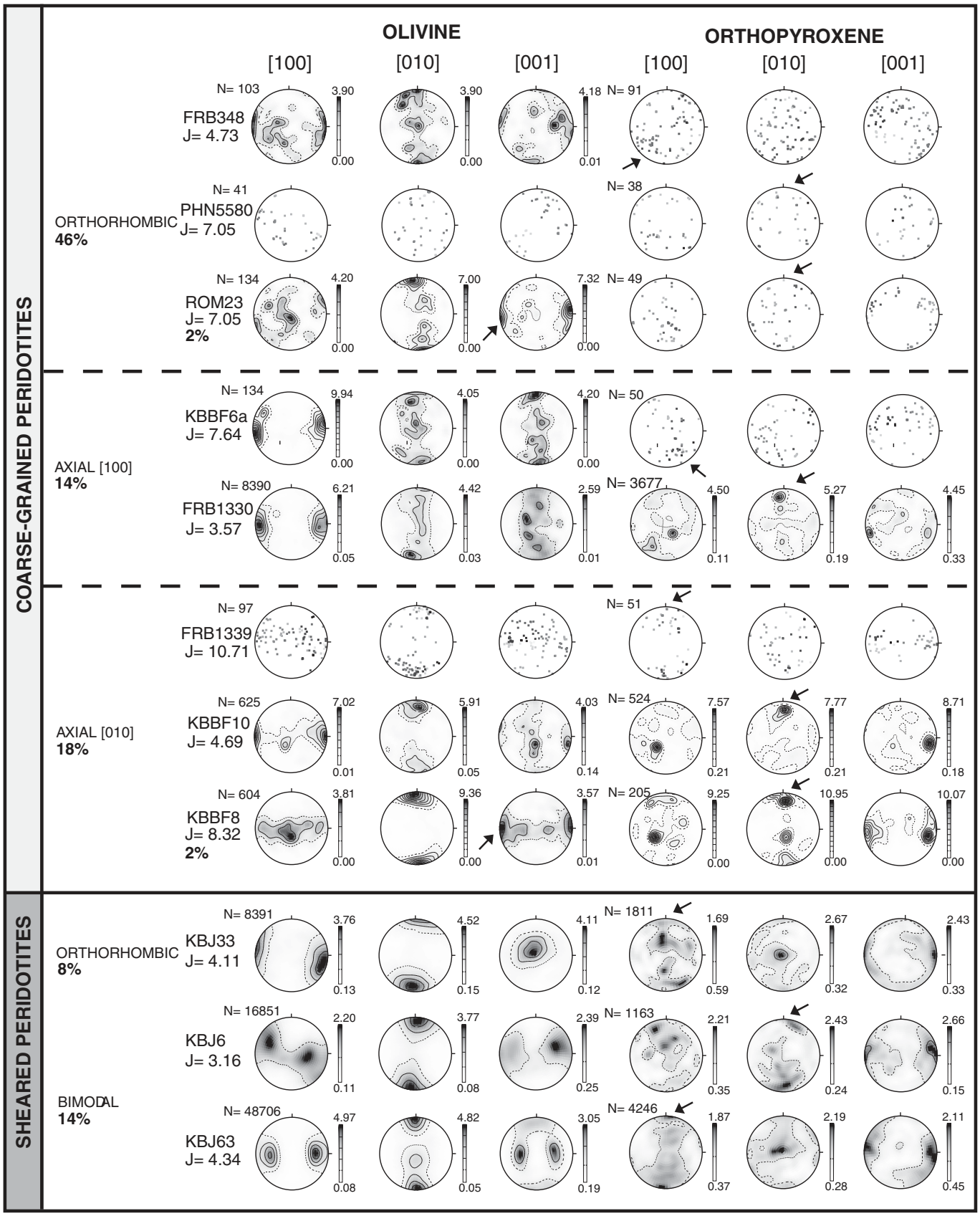

Fig. 6. Representative olivine and orthopyroxene crystal preferred orientations (CPO) of coarse-grained and sheared-peridotites. Arrows indicate the dominant dislocation glide planes in orthopyroxene and samples displaying dominant [001] glide in olivine. Lower hemisphere, equal-area stereographic projections. N is the number of measured grains. Contours at 1 multiple of a uniform distribution. CPOs were not contoured when less than 100 grains could be measured.

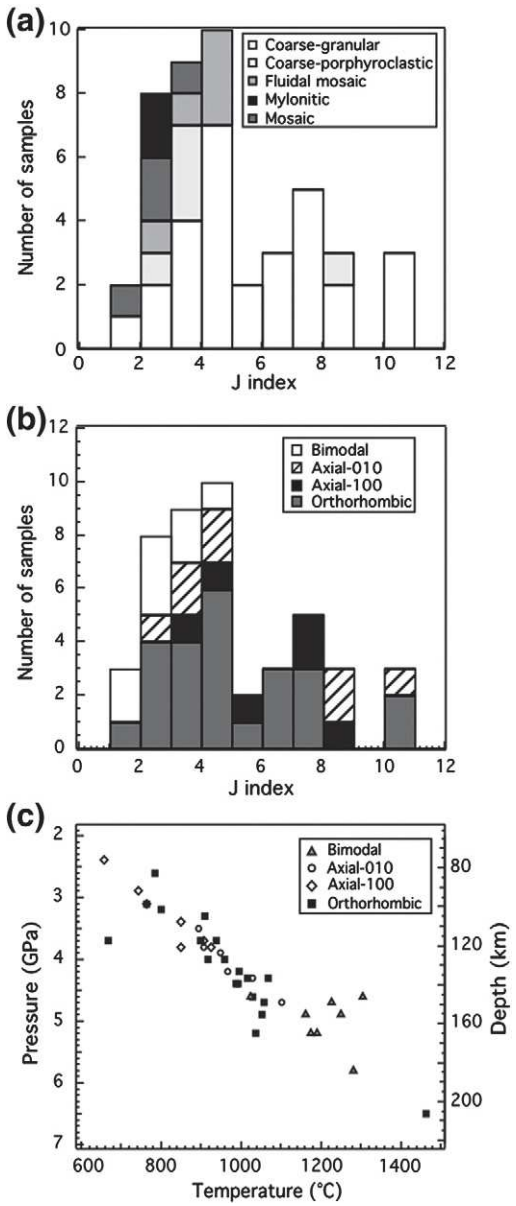

Fig. 7. (a) Olivine J-index distributions for mantle xenoliths with coarse-granular, coarse-prophyroclastic, fluidal mosaic, mylonitic, and mosaic textures. (b) Olivine J-index as a function of the CPO symmetry. (c) Olivine CPO symmetry as a function of the equilibrium pressure and temperature of the peridotite.

the band at 3675 cm^{-1} is likely to be attributed to talc (Miller et al., 1987; Post and Borer, 2000).

Sample KBJ59 from Jagersfontein, which contains high modal contents of phlogopite (14%), presents very different olivine spectra (Fig. 8a). The major peak is still located at 3571 cm^{-1}, but important O–H absorption bands are also present at 3598, 3571, 3525, and 3484 cm^{-1}. Similar spectra have been described in other Kaapvaal kimberlite xenoliths from Jagersfontein, Lesotho, and Wesselton (Grant et al., 2007; Kurosawa et al., 1997).

6.2. Pyroxenes and garnet

Orthopyroxene spectra are more homogeneous than the olivine ones (Fig. 8b). However, most measured spectra are strongly affected by alteration, exhibiting the O–H absorption bands at 3690 cm^{-1} and 3650 cm^{-1} usually attributed to hydrous sheet silicates (Miller et al., 1987; Skogby et al., 1990). The main absorption band associated to O–H bonds in orthopyroxene is observed at 3600 cm^{-1}, followed by two

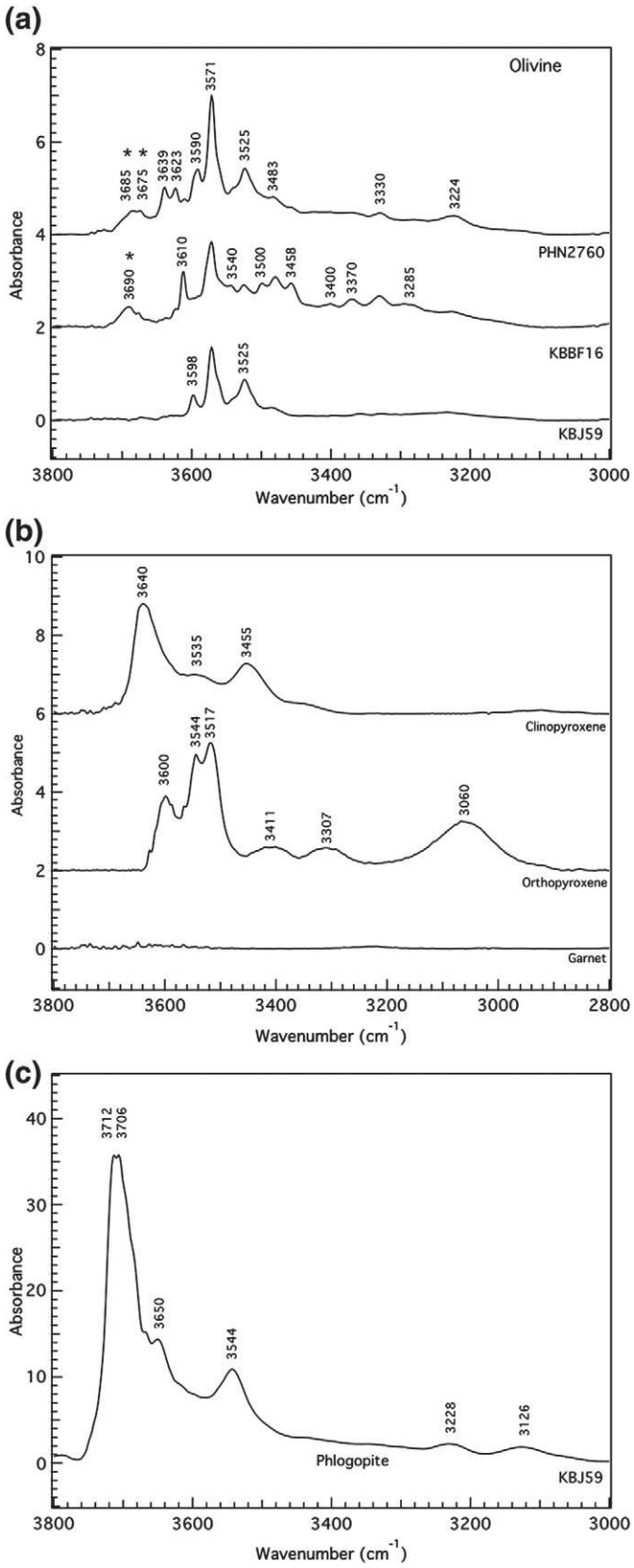

Fig. 8. Representative unpolarized infrared spectra of minerals in xenoliths from Kimberley and Jagersfontein. (a) Olivine. (b) Clinopyroxene, orthopyroxene, and garnet. (c) Phlogopite. All spectra are normalized to a sample thickness of 1 cm. Stars indicate peaks attributed to serpentine.

Table 3
Mineral OH concentrations.

Locality	Sample	Pressure	Temperature	Ol Mg #	Geothermobarometry data reference	Texture	Olivine CPO	Mineral	Section thickness	Paterson calibration[a]		Olivine–Bell calibration[b]	
										OH concentrations	OH concentrations	OH concentrations	Average OH concentrations
		(GPa)	(°C)						(μm)	(H/10^6 Si)	(ppm wt H_2O)	(ppm wt H_2O)	(ppm wt H_2O)
Kimberley	FRB348	3.7[1]	938[1]	92.3	J	CG	Ortho	ol	508	S*	S*	S*	–
								cpx-1	508	2381	146	–	–
								cpx-2	508	2626	161	–	–
								cpx-4	508	2561	157	–	–
								opx-1	508	1399	126	–	–
	FRB1404	4.4[2])	987[2]	93.5	J	CG	–	–	514	S*	S*	S*	–
	FRB1423	3.78[1]	851[1]	91.8	J	CG	Axial [100]	ol-4	513	342	21	63	
								ol-5	513	726	44	133	98
	FRB1447	4.2(2)	968(2)	92.3	J	CG	Ortho	ol-1	511	664	41	122	
								ol-3	511	660	40	121	
								ol-4	511	648	40	119	
								ol-5	511	728	45	134	124
	KBBF11	5.9[2]	1159[2]	93.6	B&N	MY	Ortho	–	465	<1	<1	<1	–
	KBBF16	4.0[3]	–	93.3	BI	CG	Ortho	ol-4	519	490	30	90	
								ol-5	519	812	50	149	
								ol-6	519	483	30	89	109
								opx-7	519	1356	122	–	–
								opx-10	519	1786	160	–	–
	KBBF18	–	850[1]	–	BI	CG	Axial [100]	–	489	S*	S*	S*	–
	PHN2760	4.9[2]	1053[2]	93.2	BI	CP	–	ol-1	502	906	55	166	
								ol-2	502	863	53	158	
								ol-3	502	840	51	154	
								ol-4	502	883	54	162	
								ol-5	502	552	34	101	
								ol-7	502	870	53	160	
								ol-8	502	878	54	161	152
Jagersfontein	KBJ59	–	890[1]	90.0	This study	CG	Ortho	ol-1	505	376	23	69	
								ol-3	505	1099	67	202	
								ol-4	505	512	31	94	
								ol-5	505	625	38	115	
								ol-6	505	362	22	66	109
Finsch	FRB1501	4.6[3]	1030[2]	93.0	This study	CP	Ortho	ol-5	500	112	7	21	
								ol-6	500	54	3	10	
								ol-7	500	69	4	13	
								ol-12	500	63	4	12	
								ol-19	520	81	5	15	
								ol-20	520	61	4	11	
								ol-21	520	79	5	14	
								ol-26	500	97	6	18	
								ol-27	500	87	5	16	
								ol-28	520	93	6	17	15
								opx-4	550	1120	100	–	–
								opx-6	550	1116	100	–	–
								opx-8	550	1127	110	–	–
	FRB1512	4.7[3]	1058[2]	92.0	This study	CP	Ortho	ol-1	520	272	17	50	
								ol-6	400	355	22	65	58
	FRB1513	5.2[3]	1037[2]	92.6	This study	CG	Ortho	ol-2	700	97	6	18	18
Premier	PHN5267	6.5[3]	1464[1]	91.3	This study	CP	Ortho	ol-l0	600	44	3	8	
								ol-15	600	43	3	8	8
								opx-2	550	934	83	–	–
								opx-3	600	662	59	–	–
Mothae	PHN1925	4.6[3]	1306[1]	90.7	This study	M	Axial [010]	ol-5	390	92	6	17	
								ol-7	390	206	13	38	
								ol-13	460	205	13	38	31

absorption bands centered at 3511–3520 and 3559–3541 cm^{-1} (Fig. 8b). Broader minor peaks around 3410, 3300, and 3060 cm^{-1} are also observed.

Clinopyroxene spectra are homogeneous (Fig. 8b). They exhibit typical patterns for mantle-derived clinopyroxenes, with major O–H absorption bands at 3640, 3535, and 3454 cm^{-1} (Grant et al., 2007; Li et al., 2008; Skogby et al., 1990). Garnet crystals were usually contaminated by serpentine and talc, displaying absorption bands 3690, 3683 and 3675 cm^{-1}. Spectra obtained from large, clear garnet crystals are however exempt of peaks; their spectra are flat (Fig. 8b), indicating anhydrous gt.

6.3. Phlogopite

Spectra in large undeformed phlogopite crystals from spinel peridotites KBBF18 and KBJ59 have three major O–H absorption bands at 3712, 3706, and 3544 cm^{-1} (Fig. 8c). Minor bands can be seen at 3650, 3228 and 3126 cm^{-1}. Peaks at 3712 and 3650 cm^{-1} are likely to be related to serpentine (Miller et al., 1987). However, an absorption band at ~3706 cm^{-1} was previously observed in phlogopite by Miller et al. (1987).

6.4. OH concentrations

OH concentrations in olivine for each sample were calculated by averaging the OH concentration estimated from spectra from 2 to 7 olivine crystals in the sample (Table 3). OH concentrations in olivine could only be determined precisely for ten samples, because spectra in olivine crystals from samples KKF18, FRB348, FRB1404, and KBBF11 displayed extensive contamination by serpentine, characterized by a broad band centered at 3690 cm^{-1}, and covering the whole range of wavenumbers for O–H stretching bands in olivine (3750–3400 cm^{-1}). Examples of serpentine-contaminated and good-quality olivine spectra are presented in Fig. 9. Water content in olivine varies between 3 and 50 wt. ppm H_2O using the Paterson calibration (9 and 150 wt. ppm H_2O after applying a conversion factor of 3 for comparison with data obtained using the Bell et al. (2003) calibration, Table 3). These values are among the highest OH concentrations in olivine measured in Kaapvaal xenoliths (Fig. 10). Still, higher OH concentrations are observed in olivine megacrysts from the Monastery kimberlite (Fig. 10).

Orthopyroxene grains are significantly more affected by alteration than olivine. Most orthopyroxene spectra exhibit some contamination by serpentine and/or amphibole, hindering an accurate determination of their OH concentration. However, in four samples, OH concentrations between 49 and 96 wt. ppm H_2O could be measured (Table 3). Sample FRB348 was the only specimen where clinopyroxene spectra were free of any contamination. OH concentrations in those clinopyroxene vary between 146 and 161 wt. ppm H_2O (Table 3).

Homogeneity in OH concentrations within a grain was checked by FTIR measurements along profiles with 15 or 25 μm step sizes across randomly oriented olivine (in samples FRB1512 and KBJ59) and orthopyroxene crystals (in FRB1513 and FRB348). All profiles in olivine indicate homogeneous OH concentrations, except in the vicinity of serpentine-filled cracks and grain boundaries as illustrated in Fig. 9. These observations are in agreement with FTIR profiles in olivine from kimberlite xenoliths by Grant et al. (2007), Peslier et al. (2008), and Kamenetsky et al. (2008), which do not show any evidence of diffusive dehydration or hydration. In orthopyroxene, contamination by serpentine and/or amphibole was too extensive that variations in water contents within a grain could not be quantified.

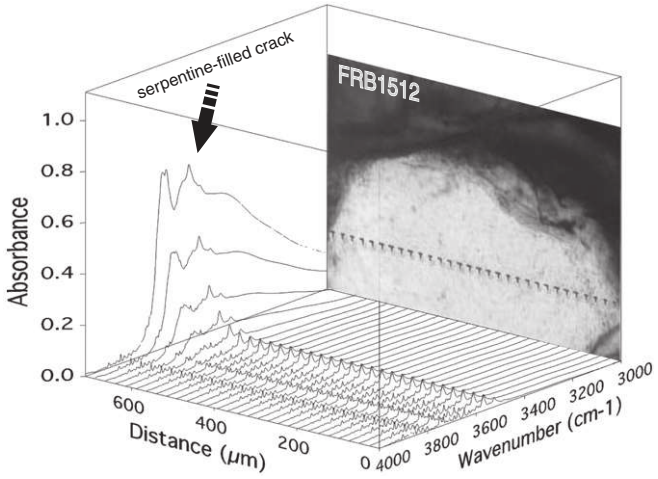

Fig. 9. Unpolarized FTIR profile along an olivine grain (random crystallographic orientation) in peridotite FRB1512. 30 spectra were measured along a 713 μm long profile with a step of 24.58 μm showing a homogeneous distribution before contamination by intergranular serpentine. All spectra were normalized to a sample thickness of 1 cm.

7. Discussion

The studied xenoliths represent samples of the cratonic mantle at depths ranging from ~50 to 250 km (Fig. 5). Extraction ages vary. Most samples come from kimberlite pipes erupted between 124 and 85 Ma, but the Premier kimberlite sampled an earlier stage of the cratonic lithosphere evolution (2000–1650 Ma, Kramers and Smith, 1983). No significant difference in deformation microstructures, CPO, or composition is observed between xenoliths from Premier and other pipes, but one should keep in mind that only 5 xenoliths from Premier were analyzed in this study. Analysis of the microstructures allows two groups to be discriminated: coarse-grained harzburgites and sheared lherzolites, which also differ by their composition (the latter are more fertile, in average). They also display different depths of origin; sheared peridotites have systematically equilibrium pressures ≥ 4.6 GPa, whereas coarse-grained microstructures occur over the entire sampled depth range. In the following these two groups will be treated separately. First, the deformation processes and the relations between deformation, annealing, and metasomatism in coarse-grained peridotites will be discussed. Then, we will examine the mechanisms and conditions of deformation that produced the sheared peridotites and discuss their timing and origin. Finally, we discuss the implications of the water content measurements for the hydration state of the Kaapvaal craton root.

7.1. Deformation and annealing in the coarse-grained peridotites

Coarse-granular microstructures, characterized by plurimilimetric anhedral olivine and orthopyroxene crystals with rare intracrystalline deformation features, like subgrains in olivine or kinks in orthopyroxene

Notes to Table 3:
[1]Brey and Köhler thermometry and Barometry; [2]O'Neill and Wood (1979) thermometry; [3]Nickel and Green (1985) barometry.
[a]OH concentrations from this study calculated using the calibration of Paterson (1982) have ±30% error (Kohlstedt et al., 1996); [b]OH concentrations corrected by a factor of 3 according to Bell et al. (2003).
*S = serpentine contamination prevented OH concentration estimations.
References: BI = Ben Ismaïl (1999); B&N: Boyd and Nixon (1978); J: James et al. (2004).
Texture: CG = Coarse-grained peridotite; MY = Mylonite.
CPO types: ortho = orthorhombic, and axial [100] crystal-preferred orientations; see main text and Fig. 6 for details.

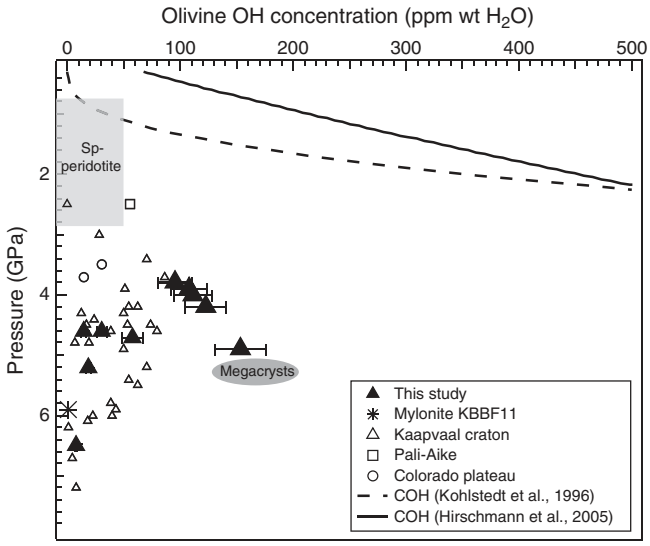

Fig. 10. OH concentration in olivine as a function of pressure in the studied xenoliths. For comparison, concentrations in olivine from previous studies on peridotite xenoliths from various cratonic and off-craton localities and in olivine megacrysts in kimberlitic magmas (Bell et al., 2004; Demouchy et al., 2006; Falus et al., 2008; Grant et al., 2007; Kurosawa et al., 1997; Li et al., 2008; Peslier and Luhr, 2006; Peslier et al., 2002; Stachel et al., 2003) are also displayed. Dashed line shows the water solubility at 1100 °C and increasing pressure from Kohlstedt et al. (1996). Solid line shows the water solubility in olivine based on Hirschmann et al. (2005).

(Fig. 2a–c), predominate among the studied garnet-bearing peridotites (66% of the samples). This microstructure (protogranular facies of Boullier and Nicolas, 1975) has often been interpreted as undeformed. However, these peridotites show clear olivine and orthopyroxene CPO (Fig. 6), with variable strength (J-index of olivine varies from <2 to >10, Fig. 7). The clear olivine CPO, together with the curvilinear to polygonal grain boundaries that characterize these samples (Fig. 2a–c), imply that plastic deformation was followed by effective recovery and grain boundary migration under static conditions (annealing). The present study, based on a larger number of samples, therefore corroborates the early interpretation of these textures by Boullier and Nicolas (1975). The highly recovered microstructures and very coarse grain sizes displayed by these peridotites imply very effective annealing, which is not coherent with the low equilibrium temperatures recorded by these xenoliths (dominantly <1000 °C). This supports an early deformation episode, perhaps associated with the formation of the cratonic root, which according to Re–Os data is older than 3 Ga (Griffin et al., 2004), followed by a long quiescence time. Fluid-enhanced grain boundary migration during the multiple metasomatic events (Bell et al., 2005; Kelemen et al., 1998; Simon et al., 2007; Wasch et al., 2009) may also have favored annealing in the Kaapvaal mantle.

In contrast, coarse-porphyroclastic peridotites preserve well-defined intracrystalline deformation features, such as undulose extinctions and subgrain boundaries in olivine or kinks in orthopyroxene, evidencing deformation by dislocation creep. These microstructures are much less common in the analyzed xenolith collection (12%). They correspond to domains, which may either have been less annealed because they were derived from shallower and cooler or less metasomatized parts of the mantle root, or have undergone deformation shortly before xenolith extraction. The latter interpretation is more probable for the deepest studied sample PHN5267 from Premier, which high equilibrium temperature (1464 °C) precludes the preservation of deformation microstructures for long times after the cessation of deformation.

Although coarse-granular microstructures are observed in all studied pipes, there are spatial differences, which were already noted by Boullier (1977). The coarsest-grained and most annealed peridotites are sampled by Jagersfontein, whereas Kimberley peridotites have finer-grained and least annealed microstructures, which preserve a weak foliation, marked by the elongation of olivine and orthopyroxene crystals (aspect ratios range from 1:2 to 1:4, Fig. 2b). Coarse-porphyroclastic microstructures are also more common in Kimberley (Table 2). This suggests either a stronger annealing or lower stress deformation in the lithospheric mantle beneath Jagersfontein. The remaining sites show, however, intermediate textures with no systematic variation.

In both coarse-granular and coarse-porphyroclastic xenoliths, the well-defined olivine CPO implies that dislocation creep was the dominant deformation process. Three olivine CPO patterns were identified: (1) axial-[100], (2) axial-[010], and (3) orthorhombic. Orthorhombic olivine CPOs are observed over the whole pressure range, while axial-[100] CPOs tend to concentrate on the top of the column (2.4–3.8 GPa). These olivine CPO patterns, characterized by a stronger concentration of [100] axes relative to [010] or [001] are coherent with simple or pure shear with dominant activation of high-temperature, low pressure, dry (010)[100] or (0kl)[100] slip systems, respectively (cf. Tommasi et al., 2000).

Axial-[010] olivine CPO, characterized by a point concentration of [010] and girdle distributions of [100] and [001] are however common in xenoliths equilibrated between 3.5 and 4.7 GPa. Such olivine CPO pattern may result from transpressional deformation (Tommasi et al., 1999), from changes in dominant glide system due to variations in physical parameters (differential stress, pressure, or water contents in olivine) during deformation, or from recrystallization (Falus et al., 2011; Tommasi et al., 2008). However, transpressional deformation should also result in dispersion of orthopyroxene [001] axes in the foliation plane, which is not observed in most studied peridotites, which show predominantly point distribution of orthopyroxene [001] axes (Fig. 6). Experimental deformation of olivine single crystals suggests that [001] glide may be favored at low temperature and high differential stresses (Durham and Goetze, 1977). The strong annealing that characterizes most coarse-grained harzburgites prevents a clear determination of the stresses and strain rates during their deformation, but their very coarse-grained microstructures is, nevertheless, more consistent with deformation under low stress conditions.

Occurrence of axial-[010] olivine CPO patterns in peridotites equilibrated at pressures 3.5–4.7 GPa might suggest that these CPO may record a change in deformation mechanism associated with an increase in confining pressure or in water contents, as the latter also increase in this depth range (Fig. 10). Experimental studies on a Griggs press (confining pressures ~2 GPa) suggested that high water fugacities and differential stresses may induce a transition from dominant [100] to dominant [001] glide (cf. review in Jung et al., 2006). Yet, according to these experiments, the water contents in olivine measured in the present study (Table 3) are not high enough to induce dominant [001] glide; they rather result in the so-called E-type fabric, characterized by [100] and [001] axes aligned parallel to the lineation and normal to the foliation, respectively. The lack of clear foliation and weak CPO (supplementary online material) in the coarse-granular peridotites for which water contents in olivine could be measured in this study does not allow discrimination of which is the dominant glide plane: (010) or (001).

Transition from dominant [100] to dominant [001] glide was also observed in experimental deformation at high confining pressures (Couvy et al., 2004); the pressure at which this transition occurred varied between experiments, ranging from 3 to 3.5 GPa (Jung et al., 2008) to ~7 GPa (Raterron et al., 2007). Equilibrium pressures for samples with axial-[010] olivine CPO (between 3.5 and 4.7 GPa) are in the same range as the Jung et al. (2008) values. Yet, orthorhombic olivine CPOs are even more common at these depths (Fig. 7b). Sole two samples have olivine [001] axes aligned parallel to the maximum concentration of orthopyroxene [001] axes, suggesting dominant

[001] glide, but they are equilibrated under slightly low pressure conditions (~3.3 GPa, Table 2).

An alternative explanation for the axial-[010] olivine CPO patterns in the coarse-grained peridotites from the Kaapvaal is dispersion of the [100] and [001] in response to recovery and subgrain rotation recrystallization (Falus et al., 2011). This interpretation is consistent with the observation that low-angle misorientations are dominantly accommodated by rotations around the [010] axis. CPO dispersion during static recrystallization may also explain the predominance of weak olivine CPO in the Kaapvaal craton (Fig. 7a). Low olivine J-indexes also predominate in peridotite xenoliths from the Siberian craton (Bascou et al., 2011). In general, cratonic peridotites yield lower J-indexes than peridotites from other tectonic settings (Fig. 11). However, although weakening of olivine CPO associated with modal metasomatism has been described in other environments (Bascou et al., 2008; Morales and Tommasi, 2011; Tommasi et al., 2004, 2008), in the present dataset, there is no clear relation between the olivine J-index, modal contents, or olivine mg# (Table 2).

Orthopyroxene CPOs are consistent with deformation by dislocation creep with activation of [001](100) and [001](010) slip systems. They are always correlated to olivine fabrics, meaning that both minerals underwent the same deformation. Well-defined CPOs are observed even in harzburgites showing high modal orthopyroxene, suggesting that they were deformed during or after the metasomatism leading to Si-enrichment. This interpretation is consistent with the observation of kinked interstitial orthopyroxene (Fig. 3a).

7.2. Evidence for metasomatism and timing relative to deformation

Textural evidence for reactive percolation of Si-rich fluids and/or melts is common in the coarse-granular harzburgites. It encompasses: (1) interpenetrating orthopyroxene and olivine boundaries (Fig. 2a–d), (2) small interstitial orthopyroxene crystals with cusped grain boundaries (Fig. 3a), (3) interstitial garnet in peridotite FRB1339 (Fig. 3d), (4) crystallization of small, interstitial, Cr-rich clinopyroxene, often associated with spinel and phlogopite (Fig. 3d), and (5) phlogopite rimming garnets or as interstitial crystals. Observation (1) may result either from orthopyroxene consumption during the extensive partial melting event that produced the most refractory olivines (Boyd and Mertzman, 1987) or from orthopyroxene crystallization at the expenses of olivine in response to reactions with Si-rich aqueous fluids or hydrous melts (Bell et al., 2005; Kelemen et al., 1998; Wasch et al., 2009). In contrast, observation (2) points to late crystallization of orthopyroxene and is consistent with the excess modal content of orthopyroxene, which characterizes the Kaapvaal harzburgites (Bell et al., 2005). The remaining observations point to partial crystallization or reaction with percolating melts at high pressure (3) and with K-rich compositions (4 and 5).

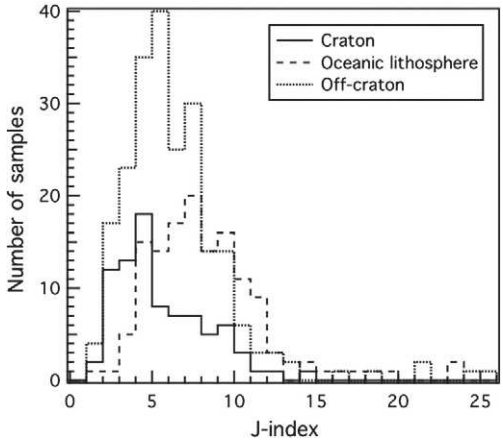

Fig. 11. Olivine J-index distributions for mantle xenoliths from cratons, off-craton continental regions, and oceanic plates. Data for cratonic samples from this study, Vauchez et al. (2005) and Bascou et al. (2011); for off-craton continental regions from Ben Ismaïl and Mainprice (1998), Vauchez and Garrido (2001), Pera et al. (2003), Duclos et al. (2005), Tommasi et al. (2006), Le Roux et al. (2007), Falus et al. (2008), Le Roux et al. (2008), Tommasi et al. (2008), Soustelle et al. (2009), and Morales and Tommasi (2011); and from oceanic plates from Ben Ismaïl and Mainprice (1998), Tommasi et al. (2004), and Soustelle et al. (2010).

Analysis of the microstructures may help in constraining the relative timing between deformation and episodes of reactive fluid percolation, even if some observations are ambiguous. Kinks in interstitial orthopyroxene (Fig. 3a) indicate pre- to syn-kinematic silica enrichment. However, undeformed orthopyroxenes with clear interstitial habitus are also observed in some samples, suggesting strongly that Si-enrichment may have continued post-kinematically. As discussed in the previous section, olivine and orthopyroxene CPOs are consistent, suggesting that both minerals recorded the same deformation, even in orthopyroxene-rich harzburgites, implying pre- to syn-kinematic metasomatism. Orthopyroxene CPO is however usually weak (the strongest values in Table 2 probably result from overestimation of the orthopyroxene CPO strength due to measurement of too few crystals), implying that post-kinematic orthopyroxene addition is also possible.

Phlogopite and clinopyroxene enrichment, on the other hand, is essentially post-kinematic, as indicated by the interstitial shapes and undeformed character of these minerals (Fig. 3d). The actual timing and processes responsible for this late metasomatism by K-rich fluids or melts (Bell et al., 2005; Grégoire et al., 2003; Griffin et al., 2003), are however still unclear; it may have happened at any point between the last deformation episode and shortly before extraction by the kimberlitic magmatism. In sample KBBF18, alignment of undeformed phlogopite and clinopyroxene parallel to the foliation (Fig. 3d) suggests nevertheless that the pre-existing deformation structure may have controlled the melt infiltration.

7.3. Sheared peridotites

Sheared peridotites are characterized by high equilibrium temperatures (between 1000 and 1300 °C) and relatively fertile compositions as pointed out by Nixon et al. (1981). They probably represent ancient coarse-granular rocks that underwent extensive dynamic and static recrystallization. Harzburgite PHN2760, with its very unusual texture (Fig. 4d), may indeed be an illustration of the first steps of formation of the sheared peridotites, which was followed by extensive fracturing and low-temperature serpentinization due to reaction with the kimberlitic melt during extrusion.

The asymmetry of the porphyroclasts in the mylonite implies simple shear deformation. Moreover, the fine recrystallized grain sizes indicate deformation under high deviatoric stresses and deformation rates (Austin and Evans, 2007), in particular considering the high equilibrium temperatures of these peridotites. Both orthopyroxene and olivine underwent dynamic recrystallization but the degree of recrystallization and the recrystallized grain size are larger in olivine than in orthopyroxene, consistent with the higher strength of orthopyroxene relative to olivine. Development of shear bands along fine-grained recrystallized orthopyroxene-rich layers suggests, that more effective grain refinement in the higher strength orthopyroxene-rich domains lead to strain localization. Boullier and Gueguen (1975) proposed that the olivine-rich domains deformed by dislocation creep whereas the fine-grained recrystallized orthopyroxene-rich layers deformed by grain sensitive creep.

Evidence of plastic deformation by dislocation creep, such as undulose extinction, subgrain boundaries, and recrystallization tails, has also been identified in mosaic and fluidal mosaic peridotites. However, the presence of polygonal recovered olivine crystals in the matrix implies that some annealing followed the deformation. The variable grain size and amount of polygonal crystals in the matrix may reflect different temperatures, annealing times, or variable

influence of fluids on the annealing process. Euhedral olivine crystals free of any deformation features (usually called tablets) are commonly observed on both strained porphyroclasts and the matrix of mosaic and fluidal mosaic peridotites. Such euhedral crystals have been often described in sheared xenoliths from South Africa (e.g., Boullier and Nicolas, 1975; Drury and Van Roermund, 1989; Skemer and Karato, 2008). Drury and Van Roermund (1989) proposed that these crystals record fluid-assisted static recrystallization, where a thin fluid film along grain boundaries enhances grain boundary mobility. Fluids may also have played an essential role in the formation of the mosaic texture, which may represent a more developed stage of fluid-assisted static recrystallization. The preservation of the fine-grained texture and deformation features in the orthopyroxene-rich shear bands may be explained by slower grain boundary migration in orthopyroxene in comparison to olivine (Skemer and Karato, 2008). Mosaic and fluidal mosaic peridotites may thus derive from porphyroclastic and mylonitic peridotites to which annealing is superimposed, respectively (Boullier and Nicolas, 1975).

Sheared peridotites display either orthorhombic or bimodal olivine CPO. The orthorhombic CPOs are consistent with deformation by dislocation creep activating high-temperature, low pressure (010)[100] slip system. The axial-[010] with a bimodal distribution of [100] and [001] axes suggest, on the other hand, simultaneous activation of the (010)[100] and (010)[001] slip systems. Similar olivine CPO were described in deep mantle xenoliths from the Tanzanian craton (Vauchez et al., 2005) and have been interpreted as resulting from activation of the two slip directions at high pressure and probably high stresses. This interpretation is consistent with the observation that bimodal olivine CPO are characteristic of sheared peridotites equilibrated at pressures > 4.5 GPa (Fig. 7c). Olivine CPO strength is always low (Fig. 7a), probably due to the extensive recrystallization (Falus et al., 2011). Orthopyroxene CPOs are coherent with deformation by dislocation creep with contribution of both [001] (100) and [001] (010) slip systems. Clinopyroxene CPO is consistent with deformation by dislocation creep, with dominant activation of the [001]{110} systems (Bascou et al., 2002). Both pyroxenes CPOs are correlated with the olivine CPO (Fig. 6 and online supplementary material), indicating that all major rock-forming minerals underwent the deformation producing the mylonitic microstructure. Indeed, clinopyroxene occurs as strained porphyroclasts and has CPO coherent with the olivine and orthopyroxene, indicating pre-mylonitization refertilization. Finally, alignment of recrystallized phlogopite in the mylonitic foliation in KBBF11 indicates that the mylonitization postpones potassic metasomatism. This observation contrasts with the pre-kinematic character of phlogopite in coarse-grained harzburgites, suggesting that mylonitization corresponds to a later deformation event.

In summary, microstructures and CPO in the sheared peridotites are consistent with post-metasomatism deformation by dislocation creep under high stress and strain rates. Fluidal mosaic and mosaic microstructures may be explained by subsequent fluid-assisted static recrystallization that may be related to the kimberlitic magmatism. The processes leading to this deformation have been widely debated in the literature. The kinked geotherm obtained from thermobarometry in mantle xenoliths from the Kaapvaal made Boyd and Nixon (1975) propose that the sheared peridotites may result from localized shearing at the lithosphere–asthenosphere boundary (LAB). This interpretation was re-proposed by Kennedy et al. (2002) for the sheared peridotites of the Slave craton. However, already in the 70s, Goetze (1975) highlighted that the observed geotherm disturbance is not consistent with shear heating and that the strain rates estimated from the microstructures and equilibrium temperatures of these rocks are too high to be produced by plate tectonics. Similar conclusions were reached by Boullier (1977) and more recently by Skemer and Karato (2008). Our observations are consistent with these conclusions, favoring the model proposed by Green and Gueguen (1974), who viewed the deformation that produced the sheared peridotites as due to ascending kimberlitic diapirs, instead of a quasi-stationary mantle flow at the LAB.

7.4. Hydration state of the Kaapvaal mantle lithosphere

OH concentrations in olivine obtained in this study are highly variable, however they show a general increase with pressure up to 5 GPa and a sharp decrease for pressures > 5.9 GPa (Fig. 12, Table 3). Maximum water contents in olivine measured in this study are among the highest ones measured in mantle peridotite xenoliths, reaching values close to those measured in kimberlite-borne megacrysts (Fig. 10). In samples equilibrated at pressures higher than 5.9 GPa, reliable estimates of water contents in olivine could be obtained for two samples, one coarse-grained peridotite and a mylonite. Both show <10 wt. ppm H_2O (Table 3), consistently with previous data in four other deep Kaapvaal peridotites by Peslier et al. (2010).

The observed increase in OH concentrations in olivine with depth up to 5 GPa is consistent with the increase of water solubility with increasing fH_2O and, hence, with pressure (Kohlstedt et al., 1996). Measured water contents remain, however, well below the olivine solubility curves of Hirschmann et al. (2005) and Kohlstedt et al. (1996), suggesting that even the most water-rich peridotites in the Kaapvaal are undersaturated in water. However, these water solubility curves in olivine only consider the effect of pressure. They do not include the effects of temperature, iron content in olivine, or the change of water fugacity with increasing solute dissolution at high pressures and temperatures and probably overestimate the solubility in the deepest part of the cratonic root (Bali et al., 2008; Ferot, 2011). Most analyzed peridotites contain phlogopite. Since hydrogen is compatible in sheet silicates, crystallization of phlogopite does not require prior saturation of the nominally anhydrous minerals (NAMs) that compose the peridotite. A recent experimental study shows that water solubility curves of mantle minerals are strongly modified by the presence of pargasite (Green et al., 2010). A similar behavior might be expected for olivine co-existing with phlogopite, but the solubility of water in NAMs in a phlogopite-bearing assemblage has not been quantified yet. In the present dataset, OH concentrations in olivine are uncorrelated with the presence or absence of phlogopite (Tables 2 and 3), although less IR peaks are observed in the phlogopite-rich sample KBJ59 (Fig. 8).

Are the measured values in olivine representative of OH concentrations at different depths in the Kaapvaal mantle? Since H behaves

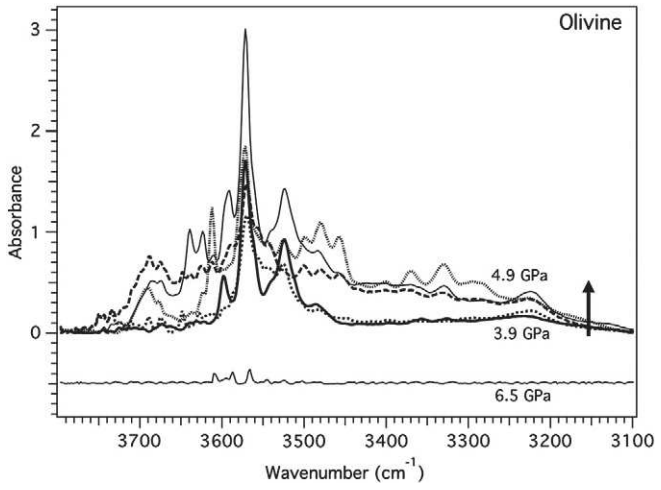

Fig. 12. Unpolarized infrared spectra of olivine showing the increase in absorbance with increasing equilibrium pressure between 3.9 GPa and 4.9 GPa and a spectrum from a deeper sample (PHN5267, equilibrated at 6.5 GPa). All spectra are normalized to a sample thickness of 1 cm.

as an incompatible element during partial melting (Bolfan-Casanova, 2005; Dixon et al., 2002; Hirschmann et al., 2005), olivines with high forsterite contents are expected to have low OH concentrations. This relation is not observed in the Kaapvaal peridotites; high OH concentrations were measured in olivines with mg# ranging from 90 to 94 (Fig. 13). This implies that the high water contents in olivine from intermediate depths in the cratonic mantle record re-hydration after the main partial melting episode that produced the mantle root. This conclusion brings additional questions. When and how did this water addition occur? What is its spatial extent?

High OH contents in olivine may result from hydration: (A) by solid-state diffusion of hydrogen from a volatile-rich asthenosphere, (B) during transport by the volatiles-rich kimberlitic magma, or (C) during metasomatism of the craton root by water-rich fluids or melts (Fig. 14). Re-hydration of lithospheric mantle in a continuous way by solid-state diffusion of hydrogen from the asthenosphere is not consistent with the observed low OH contents in olivine from peridotites equilibrated at >5.9 GPa. Moreover, even if the fast hydrogen flux along grain boundaries is taken into account (Demouchy, 2010), solid-state diffusion is a process too slow. For an average grain size of 1 μm, which is much smaller than even the smallest grains in the mylonites, and an effective hydrogen diffusion coefficient of 4.48×10^{-8} m^2/s at 1250 °C (Demouchy, 2010) more than 3 Gy would be needed to re-hydrate the entire cratonic root, and if a more representative grain size of 3 mm is considered, the H diffusion front would have progressed by less than 10 km over 3 Gy.

Scenario (B), that is, hydration during xenolith extraction by the kimberlites, is based on the observation that olivine megacrysts from kimberlites have high OH^- contents (Fig. 10), suggesting that the kimberlite magma is volatile-rich and, perhaps, water-saturated. It is also consistent with experimental data and with dehydration FTIR profiles in olivines from basalt-borne peridotite xenoliths, which both show extremely fast hydrogen diffusion in olivine at high temperature (Demouchy and Mackwell, 2006; Demouchy et al., 2006; Peslier and Luhr, 2006). Hydrogen addition to xenolithic minerals may therefore occur during the transport of the xenoliths, even if FTIR profiles do not record these exchanges (Kamenetsky et al., 2008).

In scenario (C), the re-hydration of the cratonic mantle is proposed to be associated with metasomatism by water-rich fluids or melts, for which there is abundant modal and geochemical evidence, like the Si-enrichment (Fig. 3a; Bell et al., 2005; Kelemen et al., 1998; Simon et al., 2007; Wasch et al., 2009) or the crystallization of

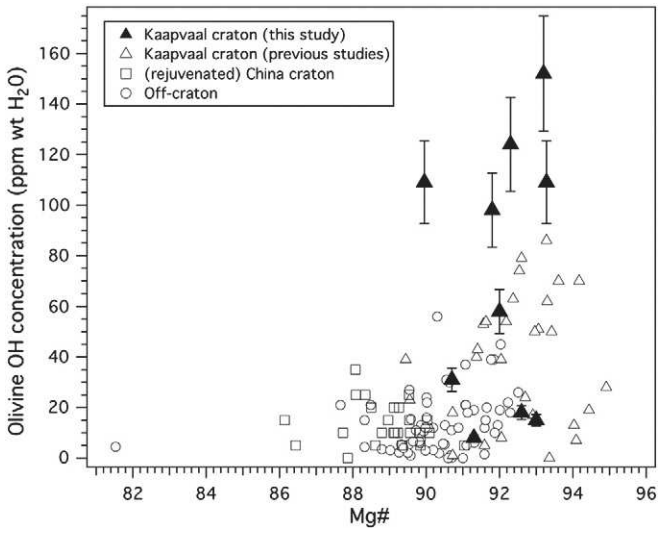

Fig. 13. OH concentration versus mg# in olivine. For comparison, data obtained in previous studies on peridotite xenoliths from various localities are also shown (Bell et al., 2004; Demouchy et al., 2006; Falus et al., 2008).

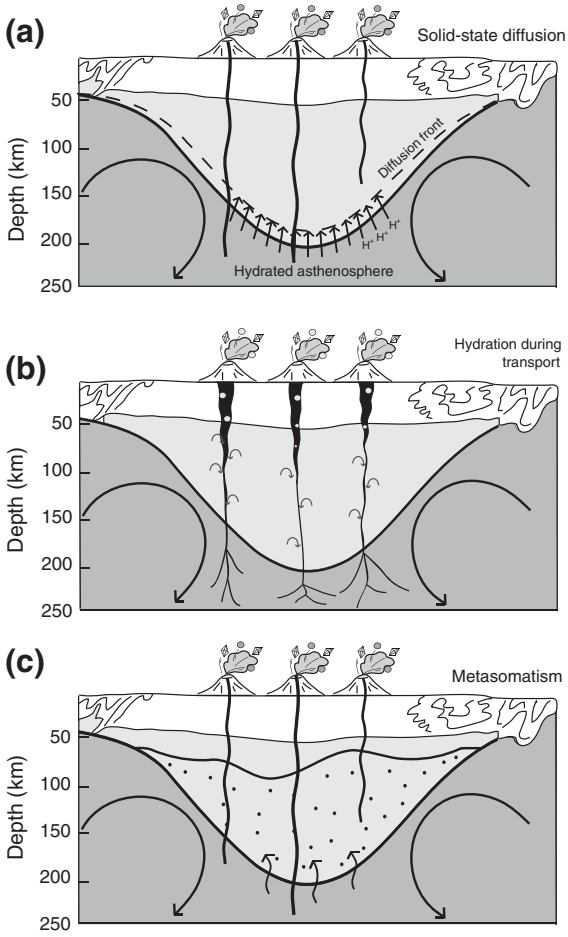

Fig. 14. Sketches illustrating the three scenarii proposed to explain the variation of OH^- concentration in olivine with depth in the Kaapvaal craton root.

secondary garnet, clinopyroxene and phlogopite (Fig. 3b and d; Grégoire et al., 2003; Simon et al., 2007). In this case, hydration may be both spatially and temporally heterogeneous, since it may be related to many distinct metasomatic episodes: from (i) early metasomatism by Si- and volatile-rich fluids that produced the high modal content of orthopyroxene in Kaapvaal harzburgites (Bell et al., 2005), which was proposed, based on Lu–Hf and Sm–Nd model ages, to be multiple episodes between 1.3 Ga and 600 Ma (Wasch et al., 2009), to (ii) late metasomatism by K-rich melts, which has caused phlogopite crystallization (Grégoire et al., 2003; Simon et al., 2007). This spatial and temporal variability is coherent with the OH^- concentration heterogeneity of the Kaapvaal olivines (Fig. 10).

In scenarios B and C, the observed vertical variation in OH^- concentrations may be accounted by considering the relative changes in water and carbon activity with pressure in volatile-rich (C–O–H) fluids, which at pressures >5 GPa, have high carbon and low water activities (Dixon et al., 1995; Newman and Lowenstern, 2002) and the variation in the mantle redox state with depth, as proposed by Peslier et al. (2010). If metasomatism is associated with percolation of basaltic magmas, change in the melt composition with progressive enrichment in volatiles during reactive percolation (O'Nions and McKenzie, 1988) may also account for the contrast in OH^- contents between the deepest and intermediate depth peridotites.

The two last scenarios have different implications for the cratonic root stability. In the first one, the root is essentially dry and the high water contents in olivine measured in the present study and in previous studies result from “contamination” during the ascent in the kimberlitic magma. In the second one, metasomatism may have hydrated and, hence, weakened at least parts of the cratonic root after

its formation. The very nature of xenolithic sampling by kimberlites prevents the evaluation of the actual volumes of the mantle affected by the metasomatic processes. Comparison between the magnetotelluric electrical conductivity data in a station close to Jagersfontein and the MT signal modeled using a constant water concentration in the cratonic mantle or a variation in water contents with depth similar to the one observed in this study (cf. the Fig. 8 in Fullea et al., 2011) suggests however that the vertical variation of water contents in olivine observed in the present study and in Peslier et al. (2010) may be representative of the present-day hydration state of the Kaapvaal mantle, favoring the last scenario and implying that metasomatism resulted in extensive re-hydration of the cratonic mantle at intermediate depths.

The annealed microstructures of Kaapvaal peridotites indicate however that rehydration was not followed by remobilization of the cratonic root. Several explanations may be proposed: (i) the extensive hydration of the intermediate depths of the cratonic root is recent and its mechanical effects have not been felt yet, (ii) the distribution of the hydrated domains is too heterogeneous, or (iii) the dry layer at its base (Fig. 10) protects the craton root from thermo-mechanical erosion by the convective mantle as proposed by Peslier et al. (2010). The latter hypothesis is appealing, but convective models testing the stability of a block with thickened lithosphere is largely eroded from its sides (edge-driven convection), unless it is >10 times wider than thick (Morency et al., 2002). This implies that a high strength layer at the base of the cratonic root may not be enough to ensure its preservation.

8. Conclusions

Coarse-granular refractory harzburgites predominate in the Kaapvaal mantle, being observed in all studied pipes at all depths. Their highly recovered microstructures and very coarse grain sizes contrast with the olivine and orthopyroxene CPO, indicating that deformation by dislocation creep was followed by effective annealing. This supports an early deformation episode, possibly associated to the formation of the cratonic root in the Archean, followed by slow cooling and a long quiescence time. Fluid-enhanced grain boundary migration during the multiple metasomatic events that affected the Kaapvaal mantle may also have favored annealing. Coarse-porphyroclastic peridotites are rarer, but present at all depths in Kimberley and in deep levels in Finsch and Premier. They represent domains less annealed or deformed shortly before extraction. Sheared peridotites with mylonitic, fluidal or mosaic microstructures, are common below 140 km depth. Their fine recrystallized grain sizes and high equilibrium temperatures imply deformation under high stress and high strain rates, not consistent with a quasi-stationary mantle flow at the lithosphere–asthenosphere boundary.

Textures and compositions of the studied xenoliths provide evidence for multiple metasomatic events with a spatially heterogeneous distribution. Analysis of the microstructures and comparison between the olivine and secondary mineral CPOs indicate that silica-enrichment episodes, which resulted in high modal orthopyroxene, were pre- to post-kinematic, and that metasomatism by K-rich fluids or melts and refertilization was post-kinematic. Deformation of phlogopite and clinopyroxene in the sheared peridotites implies that mylonitization postdated all metasomatic events.

Water contents in olivine are strongly variable, but tend to increase with depth up to 150 km, where they are among the highest measured in mantle peridotites (~150 wt. ppm H_2O; Bell et al., 2003 calibration). The deepest analyzed samples are, in contrast, almost dry. High water contents in coarse-grained peridotites are not accompanied by dominant activation of [001] glide. The bimodal olivine CPO in sheared peridotites indicates nevertheless activation of both [100] and [001] glide on the (010) plane, probably due to high pressure and stresses.

Lack of correlation between olivine mg# and water content indicates that the high water contents in olivine record re-hydration after formation of the refractory mantle root. Hydration of olivine may have occurred during either extraction of the peridotites by volatile-rich kimberlites or metasomatism by water-rich fluids/melts. Magnetotelluric electrical conductivity data in the central Kaapvaal is, however, best explained by models with a vertical variation of water contents in olivine similar to the one measured here, suggesting that the observed water contents in olivine may be representative of the present-day hydration state of the Kaapvaal mantle, favoring the metasomatism scenario. The predominance of highly annealed microstructures in the cratonic root indicates nevertheless that this re-hydration did not result in remobilization of the cratonic root.

Supplementary data to this article can be found online at http://dx.doi.org/10.1016/j.lithos.2012.05.001.

Acknowledgments

The authors thank A. Vauchez, J-M. Dautria, and S. Keshav for helpful discussions. C. Nevado and D. Delmas are thanked for providing high-quality polishing of sections for EBSD measurements. Electron microprobe analyses were carried out with the help of C. Merlet at the Service Microsonde Sud, Université Montpellier 2. FTIR analyses were performed with the assistance of D. Maurin at the Lab. Colloids, Verre et Nanomateriaux, at Université Montpellier 2, France. AT has been funded by CRYSTAL2PLATE, a EU FP7-funded Marie Curie Action under grant agreement PITN-GA-2008-215353. The EBSD-SEM national facility in Montpellier is supported by the Institut National de Sciences de l'Univers (INSU) du Centre National de la Recherche Scientifique (CNRS), France and by the Conseil Régional Languedoc-Roussillon, France.

References

Allsopp, H.L., Bristow, J.W., Skinner, E.M.W., 1985. The Rb–Sr geochronology of the Colossus kimberlite pipe, Zimbabwe. Transactions of the Geological Society of South Africa 88, 245–248.
Austin, N.J., Evans, B., 2007. Paleowattmeters: a scaling relation for dynamically recrystallized grain size. Geology 35, 343–346.
Bai, Q., Kohlstedt, D.L., 1993. Effects of chemical environment on the solubility and incorporation mechanism for hydrogen in olivine. Physics and Chemistry of Minerals 19, 460–471.
Bali, E., Bolfan-Casanova, N., Koga, K.T., 2008. Pressure and temperature dependence of H solubility in forsterite: an implication to water activity in the Earth interior. Earth and Planetary Science Letters 268, 354–363.
Bascou, J., Tommasi, A., Mainprice, D., 2002. Plastic deformation and development of clinopyroxene lattice preferred orientations in eclogites. Journal of Structural Geology 24, 1357–1368.
Bascou, J., Delpech, G., Vauchez, A., Moine, B.N., Cottin, J.Y., Barruol, G., 2008. An integrated study of microstructural, geochemical, and seismic properties of the lithospheric mantle above the Kerguelen plume (Indian Ocean). Geochemistry, Geophysics, Geosystems 9, Q04036. http://dx.doi.org/10.1029/2007GC001879.
Bascou, J., Doucet, L.S., Saumet, S., Ionov, D.A., Ashchepkov, I.V., Golovin, A.V., 2011. Seismic velocities, anisotropy and deformation in Siberian cratonic mantle: EBSD data on xenoliths from the Udachnaya kimberlite. Earth and Planetary Science Letters 304, 71–84.
Begg, G.C., Griffin, W.L., Natapov, L.M., O'Reilly, S.Y., Grand, S.P., O'Neill, C.J., Hronsky, J.M.A., Poudjom Djomani, Y., Swain, C.J., Deen, T., Bowden, P., 2009. The lithospheric architecture of Africa: seismic tomography, mantle petrology, and tectonic evolution. Geosphere 5, 23–50.
Bell, D.R., Rossman, G.R., Maldener, J., Endisch, D., Rauch, F., 2003. Hydroxide in olivine: a quantitative determination of the absolute amount and calibration of the IR spectrum. Journal of Geophysical Research 108, 2105. http://dx.doi.org/10.1029/2001JB000679.
Bell, D.R., Rossman, G.R., Moore, R.O., 2004. Abundance and partitioning of OH in a high-pressure magmatic system: megacrysts from the Monastery kimberlite, South Africa. Journal of Petrology 45, 1539–1564.
Bell, D., Grégoire, M., Grove, T., Chatterjee, N., Carlson, R., Buseck, P., 2005. Silica and volatile-element metasomatism of Archean mantle: a xenolith-scale example from the Kaapvaal craton. Contributions to Mineralogy and Petrology 150, 251–267.
Ben Ismaïl, W., 1999. La lithosphère cratonique: pétrophysique des xénolites mantelliques d'Afrique du Sud. PhD Thesis, Université de Montpellier II, 245 pp.
Ben Ismaïl, W., Mainprice, D., 1998. An olivine fabric database: an overview of upper mantle fabrics and seismic anisotropy. Tectonophysics 296, 145–157.

Ben Ismaïl, W., Barruol, G., Mainprice, D., 2001. The Kaapvaal craton seismic anisotropy: petrophysical analyses of upper mantle kimberlite nodules. Geophysical Research Letters 28, 13. http://dx.doi.org/10.1029/2000GL012419.
Berry, A.J., O'Neill, H.S.C., Hermann, J., Scott, D.R., 2007. The infrared signature of water associated with trivalent cations in olivine. Earth and Planetary Science Letters 261, 134–142.
Bolfan-Casanova, N., 2005. Water in the Earth's mantle. Mineralogical Magazine 69, 229–257.
Boullier, A.M., 1977. Structure des péridotites en enclaves dans les kimberlites d'Afrique du Sud. Conséquences sur la constitution du manteau supérieur. Bulletin de la Société Française de Minéralogie et Cristallographie 100, 214–229.
Boullier, A.M., Gueguen, Y., 1975. SP-mylonites: origin of some mylonites by superplastic flow. Contributions to Mineralogy and Petrology 50, 93–104.
Boullier, A.M., Nicolas, A., 1975. Classification of textures and fabrics of peridotite xenoliths from South African kimberlites. Physics and Chemistry of the Earth 9, 467–476.
Boyd, F.R., Mertzman, S.A., 1987. Composition and structure of the Kaapvaal lithosphere. In: Mysen, B.O. (Ed.), Magmatic Processes: Physiochemical Principles. Geochemical Society Special Publications, Washington, DC, pp. 13–24.
Boyd, F.R., Nixon, P.H., 1975. Origins of the ultramafic nodules from some kimberlites of northern Lesotho and the Monastery Mine, South Africa. Physics and Chemistry of the Earth 9, 431–454.
Boyd, F.R., Nixon, P.H., 1978. Ultramafic nodules from the Kimberley pipes, South Africa. Geochimica et Cosmochimica Acta 42 (9), 1367–1371 1373–1382.
Boyd, F.R., Gurney, J.J., Richardson, S.H., 1985. Evidence for a 150–200-km thick archean lithosphere from diamond inclusion thermobarometry. Nature 315, 387–389.
Brey, G.P., Köhler, T., 1990. Geothermobarometry in four-phase Lherzolites II. New thermobarometers, and practical assessment of existing thermobarometers. Journal of Petrology 31, 1353–1378.
Chevrot, S., Zhao, L., 2007. Multiscale finite-frequency Rayleigh wave tomography of the Kaapvaal craton. Geophysical Journal International 169, 201–215.
Couvy, H., Frost, D.J., Heidelbach, F., Nyilas, K., Ungar, T., Mackwell, S., Cordier, P., 2004. Shear deformation experiments of forsterite at 11 GPa–1400 °C in the multianvil apparatus. European Journal of Mineralogy 16, 877–889.
Davis, G.L., 1977. The ages and uranium contents of zircons from kimberlites and associated rocks. Carnegie Institution of Washington Year Book 76, 631–635.
Davis, G.L., 1978. Zircons from the mantle. US Geological Survey Open-File Report 78-701, pp. 86–88.
de Wit, M.J., Roering, Ch., Hart, R.G., Armstrong, R.A., de Ronde, C.E.G., Green, R.W.E., Tredoux, M., Pederby, E., Hart, R.A., 1992. Formation of an Archean Continent. Nature 357, 553–562.
Demouchy, S., 2010. Diffusion of hydrogen in olivine grain boundaries and implications for the survival of water-rich zones in the Earth's mantle. Earth and Planetary Science Letters 295, 305–313.
Demouchy, S., Mackwell, S., 2006. Mechanisms of hydrogen incorporation and diffusion in iron-bearing olivine. Physics and Chemistry of Minerals 33, 347–355.
Demouchy, S., Jacobsen, S.D., Gaillard, F., Stern, C.R., 2006. Rapid magma ascent recorded by water diffusion profiles in mantle olivine. Geology 34, 429–432.
Demouchy, S., Schneider, S.E., Mackwell, S.J., Zimmerman, M.E., Kohlstedt, D.L., 2009. Experimental deformation of olivine single crystals at lithospheric temperatures. Geophysical Research Letters 36, L04304. http://dx.doi.org/10.1029/2008GL036611.
Dixon, J.E., Stolper, E.M., Holloway, J.R., 1995. An experimental study of water and carbon dioxide solubilities in mid-ocean ridge basaltic liquids. Part I: Calibration and solubility models. Journal of Petrology 36, 1607–1631.
Dixon, J.E., Leist, L., Langmuir, C., Schilling, J.-G., 2002. Recycled dehydrated lithosphere observed in plume-influenced mid-ocean-ridge basalt. Nature 420, 385–389.
Doin, M.-P., Fleitout, L., Christensen, U., 1997. Mantle convection and stability of depleted and undepleted continental lithosphere. Journal of Geophysical Research 102, 2771–2787.
Drury, M.R., Van Roermund, H.L.M., 1989. Fluid assisted recrystallization in upper mantle peridotite xenoliths from kimberlites. Journal of Petrology 30, 133–152.
Duclos, M., K.S.M., Tommasi, A., Gledhill, K.R., 2005. Mantle tectonics beneath New Zealand inferred from SKS splitting and petrophysics. Geophysical Journal International 163, 760–774.
Durham, W.B., Goetze, C., 1977. Plastic flow of oriented single crystals of olivine 1. Mechanical data. Journal of Geophysical Research 82 (36), 5737–5754.
Eaton, D.W., Darbyshire, F., Evans, R.L., Grütter, H., Jones, A.G., Yuan, X., 2009. The elusive lithosphere–asthenosphere boundary (LAB) beneath cratons. Lithos 109, 1–22.
Eggler, D.H., Furlong, K.P., 1991. Destruction of subcratonic mantle keel: the Wyoming province. 5th Kimberlite Conference Extended Abstracts, pp. 85–87.
Evans, R.L., Jones, A.G., Garcia, X., Muller, M., Hamilton, M., Evans, S., Fourie, C.J.S., Spratt, J., Webb, S., Jelsma, H., Hutchins, D., 2011. Electrical lithosphere beneath the Kaapvaal craton, southern Africa. Journal of Geophysical Research 116, B04105.
Falus, G., Tommasi, A., Ingrin, J., Szabó, C., 2008. Deformation and seismic anisotropy of the lithospheric mantle in the southeastern Carpathians inferred from the study of mantle xenoliths. Earth and Planetary Science Letters 272, 50–64.
Falus, G., Tommasi, A., Soustelle, V., 2011. Effect of dynamic recrystallization on olivine crystal preferred orientations in mantle xenoliths deformed under varied stress conditions. Journal of Structural Geology 33, 1528–1540.
Ferot, A., 2011. Etude expérimentale à haute pression et haute température du stockage et de la distribution de l'eau dans le manteau supérieur terrestre. Université Blaise Pascal, Clermont-Ferrand II. 259 pp.
Finnerty, A.A., Boyd, F.R., 1987. Thermobarometry for garnet peridotite xenoliths: a basis for mantle stratigraphy. In: Nixon, P.H. (Ed.), Mantle Xenoliths. Wiley, New York, pp. 381–402.
Frets, E., Tommasi, A., Garrido, C., Padron-Navarta, J.A., Amri, I., Targuisti, K., 2012. Deformation processes and rheology of pyroxenites under lithospheric mantle conditions. Journal of Structural Geology 39, 138–157. http://dx.doi.org/10.1016/j.jsg.2012.02.019.
Fullea, J., Muller, M.R., Jones, A.G., 2011. Electrical conductivity of continental lithospheric mantle from integrated geophysical and petrological modeling: application to the Kaapvaal Craton and Rehoboth Terrane, southern Africa. Journal of Geophysical Research 116, B10202. http://dx.doi.org/10.1029/2011JB008544.
Goetze, C., 1975. Sheared lherzolites: from the point of view of rock mechanics. Geology 3, 172–173.
Grant, K., Ingrin, J., Lorand, J., Dumas, P., 2007. Water partitioning between mantle minerals from peridotite xenoliths. Contributions to Mineralogy and Petrology 154, 15–34.
Green, H.W., Gueguen, Y., 1974. Origin of kimberlite pipes by diapiric upwelling in upper mantle. Nature 249, 617–620.
Green, D.H., Hibberson, W.O., Kovacs, I., Rosenthal, A., 2010. Water and its influence on the lithosphere–asthenosphere boundary. Nature 467, 448–451.
Grégoire, M., Bell, D.R., Le Roex, A.P., 2003. Garnet lherzolites from the Kaapvaal craton (South Africa): trace element evidence for a metasomatic history. Journal of Petrology 44, 629–657.
Griffin, W.L., O'Reilly, S.Y., Natapov, L.M., Ryan, C.G., 2003. The evolution of lithospheric mantle beneath the Kalahari Craton and its margins. Lithos 71, 215–241.
Griffin, W.L., Graham, S., O'Reilly, S.Y., Pearson, N.J., 2004. Lithosphere evolution beneath the Kaapvaal Craton: Re–Os systematics of sulfides in mantle-derived peridotites. Chemical Geology 208, 89–118.
Hirschmann, M.M., Aubaud, C., Withers, A.C., 2005. Storage capacity of H_2O in nominally anhydrous minerals in the upper mantle. Earth and Planetary Science Letters 236, 167–181.
Hirth, G., Kohlstedt, D., 2003. Rheology of the upper mantle and the mantle wedge: a view from the experimentalists. AGU Geophysical Monograph 138, 83–105.
James, D.E., Fouch, M.J., Vandecar, J.C., Van der Lee, S., 2001. Tectospheric structure beneath southern Africa: the Kaapvaal Project: formation and evolution of cratons. Geophysical Research Letters 28, 2485–2488.
James, D.E., Niu, F., Rokosky, J., 2003. Crustal structure of the Kaapvaal craton and its significance for early crustal evolution. Lithos 71, 413–429.
James, D.E., Boyd, F.R., Schutt, D., Bell, D.R., Carlson, R.W., 2004. Xenolith constraints on seismic velocities in the upper mantle beneath southern Africa. Geochemistry, Geophysics, Geosystems 5, Q01002.
Jaupart, C., Mareschal, J.C., 1999. The thermal structure and thickness of continental roots. Lithos 48, 93–114.
Jordan, T.H., 1978. Composition and development of continental tectosphere. Nature 274, 544–548.
Jung, H., Katayama, I., Jiang, Z., Hiraga, T., Karato, S., 2006. Effect of water and stress on the lattice-preferred orientation of olivine. Tectonophysics 421, 1–22.
Jung, H., Mo, W., Green, H.W., 2008. Upper mantle seismic anisotropy resulting from pressure-induced slip transition in olivine. Nature Geoscience 2, 73–77.
Kamenetsky, V.S., Kamenetsky, M.B., Sobolev, A.V., Golovin, A.V., Demouchy, S., Faure, K., Sharygin, V.V., Kuzmin, D.V., 2008. Olivine in the Udachnaya-East kimberlite (Yakutia, Russia): types, compositions and origins. Journal of Petrology 49 (4), 823–839.
Keefner, J.W., Mackwell, S.J., Kohlstedt, D.L., Heidelbach, F., 2011. Dependence of dislocation creep of dunite on oxygen fugacity: implications for viscosity variations in Earth's mantle. Journal of Geophysical Research 116, B05201.
Kelemen, P.B., Hart, S.R., Bernstein, S., 1998. Silica enrichment in the continental upper mantle via melt/rock reaction. Earth and Planetary Science Letters 164, 387–406.
Kennedy, L.A., Russell, J.K., Kopylova, M.G., 2002. Mantle shear zones revisited: the connection between the cratons and mantle dynamics. Geology 30, 419–422.
Kohlstedt, D.L., Keppler, H., Rubie, D.C., 1996. Solubility of water in the alpha, beta, and gamma phases of $(Mg, Fe)_2SiO_4$. Reviews in Mineralogy and Geochemistry 123, 345–357.
Kovacs, I., O'Neill, H.C.J., Hermann, J., Hauri, E.H., 2010. Site-specific infrared O–H absorption coefficients for water substitution into olivine. American Mineralogist 95, 292–299.
Kramers, J.D., Smith, C.B., 1983. A feasibility study of U–Pb and Pb–Pb dating of kimberlites using groundmass mineral fractions and whole-rock samples. Chemical Geology 41, 23–38.
Kurosawa, M., Yurimoto, H., Sueno, S., 1997. Patterns in the hydrogen and trace element compositions of mantle olivines. Physics and Chemistry of Minerals 24, 385–395.
Le Roux, V., Bodinier, J.-L., Tommasi, A., Alard, O., Dautria, J.-M., Vauchez, A., Riches, A.J.V., 2007. The Lherz spinel lherzolite: refertilized rather than pristine mantle. Earth and Planetary Science Letters 259, 599–612.
Le Roux, V., Tommasi, A., Vauchez, A., 2008. Feedback between melt percolation and deformation in an exhumed lithosphere–asthenosphere boundary. Earth and Planetary Science Letters 274, 401–413.
Lenardic, A., Moresi, L.-N., 1999. Some thoughts on the stability of cratonic lithosphere: effects of buoyancy and viscosity. Journal of Geophysical Research 104, 12,747–12,758.
Lenardic, A., Moresi, L.N., Muhlhaus, H., 2003. Longevity and stability of cratonic lithosphere: insights from numerical simulations of coupled mantle convection and continental tectonics. Journal of Geophysical Research 108, 2303. http://dx.doi.org/10.1029/2002JB001859.
Li, J., Kornprobst, J., Vielzeuf, D., Fabriès, J., 1995. An improved experimental calibration of the olivine–spinel geothermometer. Chinese Journal of Geochemistry 14, 68–77.
Li, Z.-X.A., Lee, C.-T.A., Peslier, A.H., Lenardic, A., Mackwell, S.J., 2008. Water contents in mantle xenoliths from the Colorado Plateau and vicinity: implications for the

mantle rheology and hydration-induced thinning of continental lithosphere. Journal of Geophysical Research 113, B09210.
Malkovets, V.G., Griffin, W.L., O'Reilly, S.Y., Wood, B.J., 2007. Diamond, subcalcic garnet, and mantle metasomatism: kimberlite sampling patterns define the link. Geology 35, 339–342.
McIntyre, R.M., Dawson, J.B., 1976. Age and significance of some South African kimberlites. Abstracts of the 4th European Colloquium on Geochronology, Cosmochemistry and Isotope Geology, Amsterdam, the Netherlands. Abstract, 66.
Menzies, M.A., Fan, W., Zhang, M., 1993. Palaeozoic and Cenozoic lithoprobes and the loss of >120 km of Archean lithosphere, Sino-Korean craton, China. Geological Society of London, Special Publication 76, 71–81.
Miller, G.H., Rossman, G.R., Harlow, G.E., 1987. The natural occurrence of hydroxide in olivine. Physics and Chemistry of Minerals 14, 461–472.
Moore, R.O., 1986. A study of the kimberlite, diamonds and associated rocks and minerals from the Monastery mine, South Africa. PhD Thesis. University of Cape Town, 251 pp.
Morales, L.F.G., Tommasi, A., 2011. Composition, textures, seismic and thermal anisotropies of xenoliths from a thin and hot lithospheric mantle (Summit Lake, southern Canadian Cordillera). Tectonophysics 507, 1–15.
Morency, C., Doin, M.P., Dumoulin, C., 2002. Convective destabilization of a thickened continental lithosphere. Earth and Planetary Science Letters 202, 303–320.
Newman, S., Lowenstern, J.B., 2002. VOLATILECALC: a silicate melt–H_2O–CO_2 solution model written in Visual Basic for excel. Computers and Geosciences 28, 597–604.
Nickel, K.G., Green, D.H., 1985. Empirical geothermobarometry for garnet peridotites and implications for the nature of the lithosphere, kimberlites and diamonds. Earth and Planetary Science Letters 73, 158–170.
Nixon, P.H., Rogers, N.W., Gibson, I.L., Grey, A., 1981. Depleted and fertile mantle xenoliths from southern African kimberlites. Annual Review of Earth and Planetary Sciences 9, 285–309.
O'Reilly, S.Y., Griffin, W.R., 2010. The continental lithosphere–asthenosphere boundary: can we sample it ? Lithos 120, 1–13.
O'Neill, H.S.C., Wood, B.J., 1979. An experimental study of Fe–Mg partitioning between garnet and olivine and its calibration as a geothermometer. Contributions to Mineralogy and Petrology 70, 59–70.
O'Nions, R.K., McKenzie, D.P., 1988. Melting and continents generation. Earth and Planetary Science Letters 90, 449–456.
Paterson, M.S., 1982. The determination of hydroxyl by infrared absorption in quartz, silicate glasses and similar materials. Bulletin de Mineralogie 105, 20–29.
Pearson, D.G., Carlson, R.W., Shirey, S.B., Boyd, F.R., Nixon, P.H., 1995. Stabilisation of Archean lithospheric mantle: a Re–Os isotope study of peridotite xenoliths from the Kaapvaal craton. Earth and Planetary Science Letters 134, 341–357.
Pera, E., Mainprice, D., Burlini, L., 2003. Anisotropic seismic properties of the upper mantle beneath the Torre Alfina area (Northern Apennines, Central Italy). Tectonophysics 370, 11–30.
Peslier, A.H., Luhr, J.F., 2006. Hydrogen loss from olivines in mantle xenoliths from Simcoe (USA) and Mexico: mafic alkalic magma ascent rates and water budget of the sub-continental lithosphere. Earth and Planetary Science Letters 242, 302–319.
Peslier, A.H., Luhr, J.F., Post, J., 2002. Low water contents in pyroxenes from spinel peridotites of the oxidized, sub-arc mantle wedge. Earth and Planetary Science Letters 201, 69–86.
Peslier, A.H., Woodland, A.B., Wolff, J.A., 2008. Fast kimberlite ascent rates estimated from hydrogen diffusion profiles in xenolithic mantle olivines from southern Africa. Geochimica et Cosmochimica Acta 72, 2711–2722.
Peslier, A.H., Woodland, A.B., Bell, D.R., Lazarov, M., 2010. Olivine water contents in the continental lithosphere and the longevity of cratons. Nature 467, 78–81.
Phillips, D., Machin, K.J., Kiviets, G.B., Fourie, L.F., Roberts, M.A., Skinner, E.M.W., 1998. A petrographic and $^{40}Ar/^{39}Ar$ geochronological study of the Voorspoed kimberlite, South Africa: implications for the origin of Group II kimberlite magmatism. South African Journal of Geology 101, 299–306.
Pollack, H.N., 1986. Cratonization and thermal evolution of the mantle. Earth and Planetary Science Letters 80, 175–182.
Post, J.L., Borer, L., 2000. High-resolution infrared spectra, physical properties, and micromorphology of serpentines. Applied Clay Science 16, 73–85.
Raterron, P., Chen, J., Li, L., Weidner, D., Cordier, P., 2007. Pressure-induced slip-system transition in forsterite: single-crystal rheological properties at mantle pressure and temperature. American Mineralogist 92, 1436–1445.
Riley, T.R., Leat, P.T., Curtis, M.L., Millar, I.L., Duncan, R.A., Fazel, A., 2005. Early Middle Jurassic dolerite dykes from Western Dronning Maud Land (Antarctica): identifying mantle sources in the Karoo large igneous province. Journal of Petrology 46, 1489–1524.
Scoates, J.S., Friedman, R.M., 2008. Precise age of the platiniferous Merensky Reef, Bushveld complex, South Africa, by the U–Pb zircon chemical abrasion ID-TIMS technique. Economic Geology 103, 465–471.
Shirey, S.B., Harris, J.W., Richardson, S.H., Fouch, M.J., James, D.E., Cartigny, P., Deines, P., Viljoen, F., 2002. Diamond genesis, seismic structure, and evolution of the Kaapvaal–Zimbabwe craton. Science 297, 1683–1686.
Simon, N.S.C., Carlson, R.W., Pearson, D.G., Davies, G.R., 2007. The origin and evolution of the Kaapvaal cratonic lithospheric mantle. Journal of Petrology 48, 589–625.
Skemer, P., Karato, S.-I., 2008. Sheared lherzolite xenoliths revisited. Journal of Geophysical Research 113, B07205.
Skogby, H., Bell, D.R., Rossman, G.R., 1990. Hydroxide in pyroxene; variations in the natural environment. American Mineralogist 75, 764–774.
Smith, C.B., Allsopp, H.L., Kramers, J.D., Hutchinson, G., Roddick, J.C., 1985. Emplacement ages of Jurassic–Cretaceous South African kimberlites by the Rb–Sr method on phlogopite and whole-rock samples. Transactions of the Geological Society of South Africa 88, 249–266.
Soustelle, V., Tommasi, A., Bodinier, J.-L., Garrido, C.J., Vauchez, A., 2009. Deformation and reactive melt transport in the mantle lithosphere above a large-scale partial melting domain: the Ronda peridotite massif, southern Spain. Journal of Petrology 50, 1235–1266.
Soustelle, V., Tommasi, A., Demouchy, S., Ionov, D.A., 2010. Deformation and fluid, a rock interaction in the supra-subduction mantle: microstructures and water contents in peridotite xenoliths from the Avacha Volcano, Kamchatka. Journal of Petrology 51, 363–394.
Stachel, T., Harris, J.W., Tappert, R., Brey, G.P., 2003. Peridotitic diamonds from the Slave and the Kaapvaal cratons—similarities and differences based on a preliminary data set. Lithos 71, 489–503.
Tommasi, A., Tikoff, B., Vauchez, A., 1999. Upper mantle tectonics: three-dimensional deformation, olivine crystallographic fabrics and seismic properties. Earth and Planetary Science Letters 168, 173–186.
Tommasi, A., Mainprice, D., Canova, G., Chastel, Y., 2000. Viscoplastic self-consistent and equilibrium-based modeling of olivine lattice preferred orientations: implications for the upper mantle seismic anisotropy. Journal of Geophysical Research 105, 7893–7908.
Tommasi, A., Godard, M., Coromina, G., Dautria, J.-M., Barsczus, H., 2004. Seismic anisotropy and compositionally induced velocity anomalies in the lithosphere above mantle plumes: a petrological and microstructural study of mantle xenoliths from French Polynesia. Earth and Planetary Science Letters 227, 539–556.
Tommasi, A., Vauchez, A., Godard, M., Belley, F., 2006. Deformation and melt transport in a highly depleted peridotite massif from the Canadian Cordillera: implications to seismic anisotropy above subduction zones. Earth and Planetary Science Letters 252, 245–259.
Tommasi, A., Vauchez, A., Ionov, D.A., 2008. Deformation, static recrystallisation, and reactive melt transport in shallow subcontinental mantle xenoliths (Tok Cenozoic volcanic field, SE Siberia). Earth and Planetary Science Letters 272, 65–77.
Vauchez, A., Garrido, C.J., 2001. Seismic properties of an asthenospherized lithospheric mantle: constraints from the lattice preferred orientations in peridotite from the Ronda massif. Earth and Planetary Science Letters 192, 235–249.
Vauchez, A., Dineur, F., Rudnick, R.L., 2005. Microstructure, texture and seismic anisotropy of the lithospheric mantle above a mantle plume: insights from the Labait volcano xenoliths. Earth and Planetary Science Letters 232, 295–314.
Wasch, L.J., van der Zwan, F.M., Nebel, O., Morel, M.L.A., Hellebrand, E.W.G., Pearson, D.G., Davies, G.R., 2009. An alternative model for silica enrichment in the Kaapvaal subcontinental lithospheric mantle. Geochimica et Cosmochimica Acta 73, 6894–6917.
Yang, X.-Z., Xia, Q.K., Deloule, E., Dallai, L., Fan, Q.-C., Feng, M., 2008. Water in minerals of the continental lithospheric mantle and overlying lower crust: a comparative study of peridotite and granulite xenoliths from the North China Craton. Chemical Geology 256, 33–45.

Chapitre 3: Diffusion de l'hydrogène d'un liquide kimberlitique à la forstérite

L'hydrogène est un élément présentant des taux de diffusions élevés dans l'olivine à haute température (e.g. Demouchy et al., 2006; Demouchy and Mackwell, 2006), et ayant un impact significatif sur les propriétés physiques et chimiques du manteau (Demouchy et al., 2012; Gaetani and Grove, 1998; Hirth and Kohlstedt, 1996; Jacobsen et al., 2008; Karato, 1990; Mackwell et al., 1985). La connaissance de son impact sur la rhéologie du manteau a ainsi conduit des géologues à suggérer que de faibles teneurs en hydrogène pouvaient avoir généré un contraste de viscosité suffisant pour préserver le craton de la convection mantellique et de la tectonique des plaques durant plusieurs milliards d'années (Doin et al., 1997 ; Pollack, 1986). Pourtant, les analyses par spectroscopie infrarouge à transformée de Fourrier (IRTF) révèlent des teneurs en hydrogène élevées dans l'olivine des péridotites du Kaapvaal jusqu'à une profondeur de 150 km (Baptiste et al., 2012; Peslier et al., 2010). De telles teneurs pourraient avoir été héritées à la suite d'un épisode métasomatique et donc être représentatives de la composition de la racine cratonique en profondeur, mais la possibilité d'une contamination durant extraction par les kimberlites riches en volatiles ne peut être exclue malgré l'absence de profils de diffusion (Baptiste et al., 2012). Toutefois, aucune étude expérimentale n'a à ce jour testé ou quantifié la diffusion en hydrogène entre un liquide kimberlitique et l'olivine, nous empêchant de conclure sur l'origine exacte des teneurs en hydrogène élevées dans l'olivine dans notre étude sur les xénolites du Kaapvaal.

Le travail expérimental présenté dans ce chapitre avait donc pour objectif de tester si l'incorporation d'hydrogène par diffusion ionique pouvait avoir lieu entre un liquide kimberlitique et la forstérite à haute pression et température. Il repose sur 5 expériences au piston cylindre effectuées au laboratoire Magmas et Volcans de l'Université de Clermont-Ferrand à 1200-1300°C et 1 GPa, pour des durées de 1 min, 5h et 23h.

Les analyses de deux capsules par EBSD (Electron Back-Scattered Diffraction) et microsonde électronique montrent qu'après 5h et 23h d'expérience, une surcroissance du cristal de forstérite, possédant la même orientation cristallographique a cristallisée. Le liquide a cristallisé ailleurs sous la forme de cristaux micrométriques de forstérite automorphes aux orientations cristallographiques aléatoires, ainsi que sous la forme de cristaux nanométriques

d'une phase alumineuse et d'une phase calcique. Les analyses des teneurs en hydrogène par spectroscopie IRTF après expérience révèlent qu'aucun des cristaux de forstérite ne présente de signe d'hydratation, et ce, malgré la saturation en H_2O du système et des durées d'expérience longues. La présence de CO_2 dans le système pourrait ainsi avoir abaissé la fugacité en H_2O au point de ne pouvoir hydrater ni le cristal de forstérite, ni sa surcroissance.

De tels résultats suggèrent que les teneurs en hydrogène élevées dans les xénolites mantelliques du craton du Kaapvaal ont été acquises durant un épisode métasomatique plutôt que durant leur transport à la surface par les kimberlites, et sont certainement représentatives de la composition en profondeur de la racine cratonique.

Inhibition of forsterite hydration from CO_2-H_2O-rich kimberlitic liquid

Virginie Baptiste[1*], Sylvie Demouchy[1], Shantanu Keshav[1], Fleurice Parat[1], Nathalie Bolfan-Casanova[2] & Pierre Condamine[2]

[1]*Géosciences Montpellier, Université Montpellier 2 & CNRS, CC 60, Place E. Bataillon, 34095 Montpellier cedex 5, France.*

[2] *Laboratoire Magmas et Volcans, CNRS, 5, rue Kessler, 63000 Clermont-Ferrand, France*

Running title: Inhibition of forsterite hydration from CO_2-H_2O-rich kimberlitic liquid

(*) corresponding author: virginie.baptiste@gm.univ-montp2.fr;

Phone: +33 467144912

Fax: +33 467143603

Abstract

Knowledge of the high diffusivity of hydrogen has raised the question of the origin and relevance of high OH concentrations measured in mantle xenoliths transported by volatile-rich magmas. To test if hydrogen incorporation by ionic diffusion can occur between a volatile-rich kimberlitic liquid and forsterite at high pressure and temperature, we conducted high pressure experiments using a piston-cylinder apparatus at 1200-1300°C and 1 GPa for durations of 1 min, 5h, and 23h. Kimberlitic liquid in the system CaO-MgO-Al_2O_3-SiO_2-CO_2-H_2O and synthetic forsterite single crystals were chosen as a first simplification of the complex natural kimberlite composition. Unpolarized Fourier transform infrared spectroscopy was used to quantify OH concentrations in the crystallographically oriented forsterite. Electron backscattered diffraction and electron microprobe analysis were performed to identify the run products. After 5h and 23h, a forsterite overgrowth crystallized with the same orientation as the initial forsterite single crystal. The kimberlitic liquid has crystallized as micron-scale euhedral forsterite neocrystals with random crystallographic orientations, as well as a nano-scale aluminous phase and a calcic phase. Despite water-saturation of the system and long duration, none of the initial forsterite single crystals display signs of hydration such as hydrogen diffusion profile from the border toward the center of the crystal. The presence of CO_2 in the system may have lowered the H_2O fugacity to such extends which has prohibiting meaningful hydration of the forsterite single crystal or its overgrowth. These experimental results favor a deep mantle origin of the high OH content found in natural mantle-derived xenoliths transported in kimberlites, as reported from the Kaapvaal craton. It also points out to the fact that hydration must take place in a CO_2-poor environment.

Keywords: Kimberlite, water, hydrogen, diffusion, olivine, point defect.

Introduction

Incorporation of hydrogen in nominally anhydrous minerals (NAMs), even at trace concentrations (ppm by weight level), is known to have a significant impact on the chemical and physical properties of the rocks and minerals in Earth's mantle such as melting temperature, electrical conductivity, seismic velocities, and rheology (e.g., Karato et al., 1990; Mackwell et al., 1985; Hirth and Kohlstedt, 1996; Demouchy et al., 2012; Gaetani and Grove, 1998; Jacobsen et al., 2008). For instance, in terms of rheology, olivine controls the viscosity of the lithosphere root and its low OH^- concentrations (< 20 ppm H_2O wt based on FTIR calibration from Paterson, 1982) was proposed to increase the mantle viscosity and hence a strongly OH-depleted zone at the base of the craton root could be responsible for the longevity of the South African craton (Peslier et al., 2010; Baptiste et al., 2012). This hypothesis was tested recently by studying mantle peridotites from the Siberian craton, but was not confirmed (Doucet et al., 2014). Prior to these recent studies, several publications have reported high OH concentrations (> 30 ppm H_2O wt) in olivine from mantle xenoliths, olivine megacrysts, and kimberlitic olivine phenocrysts from several cratons (e.g., South Africa, Siberia, and Canada; see Miller et al., 1987; Matsyuk et al., 1998; Bell et al., 2004; Matsyuk and Langer, 2004; Peslier et al., 2010; Peslier, 2010, Doucet et al., 2014). In particular, relatively high OH concentrations in olivine (up to 150 ppm H_2O wt) have been reported in olivine of mantle xenoliths from the Kaapvaal craton (Peslier et al., 2010; Baptiste et al., 2012), except for the deepest and infrequent samples, which are almost dry (<10 ppm H_2O wt). Further, high OH concentrations in olivine (54-419 ppm H_2O wt) have been measured in megacrysts and macrocrysts from kimberlites (Bell et al., 2004, Matsyuk and Langer, 2004; Matveev and Stachel, 2007) suggesting that kimberlite would be a favorable environment for hydrogen incorporation in olivine.

Moreover, studies on Kaapvaal mantle xenoliths usually report homogeneous OH concentration profiles across olivine grains suggesting the absence of hydration or dehydration process caught-in-the-act (Peslier et al., 2010; Baptiste et al., 2012). However, the origin of hydrogen in olivines from the cratonic mantle still remains unclear. High OH contents in olivine in Kaapvaal xenoliths could have been inherited from (1) metasomatism, if water-saturated fluids or water-saturated percolating melts impregnated the cratonic root, or (2) during transport by the water-rich kimberlitic magmas (Brooker et al., 2011; Baptiste et al., 2012). Yet, so far,

experimental studies have not tested the second hypothesis or quantified the diffusion of hydrogen between a volatile-rich kimberlitic melt/magma and olivine.

The aim of this study is to test if hydrogen incorporation by ionic diffusion can occur between a model very volatile-rich kimberlitic liquid in the system CaO-MgO-Al_2O_3-SiO_2-CO_2-H_2O (CMAS-CO_2-H_2O) and iron-free forsterite at high pressure and temperature during transport toward the surface.

Sample preparation and experimental method

A synthetic volatile-rich kimberlite starting material was prepared with high purity oxides (SiO_2 - Aldrich, 99.995%, Al_2O_3 - Alfa Aesar, 99.998%, MgO - Alfa Aesar, 99.998%,), high purity calcium carbonate ($CaCO_3$ - Alfa Aesar, 99.998%), magnesium hydroxide (brucite, $Mg(OH)_2$ - Alfa Aesar, 99.998%), and a very pure natural magnesite ($MgCO_3$) from Oberdorf (Austria, see Buob et al., 2006). The silicate portion of the starting mixture was prepared first. The components MgO, Al_2O_3, and SiO_2 were fired in platinum (Pt) crucibles for at least 18-20 hours in air at 1250^{o}C, and $CaCO_3$ at 400^{o}C. Pt crucibles were used that had not been previously utilized to dry either iron metal or iron oxides. Afterwards, the fired oxides and $CaCO_3$ were immediately mixed in appropriate proportions, and ground for at least 1 hour under ethanol in an agate mortar. After drying under an infrared (IR) heat lamp, the mixture was decarbonated in air in a high temperature, room pressure furnace. To decarbonate, the temperature of the furnace was slowly ramped to 1000^{o}C over 10 hours, and maintained at this temperature for 6-7 hours. After this step, the mixture was taken out of the furnace, and then transferred to another high temperature furnace to prepare a glass by melting the mixture in air at 1650^{o}C for about 4 hours. To quench this liquid to a glass, the Pt-crucible containing the mixture was partially immersed in an ice-water bath, and the resulting glass was optically clear and transparent. This glass was finely ground under ethanol for about 30-40 minutes, and using the same procedure, glassing was repeated twice more. To ensure homogeneity, the silicate glass was then re-ground for 1 hour under ethanol in an agate mortar, and then dried under an IR heat lamp for about 1 hour. Finally, CO_2 and H_2O were added in the silicate glass as magnesite and brucite, respectively. Ground magnesite and brucite were fired at 250°C and 120°C, respectively in air in a Pt-crucible for over 17 hours, to obtain stochiometric components, then mixed and ground with the silicate glass in an agate mortar under ethanol for another 1 hour. The final powder was stored in a desiccator.

Table 1: Forsterite and starting material composition, average kimberlite group-I and group-II compositions, and compositions of run products from VB12.

Wt.%	Starting composition	Group I Kimberlite Average*	Group II Kimberlite Average*	Forsterite crystal composition	VB12 compositions (after run)				
					Fo single crystal	Fo overgrowth	Fo neocrystals	Al-rich phase	Ca-rich phase
SiO_2	30	26.15	33.89	44.76	43.25	43.02	43.08	4.73	28.35
TiO_2	0	2.58	1.77	0.00	0.01	0.00	0.00	0.00	0.03
Al_2O_3	4	2.76	3.76	-0.01	-0.02	0.46	1.21	53.37	1.78
FeO		-	-	0.00	-0.01	0.00	0.00	0.16	0.05
Fe_2O_3	0	10.72	8.76	-	-	-	-	-	-
MnO	0	0.19	0.18	0.00	0.01	0.00	0.00	0.00	0.01
MgO	28	25.20	23.15	55.41	56.49	54.61	54.99	25.04	18.86
CaO	14	13.20	9.96	0.00	0.00	0.43	0.31	10.20	28.75
Na_2O	0	0.16	0.25	-0.01	0.00	0.00	0.00	0.01	0.02
K_2O	0	0.83	3.63	0.00	0.00	0.00	0.00	0.01	0.00
P_2O_5	0	2.04	1.85	-	-	-	-	-	-
SO_3	0	0.17	0.21	-	-	-	-	-	-
NiO	0	0.11	0.14	0.00	0.01	0.00	0.00	0.01	0.00
Cr_2O_3	0	0.18	0.23	-0.01	0.00	0.00	0.00	0.00	0.00
LOI	-	14.71	10.75	-	-	-	-	-	-
H_2O-	-	0.27	1.34	-	-	-	-	-	-
H_2O+	-	6.67	7.33	-	-	-	-	-	-
H_2O	13	-	-	-	-	-	-	-	-
CO_2	11	8.19	4.21	-	-	-	-	-	-
total		84.29	87.78	100.16	99.78	98.51	99.60	93.53	77.85

* Average compositions from Becker and Le Roex (2006).
Fo:single crystal of crystallographically oriented forsterite

The composition of this starting composition is reported in Table 1 and was synthetized on the basis of published compositions of: (1) erupted kimberlites (Smith et al., 1985a, b; Mitchell, 1986, 1995; Becker and Le Roex, 2006; Kamenetsky et al., 2008; Kjarsgaard et al., 2009; Sparks et al., 2009, Brooker et al., 2011), (2) the results of experimental petrology of kimberlites in the system CMAS-CO_2 (Dalton and Presnall, 1998; Gudfinnsson and Presnall, 2005), and (3) the solubility of water (H_2O) in model carbonatitic melts (Keppler, 2003). From studies in the system CMAS-CO_2 (e.g., Gudfinnsson and Presnall, 2005), it appears that kimberlites are not stable liquids at 1 GPa, but at higher pressures, >5 GPa. At such high pressures, the liquid used here will be in equilibrium with forsterite, orthopyroxene (opx), clinopyroxene (cpx), and garnet. Here, the starting composition was chosen to target hydration of olivine from kimberlite liquid during transport toward the surface (e.g., then in a rising metastable kimberlitic liquid), and accordingly, the experiment were run at a lower pressure than their estimated depth of genesis, on the basis of previous experimental petrology studies (Dalton and Presnall, 1998; Gudfinnsson and Presnall, 2005).

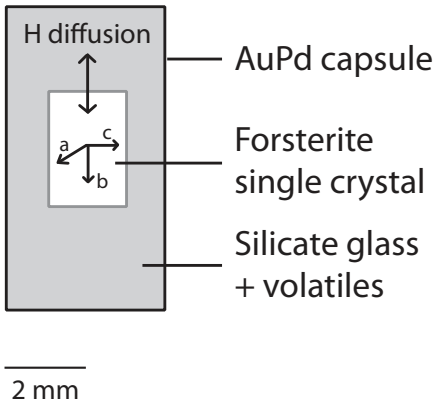

Figure 1: Schematic illustration of the capsule assembly for high pressure diffusion experiments.

High pressure assemblies were prepared by placing a crystallographically oriented single crystal of forsterite (iron-free forsterite from Roditi) within ~60 mg of starting material, in 4 mm outer diameter and 7 mm length gold-palladium ($Au_{75}Pd_{25}$) capsules (see Figure 1), which were then welded shut. AuPd capsules were chosen to minimize water loss. Single crystals of forsterite were in average 2.20 × 2.65 × 1.9 mm (for [100], [010], and [001] being the crystallographic axes, respectively). The capsules were then placed in salt (NaCl) cylinders. Experiments were

performed in a 19.1 mm non end-loaded piston cylinder apparatus (pressure calibrations detailed in Xirouchakis et al., 2001). Temperature was controlled using a $W_{74}Re_{26}$-$W_{95}Re_5$ thermocouple. Five runs were completed, and all cells were pressurized to 1.0 GPa. They were annealed at 1200°C for 1 min, 5h and 23h, or annealed at 1250 and 1300°C for 5h. Annealing duration over 2 hours at temperature above 900 °C is long enough to permit detectable hydrogenation of olivine or forsterite (Demouchy and Mackwell, 2003, 2006) at pressures above 0.2 GPa. Temperature quench rate was 50 °C.s^{-1}. Experimental conditions are summarized in Table 2. Short duration experiments were chosen to avoid significant hydrogen loss or reaction with the capsule (<50h). The experimental duration of 1 min was chosen to test if the heating up stage allows any significant hydrogen diffusion between the forsterite crystal from the volatile-rich kimberlite melt. All the experiments reported here were performed at Laboratoire Magmas et Volcans, Clermont-Ferrand (France).

Table 2: Experimental conditions in piston-cylinder.

Run	Sample	Pressure (GPa)	Temperature (°C)	Duration (min)	free fluid
1	VB7	1.0	1200	1	✔
2	VB1	1.0	1200	300	✔
3	VB6	1.0	1200	1380	✔
4	VB10	1.0	1300	300	✔
5	VB12	1.0	1250	300	✔

Sample analysis

Electron microprobe analysis (EMPA)

Major elements composition of the forsterite crystals was analyzed before experiments using a Cameca SX100 electron microprobe at Microsonde Sud facility, in Montpellier (France). Analytical conditions were a focused beam of 20 kV of accelerating voltage and 10 nA probe current at the Faraday cup. After experimental runs, the composition of the forsterite crystal and the newly formed phases was also analyzed. Results are reported in Table 1. Typical composition of natural Group-I and Group-II kimberlites from Becker and LeRoex (2006) are also provided for comparison. After experimental runs, each capsule was pierced to check for excess free fluid to insure water saturation of the liquid; each capsule has shown fluid bubbles.

Fourier transform infrared spectroscopy

Each capsule was doubly hand-polished for unpolarized *Fourier transform infrared spectroscopy (*FTIR) analysis. The sections were immersed in pure acetone for at least 12h to dissolve any intergranular CrystalBond glue before analysis. FTIR spectroscopy analyses were made at the Laboratoire des Colloïdes, Verres, Nanomatériaux in Montpellier (France) using a Bruker IFS66v coupled with a Bruker HYPERION microscope and a liquid nitrogen-cooled mercury-cadmium-telluride (MCT) detector. A Globar light source and a Ge-KBr beam splitter were used to generate unpolarized mid-infrared radiation. A background measurement was performed before analysis. Measurements were made with aperture sizes between 30 to 100 μm, with the IR beam parallels to [010] crystallographic axis of the forsterite crystals (i.e., across the basal plane of the capsule). Two hundred scans were accumulated with a resolution of 4 cm^{-1} for each measurement. A baseline correction was applied on each spectrum using the OPUS software. Spectra were then normalized to a sample thickness of 1 cm. Fractures and inclusions were strictly avoided. The sample thickness was measured using a micrometer with an accuracy of ± 1 μm. The calibration of Paterson (1982) was used to quantify the OH concentration in each mineral phase:

$$C_{OH} = \frac{X_i}{150\zeta}\int \frac{k(\bar{\nu})}{(3780-\bar{\nu})}d\bar{\nu}$$

where C_{OH} is the hydroxyl concentration (in mol H/l), ζ is an orientation factor (1/3 for unpolarized measurements), and $k(\bar{\nu})$ is the absorption coefficient in cm^{-1} for a given wavenumber $\bar{\nu}$. Xi is a density factor equal to 2750 ppm H_2O wt, for iron-free forsterite (see Bolfan-Casanova et al., 2000, for the calculation method).

Electron-backscattered diffraction

After experimental runs, sections cut through VB6 and VB12 capsules were mounted on epoxy plugs and carefully polished. Analyses were performed with a Scanning electron microscope (SEM) CamScan X500FE CrystalProbe equipped with an Electron-backscattered diffractometer (EBSD) at Geosciences Montpellier (France), using an acceleration voltage of 25kV and a working distance of 20 mm. To avoid charging of the samples, low vacuum conditions were chosen (5 Pa of gaseous nitrogen). EBSD patterns were produced by interaction between an electron beam at 20° to the horizontal sample stage (see Demouchy et al. 2011 for a

detailed description of the CrystalProbe-EBSD). Data were acquired using CHANNEL5 software. Punctual measurements were made to determine the crystallographic orientation of the forsterite single crystals and the newly produced crystalline phases.

Results

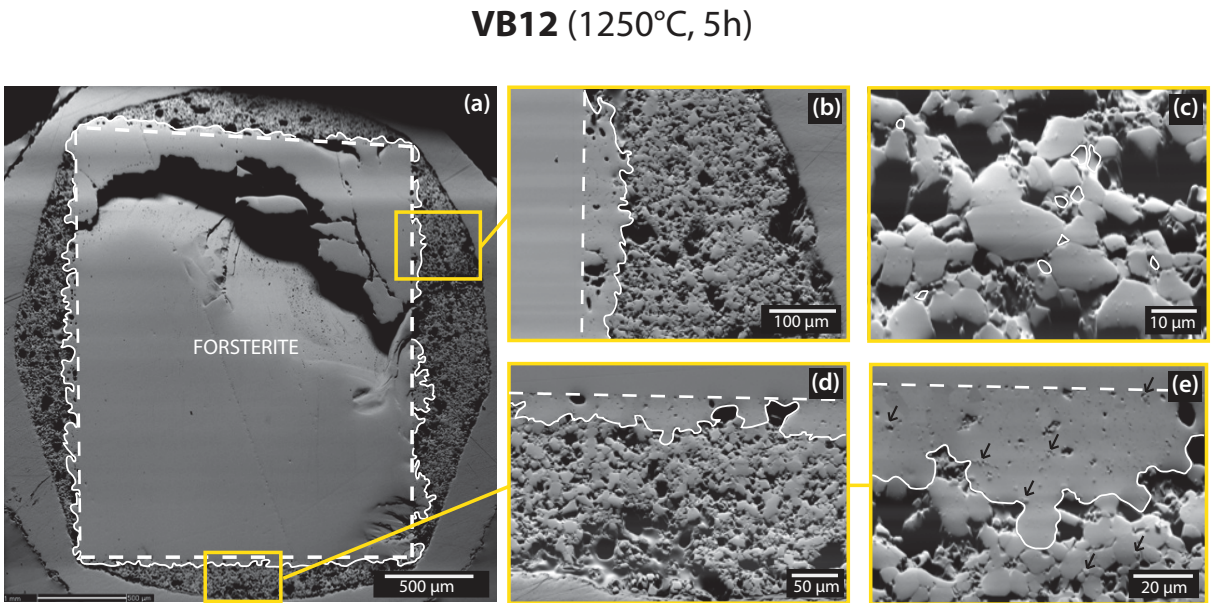

Figure 2: SEM-images of VB12 after experiment, showing (a) the entire capsule section with the forsterite single crystal displaying a well-defined overgrowth, (b) and (d) the forsterite single crystal boundary, its overgrowth, and the surrounding euhedral forsterites, (c) the euhedral forsterite and the Ca-rich phase are circled by a white line, (e) Al-rich phase within the forsterite overgrowth and close to euhedral forsterites.

Results from SEM-EBSD will be presented first, followed by the characterization by EMPA and finally FTIR results. SEM images of the typical recovered capsule are shown in Figure 2. During the experiments, the original shape of the forsterite single crystal has been well preserved, despite few fractures due to decompression. Micrometer-size forsterite overgrowths which have formed, display the same crystallographic orientation (homo-epitaxy) as the initial forsterite single crystal as shown by the Kikuchi bands pattern in Figures 3a and 3b. The width of the forsterite overgrowth increases with increasing run duration and reaches up to 135 microns after 23h. In addition, the kimberlitic melt has crystallized euhedral neocrystals of forsterite with variable crystallographic orientations as shown in Figures. 2c and 3. From EBSD and Energy Dispersive X-ray (EDX), a minor spinel-like (cubic) Al-rich crystalline phase was also identified,

occurring mostly as small crystallites (tens of nanometers) within the forsterite overgrowth as shown in Figures. 2e, and by point analysis in Figures. 3d. A Ca-rich phase with well-defined crystallographic planes has also been identified (Figures. 2, and 3e). Several vesicles were present (20 μm in diameter), but no quenched vitrified melt was observed.

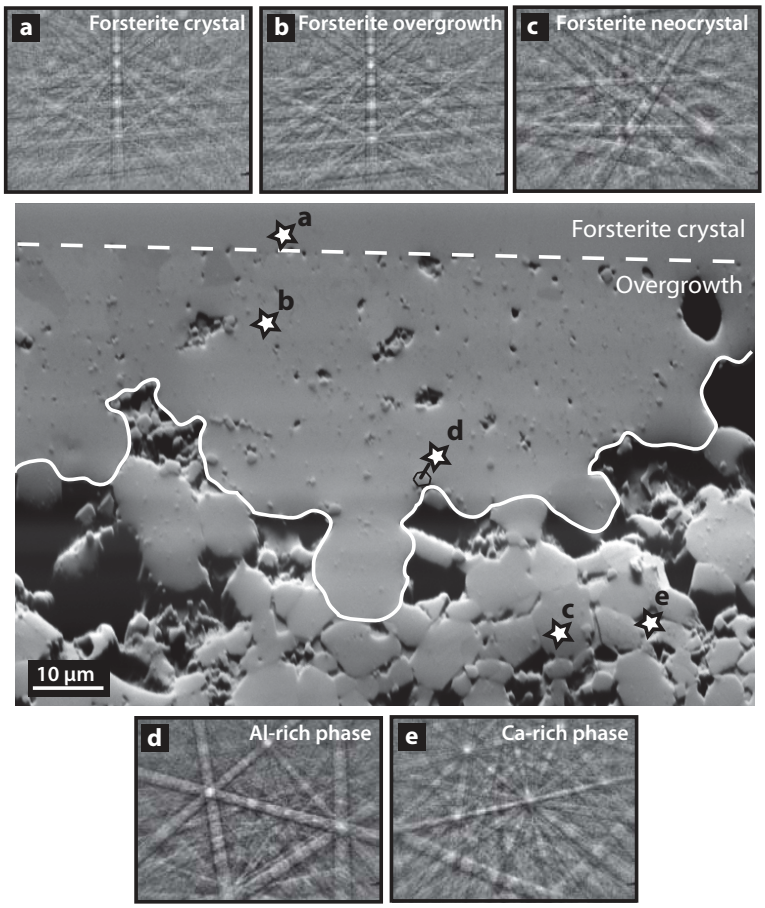

Figure 3: SEM-images of VB12 and electron back-scattered diffraction patterns (Kikuchi's bands: Kikuchi, 1928) of (a) the forsterite single crystal, (b) the forsterite overgrowth, (c) a euhedral forsterite, (d) the Al-rich spinel, (e) the Ca-rich phase.

Subsequently, EMPA analyses after EBSD reported in Table 1 reveal that the forsterite single crystal, forsterite overgrowths, and the forsterite neocrystals have very similar major element composition. The Al-rich phase has a composition closer to spinel than sapphirine and corundum (Ackermand et al., 1975), but is enriched in CaO (>10 wt.%). The Ca-rich phase has a composition close to monticellite ($CaMgSiO_4$, Deer et al., 1992, p354-355; Brooker et al., 2011)

but with lower silica content, it could be a carbonate-like phase as well. For both the Al-rich and Ca-rich phases, the size of the phase (below 10 nanometer) has significantly limited the outcomes and quality of the EMPA analyses and thus their identification.

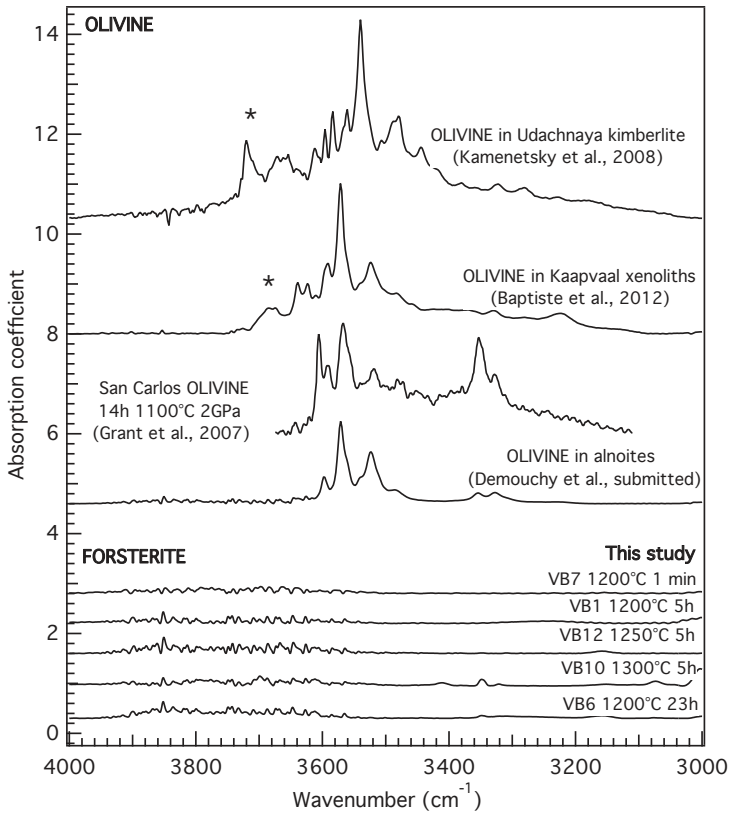

Figure 4: Unpolarized infrared spectra of the forsterite crystals after experiments (at 1 GPa) from this study. FTIR spectra from olivine in Udachnaya and Kaapvaal xenoliths (transported by kimberlite, Baptiste et al., 2012; Kamenetsky et al., 2008), in Malaita xenoliths (transported by alnoites, Demouchy et al. revised), and in San Carlos olivine hydrated after 14h in a piston-cylinder experiments at 1100°C and 2 GPa (Grant et al., 2007) are presented for comparison. All spectra are normalized to a sample thickness of 1 cm.

FTIR analyses were performed on the post-runs forsterite single crystal (center and border) as well as on the adjacent forsterite overgrowths. The unpolarized border spectra are displayed in Figures 4 and 5. For the same position in the forsterite single crystal, the FTIR spectra do not change as a function of temperature, or experimental duration (Figure 4) and display no OH bands within their absorption field in forsterite. Minor OH bands only appear after passing the interface between the forsterite single crystal and the forsterite overgrowths as shown

in Figure 5. The amplitude of these bands increases with increasing distance from the interface. The OH absorption band located at 3698 cm^{-1} is the first to appear, and always exhibits the highest absorption coefficient. It can be attributed to serpentine or brucite (Miller et al., 1987). The minor band at 3612 cm^{-1} is characteristic of iron-free forsterite (Demouchy and Mackwell, 2003, Lemaire et al., 2004) and the large broad band at 3427 cm^{-1} was previously attributed to inter-granular water (e.g., Keppler and Rauch, 2000; Demouchy et al., 2012). In the next section, we discuss the lack of hydration of the forsterite single crystal and the possible consequences for the hydration state of the lithospheric mantle.

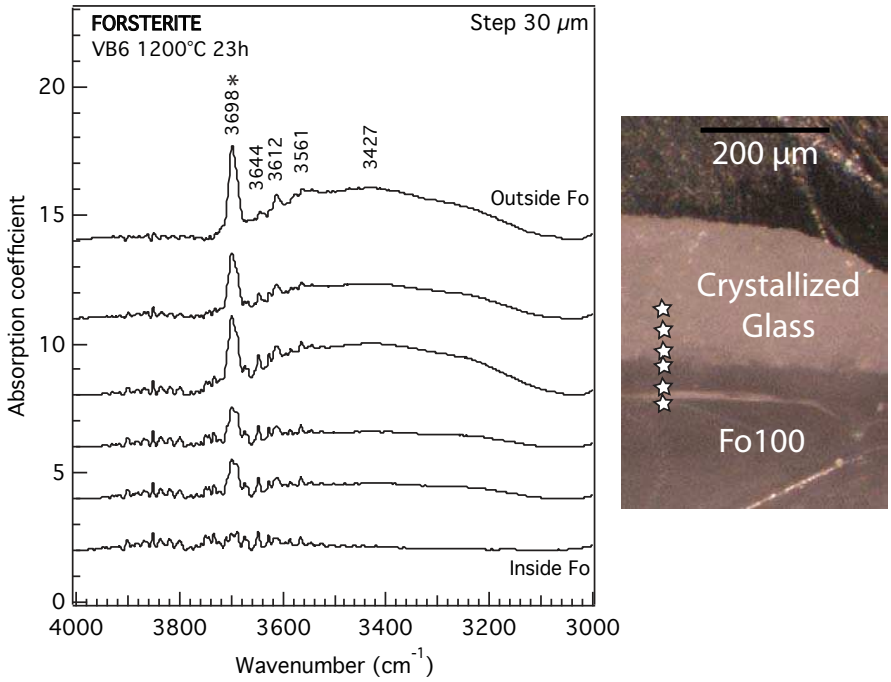

Figure 5: Unpolarized FTIR profile across the forsterite single crystal interface. Six spectra were measured with a step size of 30 μm. All spectra are normalized to a sample thickness of 1 cm. See text for OH band attribution.

Discussion

Unpolarized FTIR analyses has demonstrated that despite water-saturation of the system and long duration, none of forsterite single crystals display signs of hydration at OH saturation level or as diffusion profile of OH from the border toward the center of the crystal. Further, the absorption level of the FTIR spectra on the forsterite overgrowths does not even resemble the level of hydration from any of the characteristic spectra of mantle-derived or megacryst olivine

transported by kimberlites from cratonic regions (Baptiste et al., 2012; Bell et al., 2004; Miller et al., 1987; Peslier et al., 2010) as shown in Figure 4. They also do not match the olivine or forsterite spectra from hydration experiments at high pressure and temperature in CO_2-free system for only few hours at temperature above 1100°C as previously reported (Demouchy and Mackwell, 2003; Grant et al., 2007; Lemaire et al., 2004; Sokol et al., 2013a, 2013b; Yang et al., 2014), except for the very weak bands at 3612 cm^{-1} and maybe that at 3361 cm^{-1}. The other, more intense, IR peaks present are linked to hydrous minerals (brucite and/or serpentine), and are most likely the result of the rapid pressure and temperature quench.

Theses experiments were set up to test if a volatile-rich kimberlitic liquid could hydrate mantle-derived olivine during their transport toward the surface. Hydration during transport could have explained the absence of dehydration profile in olivine crystals transported by kimberlite as well as the high water contents reported in mantle-derived olivine from cratonic setting if hydration took place at important depths (Baptiste et al, 2012; Bell et al. 2004; Doucet et al., 2014; Kamenetsky et al., 2007; Kurosawa et al., 1997; Miller et al. 1987). In all five experiments, no OH was found in the single crystal of forsterite, whatever the duration of the experiment. At 1 GPa and at water-saturated conditions in a CO_2-free system, OH content should reach 100 ppm H_2O wt in iron-bearing olivine (Kohlstedt et al., 1996; Férot and Bolfan-Casanova, 2012; Grant et al., 2007; Mosenfelder et al., 2006) and > 25 ppm H_2O wt in iron-free olivine (e.g., Demouchy and Mackwell, 2003; Lemaire et al., 2004; Grant et al., 2006; Bali et al., 2008). The run products reported here are far from such high hydrogen concentration. Further, it is known that in mixed fluids, composed of CO_2 and H_2O (Holloway and Blank, 1994), the fugacity of H_2O is reduced with the addition of CO_2, and vice-versa. Here, our simplest interpretation is that despite the high H_2O bulk content (>10 wt.%; Table 1) in the starting kimberlitic liquid, the presence of CO_2 has lowered the H_2O fugacity to such an extent that it has prohibited hydration of the forsterite single crystal or overgrowth (Figures. 4 and 5). The effect of CO_2 on lowering H_2O fugacity in kimberlitic liquids was previously anticipated by Sokol et al. (2013b) based on high-pressure, high-temperature crystallization experiments of olivine phenocrysts from a powder with a composition of an exotic erupted kimberlite (from Udachnaya, Siberia; Kamenetsky et al., 2008). Also, a recent experimental study from Yang et al., (2014) has assessed the effect of CO_2 on lowering H_2O fugacity in a melt-free system (i.e., hydrothermal annealing of natural olivine + free H_2O + $NaHCO_3$ or $Ag_2C_2O_4$). However, in this study, hydration was not completely

inhibited and hydrogen incorporation was only reduced by a factor 2 under a pressure of 1.5-5 GPa. Thus, our results corroborate the results from Yang et al., (2014) and confirm the role of CO_2 in prohibiting significant hydration of the forsterite and olivine crystals.

The important forsterite overgrowth is a notable result from our experiments and was previously reported in hydration experiments (e.g., Kohlstedt et al., 1996; Bali et al., 2008). One may question the link between crystal overgrowth and the lack of hydration in our experiments. From over 20 measurements per crystallographic axis on the SEM images, we determine that the overgrowth length is in average after 5h at 1250°C: 72 μm parallel to [100] and 102 μm parallel to [001]; and after 23h at 1200°C: 179 μm parallel to [100] and 153 μm parallel to [001]). Two mechanisms of hydrogen diffusion can be considered based on two types of point defects in forsterite: hydrogen diffusion is rate limited by Mg-vacancy diffusivity or Si-vacancy diffusivity. Also, using the diffusion coefficients determined experimentally, one can calculate the characteristic distance (x) of hydrogen diffusion in forsterite (i.e., $x = 2 \times (Dt)^{1/2,}$ where D is the diffusion coefficient in m^2/s and *t* time in s^{-}). Assuming a Mg-vacancy (Demouchy and Mackwell 2003, Padron-Navarta, et al., 2014), it yields after 5h at 1250°C a length of 263 μm parallel to [100] and 823 μm parallel to [001]; after 23h at 1200°C a length of 419 μm parallel to [100] and 1337 μm parallel to [001]. Therefore, if this mechanism of diffusion is assumed, the characteristic distance of hydrogen diffusion exceeds by far the overgrowth length and should have permitted the full hydration of the forsterite overgrowth and significant hydration of the forsterite single crystal. Assuming a Si vacancy-controlled diffusion of hydrogen (Padron-Navarta, et al., 2014) which is a slower mechanism of diffusion, it yields after 5h at 1250°C a length of 149 μm and after 23h at 1200°C a length of 174 μm. In this case, the characteristic distance is closed to the length of the overgrowth, therefore, even if the initial forsterite single crystal was not hydrated, the overgrowth should have incorporated significant H (>20 ppm H_2O wt). All available diffusion kinetics data and solubility experiments converge toward efficient hydrogen incorporation in a CO_2-free system. Except the drastic reduction of water fugacity favored in this study, the only remaining possibility to explain the lack of hydration would be an extremely slow diffusivity of hydrogen in the order of 1 to 5×10^{-15} m^2s^{-1} and accordingly, an unrealistic low vacancy concentration at such high temperature of annealing.

Furthermore, as regards to the lack of significant data on olivine grain growth, our crystallization experiments allow to estimate the rate of grain growth of forsterite crystals. In

silicate systems with crystals and liquid at chemical equilibrium (with very small ΔT), Ostwald ripening (Ostwald, 1901) allows growth of large grains at the expense of the small ones and layer growth mechanism should control grain growth instead of continuous growth (Cabane et al., 2005). Following the relation linking grain size and time (e.g., Ardell, 1972; Kirkpatrick, 1975; Cabane et al., 2005) as:

$$d^n - d_o^n = kt,$$

where d and d_o are the final and initial grain size, n the grain growth exponent, k is the growth rate and t is time. For diffusion-control or spiral layer-growth control (i.e., screw dislocation based), it implies an exponent n equal to 3 (e.g., Cabane et al., 2005). For our experiment, at 1250 °C (VB12), it results in a growth rate of $k = 2.34 \times 10^8 \pm 0.90 \times 10^8$ μm^3/h for the [100] axis and $2.28 \times 10^8 \pm 1.14 \times 10^8$ μm^3/h for [001] axis. At 1200 °C (VB6), it yields a growth rate k of $1.34 \times 10^8 \pm 0.41 \times 10^8$ μm^3/h for [100] axis and of $0.69 \times 10^8 \pm 0.29 \times 10^8$ μm^3/h for [001] axis. Several studies on grain growth experiments in nano-scale monocrystalline aggregates (melt-free) reported generally slower forsterite (Fo_{100}) growth rates than in this study (with n equals to 4 for their case). Ohuchi and Nakamura (2007a, 2007b) obtained fast growth rates on dry and wet forsterite aggregates (2.29×10^4 and 6.31×10^3 μm^4/h, respectively) at similar pressure and temperature (1.2 GPa, 1200°C). At lower pressure and higher temperature (1-atm, 1380°C), Hiraga et al. (2010) measured slower growth rates (36 μm^4/h) from grain growth experiments on dry nano forsterite monominerallic aggregates (50 nm to 6 μm). Finally, grain growth experiments on dry nano forsterite plus 5%-enstatite aggregates conducted by Tasaka and Hiraga. (2013) at similar pressure and temperatures (1-atm, 1260-1380°C) resulted in growth rates (1.3-34.4 μm^4/s) of the same order of magnitude than Hiraga et al., (2010). In the olivine-basalt systems, based on the extrapolation from Cabane et al. (2005) and their experimental data, forsterite grain should grow of 5.79 and 9.45 μm after 5h and 23h, respectively. In our forsterite-kimberlite system, the forsterite single crystal growth more than ten times faster than the estimates from Cabane et al. (2005) for the same amount of time, emphasizing the potential role of volatiles (here CO_2 and H_2O) on the depolymerization of the melt and its effect on grain growth kinetics.

Implications

At the point defect scale, despite the simplified system under consideration, the results of this study emphasizes the complex interplay of volatiles (here CO_2 and H_2O) and their incorporation such as hydrogen in the crystalline lattice of nominally anhydrous minerals. The results point to the necessity to adjust with care the amount of the respective volatiles when quantification for 'water capacity' or 'CO_2 capacity' for the Deep Earth is attempted, since significant hydration (> 100 ppm H_2O wt) at pressure relevant of the lithospheric mantle (1-3 GPa) seems to take place in a CO_2-poor system only.

At larger scale, the main consequences from this experimental study is that the high OH concentrations measured in mantle-derived olivine from peridotites in cratonic settings must be representative of the mantle hydrogen concentration at depth (i.e., garnet stability field). They also seem to be unaffected by their transport in kimberlitic liquids from important depths. Therefore, the high OH concentrations measured in Kaapvaal craton xenoliths by Baptiste et al. (2012) were certainly acquired during their mantle history, and were likely to be controlled by metasomatism (Baptiste et al., 2012).

Acknowledgements

This study was financially supported by ANR JCJC "HyDeep" awarded to NBC. SK acknowledges partial support from the 7th framework CIG Marie-Curie EU grant (#303301).

References

Ackermand D., Seifert, F., Schreyer, W., (1975) Instability of sapphirine at high-pressure. Contributions to Mineralogy and Petrology, 50, 79-92.

Ardell, A.J. (1972) On the coarsening of grain boundary precipitates. Acta Metallurgica, 20, 601-609.

Bali, E., Bolfan-Casanova, N., Koga, K., (2008) Pressure and temperature dependence of H solubility in forsterite: an implication to water activity in the Earth interior. Earth Planet. Sci. Lett. 268, 354–363.

Baptiste, V., Tommasi, A., and Demouchy, S. (2012) Deformation and hydration of the lithospheric mantle beneath the Kaapvaal craton, South Africa. Lithos, 149, 31-50.

Becker, M., and Le Roex, A.P. (2006) Geochemistry of South African on- and off-craton, group I and group II kimberlites: Petrogenesis and source region evolution. Journal of Petrology, 47(4), 673-703.

Bell, D.R., Rossman, G.R., and Moore, R.O. (2004) Abundance and Partitioning of OH in a High-pressure Magmatic System: Megacrysts from the Monastery Kimberlite, South Africa. Journal of Petrology, 45(8), 1539-1564.

Bolfan-Casanova, N., Keppler, H., Rubie, D.C., 2000. Water partitioning between nominally anhydrous minerals in the MgO-SiO2-H2O system up to 24 GPa: Implications for the distribution of water in the Earth's mantle. Earth Planet. Sci. Lett. 182, 209–221.

Brooker, R.A., Sparks, R.S.J., Kavanagh, J.L., Field, M., (2011). The volatile content of hypabyssal kimberlite magmas: some constraints from experiments on natural rock compositions. Bull Volcanol 73, 959–981.

Buob, A., Luth, R.W., Schmidt, M.W., and Ulmer, P. (2006) Experiments on CaCO3-MgCO3 solid solutions at high pressure and temperature. American Mineralogist, 91(2-3), 435-440.

Cabane, H., Laporte, D., and Provost, A. (2005) An experimental study of Ostwald ripening of olivine and plagioclase in silicate melts: implications for the growth and size of crystals in magmas. Contributions to Mineralogy and Petrology, 150, 37-53.

Dalton, J.A., and Presnall, D.C. (1998) The continuum of primary carbonatitic kimberlitic melt compositions in equilibrium with lherzolite: Data from the system CaO-MgO-Al_2O_3-SiO_2-CO_2 at 6GPa. Journal of Petrology, 39(11-12), 1953-1964.

Deer, W.A., Howie, R.A., Zussman, J., 1992. An introduction to the Rock-forming minerals., 2nd ed. The Geological Society. London.

Demouchy S., Ishikawa A., Tommasi A., Alard, O. and Keshav S. Characterisation of the hydration in the oceanic mantle lithosphere: peridotite xenoliths from Ontong Java Plateau as an example. Revised for Lithos, September 2014.

Demouchy, S., and Mackwell, S.J. (2003) Water diffusion in synthetic iron-free forsterite. Physics and Chemistry of Minerals, 30, 786-794.

Demouchy, S., Mackwell, S., 2006. Mechanisms of hydrogen incorporation and diffusion in iron-bearing olivine. Phys. Chem. Minerals 33, 347–355.

Demouchy, S., Tommasi, A., Barou, F., Mainprice, D., and Cordier, P. (2012) Deformation of olivine in torsion under hydrous conditions. Physics of the Earth and Planetary Interiors, 202-203, 56-70.

Demouchy, S., Mainprice, D., Tommasi, A., Couvy, H., Barou, F., Frost, D.J., and Cordier, P. (2011) Forsterite to wadsleyite phase transformation under stress and consequences for the Earth's mantle transition zone. Physics of the Earth and Planetary Interiors, 184, 91-104.

Doucet, L.-S., Peslier, A.H., Ionov, D.A., Brandon, A.D., Golovin, A.V., Goncharov, A.G., and Ashchepkov, I.V. (2014) High water contents in the Siberian cratonic mantle linked to metasomatism: an FTIR study of Udachnaya peridotite xenoliths. Geochimica et Cosmochimica Acta, 137, 159-187.

Férot, A., and Bolfan-Casanova, N. (2012) Water storage capacity in olivine and pyroxene to 14 GPa: Implications for the water content of the Earth's upper mantle and nature of seismic discontinuities. Earth and Planetary Science Letters, 349-350, 218-230.

Gaetani, G.A., and Grove, T.L. (1998) The influence of water on melting of mantle peridotite. Contributions to Mineralogy and Petrology, 131, 323-346.

Grant, K., Ingrin, J., Lorand, J.P., Dumas, P., (2007). Water partitioning between mantle minerals from peridotite xenoliths. Contrib. Mineral. Petrol. 154, 15–34.

Grant, K., Kohn, S.C., Brooker, R.A., (2006). Solubility and partitioning of water in synthetic forsterite and enstatite in the system MgO-SiO_2-H_2O +/- Al_2O_3. Contrib. Mineral. Petrol. 151, 651–664.

Gudfinnsson, G.H., and Presnall, D.C. (2005) Continuous gradations among primary carbonatitic, kimberlitic, melilitic, basaltic, picritic, and komatiitic melts in equilibrium with garnet lherzolite at 3-8 GPa. Journal of Petrology, 46(8), 1645-1659.

Hiraga, T., Tachibana, C., Ohashi, N., and Sano, S. (2010) Grain growth systematics for forsterite ± enstatite aggregates: Effect of lithology on grain size in the upper mantle. Earth and Planetary Science Letters, 291, 10-20.

Hirth, G., and Kohlstedt, D.L. (1996) Water in the oceanic upper mantle: Implications for rheology, melt extraction, and the evolution of the lithosphere. Earth and Planetary Science Letters, 144, 93-108.

Holloway, J.R., and Blank, J.G. (1994) Application of experimental results to C-O-H species in natural melts. In Mineralogical Society of America Reviews in Mineralogy, 30, 187-230.

Jacobsen, S.D., Jiang, F., Mao, Z., Duffy, T.S., Smyth, J.R., Holl, C.M., and Frost, D.J. (2008) Effects of hydration on the elastic properties of olivine. Geophys. Res. Lett., 35(14), L14303.

Kamenetsky, V.S., Kamenetsky, M.B., Sobole, A.V., Golovin, A.V., Demouchy, S., Faure, K., Sharygin, V.V., Kuzmin, D.V., (2008). Olivine in the Udachnaya-East Kimberlite (Yakutia, Russia): Types, compositions and origins. J. Petrol 49, 823–839.

Karato, S. (1990) The role of hydrogen in the electrical conductivity of the upper mantle. Nature, 347, 272-273.

Keppler, H. (2003) Water solubility in carbonatite melts. American Mineralogist, 88, 1822-1824.

Keppler, H., and Rauch, M. (2000) Water solubility in nominally anhydrous minerals measured by FTIR and HNMR. Physics and Chemistry of Minerals, 27, 371-376.

Kikuchi, S. (1928) Diffraction of cathode rays by mica. Japanese Journal of Physics, 5, 83-96.

Kirkpatrick, R.J. (1975) Crystal growth from the melt: A review. American Mineralogist, 60, 798-814.

Kjarsgaard, B.A., Pearson, D.G., Tappe, S., Nowell, G.M., and Dowall, D.P. (2009) Geochemistry of hypabyssal kimberlites from Lac de Gras, Canada: Comparisons to a global database and applications to the parent magma problem. Lithos, 112S, 236-248.

Kohlstedt, D.L., Keppler, H., and Rubie, D.C. (1996) Solubility of water in the alpha, beta, and Y phases of (Mg, Fe)2SiO4. Reviews in Mineralogy & Geochemistry, 123(4), 345-357.

Kurosawa, M., Yurimoto, H., and Sueno, S. (1997) Patterns in the hydrogen and trace element compositions of mantle olivines. Physics and Chemistry of Minerals, 24(6), 385-395.

Lemaire, C., Kohn, S.C., and Brooker, R. (2004) The effect of the silica activity on the incorporation mechanisms of water in synthetic forsterite: a polarized spectroscopic study. Contrib. Mineral. Petrol., 147, 48-57.
Mackwell, S.J., Kohlstedt, D.L., and Paterson, M.S. (1985) The role of water in the deformation of olivine single-crystals. Journal of Geophysical Research-Solid Earth and Planets, 90(NB13), 1319-1333.
Matsyuk, S.S., and Langer, K. (2004) Hydroxyl in olivines from mantle xenoliths in kimberlites of the Siberian platform. Contributions to Mineralogy and Petrology, 147(4), 413-437.
Matsyuk, S.S., Langer, K., and Hösch, A. (1998) Hydroxyl defects in garnets from mantle xenoliths in kimberlites of the Siberian platform. Contributions to Mineralogy and Petrology, 132(2), 163-179.
Matveev, S., and Stachel, T. (2007) FTIR spectroscopy of OH in olivine: A new tool in kimberlite exploration. Geochimica et Cosmochimica Acta, 71(22), 5528-5543.
Miller, G.H., Rossman, G.R., and Harlow, G.E. (1987) The natural occurrence of hydroxide in olivine. Physics and Chemistry of Minerals, 14(5), 461-472.
Mitchell, R.H. (1986) Kimberlites: Mineralogy, Geochemistry, and Petrology. 442 p. Plenum Press, New York.
Mitchell, R.H. (1995) Kimberlites, Orangeites, and Related Rocks. 410 p. Plenum Press, New York.
Mosenfelder, J.L., Deligne, N.I., Asimow, P.D., and rossman, G.R. (2006) Hydrogen incorporation in olivine from 2-12 GPa. Am. Min., 91, 285-294.
Ohuchi, T., and Nakamura, M. (2007a) Grain growth in the forsterite-diopside system. Physics of the Earth and Planetary Interiors, 160, 1-21.
Ohuchi, T., and Nakamura, M. (2007b) Grain growth in the system forsterite-diopside-water. Physics of the Earth and Planetary Interiors, 161, 281-304.
Ostwald, W. (1901) Uber die vemeintliche Isomerie des roten und gelben Quecksilberoxyds und die Oberflachen-spannung Fester Korper. Zeitschrift für Physikalische Chemie, 34, 495-512.
Padrón-Navarta, J.A., Hermann, J., and O'Neill, H. (2014) Site-specific hydrogen diffusion rates in Forsterite. Earth and Planetary Science Letters, 392, 100-112.
Paterson, M.S. (1982) The determination of hydroxyl by infrared absorption in quartz, silicate glasses and similar materials. Bulletin de Minéralogie, 105(1), 20-29.
Peslier, A.H. (2010) A review of water contents of nominally anhydrous natural minerals in the mantles of Earth, Mars and the Moon. Journal of Volcanology and Geothermal Research, 197(1-4), 239-258.
Peslier, A.H., Woodland, A.B., Bell, D.R., and Lazarov, M. (2010) Olivine water contents in the continental lithosphere and the longevity of cratons. Nature, 467, 78–81.
Smith, C.B., Allsopp, H.L., Kramers, J.D., Hutchison, G., and Roddick, J.C. (1985a) Emplacement ages of Jurassic-Cretaceous South African kimberlites by the Rb-Sr method on phlogopite and whole-rock samples. South African Journal of Geology, 88, 249-266.
Smith, C.B., Gurney, J.J., Skinner, E.M.W., Clement, C.R., and Ebrahim, N. (1985b) Geochemical character of Southern African kimberlites; a new approach based on isotopic constraints. South African Journal of Geology, 88(2), 267-280.
Sokol, A.G., Kupriyanov, I.N., and Palyanov, Y.N. (2013a) Partitioning of H_2O between olivine and carbonate-silicate melts at 6.3 GPa and 1400°C: Implications for kimberlite formation. Earth and Planetary Science Letters, 383, 58-67.

Sokol, A.G., Kupriyanov, I.N., Palyanov, Y.N., Kruk, A.N., and Sobolev, N.V. (2013b) Melting experiments on the Udachnaya kimberlite at 6.3-7.5GPa: Implications for the role of H_2O in magma generation and formation of hydrous olivine. Geochimica et Cosmochimica Acta, 101, 133-155.

Sparks, R.S.J., Brooker, R.A., Field, M., Kavanagh, J., Schumacher, J.C., Walter, M.J., and White, J. (2009) The nature of erupting kimberlite melts. Lithos, 112(1), 429-438.

Tasaka, M., and Hiraga, T. (2013) Influence of mineral fraction on the rheological properties of forsterite + enstatite during grain-size-sensitive creep: 1. Grain size and grain growth laws. Journal of geophysical Research: Solid Earth, 118, 1-21.

Xirouchakis, D., Hirschmann, M.M., and Simpson, F. (2001) The effect of titanium on the silica content and on mineral-liquid partitioning of mantle-equilibrated melts. Geochimica et Cosmochimica Acta, 65, 2201-2217.

Yang, X., Dingding, L., and Xia, Q. (2014) CO2-induced small water solubility in olivine and implications for properties of the shallow mantle. Earth and Planetary Science Letters, 403, 37-47.

Chapitre 4: Contraintes pétrophysiques sur les propriétés sismiques du manteau lithosphérique sous le craton du Kaapvaal

La structure du craton du Kaapvaal a été étudiée par de multiples études sismiques au cours des dernières décennies afin de tenter de comprendre l'origine de sa longévité. Toutefois, interpréter ces données en terme de composition ou de température reste ambiguë. La plupart d'entre elles révèlent la présence d'une racine aux vitesses sismiques élevées atteignant au moins 200 km (Chevrot and Zhao, 2007; Fishwick, 2010; James et al., 2001; Li and Burke, 2006; Priestley, 1999; Priestley et al., 2006). Ces vitesses rapides ont tour à tour été attribuées à des changements de température (Priestley and Tilmann, 2009) ou de composition (Begg et al., 2009). Certains modèles tomographiques des ondes de volume montrent de plus faibles vitesses sismiques sous le complexe du Bushveld, ayant été attribuées à des compositions plus fertiles (Fouch et al., 2004; James et al., 2001) ou à un géotherme plus chaud (Fouch et al., 2004). Enfin, la conversion à 150 km mesurée par les fonctions récepteurs pourrait être liée à un changement de composition ou par un contraste d'anisotropie au sein du manteau cratonique (Savage and Silver, 2008; Wittlinger and Farra, 2007). Les études d'anisotropie sismiques révèlent des directions de polarisation des ondes SKS NNE-SSO sur l'ensemble du craton (Silver et al., 2001; Vinnik et al., 1995), interprétées tour à tour comme le produit d'OPRs fossilisées dans la lithosphère (Silver et al., 2001) ou de la réponse de l'asthénosphère au mouvement de la plaque africaine (Vinnik et al., 1995). L'interprétation de ces données n'étant pas unique, elles pourraient donc bénéficier de l'apport d'observations directes de la déformation du manteau lithosphérique et de l'anisotropie qui en résulte.

Le travail présenté dans ce chapitre repose sur le calcul des propriétés sismiques de 47 xénolites mantelliques du craton Kaapvaal à partir de leur OPRs et de leurs données de compositions (Baptiste et al., 2012). Il a pour but d'apporter des contraintes sur les vitesses sismiques et les anisotropies possibles au niveau du Kaapvaal, ainsi que de connaître leur

dépendance à la composition et aux OPRs.

Cette étude révèle que des changements de l'OPR de l'olivine n'entraînent que des variations mineures des motifs d'anisotropie sismique. L'anisotropie azimutale maximale des ondes P varie entre 2.5 et 10.2%, tandis que l'anisotropie de polarisation maximale des ondes S est comprise entre 2.7 et 8%. Par le calcul des propriétés sismiques moyennes pour des sections de 20 km, nous avons prédis l'anisotropie que devrait mesurer les ondes SKS, Rayleigh et Love pour 5 orientations de foliation et linéation différentes. Les faibles déphasages et les directions de polarisation cohérente sur l'ensemble du craton mesurés par les ondes SKS et la faible anisotropie azimutale avec $S_H > S_V$ mesurée par les ondes de surface sont le mieux expliquées par une foliation et linéation inclinées de 45°. Les compositions très hétérogènes des péridotites du Kaapvaal entraînent une variation de densité allant jusqu'à 3%, et une variation allant jusqu'à 2.3% de V_p, V_s et du rapport V_p/V_s. Un appauvrissement en Fe lié à la fusion partielle génère une augmentation de V_p et V_s, mais une diminution du rapport V_p/V_s et de la densité. L'enrichissement en orthopyroxène lié au métasomatisme entraîne une diminution de la densité et de V_p, et réduit fortement le rapport V_p/V_s. Un enrichissement en grenat, aussi attribué au métasomatisme, accroît la densité, et plus faiblement V_p et le rapport V_p/V_s. Enfin, la comparaison entre les profiles de vitesse obtenus pour nos échantillons et les modèles de vitesse 1D fournis par les études sismiques du Kaapvaal montre que : (1) les mylonites cratoniques ne représentent que des modifications locales de la racine causées et sur-échantillonnées par les kimberlites (2) les modèles sismiques sous-estiment très certainement l'hétérogénéité compositionnelle de la racine cratonique du Kaapvaal, qui se produit à une échelle bien inférieure à celle qui peut être décrite par les études sismiques.

Solid Earth, 5, 1–19, 2014
www.solid-earth.net/5/1/2014/
doi:10.5194/se-5-1-2014

Solid Earth Open Access

Petrophysical constraints on the seismic properties of the Kaapvaal craton mantle root

V. Baptiste and A. Tommasi

Géosciences Montpellier, Université Montpellier 2 & CNRS, CC 60, Place E. Bataillon, 34095 Montpellier cedex 5, France

Correspondence to: V. Baptiste (virginie.baptiste@gm.univ-montp2.fr)

Received: 1 July 2013 – Published in Solid Earth Discuss.: 1 July 2013
Revised: 25 November 2013 – Accepted: 7 December 2013 – Published:

Abstract. We calculated the seismic properties of 47 mantle xenoliths from 9 kimberlitic pipes in the Kaapvaal craton based on their modal composition, the crystal-preferred orientations (CPO) of olivine, ortho- and clinopyroxene, and garnet, the Fe content of olivine, and the pressures and temperatures at which the rocks were equilibrated. These data allow constraining the variation of seismic anisotropy and velocities within the cratonic mantle. The fastest P and S_2 wave propagation directions and the polarization of fast split shear waves (S_1) are always subparallel to olivine [100] axes of maximum concentration, which marks the lineation (fossil flow direction). Seismic anisotropy is higher for high olivine contents and stronger CPO. Maximum P wave azimuthal anisotropy (AV_p) ranges between 2.5 and 10.2 % and the maximum S wave polarization anisotropy (AV_s), between 2.7 and 8 %. Changes in olivine CPO symmetry result in minor variations in the seismic anisotropy patterns, mainly in the apparent isotropy directions for shear wave splitting. Seismic properties averaged over 20 km-thick depth sections are, therefore, very homogeneous. Based on these data, we predict the anisotropy that would be measured by SKS, Rayleigh (S_V) and Love (S_H) waves for five endmember orientations of the foliation and lineation. Comparison to seismic anisotropy data from the Kaapvaal shows that the coherent fast directions, but low delay times imaged by SKS studies, and the low azimuthal anisotropy with with the horizontally polarized S waves (S_H) faster than the vertically polarized S wave (S_V) measured using surface waves are best explained by homogeneously dipping (45°) foliations and lineations in the cratonic mantle lithosphere. Laterally or vertically varying foliation and lineation orientations with a dominantly NW–SE trend might also explain the low measured anisotropies, but this model should also result in back-azimuthal variability of the SKS splitting data, not reported in the seismological data. The strong compositional heterogeneity of the Kaapvaal peridotite xenoliths results in up to 3 % variation in density and in up to 2.3 % variation of V_p, V_s, and V_p/V_s ratio. Fe depletion by melt extraction increases V_p and V_s, but decreases the V_p/V_s ratio and density. Orthopyroxene enrichment due to metasomatism decreases the density and V_p, strongly reducing the V_p/V_s ratio. Garnet enrichment, which was also attributed to metasomatism, increases the density, and in a lesser extent V_p and the V_p/V_s ratio. Comparison of density and seismic velocity profiles calculated using the xenoliths' compositions and equilibration conditions to seismological data in the Kaapvaal highlights that (i) the thickness of the craton is underestimated in some seismic studies and reaches at least 180 km, (ii) the deep sheared peridotites represent very local modifications caused and oversampled by kimberlites, and (iii) seismological models probably underestimate the compositional heterogeneity in the Kaapvaal mantle root, which occurs at a scale much smaller than the one that may be sampled seismologically.

1 Introduction

A wealth of seismological studies have investigated the structure of the Kaapvaal craton aiming at unraveling the thermal structure, the composition, and the deformation fabric of the cratonic root and at understanding the causes of its stability since Archean times, as inferred from Re–Os model ages obtained in kimberlite-born mantle xenoliths (Pearson et al., 1995). Tomographic models and receiver function data agree on the presence of a high velocity upper mantle lid

on top of a low velocity layer (Jordan, 1978; Priestley, 1999; James et al., 2001; Li and Burke, 2006; Priestley et al., 2006). Most body and surface wave tomography models indicate that this lid is 200–250 km thick beneath the Kaapvaal craton (James et al., 2001; Chevrot and Zhao, 2007; Fishwick, 2010). A thinner high-velocity layer, extending to depths of 150 or 180 km, was, however, imaged by other models (Sebai et al., 2006; Wang et al., 2008). Receiver function studies mapped sharp decreases in seismic velocities at 150 and 200 km depths (Wittlinger and Farra, 2007; Savage and Silver, 2008; Hansen et al., 2009; Adams and Nyblade, 2011).

Discriminating between these models, which point to different cratonic root thicknesses, and interpreting these geophysical data in terms of composition and temperature requires independent observations. The high seismic velocities beneath the Kaapvaal craton have indeed been alternatively attributed to thermal effects (Priestley and Tilmann, 2009) or to changes in composition (Begg et al., 2009). Similarly, the conversion at 150 km imaged by *S* wave receiver functions was interpreted as produced by compositional layering, by anisotropy contrasts within the cratonic mantle (Wittlinger and Farra, 2007; Savage and Silver, 2008) or the lithosphere–asthenosphere boundary beneath the craton (Hansen et al., 2009). Small-scale variations in seismic properties within the cratonic root also may not be imaged or interpreted unambiguously. Beneath the Bushveld complex, some, but not all body wave tomography models imaged velocities lower than the average ones in the craton, which have been attributed to either more fertile compositions associated with the 2 Ga-old Bushveld magmatism (James et al., 2001; Fouch et al., 2004a) or to a hotter present-day geotherm (Fouch et al., 2004a).

The deformation of the Kaapvaal craton has also been extensively investigated by seismic anisotropy studies (Silver et al., 2001; Fouch et al., 2004a; Fouch et al., 2004b; Silver et al., 2004; Adam and Lebedev, 2012; Vinnik et al., 1995, 2012). Silver et al. (2001) measured fast polarization directions that consistently followed the trend of geological structures and small SKS delay times (0.62 s on average), with almost null delays in the central Kaapvaal craton. They attributed this anisotropy to fossil deformation in the mantle lithosphere. Vinnik et al. (1995) attributed the same NNE–SSW fast polarization directions to asthenospheric deformation in response to African plate motion. Significant variations of SKS delay times were measured near Kimberley, which was interpreted as the boundary between a strongly and a weakly anisotropic domain (Fouch et al., 2004b). More recently, a Rayleigh wave azimuthal anisotropy model (Adam and Lebedev, 2012) proposed that the mantle fabric at lithospheric depths parallels the Archean–Paleoproterozoic crustal structures in the Limpopo belt and in the northern Kaapvaal, but is perpendicular to the crustal structures in the western part of the craton. Vinnik et al. (2012), using *P* receiver functions and SKS waveform inversion, also observed belt-parallel, fast directions in the uppermost mantle near the Limpopo belt. They also detected a change with depth in the orientation of the fast direction; the latter aligns progressively with current plate motion at depths > 160 km. In summary, seismic anisotropy data derived from body and surface waves are mostly, but not always, consistent. Their interpretation is also not unique and may benefit from direct observations of the lithospheric mantle deformation and resulting anisotropy.

The Kaapvaal craton was affected by numerous kimberlite eruptions, mostly between the late Jurassic and the Cretaceous, but also during the Meso-Proterozoic and Paleozoic (Kramers and Smith, 1983; Allsopp et al., 1985; Phillips et al., 1998). These magmas carried xenoliths that provide direct sampling of the lithospheric mantle beneath the craton. The seismic properties of these peridotite xenoliths can be calculated from their crystal-preferred orientation (CPO) and composition data (Mainprice and Silver, 1993; Mainprice and Humbert, 1994). Such data constrain the possible seismic velocities and anisotropies within the Kaapvaal mantle root, as well as their dependence on the peridotites composition and crystal-preferred orientations. In the present study, we calculated the anisotropic seismic properties of 47 peridotite xenoliths from 9 kimberlite pipes, which sample different domains, depths, and ages of the Kaapvaal mantle root (Fig. 1). The present study represents a significant enrichment of the database of seismic properties of the Kaapvaal mantle root, as previous studies focused on either the composition- and depth-dependence of the isotropic seismic velocities (James et al., 2004) or the crystal-preferred orientation-induced anisotropy (Ben Ismaïl et al., 2001).

2 The studied data set

The 47 peridotite xenoliths used in this study come from 9 kimberlitic pipes (Kimberley, Jagersfontein, Monastery, Lentseng, De Beers, Finsch, Kamfersdam, Premier, and Mothae) from the Kaapvaal craton, with eruption ages of 1200 Ma (Premier) and 120–87 Ma (all other pipes, see Baptiste et al., 2012, for details). These peridotites are mainly composed of olivine, orthopyroxene, clinopyroxene ±garnet. When spinel is present, it is a minor phase. Thermobarometry data indicates that the studied peridotites were equilibrated at depths ranging between 83 and 187 km on a cold cratonic geotherm (Baptiste et al., 2012). The full description of the microstructures, crystal-preferred orientations (CPOs), and data on the water contents in olivine and pyroxenes in these xenoliths is presented in Baptiste et al. (2012), but their main characteristics are recalled below. The modal content, texture, olivine CPO type and intensity, and equilibration $P-T$ conditions of all studied samples are summarized in Table 1.

The studied mantle xenoliths can be separated into two textural groups: the coarse-grained, which are composed by plurimillimetric to centimetric olivine and pyroxene crystals, and the sheared peridotites, which are characterized by

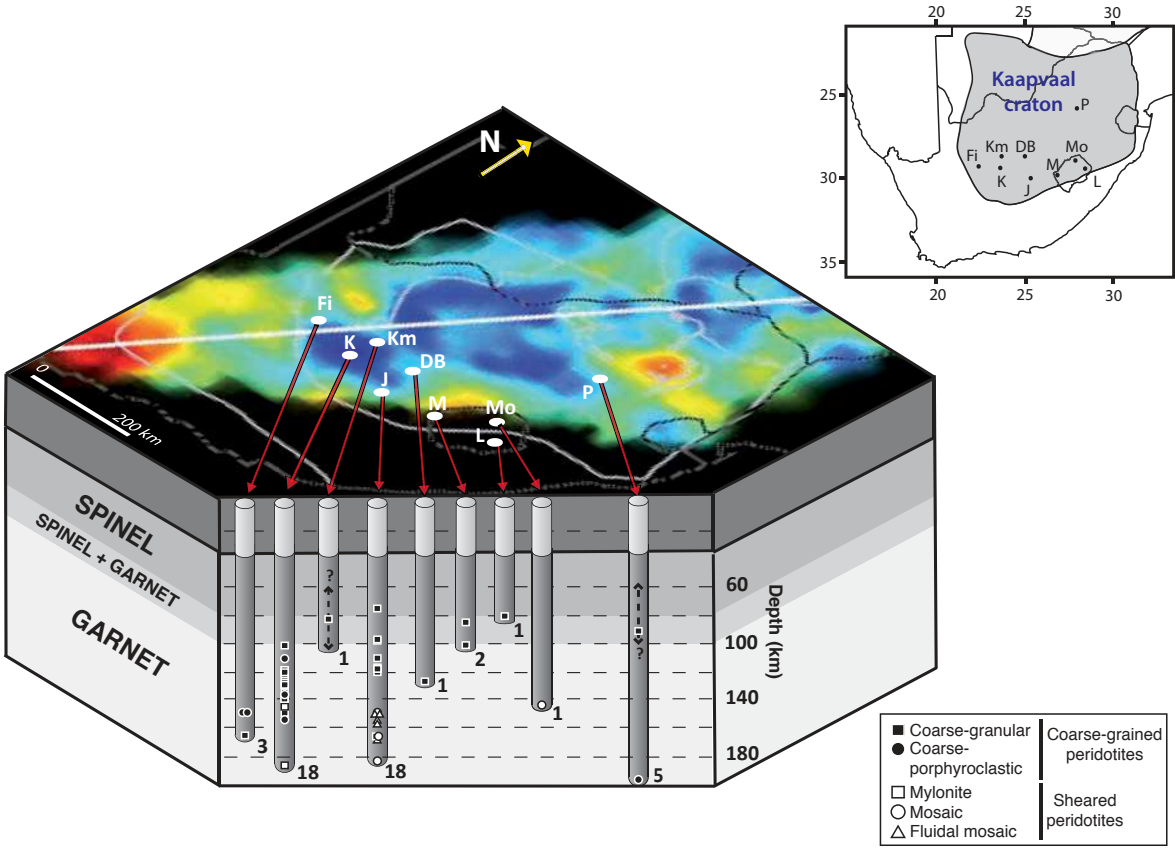

Fig. 1. Sketch displaying the location of the sampled kimberlitic pipes as well as the samples' depths and microstructures (after Baptiste et al., 2012) relatively to the *S* wave tomography model of Fouch et al. (2004a) at 150 km. Fi: Finsch, K: Kimberley, Km: Kamfersdam, J: Jagersfontein, DB: De Beers, M: Monastery, Mo: Mothae, L: Lentseng, P: Premier.

a matrix of fine-grained olivine (a few to 100 μm) and, occasionally, orthopyroxene that encloses millimeter-size garnet, pyroxene, and, sometimes, olivine porphyroclasts. The coarse-grained peridotites are the dominant textural group (72 % of the studied samples), being observed at all depths and in all pipes (Fig. 1). They display most often strongly annealed textures, but coarse-porphyroclastic microstructures are also common. The sheared peridotites are only observed in the deeper part of the sampled columns (equilibration pressures > 4.5 GPa). Their textures range from mylonitic to fluidal or mosaic-like, probably due to variable post-deformational annealing. Based on their occurrence, microstructures and thermal evolution, Baptiste et al. (2012) interpreted the coarse-grained microstructures as the typical cratonic root microstructure, resulting from an early deformation episode followed by a long quiescence time, and the sheared peridotites as recording local modifications of the cratonic microstructure just before the xenolith extraction. Their formation is probably associated with the kimberlitic activity as proposed by Green and Guegen (1974).

Coarse-grained peridotites have in average more refractory compositions than the sheared peridotites (Table 1). They are mainly harzburgites, with high orthopyroxene contents (> 20 %). Sheared peridotites are mainly lherzolites, with highly variable garnet contents (0–18 %). In the studied samples, water contents in olivine and pyroxenes are very variable; maximum water contents in olivine increase up to 150 km depth, reaching up to 150 wt. ppm H_2O (values obtained using the Bell et al. (2003) calibration; Baptiste et al., 2012). In contrast, olivines from samples equilibrated at depths > 150 km are almost dry.

3 Methods

Seismic properties of Kaapvaal xenoliths were calculated based on the olivine, orthopyroxene, clinopyroxene, and garnet CPOs, and on the modal compositions (Mainprice, 1990). The CPOs were measured by electron-backscattered diffraction (EBSD), producing crystal orientation maps, which covered the entire thin section (see Baptiste et al., 2012 for details on the EBSD data acquisition and treatment). Because olivine is the dominant phase in peridotites, largely determining their seismic properties, and because olivine compositions vary strongly among the studied samples (Table 1),

Table 1. Olivine Mg#, modal contents, equilibration conditions, calculated seismic properties and densities of the studied Kaapvaal peridotites.

Locality	Sample	Ol Mg# (%)	Modal compositions (%) Ol	Opx	Cpx	Gt	Temperature (°C)	Pressure (GPa)	Depth (km)	Density ($g\,cm^{-3}$)	$V_p^{(1)}$ ($km\,s^{-1}$)	Max AV_p (%)	$V_s^{(2)}$ ($km\,s^{-1}$)	Max AV_s pol (%)	Max AVs_1 (%)	Max AVs_2 (%)
KIMBERLEY	KBBF6a	90.8	74	13	4	9	926	3.8	121	3.3690	8.27	9.7	4.67	8.0	4.8	6.0
	KBBF6b	91.0	82	8	4	6	908	3.7	118	3.3683	8.26	9.2	4.66	7.0	3.5	5.9
	KBBF8	94.3	81	19	0	0	1029	–	138	3.3500	8.19	10.0	4.64	7.4	6.1	2.6
	KBBF9	89.8	67	16	9	8	1102	4.7	149	3.3623	8.28	5.4	4.65	4.2	2.8	2.1
	KBBF10	92.4	72	27	1	0	948	–	125	3.3398	8.19	7.9	4.65	6.0	3.5	4.9
	KBBF11	93.6	88	11	1	0	1159	5.9	187	3.3618	8.17	4.7	4.55	3.3	4.6	2.9
	KBBF14	93.0	83	16	1	0	996	–	133	3.3518	8.20	5.4	4.64	5.4	3.6	2.8
	KBBF15	92.6	65	31	0	4	1067	4.3	137	3.3442	8.21	5.2	4.65	4.7	1.2	4.5
	KBBF16	93.3	71	26	0	3	–	4.0	127	3.3476	8.21	4.0	4.66	4.1	2.2	3.0
	KBBF18	92.2	75	17	6	0	850	–	110	3.3451	8.22	7.2	4.67	6.3	4.6	3.7
	KBBF20	–	65	35	0	0	800	–	102	*3.3320	*8.17	*7.8	*4.67	*6.4	*3.2	*5.7
	FRB1402	93.2	83	9	0	8	1023	4.6	146	3.3770	8.25	4.2	4.64	3.4	3.2	0.5
	FRB1404	93.5	59	36	1	4	987	4.4	140	3.3380	8.21	3.2	4.67	3.2	2.6	2.4
	FRB1422	93.5	65	31	0	4	994	4.4	140	3.3442	8.21	5.1	4.66	4.1	3.7	2.0
	FRB1423	91.8	68	18	4	10	851	3.8	121	3.3658	8.28	7.2	4.69	5.5	2.8	3.7
	FRB1447	93.4	73	23	1	3	968	4.2	133	3.3501	8.22	3.4	4.66	3.2	1.1	2.6
	FRB348	92.3	58	28	7	7	938	3.7	118	3.3478	8.27	5.6	4.70	4.3	2.4	2.9
JAGERSFONTEIN	KBJ6	90.7	84	9	3	4	1163	4.9	152	3.3673	8.22	6.0	4.61	4.8	3.7	1.8
	KBJ8	90.9	87	13	0	0	1219	–	168	3.3689	8.21	10.2	4.60	6.8	2.3	6.4
	KBJ14	91.3	70	5	12	13	1140	4.7	149	3.3822	8.36	5.7	4.69	4.1	2.0	3.3
	KBJ30	89.4	63	11	11	15	1282	5.8	184	3.3813	8.35	4.5	4.66	3.9	2.5	1.6
	KBJ33	89.3	68	8	6	18	1217	4.8	152	3.3925	8.35	7.6	4.68	5.3	1.9	4.5
	KBJ52	92.7	75	25	0	0	900	–	118	3.3425	8.18	7.3	4.64	5.7	4.1	3.5
	KBJ54	92.3	75	23	2	0	907	3.8	121	3.3431	8.19	8.2	4.65	7.5	5.9	4.4
	KBJ56	92.5	65	28	0	7	895	3.5	111	3.3524	8.24	6.3	4.69	5.4	5.1	2.3
	KBJ60	91.5	86	13	1	0	1190	5.2	165	3.3574	8.17	7.5	4.58	6.3	4.3	2.9
	KBJ62	92.6	64	36	0	0	759	3.1	98	3.3311	8.18	7.3	4.68	7.4	4.4	5.6
	KBJ63	91.3	82	10	3	5	1250	4.9	156	3.3689	8.23	7.5	4.61	7.7	3.9	4.4
	J34	92.0	59	29	5	7	656	2.4	76	3.3457	8.26	9.8	4.75	6.8	1.8	6.1
	J41	92.4	61	39	0	0	668	3.7	118	3.3283	8.17	4.0	4.66	4.9	4.5	2.0
	J47	90.7	85	6	8	1	1227	4.7	149	3.3615	8.22	7.1	4.61	5.7	4.6	1.6
	J57	92.4	79	18	3	0	765	3.1	98	3.3457	8.21	8.6	4.67	6.0	3.4	4.7
	J63	87.7	78	10	10	2	1176	5.2	165	3.3581	8.23	4.5	4.59	3.3	2.2	1.6
MONASTERY	ROM23	92.2	66	28	4	1	910	3.3	105	3.3373	8.21	5.0	4.69	4.9	3.1	3.0
	ROM69	92.2	76	20	3	1	784	2.6	83	3.3438	8.22	2.5	4.70	3.1	2.3	2.5
LENTSENG	PHN4274	93.1	62	33	2	3	1015	4.3	137	3.3387	8.21	3.5	4.66	3.5	3.0	2.5
MOTHAE	PHN1925	89.9	63	22	11	4	1306	4.6	137	3.3462	8.26	3.4	4.67	2.7	0.8	2.5
KAMFERSDAM	PHN5580	92.6	73	27	0	0	–	–	–	**3.2814	**8.34	**5.5	**4.89	**5.2	**4.0	**3.6
DE BEERS	KBB2	93.3	66	33	0	1	917	4.0	127	3.3363	8.19	6.8	4.67	5.7	2.6	4.5
PREMIER	FRB1330	91.3	80	17	3	0	744	–	93	3.3455	8.21	9.4	4.68	6.7	2.3	6.1
	FRB1336	88.9	70	30	0	0	–	–	–	**3.3052	**8.28	**7.1	**4.85	**6.2	**4.9	**2.2
	FRB1339	91.7	71	18	8	3	–	–	–	**3.3118	**8.33	**5.1	**4.86	**4.8	**3.8	**1.9
	PHN5266	92.7	70	26	4	0	–	–	–	**3.3109	**8.29	**8.5	**4.86	**6.7	**5.0	**3.9
	PHN5267	91.3	70	19	6	5	1464	6.5	171	3.3667	8.29	6.9	4.66	4.8	2.5	4.4
FINSCH	FRB1501	93.0	70	22	0	8	1030	4.6	149	3.3620	8.24	5.5	4.65	4.6	3.3	2.1
	FRB1512	92.0	68	22	0	10	1058	4.7	149	3.3657	8.26	5.0	4.66	4.1	3.3	1.9
	FRB1513	92.6	70	27	1	2	1037	5.2	165	3.3443	8.19	4.9	4.62	5.6	4.8	2.3

Ol Mg#, modal content and P, T data from Baptiste et al. (2012).
(1) Mean P wave velocity.
(2) Mean S wave velocity.
AV_p: V_p azimuthal anisotropy; AV_s: V_s azimuthal anisotropy; AVS_1: fast V_s azimuthal anisotropy; AVS_2: slow V_s azimuthal anisotropy; maximum values.
* Seismic properties and density were calculated by only taking into account the sample equilibrium pressure and temperature, since olivine Mg# was unknown.
** Seismic properties and density were calculated by only taking into account the mean olivine Mg# of the sample, since the equilibrium conditions were unknown.

olivine elastic tensors were recalculated to account for the actual olivine mean forsterite content or Mg# (Mg + Fe / Mg) in each sample. The elastic constants variation as a function of the olivine Mg# was calculated by linear interpolation between the single-crystal elastic constant tensors measured in laboratory for fayalite, forsterite, and olivine with Mg# of 90, 91, and 93 (Kumazawa and Anderson, 1969; Suzuki et al., 1983; Webb et al., 1989; Isaak et al., 1993; Abramson et al., 1997). For orthopyroxene, clinopyroxene, and garnet, the single crystal elastic tensors of Chai et al. (1997a), Collins and Brown (1998), and Chai et al. (1997b) at ambient pressure (P) and temperature (T) were used. Due to lack of experimental data, compositional changes could not considered for these phases. The density, the elastic constants and resulting seismic properties of each sample were calculated both at ambient pressure and temperature conditions and at its equilibration pressure and temperature. In both cases, the actual olivine Mg# is considered. To account for the effect of pressure and temperature on the seismic properties, the elastic tensors and density of olivine, pyroxenes, and garnet were recalculated for depths between 40 and 200 km (a point at every 10 km depth) using the AnisPT8 software by D. Mainprice, based on published pressure and temperature derivatives of the elastic constants for all major mineral

phases (Abramson et al., 1997; Chai et al., 1997a, b; Collins and Brown, 1998) and the Kaapvaal geotherm of Baptiste et al. (2012). A Voigt–Reuss–Hill averaging was applied in all calculations. Equivalent "isotropic" seismic velocities were also estimated for each sample by averaging P and S wave velocities over all directions. Calculated seismic properties and elastic constants of all samples are summarized in Tables 1 and 2, respectively. The equilibration temperature and pressure of the samples were estimated using traditional geothermometers and geobarometers for mantle rocks, which have an uncertainty of up to ±60° C and ±0.2 GPa, respectively (see Baptiste et al. 2012 for more details). This uncertainty in the determination of the equilibration temperature and pressure results in an uncertainty in V_p and V_s of ±0.04 and 0.03 km s^{-1}, respectively. In the present study, the seismic properties as a function of depth were not calculated using the elastic tensors of the different minerals calculated at the exact equilibration depth of the samples, but at every 10 km interval along the Kaapvaal geotherm of Baptiste et al. (2012). This simplification corresponds to a maximum pressure variation of 0.15 GPa, which is lower than the geobarometer uncertainty. It does not, by consequence, increase the uncertainty of the estimated seismic velocities. A probable additional source of uncertainty in the seismic velocities estimations at depth is the one related with the uncertainties in temperature and pressure derivatives of the elastic constants. However, the existing experimental data does not allow constraining this uncertainty. The three-dimensional distribution of seismic velocities and birefringence of S waves relative to the samples' structural reference frame are displayed on lower hemisphere stereograms.

The mean seismic properties of six 20 km-thick sections between 70 and 190 km depth were calculated by averaging the olivine composition and modal contents and adding up the crystal-preferred orientations of all samples equilibrated within the corresponding depth interval. This approach results in an upper bound for the estimated anisotropy, since the CPO summation is performed considering that the structural reference frames of all samples are parallel, that is, that the orientation of the foliation and lineation is the same for all samples within each depth interval.

To analyze the relations between the olivine CPO symmetry and intensity and the seismic anisotropy, the olivine CPO symmetry was characterized using the dimensionless BA index defined as

$$\mathrm{BAindex} = \frac{1}{2}\left(2 - \left(\frac{\mathrm{P010}}{\mathrm{G010}+\mathrm{P010}}\right) - \left(\frac{\mathrm{G100}}{\mathrm{G100}+\mathrm{P100}}\right)\right), \quad (1)$$

where P and G are indexes used to characterize the shape of the distribution (P for Point and G for Girdle) of the olivine principal axes ([100], [010] and [001]); these indexes were calculated from the eigenvalues of the normalized orientation matrix as P = $\lambda 1 - \lambda 3$ and G = $2(\lambda 2 - \lambda 3)$, calculated using the MTEX texture analysis toolbox (Hielscher and Schaeben, 2008; Mainprice et al., 2011). This index allows the classification of the olivine CPO into 3 types: axial [010] (BA < 0.4), orthorhombic (0.4 < BA < 0.6), and axial [100] (BA > 0.6).

The olivine CPO intensity is characterized by the dimensionless J index, which is the volume-averaged integral of the squared orientation densities defined as

$$J = \mathrm{f(g)}^2\,\mathrm{d}g, \quad (2)$$

where $f(g)$ is the orientation distribution function (ODF) and $\mathrm{d}g = \mathrm{d}\varphi_1\mathrm{d}\varphi\mathrm{d}\varphi_2 \sin\varphi\pi^2 \cdot \varphi_1$, φ, and φ_2 are the Euler angles that define the rotations allowing for coincidence between the crystallographic and external reference frames. In natural peridotites, olivine CPO J indexes vary between 2 and 20, with a peak at 8–10 (Ben Ismaïl and Mainprice, 1998; Tommasi et al., 2000). J indexes were calculated based on the mean orientation of each grain, using the SuperJctf program by D. Mainprice (ftp://www.gm.univ-montp2.fr/mainprice//CareWare_Unicef_Programs/) with a 10° Gaussian half-width, 1° cells, and truncation of the ODF at 22°.

4 Results

4.1 Seismic anisotropy

Seismic anisotropy patterns for samples representative of the different microstructures and olivine CPO symmetry patterns observed among Kaapvaal xenoliths (Table 1 and Baptiste et al., 2012) are illustrated in Fig. 2. At first order, seismic anisotropy patterns for all samples have similar characteristics, independently of the peridotite microstructure and olivine CPO symmetry. The fastest and slowest P wave and slow S wave (S_2) propagation directions are aligned with the olivine [100] and [010] axes maxima, respectively. The orientation of the [100] maximum also controls the direction of polarization of the fast S wave (S_1). Moreover, when the lineation (crystals elongation marking the structural X direction) and foliation (crystals flattening marking the plane normal to the Z structural direction) could be identified, the [100] maximum corresponds to the lineation, which marks the fossil flow direction. The fast split shear wave (S_1) is thus polarized in the plane containing the wave propagation direction and the fossil flow direction in the mantle lithosphere. The highest V_p/V_{S_1} ratio is also parallel to this direction and the lowest V_p/VS_1 ratio is observed for waves propagating normal to it.

Changes in olivine CPO symmetry result in second order variations in the seismic anisotropy pattern. Peridotites displaying an axial [100] CPO tend to show slow P wave velocities for all directions normal to the lineation, instead of a clear V_p minimum at high angle to the foliation. S wave polarization anisotropy patterns are also sensitive to the CPO symmetry. Samples with an axial [100] olivine CPO display high V_s anisotropy (AV_s) for directions of propagation in the foliation plane, but at high angle to the lineation (Y structural direction) and a minimum anisotropy for propagation along

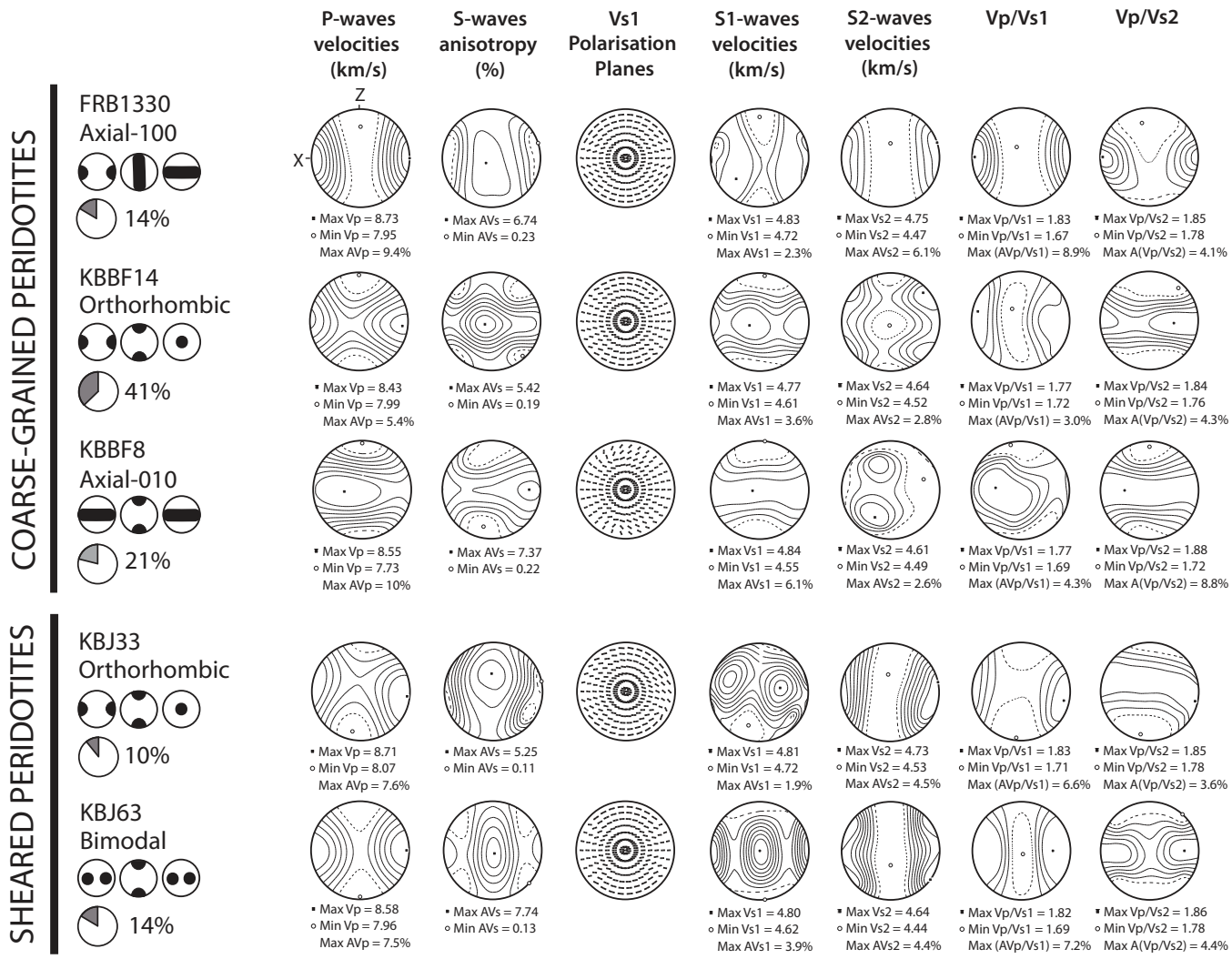

Fig. 2. Calculated seismic properties of the Kaapvaal coarse-grained and sheared peridotites showing different olivine CPO patterns. From left to right, are displayed the 3-D distributions of P wave velocities (V_p), S wave polarization anisotropy (V_s), the orientation of fast shear wave polarization plane, S_1 wave velocities (V_{S_1}), S_2 wave velocities (V_{S_2}), V_p/V_{S_1}, and V_p/V_{S_2}. Black squares and white spots indicate maximum and minimum values, respectively.

the lineation (X direction) and more rarely at 45° to the lineation in the XZ plane. The slowest S_1 wave propagation is always located at high angle to the foliation (parallel to the Z structural direction), while the fastest propagation is in the foliation plane, at 45° to the lineation. S_2 wave velocity is maximum close to the lineation or in the XZ plane, at $\sim 10°$ to the lineation. The V_p/V_{S_1} ratio is highest parallel to the lineation (X structural direction) and lowest at high angle to the foliation (Z structural direction).

In contrast, peridotites with an axial [010] CPO show high S wave polarization anisotropy for propagations along the foliation plane and low anisotropy for S waves traveling at high angle to the foliation. The strongest S wave birefringence is usually observed for waves propagating at low angle to the lineation, but it may also be oblique to it. S_1 wave velocity is higher in the foliation plane. The fastest S_1 waves may be aligned with either the X or the Y structural directions or even at 45° to these directions. This variability in the orientation of the maximum S wave birefringence and of the fastest S_1 waves depends on the actual symmetry of the olivine CPO; samples with lower BA indexes have both maxima at low angle to the X structural direction. S_2 wave velocity is minimum along the XZ plane. The V_p/V_{S_1} ratio tends to show high values in the foliation plane and low values at high angle to it (Z structural direction).

Peridotites with an orthorhombic CPO show patterns intermediate between the two described previously. The maximum S wave polarization anisotropy is at low angle to the Y structural direction, similarly to that observed for samples with an axial [100] CPO, but, the minimum S wave

anisotropy is in the XZ plane, at 45° to both the lineation (X structural direction) and to the foliation (Z structural direction). The S_1 wave velocity is most often the highest along the foliation plane, parallel to both X and Y structural directions, or at 45° to these axes. The slowest S_1 wave propagation is at high angle to the foliation (Z structural direction). The S_2 wave velocity is maximum parallel to the lineation or at 45° to the lineation in the XZ plane, as in the example displayed in Fig. 2. It is minimum along the YZ plane. The maximum V_p/V_{S_1} ratio is observed along the foliation plane and the minimum V_p/V_{S_1} ratio is located close to the Z structural direction.

Peridotites with bimodal olivine CPO have also intermediate patterns, with maximum S wave polarization anisotropy for propagation directions close to the Y structural direction. The minimum S wave polarization anisotropy is observed for propagation directions at 45° to the lineation in the XZ plane. In a few cases, however, the S wave polarization anisotropy is minimum at high angle to the foliation. S_1 wave velocity is the highest in the foliation plane, close to both X and Y structural directions and it is the lowest at high angle to the foliation (Z structural direction). The S_2 wave velocity is the highest along the YZ plane. The V_p/V_{S_1} ratio is maximum along the foliation and minimum at high angle to the foliation (Z structural direction).

Despite the weak variation in the patterns, xenoliths from the Kaapvaal craton show a wide range of seismic anisotropy intensities (Fig. 3, Table 1). Maximum anisotropy values range between 2.5 and 10.2 % for P wave azimuthal anisotropy (AV_p), between 2.7 and 8 % for S wave polarization anisotropy (AV_s), between 0.8 and 6.1 % for S_1 wave propagation anisotropy (AVS_1), and between 0.5 and 6.4 % for S_2 wave propagation anisotropy (AV_{S2}). All anisotropies show a positive covariance with the olivine CPO strength (Fig. 3a, b); samples with stronger olivine CPOs are more anisotropic. Yet, this variation is not linear, as observed in previous studies (Ben Ismaïl and Mainprice, 1998): anisotropy increases fast with increasing CPO strength up for low J indexes ($\leq$4), but slow afterwards, tending to stabilize for J indexes > 8. Coarse-grained peridotites show more variable olivine CPO intensities (J indexes range between 2–11). However, their maximum seismic anisotropies are in the same range as those displayed by the sheared peridotites (Fig. 3a, b). These variations suggest that the modal composition has also an important effect on the seismic anisotropy of these samples.

The presence of pyroxenes and garnet is known to dilute the bulk anisotropy of the rock (Mainprice and Silver, 1993; Mainprice et al., 2000). Samples with high modal olivine, and therefore lower pyroxene and/or garnet contents, tend to have higher maximum AV_p, AVS_1 and AV_{S2}. However, the dependence is weaker than the one on the olivine CPO strength (compare Fig. 3c and a). The dependence on the olivine content is even less marked for the S wave polarization anisotropy (Fig. 3d).

There is no simple relation between the olivine CPO symmetry, characterized by the BA index, and the maximum P, S, S_1, and S_2 wave anisotropies (Fig. 3e, f). Samples with an olivine axial [100] CPO tend to show higher maximum P and S_2 propagation anisotropies than those with an orthorhombic CPO, which are themselves more anisotropic than those with an axial [010] CPO. The relation is less clear, however, for S wave polarization and S_1 propagation anisotropies. Moreover, this relation probably reflects more a variation in the olivine CPO intensity then a strong dependence on the olivine CPO symmetry. In the studied data set, samples with axial [100] tend to have stronger olivine CPO, but this behavior is not a general one in naturally deformed peridotites, which may also display very strong axial [010] olivine CPO patterns (e.g., Tommasi et al., 2008).

4.2 Effect of compositional variations on the density and isotropic seismic velocities

Kaapvaal mantle xenoliths record a long and complex history. Early partial melting and extraction of high melt fractions are evidenced by the refractory compositions (olivine Mg# > 92), which are common among the coarse-grained peridotites (Table 1). However, the large variability in modal and chemical compositions of these xenoliths implies that the craton mantle root has been subsequently modified by multiple metasomatic events. The high orthopyroxene content observed in many coarse-grained peridotites has been attributed to percolation of Si-rich fluids and/or melts (e.g., Bell et al., 2005; Wasch et al., 2009; Baptiste et al., 2012). In many xenoliths, secondary crystallization of phlogopite, clinopyroxene and garnet point to reactions with percolating K-rich melts at high pressure (e.g., Grégoire et al., 2003; Griffin et al., 2003; Bell et al., 2005; Baptiste et al., 2012). These metasomatic events may have also allowed for rehydration of the Kaapvaal mantle root above 150 km depth (Baptiste et al., 2012). Finally, local high-stress deformation, which was probably shortly predated by a late metasomatic event by K-rich fluids and/or melts (Wasch et al., 2009), produced the sheared peridotites (Baptiste et al., 2012).

This compositional variability resulted in significant variations in both density and seismic velocities as illustrated in Fig. 4, where densities and isotropic P and S wave velocities at ambient conditions are displayed as a function of the olivine Mg#, the orthopyroxene, and the garnet content of each sample. The density of Kaapvaal samples varies by up to 3 % (Fig. 4a e, i). It decreases with increasing olivine Mg# and orthopyroxene content, but strongly increases with increasing garnet content. The linear correlation with the garnet content is particularly striking. This later effect is dominant in the sheared peridotites, where the garnet content may attain up to 18 %.

P wave velocities vary by up to 2.2 % with the peridotites composition (Fig. 4b, f, j). There is a weak positive covariance between P wave velocities and garnet content. P wave

Table 2. Elastic constants in megabars (Mbar) calculated using Voigt–Reuss–Hill averaging and the elastic constants of enstatite (Chai et al., 1997a), diopside (Collins and Brown, 1998), garnet (Chai et al., 1997b), and olivine elastic tensors recalculated to account for the actual olivine Mg# in each sample, based on the single-crystal elastic constant tensors for fayalite, forsterite, and olivine with Mg# of 90, 91 and 93 (Kumazawa and Anderson, 1969; Suzuki et al., 1983; Webb et al., 1989; Isaak et al., 1993; Abramson et al., 1997).

Locality	Sample	C11	C22	C33	C44	C55	C66	C12	C13	C14	C15	C16	C23	C24	C25	C26	C34	C35	C36	C45	C46	C56
KIMBERLEY	KBBF6a	2.1600	2.6174	2.2429	0.7689	0.6740	0.7329	0.8049	0.8439	0.0014	0.0056	0.0159	0.8139	0.0077	0.0012	0.0161	0.0223	0.0120	0.0085	0.0093	−0.0051	0.0025
	KBBF6b	2.1614	2.5764	2.2501	0.7556	0.6664	0.7421	0.8135	0.8370	−0.0054	−0.0156	0.0171	0.8165	−0.0169	−0.0058	0.0196	−0.0034	−0.0020	0.0029	0.0014	−0.0034	−0.0060
	KBBF8	2.0052	2.3564	2.4182	0.7834	0.6926	0.6801	0.7947	0.7908	0.0040	0.0156	−0.0021	0.8264	−0.0262	−0.0027	−0.0015	−0.0221	0.0196	−0.0003	0.0005	0.0002	−0.0073
	KBBF9	2.1736	2.4113	2.3372	0.7573	0.7079	0.7222	0.8452	0.8475	0.0018	0.0148	0.0131	0.8649	0.0037	−0.0011	0.0113	0.0142	0.0134	-0.0016	0.0017	0.0014	0.0106
	KBBF10	2.1134	2.4711	2.2052	0.7482	0.6726	0.7237	0.7736	0.7940	−0.0017	−0.0021	0.0095	0.7817	0.0137	−0.0029	0.0098	0.0062	−0.0029	−0.0009	0.0085	−0.0045	0.0041
	KBBF11	2.1584	2.3682	2.2252	0.7137	0.6704	0.7026	0.8370	0.8492	0.0017	0.0022	0.0063	0.8611	0.0108	−0.0002	0.0021	0.0081	−0.0014	0.0031	0.0015	−0.0023	0.0055
	KBBF14	2.1386	2.3764	2.6650	0.7599	0.6847	0.7116	0.8074	0.8050	0.0022	0.0039	0.0031	0.8123	0.0071	0.0015	0.0078	0.0184	0.0086	−0.0011	0.0014	0.0048	0.0007
	KBBF15	2.1818	2.3652	2.2124	0.7426	0.6903	0.7403	0.8056	0.8075	−0.0132	0.0132	0.0107	0.8058	0.0366	−0.0003	0.0216	0.0384	0.0086	−0.0018	0.0082	0.0064	0.0123
	KBBF16	2.2368	2.3379	2.1751	0.7433	0.7055	0.7431	0.8045	0.8074	0.0069	−0.0122	−0.0190	0.8099	0.0041	0.0064	−0.0181	0.0121	−0.0032	−0.0052	−0.0141	−0.0067	0.0088
	KBBF18	2.1390	2.4690	2.2471	0.7535	0.6870	0.7203	0.7915	0.7984	0.0016	0.0000	−0.0016	0.7852	0.0088	−0.0005	0.0082	−0.0106	0.0001	−0.0001	0.0035	−0.0058	−0.0033
	KBBF20	*2.1224	*2.345	*2.1857	*0.7783	*0.705	*0.7222	*0.7523	*0.7805	*−0.0149	*−0.0033	*0.0159	*0.8011	*0.0786	*0.0118	*−0.0034	*0.0558	*0.0001	*−0.0015	*−0.0004	*−0.0047	*0.0383
	FRB1402	2.2061	2.3580	2.3435	0.7481	0.7164	0.7143	0.8438	0.8511	0.0006	−0.0300	0.0054	0.8454	−0.0018	−0.0036	0.0101	−0.0035	−0.0343	0.0014	0.0004	−0.0119	0.0008
	FRB1404	2.1869	2.3028	2.2378	0.7427	0.7145	0.7375	0.8114	0.7987	−0.0035	0.0001	−0.0175	0.7990	−0.0050	−0.0008	−0.0227	0.0118	−0.0066	0.0046	−0.0170	−0.0052	0.0011
	FRB1422	2.3020	2.1990	2.2797	0.7157	0.7279	0.7266	0.8119	0.7965	0.0052	0.0247	0.0476	0.7985	−0.0138	0.0052	0.0436	−0.0100	0.0027	−0.0066	0.0125	0.0113	0.0080
	FRB1423	2.1669	2.4982	2.3049	0.7677	0.6995	0.7445	0.8137	0.8346	−0.0053	−0.0015	0.0073	0.8259	−0.0154	0.0053	0.0070	−0.0169	−0.0026	0.0002	0.0074	−0.0062	−0.0077
	FRB1447	2.2415	2.3276	2.2290	0.7341	0.7024	0.7401	0.8055	0.8075	0.0019	0.0189	0.0064	0.8056	0.0197	0.0034	0.0024	0.0206	0.0117	−0.0047	0.0013	0.0030	0.0096
	FRB348	2.3286	2.3646	2.1892	0.7347	0.7297	0.7578	0.8134	0.8002	−0.0027	0.0033	0.0421	0.8119	0.0291	−0.0083	0.0346	0.0268	−0.0062	0.0003	0.1120	0.0065	0.0195
JAGERSFONTEIN	KBJ6	2.2117	2.3819	2.3190	0.7547	0.6901	0.7053	0.8441	0.8364	−0.0029	−0.0033	0.0068	0.8614	−0.0092	−0.0002	0.0057	−0.0190	−0.0063	0.0057	−0.0046	0.0026	−0.0081
	KBJ8	2.1437	2.5764	2.1707	0.7389	0.6493	0.7355	0.8320	0.8593	0.0008	−0.0163	0.0267	0.8386	0.0163	−0.0106	0.0458	0.0111	−0.0170	−0.0025	0.0134	0.0023	0.0063
	KBJ14	2.2506	2.4998	2.3425	0.7652	0.7101	0.7546	0.8722	0.8754	−0.0026	−0.0147	0.0115	0.8805	0.0071	−0.0025	0.0252	0.0048	−0.0145	−0.0014	0.0097	−0.0041	0.0023
	KBJ30	2.2488	2.4582	2.3794	0.7645	0.7093	0.7313	0.8902	0.8869	−0.0035	−0.0073	0.0065	0.8980	0.0015	−0.0043	0.0035	−0.0037	−0.0091	0.0021	0.0019	−0.0036	−0.0019
	KBJ33	2.2248	2.5585	2.3411	0.7687	0.6996	0.7582	0.8629	0.8864	−0.0043	−0.0155	0.0232	0.8917	0.0233	−0.0077	0.0316	0.0130	−0.0179	−0.0010	0.0107	−0.0034	0.0097
	KBJ52	2.2035	2.4416	2.1234	0.7254	0.6871	0.7387	0.7953	0.7927	−0.0010	−0.0212	0.0079	0.7794	0.0118	−0.0097	−0.0143	0.0006	−0.0161	0.0058	0.0000	−0.0208	0.0015
	KBJ54	2.2153	2.2867	2.4037	0.7625	0.7020	0.6838	0.7860	0.7916	0.0009	−0.0192	−0.0310	0.7927	0.0102	−0.0075	−0.0489	0.0442	−0.0174	−0.0112	−0.0221	−0.0137	0.0137
	KBJ56	2.1418	2.3781	2.3544	0.7536	0.7152	0.7349	0.7922	0.8008	−0.0049	−0.0040	−0.0275	0.7929	−0.0061	0.0041	−0.0509	0.0057	−0.0090	0.0138	−0.0006	0.0017	−0.0021
	KBJ60	2.0658	2.3988	2.2948	0.7523	0.6646	0.6907	0.8171	0.8336	0.0013	0.0039	0.0088	0.8512	0.0038	−0.0005	0.0078	−0.0018	−0.0015	−0.0005	−0.0036	−0.0016	0.0030
	KBJ62	2.1179	2.4316	2.1733	0.7726	0.6807	0.7351	0.7584	0.7640	−0.0004	0.0002	0.0022	0.7763	−0.0364	−0.0035	−0.0210	−0.0027	−0.0119	0.0242	0.0064	−0.0182	0.0064
	KBJ63	2.1334	2.4778	2.2230	0.7773	0.6667	0.7192	0.8461	0.8455	0.0009	−0.0028	−0.0023	0.8786	0.0027	−0.0027	−0.0058	−0.0035	0.0008	−0.0006	−0.0039	0.0019	−0.0003
	J34	2.1540	2.5660	2.1857	0.7884	0.6897	0.7790	0.7848	0.7536	−0.0031	0.0206	−0.0073	0.7843	0.0087	0.0102	−0.0165	−0.0015	0.0214	0.0155	−0.0027	0.0061	0.0042
	J41	2.1366	2.2972	2.2589	0.7585	0.7003	0.7067	0.7728	0.7694	−0.0009	0.0057	0.0082	0.7780	0.0153	−0.0045	0.0012	−0.0179	−0.0023	−0.0053	−0.0083	−0.0013	0.0013
	J47	2.0888	2.4032	2.3554	0.7546	0.6832	0.6981	0.8293	0.8381	0.0013	0.0078	0.0090	0.8698	−0.0066	0.0050	0.0071	0.0151	0.0097	0.0070	0.0045	0.0044	0.0033
	J57	2.2094	2.4552	2.1555	0.7644	0.6801	0.7316	0.7790	0.7931	−0.0047	0.0242	−0.0098	0.7893	0.0281	0.0081	−0.0044	0.0180	0.0210	0.0053	-0.0027	0.0096	−0.0009
	J63	2.1674	2.3572	2.2985	0.7324	0.6919	0.7018	0.8557	0.8508	0.0028	0.0077	0.0073	0.8719	−0.0123	0.0001	0.0047	−0.0180	0.0069	−0.0007	0.0001	0.0048	−0.0088
MONASTERY	ROM23	2.1676	2.3192	2.2399	0.7534	0.7260	0.7418	0.7872	0.7800	0.0017	−0.0391	0.0188	0.7975	−0.0075	−0.0016	0.0030	−0.0303	−0.0236	−0.0004	0.0099	−0.0185	−0.0103
	ROM69	2.2753	2.2929	2.2192	0.7600	0.7223	0.7367	0.7644	0.7835	−0.0031	−0.0066	0.0048	0.7937	0.0035	−0.0124	0.0077	−0.0113	-0.0215	0.0036	0.0067	−0.0027	0.0010
LENTSENG	PHN4274	2.1888	2.3263	2.2424	0.7428	0.7190	0.7144	0.7991	0.8029	0.0159	−0.0095	0.0013	0.8002	−0.0199	0.0046	−0.0078	−0.0126	−0.0111	−0.0047	−0.0093	0.0020	0.0018
MOTHAE	PHN1925	2.2229	2.3552	2.2732	0.7414	0.7096	0.7357	0.8226	0.8247	0.0003	−0.0066	−0.0004	0.8326	0.0183	0.0002	-0.0083	0.0241	−0.0057	0.0025	−0.0035	−0.0045	0.0109
KAMFERSDAM	PHN5580	**2.1736	**2.373	**2.2914	**0.8095	**0.7614	**0.7901	**0.7172	**0.7128	**−0.0114	**−0.0046	**−0.0152	**0.7163	**−0.032	**−0.0143	**−0.0482	**−0.0107	**0.0071	**0.0256	**0.0069	**−0.0025	**−0.0085
DE BEERS	KBB2	2.1587	2.4200	2.1824	0.7440	0.6834	0.7392	0.7736	0.7905	−0.0042	0.0159	−0.0089	0.7725	0.0078	0.0013	−0.0088	−0.0025	0.0332	0.0139	0.0029	0.0004	−0.0014
PREMIER	FRB1330	2.1317	2.5519	2.1425	0.7644	0.6702	0.7469	0.7729	0.7992	0.0000	0.0118	−0.0079	0.7807	−0.0113	0.0042	−0.0089	−0.0004	0.0096	−0.0014	−0.0038	0.0043	−0.0007
	FRB1336	**2.2550	**2.1943	**2.3222	**0.8001	**0.7928	**0.7580	**0.7155	**0.7224	**0.0034	**0.5060	**−0.0450	**0.7226	**0.0491	**−0.0018	**−0.0439	**0.5300	**0.0431	**−0.0083	**−0.0238	**0.0174	**0.0145
	FRB1339	**2.2486	**2.3529	**2.3271	**0.7881	**0.7751	**0.7731	**0.7287	**0.7385	**−0.0001	**−0.0510	**0.0225	**0.7201	**−0.0199	**0.0122	**0.0136	**0.0031	**−0.0546	**0.0074	**0.0074	**−0.021	**−0.0110
	PHN5266	**2.2466	**2.2858	**2.2703	**0.7922	**0.7830	**0.7936	**0.7158	**0.7234	**0.0008	**0.0552	**−0.0103	**0.7152	**−0.0564	**0.0136	**−0.0104	**−0.0565	**0.0743	**−0.0190	**−0.0308	**0.0413	**−0.0435
	PHN5267	2.2229	2.4937	2.2670	2.2732	0.6895	0.7366	0.8408	0.8572	−0.0078	−0.0324	−0.0068	0.8623	0.0021	−0.0138	−0.0110	0.0076	−0.0234	−0.0131	−0.0111	−0.0134	−0.0067
FINSCH	FRB1501	2.1482	2.4002	2.3306	0.7620	0.6975	0.7185	0.8152	0.8274	0.0056	0.0036	0.0002	0.8403	0.0012	0.0025	−0.0028	−0.0076	0.0036	−0.0067	−0.0033	−0.0004	−0.0007
	FRB1512	2.1689	2.3907	2.3505	0.7573	0.7040	0.7194	0.8214	0.8350	−0.0033	−0.0124	0.0012	0.8417	−0.0001	−0.0122	0.0050	0.0042	−0.0250	−0.0024	−0.0016	−0.0056	−0.0014
	FRB1513	2.1300	2.3269	2.3105	0.7450	0.6878	0.6906	0.8008	0.8197	−0.0035	0.0182	0.0107	0.8198	0.0117	0.0038	0.0029	−0.0214	0.0035	0.0083	0.0037	0.0005	−0.0044

* Seismic properties were calculated by only taking into account the sample equilibrium pressure and temperature, since olivine Mg# was unknown.
** Seismic properties were calculated by only taking into account the mean olivine Mg# of the sample, since the equilibrium conditions were unknown.

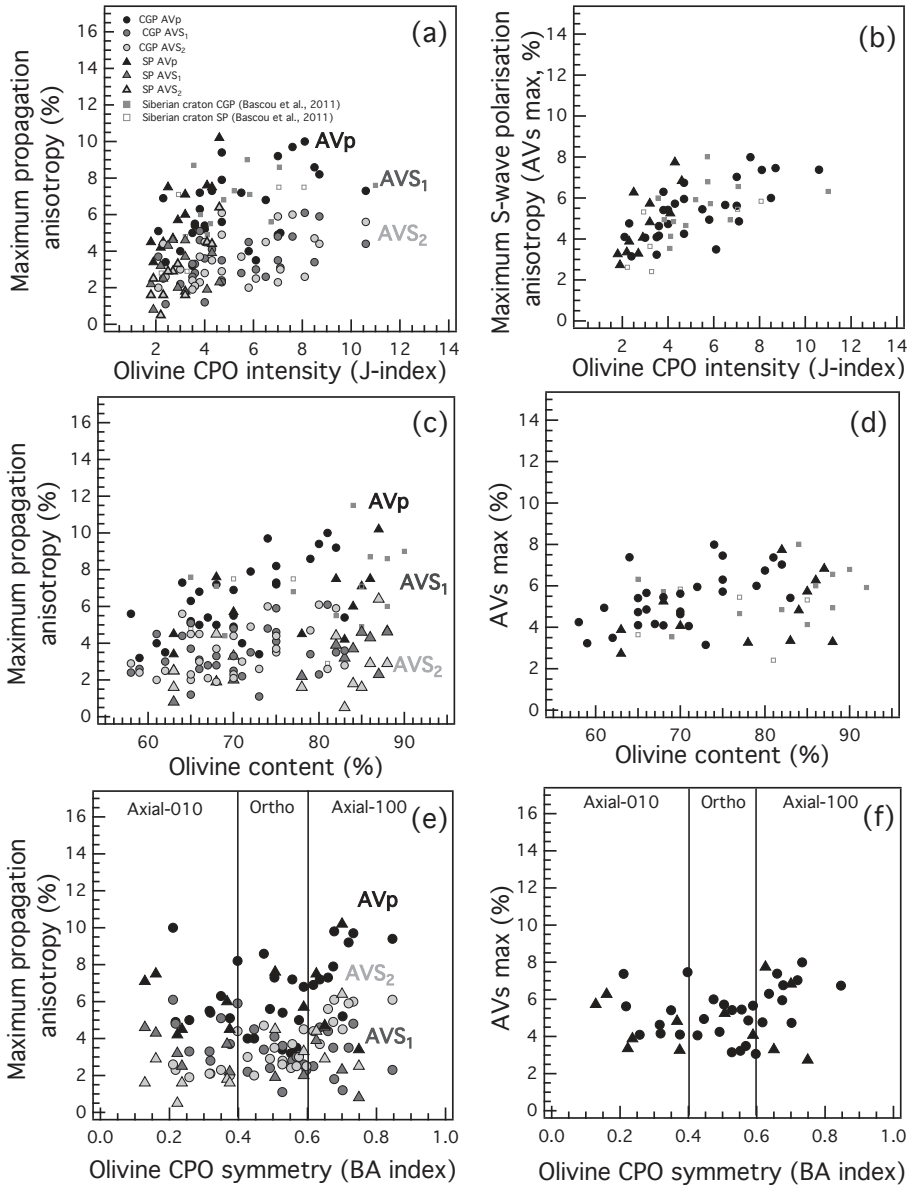

Fig. 3. Dependence of the maximum P, S_1 and S_2 wave anisotropies (AV_p, AVS_1 and AVS_2), and of the maximum S wave polarization anisotropy (AV_s) on the olivine CPO strength (characterized by the J index), the olivine content and the BA index.

velocities in coarse-grained peridotites also tend to increase with increasing olivine Mg# (Fig. 4b) and decreasing orthopyroxene content (Fig. 4f), but the competing effects of olivine Mg# and orthopyroxene content results in dispersion of P wave velocities of the coarse-grained peridotites in all diagrams. In contrast, P wave velocities in sheared peridotites increase strongly with olivine Mg#, probably because the latter have lower orthopyroxene contents.

The isotropic S wave velocities of the Kaapvaal mantle xenoliths show a clear linear correlation with olivine Mg# (Fig. 4c), varying by up to 2.4 %. This variation is consistent with previous data showing that an increase in the olivine Mg# in a dunite results in a linear increase in V_s (Tommasi et al., 2004). No clear co-variation is observed between the orthopyroxene and garnet contents and V_s in neither coarse-grained nor sheared peridotites, although S wave velocities are on average higher in the coarse-grained peridotites, which have higher orthopyroxene contents (Fig. 4g and k).

The V_p/V_s ratio is also sensitive to compositional changes (Fig. 4d, h, l), varying by up to 2.3 %. It decreases with increasing olivine Mg# and orthopyroxene content and increases with garnet content. The V_p/V_s ratio is very sensitive to the orthopyroxene content, as indicated by the strong linear correlation between the two parameters (Fig. 4h).

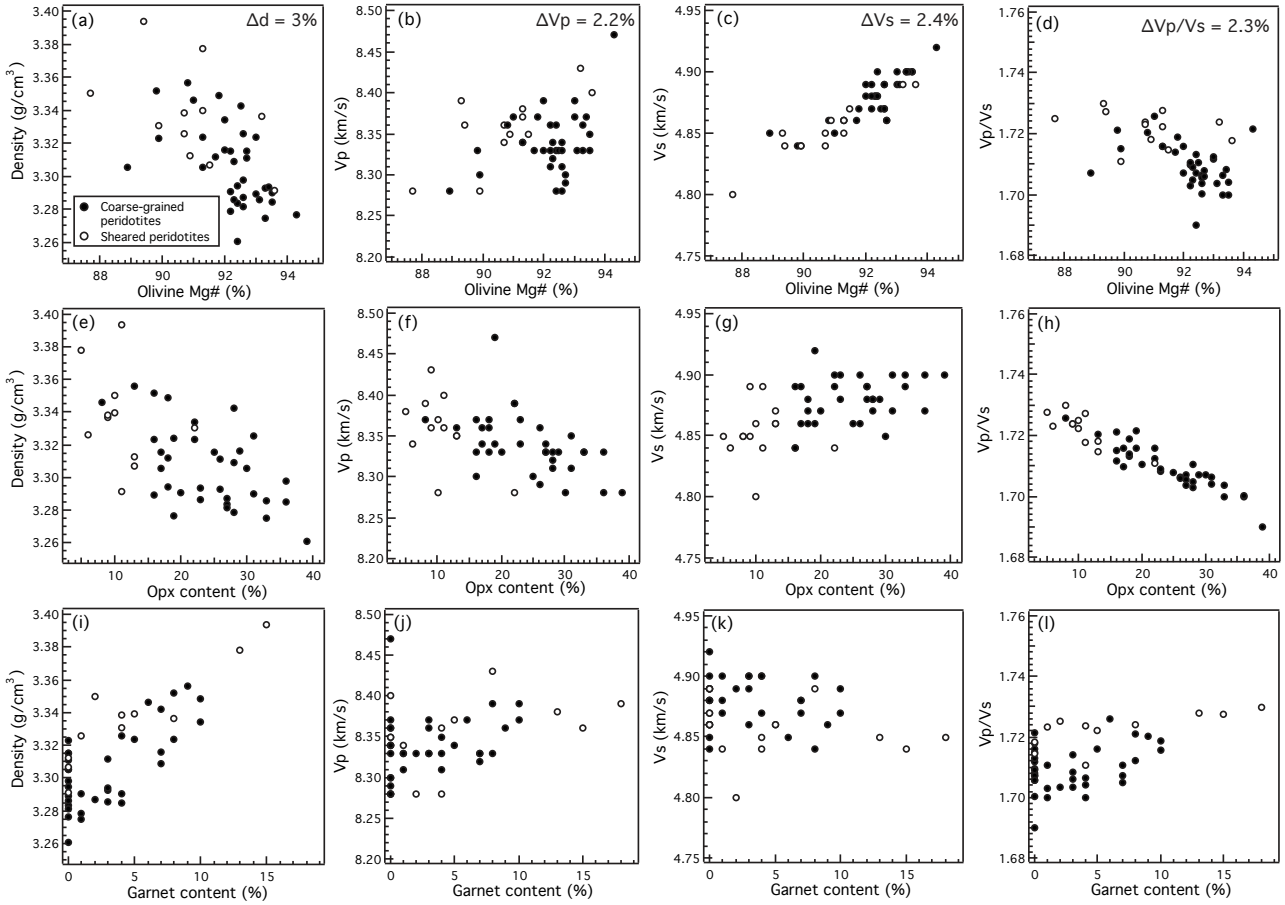

Fig. 4. Evolution of the samples' densities, *P* wave velocities (V_p), *S* wave velocities (V_s), and V_p/V_s ratios with olivine Mg#, orthopyroxene (opx) content, and garnet contents.

Sheared peridotites have a higher and less variable V_p/V_s ratio than coarse-grained peridotites, probably due to their lower modal orthopyroxene.

4.3 Evolution of seismic properties and density with depth

The variations of the isotropic *P* and *S* wave velocities (V_p, V_s), V_p/V_s ratio, and density with depth in the present Kaapvaal xenolith suite and in the one studied by James et al. (2004) are plotted in Fig. 5. The isotropic *P* wave velocities calculated for the equilibration pressure and temperature and for the composition of our samples do not show a monotonic increase with depth. They are highly heterogeneous, being comprised between 8.17 and 8.36 km s^{-1} over the entire depth section. This result contrasts with the one from James et al. (2004), who observed a regular increase in V_p up to 180 km depth, though with some dispersion in the depth interval of 120–150 km, and a marked decrease below this depth. One may argue that the present data set does not sample well the deepest part of the root (below 180 km), but at shallower depths the peridotites analyzed in this study tend to display, on average, higher and more variable *P* wave velocities than those reported by James et al. (2004). In contrast, the isotropic *S* wave velocities decrease and the V_p/V_s ratio increases almost linearly with depth, in excellent agreement with the results of James et al. (2004) for depths above 180 km. The dispersion of calculated densities and *P* wave velocities at a given depth tends to be higher than for V_s or the V_p/V_s ratio, indicating a stronger dependence on the composition.

Compositions, olivine CPOs, and anisotropic seismic properties of average samples (obtained by summing the CPO and averaging the compositions of all samples in a 20 km-thick depth interval) for six depths between 70 and 190 km depth are presented in Fig. 6. With increasing depth, olivine and garnet contents increase, while the orthopyroxene content decreases. The variability of olivine Mg# increases as well, with a higher proportion of normal to Fe-rich olivines (Mg#$\leq$90) in the deeper part of the cratonic root, and the olivine CPO patterns change from axial [100] to more orthorhombic. These variations do not result, however, in marked changes in seismic anisotropy with depth.

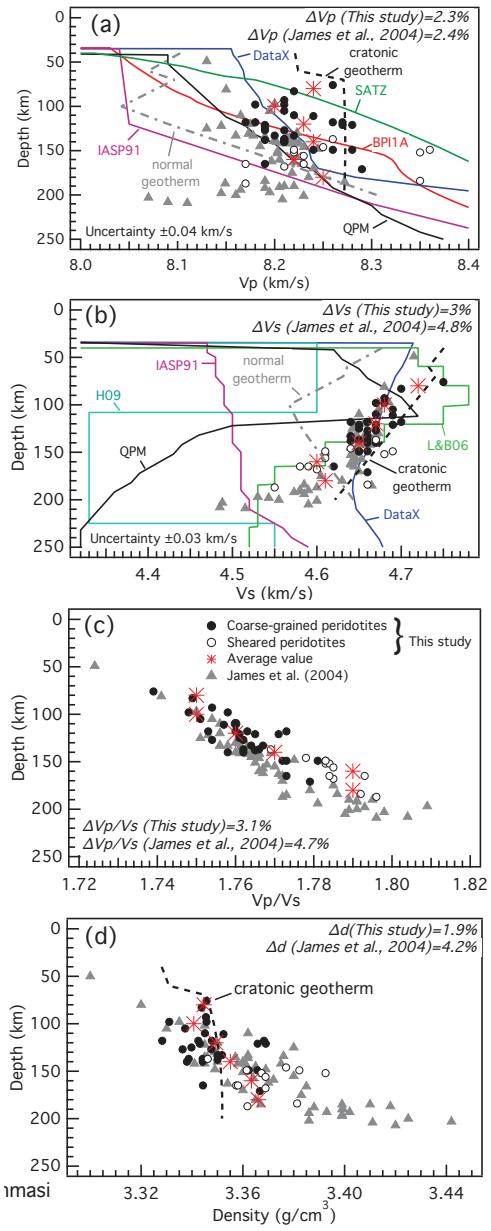

Fig. 5. Variation with depth of the isotropic seismic velocities and density of the studied peridotite xenoliths: **(a)** V_p, **(b)** V_s, **(c)** V_p/V_s ratio, and **(d)** density. For comparison, the density and seismic properties of a peridotite with a standard composition (between 40 and 70 km: 65 % olivine with Mg#90, 23 % orthopyroxene, 12 % clinopyroxene; between 70 and 200 km: 65 % olivine with Mg#90, 20 % orthopyroxene, 10 % clinopyroxene, 5 % garnet) for both a "cratonic geotherm" as estimated by Baptiste et al. (2012) and a "normal geotherm" producing a 100 km-thick lithosphere are shown as black and gray dashed lines, respectively. The IASP91 reference model and different seismic models for southern Africa (BPI1A: Simon et al., 2002; DataX: Larson et al., 2006; H06: Hansen et al., 2009; L&B06: Li and Burke, 2006; QPM: Qiu et al., 1996; SATZ: Zhao et al., 1999) are also shown (colored lines). Uncertainties in the seismic velocity estimates due to the uncertainty in the determination of the equilibration pressure and temperature of the xenoliths are shown in **(a)** and **(b)**.

The maximum P wave anisotropy varies between 4.5 and 7.9 %. The fastest P wave propagation direction is always aligned with the olivine [100] axes maximum, that is, with the lineation. Between 70 and 110 km, P wave propagation is slow in all directions at high angle to the olivine [100] axes maximum. At greater depths, P wave propagation is the slowest parallel to the olivine [010] axes maximum.

The maximum S wave birefringence varies between 3.8 and 5.8 %. The fast split shear wave (S_1) is always polarized in a plane containing the propagation direction and the olivine [100] axes maximum. The maximum S wave polarization anisotropy is observed for waves propagating along the structural direction Y at all depths. The apparent isotropy direction, however, changes slightly with depth. It is always contained in the XZ plane (that is the plane that contains the lineation and the normal to the foliation), but it is very close to the lineation above 100 km depth, where axial [100] olivine CPO patterns dominate, and at 45° to the lineation in the deeper layers, where the olivine CPO has a dominantly pattern.

The propagation of S_1 waves is always fastest along the foliation plane and slowest at a high angle to it, close to the Z structural axis. However, the fastest propagation direction varies with depth. Between 70 and 90 km, it is parallel to the lineation and Y structural axis, while between 90 and 130 km, it is located at 45° to the lineation. At greater depths, S_1 wave propagation is fast in all directions within the foliation plane. In contrast, the S_2 wave propagation anisotropy does not change with depth. The fastest propagation direction of S_2 waves is always located on the XZ plane, at about 30° to the lineation, while the slowest velocities are found along the YZ plane. Finally, the V_p/V_{S_1} ratio is always maximum parallel to the alignment of olivine [100] axes and minimum along the YZ plane.

5 Discussion

5.1 Compositional effects on isotropic seismic properties

In the studied data set, P and S wave velocities, the V_p/V_s ratio, and density vary with sample composition (Fig. 4) by 2.2, 2.4, 2.3, and 3 %, respectively. Melt depletion tends to decrease the density and the V_p/V_s ratio, but to increase V_p and V_s. Metasomatism may result in refertilization, that is, enrichment in pyroxenes and/or garnet, depending on the melt composition and depth. Enrichment in orthopyroxene decreases the whole rock density and P wave velocities, but increases S wave velocities and, hence, strongly reduces the V_p/V_s ratio. Garnet enrichment tends to strongly increase density and slightly P wave velocities and the V_p/V_s ratio. However, it has little effect on S wave velocities.

The V_p/V_s ratio is more sensitive to orthopyroxene content than to the olivine Mg# or garnet content. High V_s

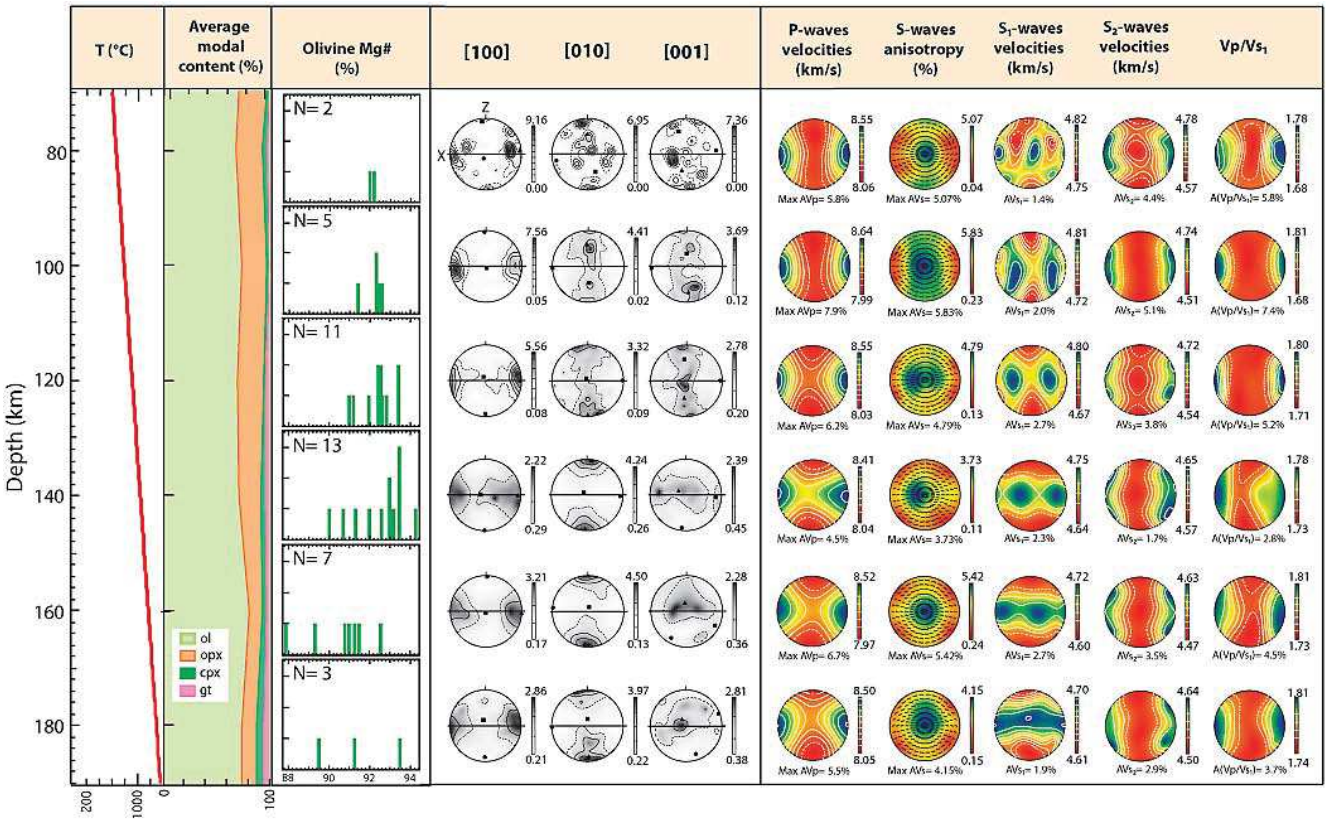

Fig. 6. Mean compositions, CPOs and seismic properties of five 20-km sections between 70 and 190 km depth calculated by averaging the olivine composition and modal contents of the samples originated from these depths. From left to right, are displayed: the geotherm of Baptiste et al. (2012), the average modal content of the samples, the number and the olivine Mg# of the samples in each depth section, the average olivine crystal-preferred orientations, and the 3-D distributions of P wave velocities (V_p), S wave polarization anisotropy (V_s), the orientation of the fast shear wave polarization plane, S_1 wave velocities (V_{S_1}), S_2 wave velocities (V_{S_2}), and V_p/V_{S_1} ratio.

($\sim 4.7\,\mathrm{km\,s^{-1}}$) and low V_p/V_s ratios (1.65–1.70) observed locally above the flat slab in central Chile–Argentina were indeed interpreted by Wagner et al. (2008) as due to orthopyroxene enrichment. Yet, although extremely high orthopyroxene contents (> 30 %) are observed in the Kaapvaal mantle xenoliths, such an orthopyroxene enrichment can at most produce V_p/V_s ratios of 1.7. These results are consistent with V_p/V_s ratios in mantle xenoliths from subduction environments, in which reactive percolation of Si-rich fluids produced enrichment of orthopyroxene at the expenses of olivine in the supra-slab mantle (Soustelle and Tommasi, 2010). This led Soustelle and Tommasi (2010) to propose that the very low V_p/V_s ratios (1.65–1.70) observed locally in the mantle wedge do not result from Si enrichment in the mantle, but from the intrinsic anisotropy of the peridotites, representing regions in the mantle dominantly sampled by seismic waves propagating at a high angle to lineation. Analysis of the anisotropy of the V_p/V_{s1} ratio in the Kaapvaal peridotites (Figs. 2, 6) corroborates this conclusion.

Among the studied Kaapvaal peridotites, compositional changes result in density variations by up to 3 %, while V_p, V_s and the V_p/V_s ratio vary at most by 2.4 % (Fig. 4). These variation ranges are slightly higher than the ~ 2 % density and the 1.0–1.4 % V_s changes that Griffin et al. (2009) estimated to result from an increase of fertility in the mantle lithosphere by comparing data from domains where the crust has been stable since $\geq$2.5 Ga (Archons) and domains formed or modified at < 1 Ga (Tectons). They are, however, in agreement with the 2–3 % seismic velocity change due compositional variations estimated by Schutt and Lesher (2010) for the Kaapvaal mantle.

The P wave velocities calculated for the equilibration pressure and temperature of Kaapvaal xenoliths vary strongly at all depths (Fig. 5a). Between 90 and 150 km, the total variation of P wave velocity is of ~ 1.2 %, but reaches up to 2.3 % when the sheared peridotites, which were equilibrated at greater depths, are considered. Such lateral heterogeneity in P wave velocity may be explained by the compositional heterogeneity of the cratonic root, as discussed above. This interpretation is corroborated by the strong variability of density at all depths (Fig. 5d). A lower proportion of deep sheared peridotites and a stronger compositional

heterogeneity within the presently studied xenolith suite may thus explain the discrepancy between our *P* wave data and that of James et al. (2004) (Fig. 5a). The 3 % decrease in *S* wave velocity, 3 % increase in the V_p/V_s ratio, and 2 % increase in density with depth observed in the present study (Fig. 5b, c, d), are in good agreement with the results of James et al. (2004). These variations are the result of the conjugate effects of changes in pressure, temperature, and composition within the cratonic mantle, and corroborate a higher sensitivity of *S* wave velocity to temperature.

To discriminate between thermal and compositional effects on *P* and *S* wave velocity profiles, we calculated the seismic properties and density of a sample with a standard composition (between 40 and 70 km: 65 % olivine with Mg#90, 23 % orthopyroxene, 12 % clinopyroxene; between 70 and 200 km: 65 % olivine with Mg#90, 20 % orthopyroxene, 10 % clinopyroxene, 5 % garnet), for both the cratonic geotherm estimated by Baptiste et al. (2012) and a "normal" 100 km-thick lithosphere (Fig. 5). The cooler cratonic geotherm results in an increase in V_p and V_s by up to 2.8 and 3.1 %, respectively, relative to the seismic velocities in a "normal" 100 km-thick lithosphere. This variation is smaller than the one resulting from compositional heterogeneity among the Kaapvaal xenoliths (Fig. 5). In a 100 km-thick lithosphere, the faster increase in temperature relative to pressure results in decrease of both *P* and *S* wave velocities with depth; this trend is changed at sublithospheric depths, where the pressure effect becomes dominant, leading to an increase in seismic velocities. Within the cratonic mantle lithosphere, the slower temperature increase with depth is largely compensated by the increase in pressure, leading to almost constant *P* wave velocities and a slower decrease of *S* wave velocity with depth. The introduction of garnet at 70 km depth results in a sharp increase in both *P* wave and *S* wave velocities for both geotherms. The stronger increase in *P* wave velocities indicates a stronger effect of this change in mineralogical composition (crystallization of garnet at the expenses of the pyroxenes and spinel) on the *P* wave velocities relative to *S* waves. This effect is not sampled in the present data set due to the small fraction of spinel peridotites analyzed and to the refractory composition of most shallow peridotites, which did not allow crystallization of garnet (Fig. 1, Table 1).

The marked variations in density and *S* wave velocity among the deepest xenoliths (Fig. 5), which are mainly sheared peridotites, further highlight the strong compositional control on the isotropic seismic velocities. They may be attributed to the strong variability in the garnet content and in the olivine Mg# that characterize the sheared peridotites (Fig. 4), and that has been attributed to heterogeneous refertilization shortly preceding mylonitization and extraction by the kimberlite (Smith and Boyd, 1987; Baptiste et al., 2012). At shallower depths, the variations in density can be attributed to the variability in orthopyroxene content and olivine Mg#.

5.2 Comparison with seismological velocity profiles and tomographic models for the Kaapvaal mantle

Comparison of the velocity profiles in Fig. 5 with one-dimensional *P* wave velocity (V_p) profiles for the Kaapvaal highlights that most *P* wave models show an increase of velocity with depth between 50 and 200 km depth, consistent with James et al. (2004) data (Fig. 5a). *P* wave velocities for our individual samples do not show a clear trend, due to the strong variability at all depths. However, except for the shallowest layer, which displays an average V_p significantly higher than those estimated in most tomographic models, but that is only based on two samples, the average V_p tends to increase slightly with depth. Between 90 and 180 km, the range of variation of V_p in the studied xenoliths is consistent with most *P* wave tomography models, except for the SATZ model of Zhao et al. (1999), which overestimates V_p, and the global model IASP91, which as expected strongly underestimates V_p in a cratonic root such as the Kaapvaal. The DataX model by Larson et al. (2006) is the model that fits the best our data, while the QPM model by Qiu et al. (1996) is the most coherent with the xenolith data of James et al. (2004). The decrease of V_p associated with the predominance of deep sheared peridotites between 180 and 200 km in the James et al. (2004) data is not fitted by any *P* wave tomographic model. This observation reinforces the idea that these sheared peridotites correspond to local modifications of the mantle lithosphere caused and oversampled by kimberlites.

The discrepancy between 1-D seismic profiles and xenoliths' velocities is still more marked for *S* waves (Fig. 5b). Most models do not fit neither our, nor the xenolith-based isotropic *S* wave velocity profiles of James et al. (2004), but there is a fit with the DataX model of Larson et al. (2006) and, in to lesser extent, with the model L&B06 of Li and Burke (2006). The QPM model of Qiu et al. (1996) and the model of Hansen et al. (2009) (H09) display a marked decrease of V_s at 110–120 km that is not observed in the xenolith data. The latter implies that the cratonic root is at least 180 km thick. The gradual increase in the isotropic *S* wave velocities calculated based on Kaapvaal xenolith data (Fig. 5b) is also at odds with the seismic discontinuity imaged by *S* wave receiver functions at ∼150 km depth (Wittlinger and Farra, 2007; Savage and Silver, 2008; Hansen et al., 2009). This suggests that this discontinuity has not a compositional origin.

P and *S* wave tomography studies reported lateral velocity perturbations of 0.5 % (James et al., 2001; Fouch et al., 2004a), while surface wave studies imaged velocity perturbations as high as 5–7 % within the Kaapvaal cratonic root (Ritsema and van Heijst, 2000; Priestley et al., 2006; Chevrot and Zhao, 2007; Fishwick, 2010). Priestley and Tilmann (2009) attributed the velocity variations within the Kaapvaal lithospheric mantle to thermal effects. On the contrary, Begg et al. (2009) highlighted that xenolith thermometry implies

a very narrow geotherm range and suggested that lateral *S* wave velocity variations within the cratonic root are mainly due to compositional changes. A characteristic example of this intracratonic seismic velocity heterogeneity are the lower velocities (~ 0.5 % for V_p and ~ 0.8 % for V_s) imaged below the Bushveld complex by body wave tomographies (James et al., 2001; Fouch et al., 2004a) (Fig. 1), but not by surface wave tomographies (e.g., Priestley and Tilmann, 2009), probably due to their poorer lateral resolution. The degree of variation of isotropic *P* and *S* wave velocities observed in the present study is higher, in particular for *P* waves, than any intracratonic velocity perturbation imaged by body wave tomographies. The latter may therefore be explained by compositional variations within the cratonic mantle lithosphere, such as, enrichment in Fe due to reactive melt percolation beneath the Bushveld.

The present data cannot, however, explain the much higher velocity anomalies inferred from surface wave data (7–8 %). Moreover, the variations in the xenolith *P* wave velocity at all depths are stronger than the *S* wave ones, what renders the explanation of the strong velocity gradients inferred from surface waves still more difficult. Partial melting within the lithosphere is a highly improbable cause for these velocity perturbations because of the cold geotherm beneath the Kaapvaal craton. The possible role of water content changes on seismic wave velocity is more difficult to access. Jacobsen et al. (2008) demonstrated that the combined effects of 3 mol % Fe and 0.8 wt. % H_2O reduce the olivine shear and bulk moduli. However, the effects of low water contents, similar to those measured in the Kaapvaal peridotites (≤ 150 wt. ppm H_2O, Baptiste et al., 2012; Peslier et al., 2010) on olivine elastic properties are poorly constrained.

At a given depth, the calculated variation in seismic velocity is almost as strong within xenoliths derived from a single pipe or from closely spaced localities as within the entire data set. Indeed, V_p and V_s varies by up to 1.1 % among xenoliths from Kimberley equilibrated between a 110 and 130 km depth (Fig. 5). V_p and V_s variations by up to 2.1 % are observed among Jagersfontein xenoliths equilibrated between a 150 and 170 km depth. V_p and V_s variations among xenoliths from closely spaced pipes (Jagersfontein, Kimberley and DeBeers, which are all within 100 km, Fig. 1) may reach 1.2 and 1.3 % between a 110 and 130 km depth. Such small-scale variations cannot be imaged by seismic tomography, which probably underestimates the heterogeneity of the subcratonic lithospheric mantle.

5.3 Seismic anisotropy

The changes in olivine CPO symmetry of the Kaapvaal peridotite xenoliths result in slight variations of the seismic anisotropy patterns (Fig. 2). Analysis of the individual sample's seismic anisotropy shows strong variations at all depths (Table 1), but average values for different depth ranges are rather homogeneous (Fig. 6). Maximum *P* and *S* wave average anisotropies (Fig. 6) are coherent with the values for the Kaapvaal mantle xenoliths reported by Long and Christensen (2000), but higher than those calculated by Ben Ismaïl et al. (2001). They are also coherent with the anisotropies calculated from Siberian xenoliths reported by Bascou et al. (2011).

The polarization and propagation anisotropies calculated for the Kaapvaal xenoliths may be compared to seismic anisotropy data obtained using both body and surface waves, which sample the Kaapvaal mantle root in different directions and with variable vertical and lateral resolutions. SKS splitting measurements sample the mantle along a vertical direction, and have no vertical but good lateral resolution ($\sim$50 km at lithospheric depths), whereas surface waves sample the mantle along horizontal directions. Moreover, the analysis of surface wave data with different periods allows discriminating between the lithospheric and sublithospheric contributions to seismic anisotropy.

The fast SKS polarization, which samples vertically the Kaapvaal's lithospheric and sublithospheric mantle, and the fast Rayleigh propagation at 70–120 s periods, which sample the Kaapvaal lower lithosphere, are characterized by a NNE–SSW orientation within the western and central part of the craton, and an E–W orientation in its northern part (Silver et al., 2001; Adam and Lebedev, 2012). This suggests that the deep mantle lithosphere beneath the Kaapvaal displays olivine CPO with consistent orientations at the length scales of tens to hundreds of kilometers.

We can therefore use the availability of both SKS splitting and surface wave anisotropy data in the Kaapvaal craton to try to determine the orientation of the foliation and of the lineation in the lithospheric mantle beneath the Kaapvaal craton. The idea is that both SKS and surface waves sample the same mantle lithosphere, which has a unique 3-D seismic anisotropy pattern, but SKS only probes the *S* wave polarization anisotropy in the vertical direction, while Rayleigh and Love waves travel along horizontal paths, allowing therefore to probe the *S* wave polarization and azimuthal anisotropies in the horizontal plane. To do so, we have estimated the anisotropy that would be measured by SKS, Rayleigh (S_V) and Love (S_H) waves for five endmember orientations of the foliation and lineation (Fig. 7). A delicate point in this analysis is to determine whether the horizontally S_H or the vertically polarized *S* wave S_V is the fast propagating S_1 wave, but this distinction can be made by analyzing the *S* wave polarization anisotropy in the horizontal plane for each case. S_1 is always polarized in a plane containing the lineation. Hence, when the lineation is vertical, S_1 corresponds to S_V (case 3). When it is horizontal, S_1 corresponds to S_H (cases 1, 2 and 5). For a 45° dipping lineation (case 4), the fastest wave is polarized in the horizontal or in the vertical plane depending on the propagation azimuth, but the birefringence is always higher when the fastest wave is polarized in the horizontal plane, implying that when significant anisotropy can be measured S_1 is equal to S_H.

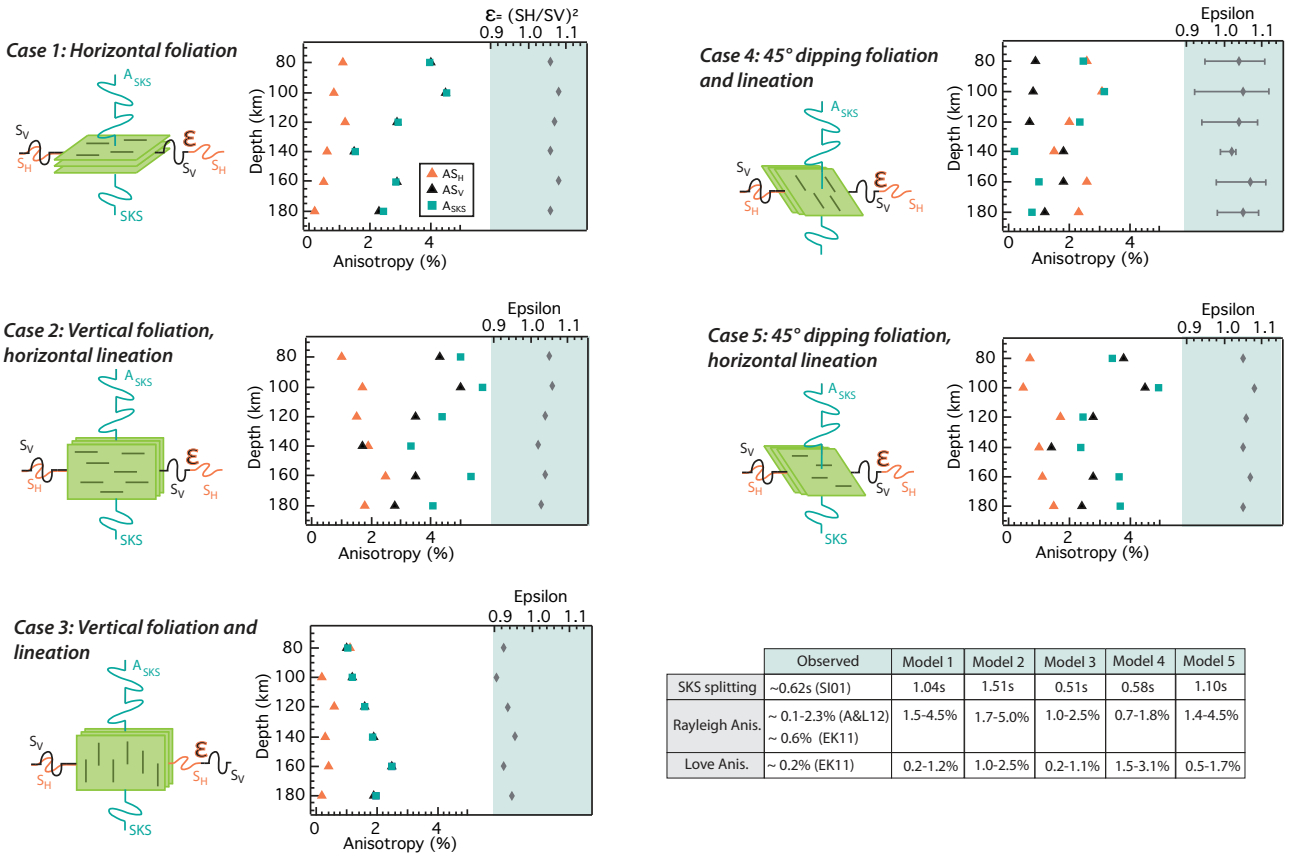

	Observed	Model 1	Model 2	Model 3	Model 4	Model 5
SKS splitting	~0.62s (SI01)	1.04s	1.51s	0.51s	0.58s	1.10s
Rayleigh Anis.	~ 0.1-2.3% (A&L12) ~ 0.6% (EK11)	1.5-4.5%	1.7-5.0%	1.0-2.5%	0.7-1.8%	1.4-4.5%
Love Anis.	~ 0.2% (EK11)	0.2-1.2%	1.0-2.5%	0.2-1.1%	1.5-3.1%	0.5-1.7%

Fig. 7. Calculated surface wave polarization anisotropy ($\varepsilon = (S_H/S_V)^2$), maximum azimuthal anisotropy of horizontally propagating S_H and S_V, and the maximum SKS anisotropy for the depth-averaged samples in five different "endmember" orientations of the foliation and the lineation: (1) horizontal foliation, (2) vertical foliation with a horizontal lineation, (3) vertical foliation and lineation, (4) 45° dipping foliation and lineation, and (5) 45° dipping foliation with a horizontal lineation. The table describes how well these different "endmember" models match SKS- and surface wave data (SI01: Silver et al., 2001; A&L12: Adam and Lebedev, 2012; EK11: Ekström, 2011).

If the foliation is horizontal (case 1), SKS waves and S_V waves will measure similar polarization and azimuthal anisotropies comprised between 1.5 and 4.5 % in the mantle lithosphere, while S_H waves will detect almost no azimuthal anisotropy (≤ 1 %) at all depths. Because S_H is faster than S_V, the surface wave polarization anisotropy (epsilon) is higher than 1 at all depths. If the foliation is vertical and the lineation horizontal (case 2), SKS waves sample a highly anisotropic direction (3.5 to 5.5 %) at all depths. The S_V wave propagation (2–4 %) anisotropy is, at all depths, twice as strong as that of the S_H waves (1–2 %). As in case 1, the surface wave polarization anisotropy is higher than 1 at all depths. If the foliation and the lineation are vertical (case 3), the surface wave polarization anisotropy is smaller than 1, indicating that S_V is always faster than S_H. SKS and S_V waves will measure low anisotropies, comprised between 1.0 and 2.5 %. The anisotropy measured by S_H waves should be even lower (< 0.5 %). A 45° dipping foliation and lineation (case 4) should produce SKS anisotropies higher than 2 % and S_V wave azimuthal anisotropy lower than 1 % between 80 and 120 km. At greater depths, SKS wave anisotropy will be lower than 1 %, while S_V wave azimuthal anisotropy will vary between 1 and 2 %. The S_H wave azimuthal anisotropy will always be comprised between 1.5 and 2 %. The surface wave polarization anisotropy will be strongly dependent on the propagation direction. Finally, if we consider a 45° dipping foliation and a horizontal lineation (Case 5), the SKS and S_V waves should measure polarization and azimuthal anisotropies varying between 1.5 and 5 %, while S_H waves will measure azimuthal anisotropies lower than 2 %. As in cases 1 and 2, the surface wave polarization anisotropy is higher than 1, indicating that S_H is faster than S_V at all depths.

These predictions can be compared to the anisotropy detected using SKS and surface waves (Table in Fig. 7). Beneath the Kaapvaal craton, SKS delay times are low. Vinnik et al. (1995) first measured SKS delay times comprised between 0.4 and 1.4 s. Silver et al. (2001) obtained similar SKS delay times, between 0.3 and 1.1 s, with an average value of 0.62 s. Low delay times (0.15 to 0.75 s) were also obtained in

a denser network near Kimberley by Fouch et al. (2004b). If we consider a 150 km-thick homogeneous anisotropic lithospheric mantle, these delay times yield anisotropies comprised between 0.9 and 3.4 %, with an average of 1.9 %. Such low SKS anisotropies are only obtained for either a vertical or a 45° dipping foliation and lineation (cases 3 and 4 in Fig. 7).

Surface wave data consistently points to S_H faster than S_V in the Kaapvaal lithospheric mantle (Freybourger et al., 2001; Sergei Lebedev, personal communication). This is consistent with receiver function data, which imaged a 160 km-thick anisotropic mantle keel with vertical slow axis ($V_{S_H} > V_{S_V}$) and decreasing anisotropy with depth due to a decrease in V_{S_H} while V_{S_V} remains constant (Wittlinger and Farra, 2007). These observations are not consistent with case 3 (Fig. 7), since vertical lineations always result in $V_{S_H} < V_{S_V}$. Moreover, coherent fast SKS polarization directions like those measured by Silver et al. (2001) are not expected if the lineation is vertical (case 3). They might however be produced by a 45° dipping foliation (case 4). Surface wave azimuthal anisotropies generated for case 4 range between 0.5 and 3 %, being consistent with the low azimuthal anisotropies inferred in both global and regional surface wave models (Ekström, 2011; Adam and Lebedev, 2012). However, case 4 produces a S_H azimuthal anisotropy that is stronger than the S_V one, which is not consistent with the stronger Rayleigh azimuthal anisotropy (~ 2 %) relative to the Love azimuthal anisotropy (~ 1 %) imaged beneath South Africa in the global surface wave model of Ekström (2011), and in the recent regional anisotropic tomography model for the Kaapvaal by Adam and Lebedev (2012). Such a relation is obtained in the cases where the lineation is horizontal (cases 1, 2, and 5 in Fig. 7), but too strong Rayleigh azimuthal and SKS polarization anisotropies accompany it.

Low SKS birefringence may result from vertical variations of the seismic anisotropy. Indeed, beneath the western Kaapvaal (Kimberley block), the Rayleigh wave azimuthal anisotropy shows a change of fast propagation directions from N–S in the crust to E–W in the mantle (Adam and Lebedev, 2012). A change with depth in the orientation of the fast direction from E–W to N–S was also detected at depths > 160 km beneath the Limpopo belt by a study associating *P* wave receiver functions and SKS waveforms inversion (Vinnik et al., 2012). The seismic discontinuity imaged by *S* wave receiver functions at ∼150 km depth (Wittlinger and Farra, 2007; Savage and Silver, 2008; Hansen et al., 2009) also points to vertical variations in the deformation structure within the cratonic root, since drastic changes in composition or *S* wave velocities with depth are not observed in neither our data set nor in that of James et al. (2004). Most cases presented in Fig. 7 show a decrease in anisotropy at 140 km depth, which would be consistent with the observations of Wittlinger and Farra (2007), but the associated gradient in seismic velocities is too weak to produce a strong impedance contrast. Peslier et al. (2010) and Baptiste et al. (2012) did measure a marked decrease in OH concentrations in olivine at depths greater than 160 km. Yet the change in elastic properties produced by variations of OH contents from 150 ppm to a few ppm is probably too weak (Jacobsen et al., 2008) to explain the receiver function signal. A sharp change in the orientation of the foliation and lineation and the associated change in seismic anisotropy might produce the needed impedance contrast. It is also consistent with the anisotropic surface wave models and with the results of *P* receiver functions and SKS waveforms inversion, which propose change in the orientation of the fast direction at depths > 160 km (Adam and Lebedev, 2012; Vinnik et al., 2012). However, such a vertical variation in seismic anisotropy should produce a backazimuthal dependence of the shear wave splitting, which was not described in the regional studies (Silver et al., 2001; Fouch et al., 2004a; Silver et al., 2004; Vinnik et al., 1995).

In conclusion, no simple model may account for all seismic anisotropy data in the Kaapvaal. The two models that best explain the observations are (i) the presence of dipping foliations and lineations within the cratonic lithosphere, at ca. 160 km depth and (ii) a vertical variation in seismic anisotropy within the Kaapvaal mantle lithosphere, with dominant horizontal frozen flow directions in the shallower layer. In the second case, we may speculate that it might represent an interface marking a change in the geodynamical process responsible for the formation and thickening of the mantle root. A possible geodynamic scenario allowing for the development of 45° dipping foliations and lineations within the cratonic lithosphere would be the formation of the Kaapvaal craton keel by subduction stacking, as suggested by several geochemical and petrological studies (Shirey et al., 2001; Simon et al., 2007; Pearson and Wittig, 2008). However, in this case, fast SKS polarization directions normal to the main sutures should be expected, rather than the parallel to slightly oblique directions measured in the Kaapvaal craton (Silver et al., 2001). These predictions are also at odds with the parallelism between fast Rayleigh wave propagation directions and the Archean–Paleoproterozoic crustal structures in the Limpopo belt and in the northern Kaapvaal, but they may explain the fast Rayleigh wave propagation directions perpendicular to the crustal structures in the western part of the craton (Adam and Lebedev, 2012). On the other hand, if the cratonic root formed by episodic injection of small (100–200 km) diapiric upwellings (de Smet et al., 1998, 1999), a horizontal foliation and variable flow direction are to be expected across the craton. Such a variability of the structure within the root may explain the low SKS delay times measured in the craton, but would fail to explain the coherent fast polarization direction of SKS waves and fast propagation direction of Rayleigh waves over length scales of several hundreds of kilometers in the Kaapvaal mantle lithosphere (Silver et al., 2001; Adam and Lebedev, 2012).

6 Conclusions

The strong compositional heterogeneity of the Kaapvaal peridotite xenoliths results in up to 3 % variation in density, while V_p, V_s and the V_p/V_s ratio vary by up to 2.3 %. These variations are slightly higher than the velocity perturbations imaged by body wave tomography, but cannot explain the strong velocity anomalies reported by surface wave studies. Melt depletion tends to increase V_p and V_s and to decrease the V_p/V_s ratio and density. Orthopyroxene enrichment decreases the density and V_p, and strongly reduces the V_p/V_s ratio. Enrichment in garnet tends to increase the density strongly and slightly V_p and the V_p/V_s ratio, but has little to no effect on V_s. The V_p/V_s ratio is more sensitive to the orthopyroxene content than to olivine Mg# and garnet content. The present data also highlights that compositional heterogeneity in the Kaapvaal mantle root occurs at a scale much smaller than the one that may be sampled by seismic tomography, since at a given depth, the calculated variation in seismic velocity within xenoliths derived from a single pipe or from closely spaced localities is almost as strong as within the entire data set. Seismic tomography thus probably strongly underestimates the heterogeneity of the subcratonic lithospheric mantle.

Vertical density and seismic velocity profiles calculated using the xenoliths' compositions and equilibration conditions show that V_s decreases, whereas the V_p/V_s ratio and density increase with increasing depth. V_p does not show a clear trend; it is highly variable at all depths. Comparison of these xenolith-based seismic profiles with 1-D velocity profiles derived from seismological data in the Kaapvaal highlights clear discrepancies between seismological and xenolith-based data. For P waves, the DataX model by Larson et al. (2006) fits our data the best, while the QPM model by Qiu et al. (1996) is the most coherent with data of James et al. (2004). For S waves, most models, except for the DataX model of Larson et al. (2006) and, in a lesser extent, the model L&B06 of Li and Burke (2006), do not fit neither our, nor data of James et al. (2004), which imply that the cratonic root is at least 180 km thick. No seismological velocity model fits the decrease of V_p indicated by deep sheared peridotites between 180 and 200 km, reinforcing the idea that they represent very local modifications of the lithosphere caused and oversampled by kimberlites.

Changes in olivine CPO symmetry of the Kaapvaal peridotite xenoliths result only in slight variation of the seismic anisotropy patterns. Seismic anisotropy increase with the olivine J index and olivine content, but there is no simple relation with the olivine CPO symmetry (BA index). Maximum anisotropy values range between 2.5 and 10.2 % for P wave azimuthal anisotropy (AV_p) and between 2.7 and 8 % for S wave polarization anisotropy (AV_s) in agreement with existing xenolith data. The maximum P wave anisotropy of each 20 km interval varies between 4.5 and 7.9 %, whereas S wave anisotropy is comprised between 3.7 and 5.8 %. Models considering endmember orientations of the foliation and lineation in the subcratonic mantle lithosphere show that the simplest model that might produce both coherent fast directions over large domains, but low delay times imaged by SKS studies, and the low azimuthal surface wave anisotropy with S_H faster than S_V in the subcratonic mantle lithosphere is the presence of 45° dipping foliations and lineations. Yet, this model fails to account for the relative importance of the Rayleigh and Love azimuthal anisotropies. This observation and the discontinuity observed at ca. 160 km depth by receiver functions are best explained by a vertical variation in seismic anisotropy, due to a sharp change in orientation of the frozen deformation structures in the Kaapvaal mantle lithosphere. However, this scenario is at odds with the observation of coherent fast polarization direction of SKS waves and fast propagation direction of Rayleigh waves over scales of several hundreds of kilometers in the Kaapvaal mantle lithosphere (Silver et al., 2001; Adam and Lebedev, 2012).

Acknowledgements. The authors thank A. Vauchez and D. Mainprice for helpful discussions. D. Mainprice provided the programs for calculating seismic properties. C. Nevado and D. Delmas are thanked for providing high-quality polishing of sections for EBSD measurements. The two anonymous reviewers are thanked for their helpful comments. The EBSD-SEM national facility in Montpellier is supported by the Institut National de Sciences de l'Univers (INSU) du Centre National de la Recherche Scientifique (CNRS), France and by the Conseil Régional Languedoc-Roussillon, France.

Edited by: W. Geissler

References

Abramson, E. H., Brown, J. M., Slutsky, L. J., and Zaug, J.: The elastic constants of San Carlos olivine to 17 GPa, J. Geophys. Res., 102, 12253–12263, 1997.

Adam, J. M.-C.and Lebedev, S.: Azimuthal anisotropy beneath southern Africa from very broad-band surface wave dispersion measurements, Geophys. J. Int., 191, 155–174, 2012.

Adams, A. and Nyblade, A.: Shear wave velocity structure of the southern African upper mantle with implications for the uplift of southern Africa, Geophys. J. Int., 186, 808–824, 2011.

Allsopp, H. L., Bristow, J. W., and Skinner, E. M. W.: The Rb–Sr geochronology of the Colossus kimberlite pipe, Zimbabwe, Transactions of the Geological Society of South Africa, 88, 245–248, 1985.

Baptiste, V., Tommasi, A., and Demouchy, S.: Deformation and hydration of the lithospheric mantle beneath the Kaapvaal craton, South Africa, Lithos, 149, 31–50, 2012.

Bascou, J., Doucet, L. S., Saumet, S., Ionov, D. A., Ashchepkov, I. V., and Golovin, A. V.: Seismic velocities, anisotropy and deformation in Siberian cratonic mantle: EBSD data on xenoliths from the Udachnaya kimberlite, Earth Planet. Sc. Lett., 304, 71–84, 2011.

Begg, G. C., Griffin, W. L., Natapov, L. M., O'Reilly, S. Y., Grand, S. P., O'Neill, C. J., Hronsky, J. M. A., Poudjom Djo-

mani, Y., Swain, C. J., Deen, T., and Bowden, P.: The lithospheric architecture of Africa: seismic tomography, mantle petrology, and tectonic evolution, Geosphere, 5, 23–50, 2009.

Bell, D. R., Rossman, G. R., Maldener, J., Endisch, D., and Rauch, F.: Hydroxide in olivine: a quantitative determination of the absolute amount and calibration of the IR spectrum, J. Geophys. Res., 108, B2, ECV8.1–ECV8.9, 2003.

Bell, D., Grégoire, M., Grove, T., Chatterjee, N., Carlson, R., and Buseck, P.: Silica and volatile-element metasomatism of Archean mantle: a xenolith-scale example from the Kaapvaal Craton, Contrib. Mineral. Petr., 150,251–267, 2005.

Ben Ismaïl, W., and Mainprice, D.: An olivine fabric database: an overview of upper mantle fabrics and seismic anisotropy, Tectonophysics, 296, 145–157, 1998.

Ben Ismaïl, W., Barruol, G., and Mainprice, D.: The Kaapvaal craton seismic anisotropy: petrophysical analyses of upper mantle kimberlite nodules, Geophys. Res. Lett., 28, 2497–2500, 2001.

Chai, M., Brown, J. M, and Slutsky, L. J.: The elastic constants of an aluminous orthopyroxene to 12.5 GPa, J. Geophys. Res., 102, 14770–14785, 1997a.

Chai, M., Brown, J. M., and Slutsky, L. J.: The elastic constants of pyrope-grossular-almandine garnets to 20 GPa, Geophys. Res. Lett., 24, 523–526, 1997b.

Chevrot, S. and Zhao, L.: Multiscale finite-frequency Rayleigh wave tomography of the Kaapvaal craton, Geophysical Journal International, 169, 1, 201–215, 2007.

Collins, M. D. and Brown, J. M.: Elasticity of an upper mantle clinopyroxene, Phys. Chem. Miner., 26, 7–13, 1998.

de Smet, J. H., van den Berg, A. P., and Vlaar, N. J.: Stability and growth of the continental shields in mantle convection models including melt production, Tectonophysics, 296, 15–29, 1998.

de Smet, J. H., van den Berg, A. P., and Vlaar, N. J.: The evolution of continental roots in numerical thermo-chemical mantle convection models including differentiation by partial melting, Lithos, 48, 153–170, 1999.

Ekström, G.: A global model of Love and Rayleigh surface wave dispersion and anisotropy, 25–250 s, Geophys. J. Int., 187, 1668–1686, 2011.

Fishwick, S.: Surface wave tomography: imaging of the lithosphere-asthenosphere boundary beneath central and southern Africa?, Lithos, 120, 63–73, 2010.

Fouch, M. J., James, D. E., VanDecar, J. C., and van der Lee, S.: Mantle seismic structure beneath the Kaapvaal and Zimbabwe Cratons, S. Afr. J. Geol., 107, 33–44, 2004a.

Fouch, M. J., Silver, P. G., Bell, D. R., and Lee, J. N.: Small-scale variations in seismic anisotropy near Kimberley, South Africa, Geophys. J. Int., 157, 764–774, 2004b.

Freybourger, M., Gaherty, J. B., Jordan, T. H., and the Kaapvaal Seismic Group: Structure of the Kaapvaal craton from surface waves, Geophys. Res. Lett., 28, 2489–2492, 2001.

Green, H. W. and Gueguen, Y.: Origin of kimberlite pipes by diapiric upwelling in upper mantle, Nature, 249, 617–620, 1974.

Grégoire, M., Bell, D. R., and Le Roex, A. P.: Garnet lherzolites from the Kaapvaal craton (South Africa): trace element evidence for a metasomatic history, J. Petrol., 44, 629–657, 2003.

Griffin, W. L., O'Reilly, S. Y., Afonso, J. C., and Begg, G. C.: The composition and evolution of lithospheric mantle: a re-evaluation and its tectonic implications, J. Petrol., 50, 7, 1185–1204, 2009.

Griffin, W. L., O'Reilly, S. Y., Natapov, L. M.,and Ryan, C. G.: The evolution of lithospheric mantle beneath the Kalahari craton and its margins, Lithos, 71, 215–241, 2003.

Hansen, S. E., Nyblade, A. A., Julià, J., Dirks, P. H. G. M., and Durrheim, R. J.: Upper-mantle low-velocity zone structure beneath the Kaapvaal craton from *S* wave receiver functions, Geophys. J. Int., 178, 1021–1027, 2009.

Hielscher, R. and Schaeben, H.: A novel pole figure inversion method: specification of the MTEX algorithm, J. Appl. Crystallogr., 41, 1024–1037, 2008.

Isaak, D., Graham, E. K., Bass, J. D., and Wang, H.: The elastic properties of single-crystal fayalite as determined by dynamical measurement techniques, Pure Appl. Geophys., 141, 393–414, 1993.

Jacobsen, S. D., Jiang, F., Mao, Z., Duffy, T. S., Smyth, J. R., Holl, C. M., and Frost, D. J.: Effects of hydration on the elastic properties of olivine, Geophys. Res. Lett., 35, L14303, doi:10.1029/2008GL034398, 2008.

James, D. E., Fouch, M. J., Vandecar, J. C., and Van der Lee, S.: Tectospheric structure beneath southern Africa: The Kaapvaal Project: formation and evolutions of cratons, Geophys. Res. Lett., 28, 2485–2488, 2001.

James, D. E., Boyd, F. R., Schutt, D., Bell, D. R., and Carlson, R. W.: Xenolith constraints on seismic velocities in the upper mantle beneath southern Africa, Geochem. Geophy. Geosy., 5, Q01002, doi:10.1029/2003GC000551, 2004.

Jordan, T. H.: Composition and development of continental tectosphere, Nature, 274, 5671, 544–548, 1978.

Kramers, J. D.and Smith, C. B.: A feasibility study of U–Pb and Pb–Pb dating of kimberlites using groundmass mineral fractions and whole-rock samples, Chem. Geol., 41, 23–38, 1983.

Kumazawa, M. and Anderson, O. L.: Elastic moduli, pressure derivatives, and temperature derivatives of single-crystal olivine and single-crystal forsterite, J. Geophys. Res., 74, 5961–5972, 1969.

Larson, M. A., Snoke, J. A., and James, D. E.: *S*-wave velocity structure, mantle xenoliths and the upper mantle beneath the Kaapvaal craton, Geophys. J. Int., 167, 171–186, 2006.

Li, A. and Burke, K.: Upper mantle structure of southern Africa from Rayleigh wave tomography, J. Geophys. Res., 111, B10303, doi:10.1029/2006JB004321, 2006.

Long, C. and Christensen, N. I.: Seismic anisotropy of South African upper mantle xenoliths, Earth Planet. Sc. Lett., 179, 551–565, 2000.

Mainprice, D.: A FORTRAN program to calculate seismic anisotropy from the lattice preferred orientation of minerals, Computat. Geosci., 16, 385–393, 1990.

Mainprice, D. and Humbert, M.: Methods of calculating petrophysical properties from lattice preferred orientation data, Surv. Geophys., 15, 575–592, 1994.

Mainprice, D. and Silver, P. G.: Interpretation of SKS-waves using samples from the subcontinental lithosphere, Phys. Earth Planet. In., 78, 257–280, 1993.

Mainprice, D., Barruol, G., and Ben Ismaïl, W.: The seismic anisotropy of the Earth's mantle: from single crystal to polycrystal, in: AGU Geophysical Monograph, edited by: Karato, A. M. F. S., Libermann, R. C., Masters, G., and Stixrude, L., AGU, Washington, DC, 117, 237–264, 2000.

Mainprice, D., Hielscher, R., and Schaeben, H.: Calculating anisotropic physical properties from texture data using the MTEX open source package, in: Deformation Mechanisms, Rheology and Tectonics: Microstructures, Mechanics and Anisotropy, edited by: Prior, D. J., Rutter, E. H., and Tatham, D. J., Geological Society, Special Publications, London, 175–192, 2011.

Pearson, D. G. and Wittig, N.: Formation of Archaean continental lithosphere and its diamonds: the root of the problem, J. Geol. Soc., 165, 895–914, 2008.

Pearson, D. G., Carlson, R. W., Shirey, S. B., Boyd, F. R., and Nixon, P. H.: Stabilisation of Archaean lithospheric mantle: A Re-Os isotope study of peridotite xenoliths from the Kaapvaal craton, Earth Planet. Sci. Lett., 134, 341–357, 1995.

Peslier, A. H., Woodland, A. B., Bell, D. R., and Lazarov, M.: Olivine water contents in the continental lithosphere and the longevity of cratons, Nature, 467, 78–81, 2010.

Phillips, D., Machin, K. J., Kiviets, G. B., Fourie, L. F., Roberts, M. A., Skinner, E. M. W.: A petrographic and $^{40}Ar/^{39}Ar$ geochronological study of the Voorspoed kimberlite, South Africa: implications for the origin of group II kimberlite magmatism, special issue, S. Afr. J. Geol., 101, 299–306, 1998.

Priestley, K.: Velocity structure of the continental upper mantle: evidence from southern Africa, Lithos, 48, 45–56, 1999.

Priestley, K. and Tilmann, F.: Relationship between the upper mantle high velocity seismic lid and the continental lithosphere, Lithos, 109, 112–124, 2009.

Priestley, K., McKenzie, D., and Debayle, E.: The state of the upper mantle beneath southern Africa, Tectonophysics, 416, 101–112, 2006.

Qiu, X., Priestley, K., and McKenzie, D.: Average lithospheric structure of southern Africa, Geophys. J. Int., 127, 563–587, 1996.

Ritsema, J. and van Heijst, H.: New seismic model of the upper mantle beneath Africa, Geology, 28, 63–66, 2000.

Savage, B. and Silver, P. G.: Evidence for a compositional boundary within the lithospheric mantle beneath the Kalahari craton from *S* receiver functions, Earth Planet. Sc. Lett., 272, 600–609, 2008.

Schutt, D. L. and Lesher, C. E.: Compositional trends among Kaapvaal Craton garnet peridotite xenoliths and their effects on seismic velocity and density, Earth Planet. Sc. Lett., 300, 367–373, 2010.

Sebai, A., Stutzmann, E., Montagner, J.-P., Sicilia, D., and Beucler, E.: Anisotropic structure of the African upper mantle from Rayleigh and Love wave tomography, Phys. Earth Planet. In., 155, 48–62, 2006.

Shirey, S. B., Carlson, R. W., Richardson, S. H., Menzies, A. H., Gurney, J. J., Pearson, D. G., Harris, J. W., and Wiechert, U.: Archean emplacement of eclogitic components into the lithospheric mantle during formation of the Kaapvaal Craton, Geophys. Res. Lett., 28, 2509–2512, 2001.

Silver, P. G., Gao, S. S., Liu, K. H., and the Kaapvaal Seismic Group: Mantle deformation beneath southern Africa, Geophys. Res. Lett., 28, 2493–2496, 2001.

Silver, P. G., Fouch, M. J., Gao, S. S., Schmitz, M., and the Kaapvaal Seismic Group: Seismic anisotropy, mantle fabric, and the magmatic evolution of Precambrian southern Africa, S. Afr. J. Geol., 107, 45–58, 2004.

Simon, R. E., Wright, C., Kgaswane, E. M., and Kwadiba, M. T. O.: The *P* wavespeed structure below and around the Kaapvaal craton to depths of 800 km, from traveltimes and waveforms of local and regional earthquakes and mining-induced tremors, Geophys. J. Int., 151, 132–145, 2002.

Simon, N. S. C., Carlson, R. W., Pearson, D. G., and Davies, G. R.: The origin and evolution of the Kaapvaal cratonic lithospheric mantle, J. Petrol., 48, 3, 589–625, 2007.

Smith, D. and Boyd, F. R.: Compositional heterogeneities in a high temperature lherzolite nodule and implications for mantle processes, in: Mantle Xenoliths, edited by: Nixon, P. H., John Wiley, Hoboken, NJ, 551–561, 1987.

Soustelle, V. and Tommasi, A.: Seismic properties of the suprasubduction mantle: constraints from peridotite xenoliths from the Avacha volcano, southern Kamchatka, Geophys. Res. Lett., 37, L13307, 1–5, 2010.

Suzuki, I., Anderson, O. L., and Sumino, Y.: Elastic properties of a single-crystal forsterite Mg_2SiO_4, up to 1,200 K, Phys. Chem. Miner., 10, 38–46, 1983.

Tommasi, A., Mainprice, D., Canova, G., and Chastel, Y.: Viscoplastic self-consistent and equilibrium-based modeling of olivine lattice preferred orientations: Implications for the upper mantle seismic anisotropy, J. Geophys. Res., 105, 7893–7908, 2000.

Tommasi, A., Godard, M., Coromina, G., Dautria, J.-M., and Barsczus, H.: Seismic anisotropy and compositionally induced velocity anomalies in the lithosphere above mantle plumes: a petrological and microstructural study of mantle xenoliths from French Polynesia, Earth Planet. Sc. Lett., 227, 539–556, 2004.

Tommasi, A., Vauchez, A., and Ionov, D. A.: Deformation, static recrystallisation, and reactive melt transport in shallow subcontinental mantle xenoliths (Tol Cenozoic volcanic field, SE Siberia), Earth Planet. Sc. Lett., 272,65–77, 2008.

Vinnik, L., Green, R. W. E., and Nicolaysen, L. O.: Recent deformation of the deep continental root beneath southern Africa, Nature, 375, 50–52, 1995.

Vinnik, L., Kiselev, S., Weber, M., Oreshin, S., and Makeyeva, L.: Frozen and active seismic anisotropy beneath southern Africa, Geophys. Res. Lett., 39,1–6, 2012.

Wagner, L. S., Anderson, M. L., Jackson, J. M., Beck, S. L., and Zandt, G.: Seismic evidence for orthopyroxene enrichment in the continental lithosphere, Geology, 36, 12, 935–938, 2008.

Wang, Y., Wen, L., and Weidner, D.: Upper mantle S_H- and *P*-velocity structures and compositional models beneath southern Africa, Earth Planet. Sc. Lett., 297, 596–608, 2008.

Wasch, L. J., van der Zwan, F. M., Nebel, O., Morel, M. L. A., Hellebrand, E. W. G., Pearson, D. G., and Davies, G. R.: An alternative model for silica enrichment in the Kaapvaal subcontinental lithospheric mantle, Geochim. Cosmochim. Ac., 73, 6894–6917, 2009.

Webb, S. L.: The elasticity of the upper mantle orthosilicates olivine and garnet to 3 GPa, Phys. Chem. Miner., 16, 684–692, 1989.

Wittlinger, G. and Farra, V.: Converted waves reveal a thick and layered tectosphere beneath the Kalahari super-craton, Earth Planet. Sc. Lett., 254, 404–415, 2007.

Zhao, M., Langston, C. A., Nyblade, A., and Owens, T. J.: Upper mantle velocity structure beneath southern Africa from modeling regional seismic data, J. Geophys. Res., 104, 4783–4794, 1999.

Chapitre 5 : Déformation, hydratation et anisotropie du manteau lithosphérique sous un rift actif

Le rifting est un processus complexe entraînant l'amincissement d'une plaque continentale. Bien que le manteau représente plus de 60% de la lithosphère, peu de choses sont connues sur le rôle du manteau sur l'initiation du rifting, mais aussi sur la façon dont le manteau accommode la déformation durant le rifting. Vauchez et al. (1997) et Tommasi et Vauchez (2001) suggérèrent que l'extension continental se produit sous un régime de déformation en transtension produit par la réactivation d'ancienne OPR de l'olivine préservée dans la lithosphère. En plus de subir à des forces extensives, la lithosphère est soumise à une percolation extensive de magmas. Buck (2006) proposa ainsi que l'intrusion de filons pourrait aider à initier l'extension au cœur de la lithosphère continentale.

Le travail présenté dans ce chapitre repose sur l'analyse de 53 xénolites mantelliques de la Divergence Nord Tanzanienne provenant de 4 localités différentes : deux au cœur du rift Est-Africain (Pello Hill et Eledoi) et deux au cœur de la ceinture volcanique transverse (Lashaine et Olmani). Cette étude est basée sur la caractérisation des microstructures, des OPRs, des teneurs en hydrogène dans l'olivine des xénolites tanzaniens, ainsi que sur le calcul de leurs propriétés sismiques. Elle vise à mieux comprendre les relations entre déformation et percolation de fluides et magmas au début du rifting ainsi que son régime de déformation.

L'analyse de ces échantillons révèle une variation significative des microstructures et des OPRs en fonction de leur provenance. Au cœur du rift, les microstructures porphyroclastiques et mylonitiques enregistrent une déformation par fluage dislocation récente, ainsi que de fortes variations de température. Les cristaux d'orthopyroxène très étirés dans les mylonites suggèrent une initiation de la déformation à faible contrainte et probablement basse température. Le remplacement de l'orthopyroxène par l'olivine dans les péridotites porphyroclastiques et mylonitiques indique des réactions magmas-roches syn-cinématiques et une déformation se poursuivant sous des conditions proches du solidus.

Enfin, les exsolutions dans les orthopyroxènes suggèrent un refroidissement important avant extraction des xénolites. Les OPRs de l'olivine de type axial-[100] et l'orientation des directions de polarisation des ondes SKS suggère que le rift s'est formé sous un régime en transtension (Vauchez et al., 2000).

Au cœur de la ceinture volcanique transverse, à Lashaine, les microstructures granulaires à gros grains indiquent une déformation par fluage dislocation à faibles contraintes déviatoriques suivie par du recuit. Les OPRs de l'olivine de type orthorhombique à axial-[010] peuvent être associées à la formation de la chaîne Mozambique ou un événement plus ancien (probablement Archéen, Gibson et al., 2013). A Olmani, des microstructures et des OPRs intermédiaires sont observées, suggérant une déformation hétérogène au sein de la ceinture volcanique transverse, probablement lié au développement du graben de Pangani.

Les teneurs en hydrogène dans l'olivine sont comprises entre 2 et 18 ppm wt. H_2O, mais ne varient pas en fonction de la localité, de la microstructure ou du type d'OPR. La présence d'hydrogène dans l'olivine au Mg# élevé suggère une réhydration par métasomatisme. Toutefois, l'absence de corrélation spatiale entre les veines tardives et les teneurs en hydrogène dans l'olivine et l'absence de profil de diffusion dans l'olivine indiquent que l'hydratation de ces échantillons n'a eu lieu ni durant cet épisode métasomatique, ni durant l'extraction des xénolites à la surface.

Deformation, hydration, and anisotropy of the lithospheric mantle in an active rift: constraints from mantle xenoliths from the North Tanzanian Divergence of the East African Rift

Virginie Baptiste[1], Alain Vauchez[1], Andréa Tommasi[1], Sylvie Demouchy[1] and Roberta L. Rudnick[2]

[1]*Géosciences Montpellier, Université Montpellier 2 & CNRS, CC 60, Place E. Bataillon, 34095 Montpellier cedex 5, France.*

[2] *Department of Geology, University of Maryland, College Park, Maryland 20742, USA.*

Running title: Deformation of the mantle lithosphere in an active rift

(*) corresponding author: virginie.baptiste@gm.univ-montp2.fr;

Phone: +33 467144912

Fax: +33 467143603

Abstract

We have analyzed the microstructures and crystal preferred orientations (CPO) and calculated the seismic properties of 53 mantle xenoliths from 4 localities within the North Tanzanian Divergence of the East African rift: 2 within the rift axis and 2 in the transverse volcanic belt. Olivine OH concentrations were measured in fifteen xenoliths. Most samples have harzburgitic to dunitic compositions and high olivine Mg#. Microstructures and olivine CPO patterns vary strongly depending on the location. In-axis peridotites display mylonitic to porphyroclastic microstructures, which record recent deformation by dislocation creep. Highly stretched orthopyroxenes in mylonites indicate that the deformation was initiated under high stress and probably low temperature. Orthopyroxene replacement by olivine in mylonitic and porphyroclastic peridotites suggest synkinematic melt-rock reactions and further deformation under near-solidus conditions. Exsolutions in orthopyroxene imply significant cooling between melt-assisted deformation and xenolith extraction. Late hydrous metasomatism is evidenced by the occurrence of veins crosscutting the microstructure and interstitial clinopyroxene and phlogopite. Axial-[100] olivine CPOs predominate, suggesting activation of the high temperature, low pressure [100]{0kl} slip systems and, probably, transtensional deformation. In the volcanic belt, Lashaine peridotites display very coarse-granular textures, indicating deformation by dislocation creep under low deviatoric stress conditions followed by annealing. They have orthorhombic to axial-[010] olivine CPO symmetries. The latter are consistent with activation of the [001](010) slip system in addition to the dominant [100](010) system and may result from transpressional deformation. Intermediate microstructures and CPOs in Olmani suggest heterogeneous deformation within the volcanic belt. Olivine OH concentrations range between 2 and 12 ppm wt. H_2O. No systematic variations are observed between in- and off-axis samples. Maximum P wave azimuthal anisotropy (AVp) ranges between 3.3 and 18.4%, and the maximum S wave polarization anisotropy (AVs) between 2.3 and 13.2%. Comparison between seismic properties of in-axis peridotites and SKS splitting data suggests transtensional deformation in the lithospheric mantle beneath the rift.

1. Introduction

Continental rifting is a complex process that results in localized thinning and, in some cases, in disruption of a continental plate. While the surface expression of this deformation is clear and usually well understood, little is known about how the lithospheric mantle deforms to accommodate rifting. The widely differing surface expression of continental rifting has led to contrasting lithospheric extension models. McKenzie (1978) proposed a symmetrical rift model, where the lithosphere deforms by homogeneous thinning and stretching in response to far field extensional forces. To account for the observations in the Basin and Range, Wernicke (1981, 1985) proposed an asymmetrical extension model, in which the deformation is localized on a lithospheric-scale detachment fault. However, such models cannot account for the narrow rift valley and the strong mantle lithosphere thinning observed in East Africa (Dugda et al., 2007, 2009). The latter observations are in better agreement with the Nicolas et al. (1994) model, where rifting occurs via lithospheric rupture and rise of an asthenospheric wedge within the lithospheric mantle. The later model has been further developed by Vauchez et al. (1997) and Tommasi and Vauchez (2001), who, based on the analysis of the influence of inherited structures on the localization of continental breakup, suggested that most major rifts start forming through a transtensional deformation regime produced by the reactivation of the olivine crystallographic fabric frozen in the lithospheric mantle. Numerical models in which the upper mantle has an anisotropic viscosity controlled by the evolution of olivine crystallographic orientations corroborate this assumption (Tommasi et al., 2009). Rheological heterogeneities, both in the crust and in the mantle, also have a major effect on the localization of rifting (e.g., Dunbar and Sawyer, 1989; Nyblade and Brazier, 2002; Vauchez et al., 1997).

In addition to being deformed by an extensional regime, the lithosphere within an active rift is often subjected to extensive magma percolation. Dyke intrusions have been proposed to help initiate extension in a thick continental lithosphere (Buck, 2006). The major role of magmas in rifting has been corroborated by seismic anisotropy data in the Afars, which unambiguously point to aligned melt pockets throughout the crust and lithospheric mantle (Bastow et al. 2010; Kendall et al. 2005). At a smaller scale, the presence of melt may result in weakening of mantle rocks (Hirth and Kohlstedt, 2003; Zimmerman and Kohlstedt, 2004). It may trigger strain localization if melt is heterogeneously distributed (e.g., Le Roux et al., 2008) or promote homogeneous deformation if it is homogeneously distributed through a large volume (Vauchez et al., 2012). Melt- or fluid-rock reaction may also result in

softening through crystallization of weaker phases and/or associated grain size reduction and phase mixing (e.g., Dijkstra et al. 2002; Soustelle et al. 2010).

Mantle xenoliths provide a valuable means by which to study the deformation of mantle lithosphere during rifting. They allow for quantification of the hydration state and characterization of melt-rock reactions and of their timing relative to the deformation. Moreover, the analysis of the microstructures and crystallographic preferred orientations (CPO) bring constraints on the deformation mechanisms and conditions in the lithospheric mantle below active rifts. In the present study, we explore the relations between deformation, melt or fluids percolation, and hydration in a series of mantle xenoliths from four localities in the North Tanzanian Divergence region (East African Rift). This region, still in the early stages of rifting, offers favorable conditions to study the expression of rifting on the lithospheric mantle. In addition, we estimate the seismic anisotropy of these rocks based on their CPO and mineralogical composition and compare these results to seismic anisotropy measurements performed within and around the East African Rift.

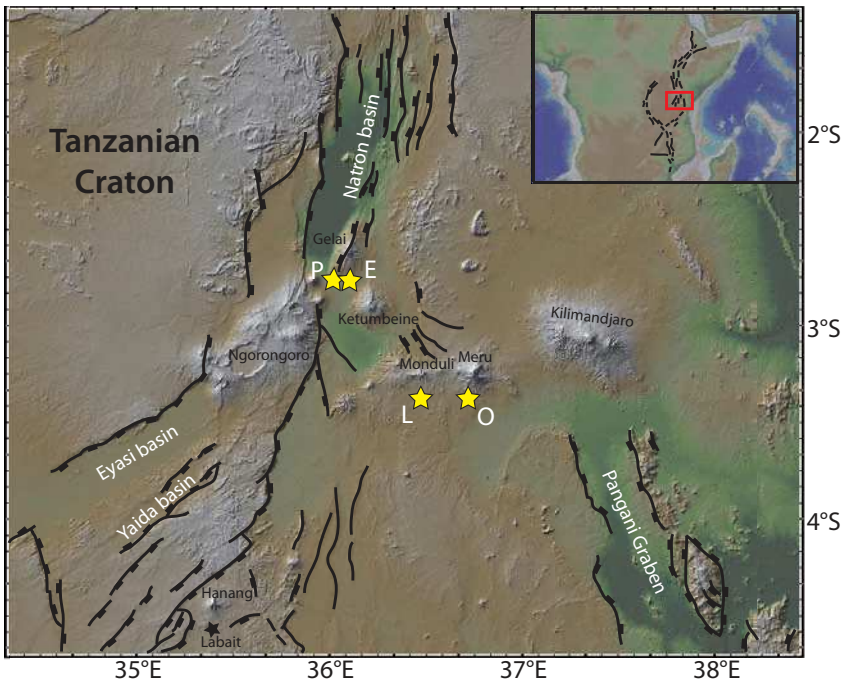

Figure 1: Digital topographic map (http://www.geomapapp.org, topography data from Ryan et al., 2009) showing the North Tanzania Divergence and the location of the xenolith localities studied here (P: Pello Hill, E: Eledoi, L: Lashaine, and O: Olmani), as well as the Tanzania craton and main volcanoes. Major volcanoes are labeled. Labait is another locality containing abundant mantle xenoliths, which microstructures and crystal preferred orientations were studied by Vauchez et al. (2005).

2. Geological setting

The East African Rift is one of the few active continental rifts on Earth. It extends over ~ 4000 km, from the Afar triple junction in the Red Sea to the Gulf of Mozambique (Fig. 1), mostly following the trend of older orogenic belts (Nyblade and Brazier, 2002; Vauchez et al., 1997 and references therein). Rifting and volcanism started 35 Ma ago in Ethiopia and northern Kenya (MacDonald et al., 2001; Morley et al., 1992) in a lithosphere stabilized since the Neoproterozoic. It migrated southwards, reaching southern Kenya 8-5 Ma ago (Cerling and Powers, 1977; Crossley and Knight, 1981). The youngest section of the East African Rift splits into two branches around the Tanzania craton. In the Eastern branch, extension is accompanied by intense magmatic activity concentrated within the rift valley. The region experiences relatively intense present-day seismic activity, with earthquakes mainly located within the rift valley or in its immediate surroundings (e.g., Albaric et al., 2010; Nyblade et al., 1996). A major faulting episode at 1.0 ± 0.2 Ma (MacIntyre et al., 1974) gave rise to the present-day rift valley morphology. In addition, off-axis volcanic activity is observed in the North Tanzanian Divergence, south of which rifting occurs in a more diffuse manner, with deformation accommodated in many branches (Figure 1). Seismic studies show that crustal and lithospheric thicknesses in this young rifting domain vary between 36-44 km and 100-150 km, respectively (Dugda et al., 2009; Julià et al., 2005).

Mantle xenoliths occur in both in- and off-axis volcanoes, providing an exceptional opportunity to study the tectono-thermal evolution of the mantle lithosphere in response to the progression of the East African Rift along the boundary between the Tanzanian craton and the N¬eoproterozoic Mozambique Belt. The present study focuses on 53 mantle xenoliths from four localities from the North Tanzanian Divergence (Fig. 1): two within the rift valley (Pello Hill and Eledoi) and two within the transverse volcanic belt (Lashaine and Olmani). The xenoliths from the cratered tuff cone of Pello Hill and from the Eledoi explosion crater were collected in fine-grained scoria with a bulk-rock chemistry similar to olivine-melilitites and olivine-nephelinites (Dawson and Smith, 1988). The formation of these craters postdates the major rift faulting episode at 1.2 Ma (Dawson and Smith, 1988). The Lashaine tuff cone and the Olmani cinder cone are ankaramite rift-related volcanoes erupted during the Neogene. They are located in a part of the Mozambique Belt characterized by Archean crustal material reworked in the Neoproterozoic by the Mozambique orogeny (Mansur et al., 2014 and references therein; Möller et al., 1998).

Table 1: Texture, equilibrium temperatures, olivine Mg#, modal contents, olivine CPO, olivine J-index, olivine BA index, and calculated density and seismic properties of the studied Tanzanian peridotites.

Locality	Sample	Thin section	Texture	Temperature	Ol mg#	Opx mg#	Reference for mg# and T data	Modal compositions* (%)						Olivine	Olivine	Olivine	Density	Max AVp	Max AVs pol	Max AVS_1	Max AVS_2
								ol	opx	cpx	gt	phl	amph	CPO type	J-index	BA index	($g.cm^{-3}$)	(%)	(%)	(%)	(%)
				(°C)	(%)	(%)															
Eledoi	EL3	EL3	P	1068	92.1	92.5	This study	88	11	1	0	0	0	Axial-[100] to ortho	3.31	0.73	3.3493	9.0	6.1	3.0	5.1
	EL6	EL6	P	-	90.3	-	LCT01	98 (86)	2 (2)	0 (10)	0 (0)	0 (2)	0 (0)	Axial-[100] to ortho	4.63	0.78	3.3401	10.7	7.0	3.5	5.6
	EL8	EL8	P	1063	92.4	93.3	This study	92	6	2	0	0	0	Axial-[100]	3.82	0.78	3.3515	11.4	8.1	3.8	6.2
	EL10	EL10	P	-	92.4	-	LCT01	97	1	2	0	0	0	Ortho	3.15	0.62	3.3540	9.4	5.8	2.8	5.5
	EL11	EL11	P	-	90.8	-	LCT01	92	7	1	0	0	0	Axial-[100]	2.88	0.69	3.3515	8.8	5.6	3.2	4.2
	EL12	EL12	P	1060	91.8	92.5	This study	88	10	2	0	0	0	Axial-[100]	4.34	0.90	3.3495	11.2	7.6	3.4	6.0
	EL14	EL14	CG	-	84.1	-	LCT01	100 (93)	0 (0)	0 (4)	0 (0)	0 (3)	0 (0)	Axial-[100]	4.46	0.87	3.3372	9.4	3.1	3.1	6.0
	EL15	EL15	P	1052	90.1	91.5	This study	85 (61)	15 (11)	0 (23)	0	0 (5)	0	Axial-[100]	3.31	0.74	3.3154	4.1	3.9	3.3	1.8
	EL16	EL16	P	-	92.1	-	LCT01	91	0	9	0	0	0	Axial-[100]	2.14	0.84	3.3525	7.5	4.9	1.6	4.5
Pello Hill	PEL1	PEL1	P	-	88.4	-	LCT01	95	4	1	0	0	0	Ortho	3.38	0.84	3.3528	9.9	6.3	2.9	5.4
	PEL7	PEL7	P	-	92.3	92.9	This study	86	13	1	0	0	0	Ortho	5.38	0.70	3.3484	12.3	8.0	4.1	6.6
	PEL9	PEL9	P	-	93.3	-	LCT01	96 (95)	4 (4)	0 (0)	0 (0)	0 (1)	0 (0)	Axial-[100]	4.77	0.87	3.3475	12.2	8.2	5.0	6.1
		PEL9-bis	P	-	-	-		93	7	0	0	0	0	Axial-[100]	4.71	0.90	3.3516	12.0	7.9	4.3	6.2
	PEL11	PEL11	CG	-	86.7	-	LCT01	100	0	0	0	0	0	Ortho	3.27	0.45	3.3550	4.8	4.9	3.6	2.1
	PEL12	PEL12A	P	-	92.6	-	LCT01	83 (78)	16 (15)	1 (1)	0 (0)	0 (1)	0 (5)	Axial-[100]	3.40	0.86	3.3276	8.7	5.9	2.3	5.0
		PEL12B	P	-	-	-		82 (77)	17 (16)	1 (1)	0 (0)	0 (2)	0 (4)	Axial-[100]	3.16	0.89	3.3244	8.3	5.6	3.0	4.6
	PEL15	PEL15	M	-	92.4	92.9	LCT01	77	21	2	0	0	0	Ortho	3.64	0.61	3.3441	7.4	5.5	3.1	4.2
	PEL16	PEL16	P	-	92.5	93.2	LCT01	90	9	1	0	0	0	Axial-[100] to ortho	6.69	0.82	3.3506	13.5	8.9	5.0	6.6
	PEL17	PEL17	M	-	92.4	92.6	LCT01	87 (86)	12 (12)	1 (1)	0 (0)	0 (0)	0 (1)	Axial-[100]	4.71	0.79	3.3434	9.6	6.5	2.1	6.1
		PEL17A	M	-	-	-		76 (75)	23 (23)	1 (1)	0 (0)	0 (0)	0 (1)	Axial-[100]	3.29	0.84	3.3434	9.6	6.5	2.1	6.1
		PEL17B	M	-	-	-		75 (74)	25 (25)	0 (0)	0 (0)	0 (0)	0 (1)	Axial-[100]	4.23	0.79	3.3428	9.7	6.9	2.7	5.9
	PEL20	PEL20	P	-	92.3	-	LCT01	97	0	3	0	0	0	Ortho	3.79	0.69	3.3542	9.0	7.3	3.8	6.1
	PEL21	PEL21A	P	-	91.3	-	LCT01	100 (84)	0 (0)	0 (8)	0 (0)	0 (0)	0 (8)	Axial-[100]	3.20	0.78	3.3300	10.0	6.5	3.1	5.2
		PEL21B	P	-	-	-		100 (86)	0 (0)	0 (8)	0 (0)	0 (1)	0 (5)	Axial-[100]	3.31	0.81	3.3330	9.4	6.2	3.1	5.1
	PEL22	PEL22A	P	1090	91.5	91.6	This study	96 (90)	4 (4)	0 (5)	0 (0)	0 (0)	0 (1)	Axial-[100] to ortho	4.26	0.70	3.3488	11.0	7.1	4.0	5.3
		PEL22B	P	-	-	-		95 (88)	5 (5)	0 (6)	0 (0)	0 (0)	0 (1)	Axial-[100] to ortho	4.21	0.70	3.3457	10.5	7.0	3.9	5.2
	PEL27	PEL27	P	-	92.3	-	LCT01	95	0	5	0	0	0	Axial-[100] to ortho	3.76	0.79	3.3536	11.8	7.5	3.5	6.5
	PEL33	PEL33	P	1090	92.4	93.1	This study	83	16	1	0	0	0	Axial-[100]	3.79	0.64	3.3469	9.1	6.5	3.8	4.8
	PEL34	PEL34A	P	-	92.4	-	LCT01	86 (85)	12 (12)	2 (2)	0 (0)	0 (0)	0 (1)	Axial-[100]	4.01	0.89	3.3457	10.8	7.2	3.0	6.1
		PEL34B	P	-	-	-		86 (85)	13 (13)	1 (1)	0 (0)	0 (0)	0 (1)	Axial-[100]	4.17	0.91	3.3455	10.6	7.0	2.9	6.1
	PEL38	PEL38	P	-	91.2	-	LCT01	93 (92)	7 (7)	0 (0)	0 (0)	0 (0)	0 (1)	Axial-[100]	4.99	0.83	3.3516	11.3	7.6	3.6	6.3
	PEL39	PEL39	P	-	90.1	-	LCT01	100 (78)	0 (0)	0 (21)	0 (0)	0 (1)	0 (0)	Axial-[100]	3.16	0.90	3.3436	7.8	4.5	2.5	3.4
	PEL40	PEL40A	P	-	91.0	-	LCT01	89 (75)	11 (9)	0 (12)	0 (0)	0 (3)	0 (1)	Ortho	4.55	0.66	3.3277	10.0	7.6	5.0	5.5
		PEL40B	P	-	-	-		88 (76)	12 (10)	0 (12)	0 (0)	0 (1)	0 (1)	Ortho	4.71	0.69	3.3383	10.2	7.1	4.0	5.7
	PEL41	PEL41	CG	-	87.9	-	LCT01	100 (79)	0 (0)	0 (15)	0 (0)	0 (3)	0 (3)	Axial-[100]	3.16	0.79	3.3256	6.4	4.9	1.8	4.4

Table 1 (suite)

Locality	Sample	Thin section	Texture	Temperature	Ol mg#	Opx mg#	Reference for mg# and T data	Modal compositions* (%)						Olivine	Olivine	Olivine	Density	Max AVp	Max AVs pol	Max AVS_1	Max AVS_2
				(°C)	(%)	(%)		ol	opx	cpx	gt	phl	amph	CPO type	J-index	BA index	($g.cm^{-3}$)	(%)	(%)	(%)	(%)
Lashaine	89-664	89-664	VCG	-	-	-	-	93	7	0	0	0	0	Axial-[010] to ortho	5.97	0.67	3.3518	8.0	6.5	2.8	4.9
		89-664A	VCG	1075	90.2	91.0	This study	85	13	2	0	0	0	Axial-[010] to ortho	5.47	0.66	3.3484	5.9	4.5	2.6	3.8
		89-664B	VCG	-	-	-	-	94	5	1	0	0	0	Axial-[010] to ortho	5.42	0.66	3.3523	6.8	5.1	1.7	4.0
	89-680	89-680	CG	1150	93.0		R94	73	24	2	0	1	0	Axial-[010]	1.86	0.40	3.3371	4.1	3.4	2.4	1.8
	L1	L1A	VCG	-	-	-	-	75	15	10	0	0	0	Ortho	21.3**	0.49	3.3449	9.1	6.6	4.1	5.8
		L1B	VCG	-	-	-	-	68	29	3	0	0	0	Ortho	4.27	0.74	3.3399	6.1	4.7	1.1	4.1
	LS4	LS4A	VCG	-	92.4	-	LCT01	78	14	3	5	0	0	Ortho	24.7**	0.46	3.3700	10.0	7.2	4.5	6.3
		LS4B	VCG	-	-	-	-	72	21	2	5	0	0	Ortho	13.7**	0.48	3.3669	3.4	3.7	2.3	2.9
	LS9	LS9B	VCG	1015	92.1	93.0	This study	73 (72)	19 (19)	8 (8)	0 (0)	0 (1)	0 (0)	Axial-[010]	4.57	0.32	3.3379	3.3	3.5	2.2	2.4
	LS11	LS11A	VCG	-	92.3	92.9	This study	82	13	3	2	0	0	Axial-[010] to ortho	11.6**	0.39	3.3569	10.1	6.7	4.3	5.1
		LS11B	VCG	-	-	-	-	71 (70)	24 (24)	2 (2)	3 (3)	0 (1)	0 (0)	Axial-[010] to ortho	10.5**	0.30	3.3563	6.8	6.2	4.7	3.8
	LS15	LS15	G	-	88.2	-	LCT01	100	0	0	0	0	0	Axial-[010]	2.19	0.32	3.3550	8.1	4.9	4.0	2.1
Olmani	03-TZ-14E	03-TZ-14E1	CP	-	-	-	-	68	32	0	0	0	0	Axial-[100] to ortho	6.00	0.80	3.3462	11.2	7.6	3.9	6.0
		03-TZ-14E2	CP	-	-	-	-	89	10	0	0	0	0	Axial-[100] to ortho	7.41	0.67	3.6493	11.4	7.2	3.9	5.9
	03-TZ-14H	03-TZ-14H	P	-	-	-	-	90	9	1	0	0	0	Axial-[100]	5.31	0.86	3.3503	12.4	7.9	3.7	6.7
	03-TZ-14I	03-TZ-14I	CP	-	-	-	-	97	3	0	0	0	0	Axial-[100] to ortho	3.78	0.64	3.3540	11.1	8.2	5.3	5.4
	03-TZ-14J	03-TZ-14J1	CP	-	-	-	-	99	1	0	0	0	0	Axial-[100] to ortho	43.2**	0.66	3.3545	18.4	13.3	8.3	8.5
		03-TZ-14J2	CP	-	-	-	-	100	0	0	0	0	0	Axial-[100] to ortho	44.5**	0.66	3.3550	13.5	9.2	5.0	7.8
	03-TZ-14K	03-TZ-14K	CG	-	87.6	88.8	This study	43	53	4	0	0	0	Axial-[100] to ortho	1.81	0.45	3.3279	3.9	2.6	2.1	1.8
	03-TZ-14L	03-TZ-14L	CG	-	-	-	-	89	10	1	0	0	0	Axial-[100] to ortho	4.57	0.79	3.3498	11.7	7.8	3.8	6.3
	03-TZ-14M	03-TZ-14M1	CP	-	-	-	-	82	18	0	0	0	0	Axial-[100]	5.59	0.79	3.3462	12.5	7.5	3.9	6.3
		03-TZ-14M2	CP	-	-	-	-	84	16	0	0	0	0	Axial-[100]	5.75	0.71	3.3472	12.7	7.4	4.2	6.1
	03-TZ-14N	03-TZ-14N1	VCG	-	-	-	-	100	0	0	0	0	0	Ortho	5.24	0.47	3.3547	10.2	7.7	5.5	4.3
		03-TZ-14N2	VCG	-	-	-	-	100	0	0	0	0	0	Ortho	5.41	0.64	3.3550	10.1	6.5	4.2	4.5
	OL3	OL3A	CG	1066	92.1	92.4	This study	44	53	3	0	0	0	Axial-[100]	1.87	0.88	3.3282	3.7	2.3	0.6	2.2
		OL3B	CG	-	-	-	-	44	53	3	0	0	0	Axial-[100]	1.87	0.88	3.3282	3.7	2.3	0.6	2.1
	OL10	OL10	VCG	-	93.1	-	LCT01	95	5	0	0	0	0	Axial-[100]	5.28	0.92	3.3525	11.6	7.3	3.4	6.2
	OL-NN1	OL-NN1	P	-	-	-	-	98 (97)	2 (2)	0 (0)	0 (0)	0 (1)	0 (0)	Axial-[100]	5.45	0.80	3.3485	13.8	9.8	5.0	7.1
	OL-NN2	OL-NN2	CG	-	-	-	-	98 (97)	0 (0)	2 (2)	0 (0)	0 (1)	0 (0)	Axial-[100] to ortho	4.00	0.59	3.3544	12.0	8.5	4.9	6.0
	OL-NN3	OL-NN3	P	-	-	-	-	97	0	3	0	0	0	Axial-[100] to ortho	8.95	0.72	3.3542	14.5	9.1	5.4	6.8
	89-772	89-772	VCG	950	87.6	-	R94	98	0	2	0	0	0	Axial-[010]	3.11	0.30	3.3544	6.1	3.9	2.7	2.5
	89-773	89-773	VCG	1080	93.6	-	R94	85	15	0	0	0	0	Axial-[100] to ortho	6.51	0.93	3.3471	12.5	7.8	3.8	6.4
	89-774	89-774	VCG	-	93.5	-	R94	100	0	0	0	0	0	Ortho	8.08	0.48	3.3550	10.6	7.5	5.2	4.1
	89-776	89-776	VCG	1120	94.4	-	R94	97	0	3	0	0	0	Axial-[100]	7.85	0.62	3.3544	11.8	8.2	3.8	6.4

* Modal compositions determined from EBSD maps. Values between parentheses give the modal contents including veins.
** Olivine J-index values overestimated because of the small number of grains indexed in very coarse-granular peridotites.
Reference for mg# and T data: R94= Rudnick et al. 1994; LCT01= Lee, 2001
CPO types: ortho= orthorhombic, axial-[100], axial-[010], axial-[100] to orthorhombic, and axial-[010] to orthorhombic crystal-preferred orientations, see main text for details.
J-indexes could not be calculated for samples in which less than 100 grains were measured.
Textures: G= granular; CG= Coarse-granular; VCG= Very coarse-granular; P= Porphyroclastic; CP= Coarse-porphyroclastic; M= Mylonitic

3. Methods

3.1 Pressure and temperature estimates

Major elements composition of olivine, orthopyroxene, clinopyroxene, garnet, and spinel were analyzed in 15 samples using a Cameca SX100 electron microprobe at Microsonde Sud facility, in Montpellier (France). Analytical conditions were a 20 kV accelerating voltage and a 10 nA probe current. Core and rim composition of 3 to 4 grains were measured for each mineral (mineral compositions of the analyzed samples presented in the online Supplementary Material Table 1).

When orthopyroxene and clinopyroxene were both present, the sample equilibrium temperature was calculated using the two pyroxenes Fe-Mg exchange geothermometer from Brey and Köhler (1990), which has an uncertainty of ±50°C. However, many of the samples are clinopyroxene-free harzburgites to dunites. To verify if other thermometers (Brey and Köhler, 1990; Fabriès, 1979; Li et al., 1995; Sachtleben and Seck, 1981; Wells, 1977; Witt-Eickschen and Seck, 1991) could be used to calculate the equilibrium temperatures for the clinopyroxene-free peridotites, the consistency between the temperatures calculated with the two pyroxenes geothermometer of Brey and Köhler (1990) and these thermometers was tested for the clinopyroxene-bearing peridotites. Because the discrepancies between the equilibrium temperatures obtained using different thermometers were large, we choose not to present temperatures calculated for the clinopyroxene-free samples. The equilibrium pressure was estimated in one garnet-bearing harzburgite from Lashaine (LS11) using the orthopyroxene-garnet barometer of Nickel and Green (1985), which has uncertainties of 0.2 GPa.

3.2 Electron-backscattered diffraction (EBSD)

The crystallographic preferred orientation (CPO) of olivine, pyroxenes, pargasite, phlogopite, spinel, and garnet was measured by indexation of electron back-scattered diffraction (EBSD) patterns at the SEM-EBSD facility, Geosciences Montpellier. These patterns are produced by interaction of a vertical incident electron beam and a carefully polished thin section tilted at 70° to the horizontal. Measurements were performed in a JEOL JSM 5600 scanning electron microscope using an acceleration voltage of 17 kV and a working distance of 23 mm. For each sample, maps covering nearly the entire thin section were obtained using steps between 100 and 30 μm, depending on grain size. Indexing rates varied between 60 to 90% depending of the mineral species and degree of fracturing present in the thin section. Phlogopite, when present, was usually poorly indexed. Orthopyroxene was sometimes misindexed as

clinopyroxene. Careful post-acquisition data treatment controlled by comparison between EBSD maps and microscopic observations was performed to reduce inaccurate mineral determination as well as misindexation due to olivine pseudosymmetry. Modal composition, grain sizes, and shape-preferred orientations were also obtained from the EBSD maps.

Crystal-preferred orientation data are displayed in pole figures, presented as lower hemisphere stereographic projections. Data were plotted as one point per grain to prevent over-representation of large grains. When the foliation and lineation could be identified, the orientation of the main crystallographic directions: [100], [010] and [001] for olivine and pyroxenes, was plotted relatively to the principal axes of the deformation ellipsoid X, Y, and Z. Because the foliation and lineation could not be identified in coarse-grained samples, thin sections were cut in random orientations. To make comparison between different samples easier, we rotated the CPO of randomly oriented samples into a common orientation in which the maximum concentration of olivine [100] and [010] axes are parallel to the E–W and the N–S directions of the pole figure, respectively.

To characterize the olivine CPO symmetry we computed the dimensionless BA index (where B and A stand for [010] and [100] axes, respectively, Mainprice et al., 2014) defined as:

$$BAindex = \frac{1}{2}\left(2 - \left(\frac{P010}{G010 + P010}\right) - \left(\frac{G100}{G100 + P100}\right)\right) \quad (1)$$

where P and G are the Point and Girdle fabric indices (Vollmer, 1990) of the olivine principal axes [100] and [010]. These indexes were calculated from the eigenvalues of the normalized orientation matrix, as P=λ1-λ3 and G=2(λ2-λ3) using the MTEX texture analysis Matlab toolbox (Hielscher and Schaeben, 2008; Mainprice et al., 2011). The BA index allows a classification of the olivine CPO symmetry into 3 types: axial-[010] (BA index<0.35), orthorhombic (0.35<BA index<0.65), and axial-[100] (BA index>0.65).

The strength of the fabric was quantified using the dimensionless J-index, which is the volume-averaged integral of squared orientation densities:

$$J = \int f(g)^2 dg \quad (2)$$

where f(g) is the orientation distribution function (ODF) and dg = dφ1dφdφ2 sinφπ2 (Bunge, 1982). φ1, φ, and φ2 are the Euler angles that define the rotations allowing for coincidence between the crystallographic and external reference frames. Olivine CPO in natural peridotites is characterized by J-indexes mostly between 2 and 20, with a peak at 8–10 (Ben Ismaïl and Mainprice, 1998; Tommasi et al., 2000). The J-index for each sample was

calculated based on the mean orientation of each grain using the MTEX texture analysis Matlab toolbox (Hielscher and Schaeben, 2008).

3.3 Seismic properties

Seismic properties of Tanzanian xenoliths were calculated using the CPO of all major phases and their respective modal content estimated from EBSD maps (Mainprice, 1990). For olivine, orthopyroxene, clinopyroxene, garnet, amphibole, and phlogopite single-crystal elastic constant tensors at ambient conditions were used (Abramson et al., 1997; Bezacier et al., 2010; Chai et al., 1997a, Chai et al., 1997b, Collins and Brown, 1998). A Voigt-Reuss-Hill averaging was applied in all calculations. The seismic anisotropy parameters and the elastic constants of all samples are presented in Table 1 and online Supplementary Material 2, respectively.

Average seismic properties were also calculated for Lashaine, Olmani, and rift axis localities by averaging the individual samples elastic constant tensors for each locality. This calculation results in a maximum estimation of the seismic anisotropy for the locality, as it relies on the assumption of a common orientation of the foliation and lineation for all samples.

3.4 Fourier transform infrared spectroscopy (FTIR)

Fifteen double-polished thin sections were prepared for unpolarized FTIR analysis. Before analysis, the sections were immersed in pure acetone for at least 12h to dissolve any intergranular CrystalBond glue. FTIR spectroscopy analyses were performed at the Laboratoire des Colloïdes, Verres, Nanomatériaux at Montpellier University using a Bruker IFS66v coupled with a Bruker HYPERION microscope and mercury-cadmium-telluride (MCT) detector cooled by liquid nitrogen. A Globar light source and a Ge-KBr beam splitter were used to generate unpolarized mid-infrared radiation. A background measurement was performed at the beginning of the analysis of each sample and repeated when necessary. Measurements were made on olivine, orthopyroxene, and garnet crystals using a square aperture 30 to 100 μm wide. No measurement could be made on clinopyroxene crystals, which were too small and too altered. Two hundred scans were accumulated with a resolution of 4 cm^{-1} for each measurement. A baseline correction was applied on each spectrum using the OPUS software. Spectra were then normalized to a sample thickness of 1 cm. The sample thickness was measured using a micrometer with a tolerance of ± 1 μm, and was always near 500 μm (Table 2). Fractures and inclusions were strictly avoided.

Table 2: Mineral OH concentrations derived from FTIR analyses.

Locality	Sample	Temperature (°C)	Ol Mg #	Reference for mg# and T data	Texture	Texture complement	Olivine CPO	Mineral	Section thickness (µm)	Paterson calibration[a]			Olivine - Withers calibration[b]	
										OH concentrations ($H/10^6$ Si)	OH concentrations (ppm wt H_2O)	Average OH concentrations (ppm wt H_2O)	OH concentrations (ppm wt H_2O)	Average OH concentrations (ppm wt H_2O)
Eledoi	EL6	-	90.3	LCT01	Granular	Vein-bearing	Axial-[100] to ortho	ol-4	538	114	7	**9**	13	**15**
								ol-8	538	160	10		18	
								ol-12	538	151	9		17	
								ol-13	538	192	12		21	
								ol-14	538	74	5		8	
	EL15a	1052	90.1	This study	Granular	Vein-bearing	Axial-[100]	ol-1	541	65	4	**8**	7	**14**
								ol-2	541	103	6		11	
								ol-5	541	126	8		14	
								ol-11	541	185	11		20	
								ol-12	541	178	11		20	
								opx-2	541	2204	198	**209**	-	-
								opx-3	541	2507	225		-	
								opx-4	541	1657	149		-	
								opx-5	541	2031	182		-	
								opx-9	541	2121	190		-	
								opx-10	541	3427	308		-	
	EL15b	1052	90.1	This study	Granular	Vein-bearing	Axial-[100]	ol-2	527	70	4	**4**	8	**7**
								ol-3	527	48	3		5	
								ol-4	527	56	3		6	
								ol-5	527	49	3		5	
								ol-7	527	46	3		5	
								ol-10	527	49	3		5	
								ol-11	527	109	7		12	
								opx-1	527	2482	223	**186**	-	-
								opx-3	527	1902	171		-	
								opx-4	527	1862	167		-	
								opx-7	527	2043	183		-	
Pello Hill	PEL7	-	92.3	LCT01	Porphyroclastic	-	Ortho	ol-5	528	99	6	**6**	11	**11**
								ol-8	528	78	5		9	
								ol-9	528	160	10		18	
								ol-10	528	43	3		5	
								opx-2	528	1538	138	**133**	-	-
								opx-3	528	1419	127		-	
	PEL15	-	92.4	LCT01	Mylonitic	-	Ortho	ol-2	496	77	5	**3**	8	**5**
								ol-5	496	28	2		3	
								ol-8	496	32	2		4	
								opx-1	496	1727	155	**212**	-	-
								opx-2	496	2764	248		-	
								opx-3	496	1930	173		-	
								opx-4	496	2488	223		-	
								opx-5	496	2561	230		-	
								opx-6	496	2789	250		-	
								opx-7	496	2416	217		-	
								opx-8	496	2233	201		-	
								opx-10	496	2313	208		-	

Table 2 (suite)

Locality	Sample	Temperature (°C)	Ol Mg #	Reference for mg# and T data	Texture	Texture complement	Olivine CPO	Mineral	Section thickness (µm)	Paterson calibration[a]			Olivine - Withers calibration[b]	
										OH concentrations ($H/10^6$ Si)	OH concentrations (ppm wt H_2O)	Average OH concentrations (ppm wt H_2O)	OH concentrations (ppm wt H_2O)	Average OH concentrations (ppm wt H_2O)
	PEL16	-	92.5	This study	Porphyroclastic	-	Axial-[100] to ortho	ol-2	506	46	3	**4**	5	**7**
								ol-4	506	59	4		6	
								ol-5	506	51	3		6	
								ol-7	506	78	5		9	
								ol-8	506	91	6		10	
	PEL17	-	92.4	This study	Mylonitic	-	Axial-[100]	ol-2	543	24	1	**2**	3	**4**
								ol-3	543	49	2		5	
								opx-1	543	1053	65	**97**	-	-
								opx-2	543	1632	100		-	
								opx-4	543	2739	168		-	
								opx-6	543	1268	78		-	
								opx-7	543	1231	75		-	
	PEL34	-	-	LCT01	Porphyroclastic	-	Axial-[100]	ol-1	537	46	3	**3**	-	-
								ol-2	537	33	2		-	
								ol-3	537	63	4		-	
								ol-5	537	36	2		-	
								ol-6	537	48	3		-	
								ol-7	537	50	3		-	
								ol-8	537	42	3		-	
								ol-9	537	57	4		-	
	PEL39	-	90.1	LCT01	Granular	-	Axial-[100]	ol-5	476	28	2	**3**	3	**5**
								ol-6	476	46	3		5	
								ol-9	476	49	3		5	
								ol-10	476	67	4		7	
	PEL40	-	91.0	LCT01	Porphyroclastic	vein-bearing	Ortho	ol-1	567	52	3	**5**	6	**10**
								ol-2	567	131	8		14	
								ol-4	567	79	5		9	
	PEL41	-	87.9	LCT01	Coarse-granular	vein-bearing	Axial-[100]	ol-1	499	216	13	**12**	24	**21**
								ol-2	499	259	16		29	
								ol-3	499	288	18		32	
								ol-4	521	171	10		19	
								ol-5	521	182	11		20	
								ol-6	521	158	10		17	
								ol-7	499	239	15		26	
								ol-9	499	45	3		5	
								ol-10	521	179	11		20	
Olmani	89-772	950	87.6	R94	Very coarse-granular	-	Axial-[010]	ol-2	528	86	5	**5**	9	**10**
	OL10	-	93.1	LCT01	Very coarse-granular	-	Axial-[100]	ol-1	564	50	3	**3**	6	**6**
								ol-2	564	75	5		8	
								ol-3	564	50	3		6	
								ol-4	564	51	3		6	
								ol-8	564	43	3		5	
	03TZ14J	-	-	-	Coarse porphyroclastic	-	Axial-[100] to ortho	ol-1	500	85	5	**4**	9	-
								ol-2	500	75	5		8	
								ol-3	500	72	4		-	
								ol-5	500	57	3		-	
								ol-6	500	85	5		-	
Lashaine	LS11	-	92.3	This study	Very coarse-granular	-	Axial-[010] to ortho	ol-1	491	203	12	**12**	22	**21**
								ol-2	491	215	13		24	
								ol-3	491	204	13		22	
								ol-4	491	196	12		22	
								ol-5	491	154	9		17	
								opx-2	491	1133	98	**121**	-	-
								opx-3	491	1648	143		-	

[a] OH concentrations from this study calculated using the calibration of Paterson (1982) have ±30% error (Kohlstedt et al., 1996); [b] OH concentrations corrected by a factor of 1.8 according to Withers et al. (2012).
Reference for mg# and T data: R94= Rudnick et al., 1994; LCT01= Lee, 2001.

CPO types: Ortho= orthorhombic, axial-[100], axial-[010], axial-[100] to orthorhombic, and axial-[010] to orthorhombic crystal-preferred orientations, see text for details.

The calibration of Paterson (1982) was used to quantify the OH concentration:

$$C_{OH} = \frac{X_i}{150\zeta}\int \frac{k(\bar{v})}{(3780-\bar{v})}d\bar{v} \quad (3)$$

where C_{OH} is the hydroxyl concentration (in mol H/l), ζ is an orientation factor (1/3 for unpolarized measurements), and $k(\bar{v})$ is the absorption coefficient in cm^{-1} for a given wavenumber $\bar{v}$. X_i is a density factor, which depends on the mineral phase ($X_{i(ol,\ Fo90)}$ = 2695 wt. ppm H_2O, $X_{i(orthopyroxene)}$ = 2812 wt. ppm H_2O). The uncertainty in the resulting OH concentrations are ~30% (Kohlstedt et al., 1996).

We also converted the olivine OH concentrations (See Table 2) obtained using the calibration of Paterson (1982) to the new calibration of Withers et al. (2012). The conversion factor between the two calibrations is a function of the sample thickness and of the OH concentration obtained with the calibration of Paterson (1982). Here, the sample thickness is comprised between 476 and 567 μm and the olivine OH concentrations range between 1 and 18 wt. ppm H_2O. Therefore, the olivine OH concentrations must be multiplied by a factor of 1.8 (see Withers et al., 2012, Supplementary material Figure 1).

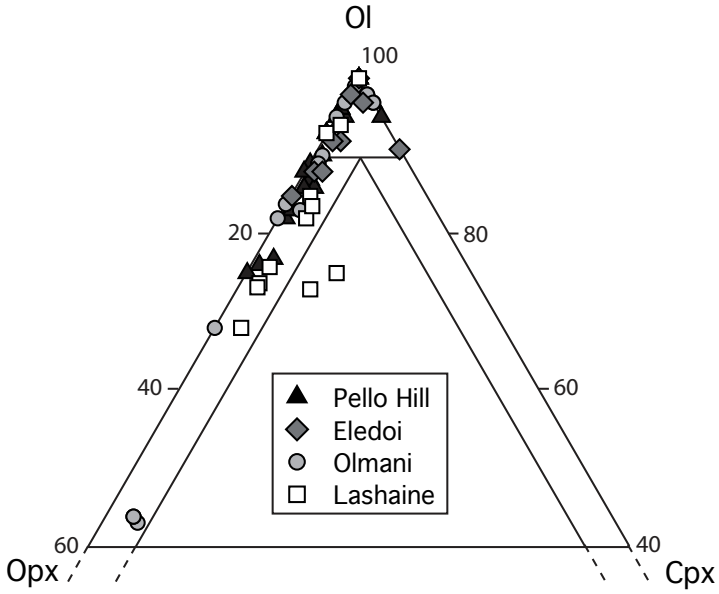

Figure 2: Olivine-orthopyroxene-clinopyroxene modal ratios in the studied peridotites studied here. Modal compositions are derived from EBSD maps, not considering metasomatic veins and pockets, and recalculated for a total of 100% of olivine+orthopyroxene+clinopyroxene.

4. Results

4.1 Compositions and equilibrium conditions

All samples are garnet-free peridotites, except for four Lashaine peridotites (LS11, LS4, L1, and 89-680). Most samples have harzburgitic to dunitic compositions (Fig. 2 and Table 1). Orthopyroxene contents vary mainly between 0 and 20%, but several samples from Lashaine, Olmani and Pello Hill display higher modal orthopyroxene contents (22 to 32%) and two samples from Olmani have >50% orthopyroxene (OL3 and 03TZ14K). Secondary minerals present in diffuse veins or pockets include clinopyroxene, amphibole, phlogopite, and spinel. Veins may comprise up to 15% of the total rock (modal contents including the veins are given in parentheses in Table 1).

Mineral compositions are presented in the online Supplementary Material Table 1. In most samples, olivine has a high Mg# (Mg#: atomic Mg/(Fe+Mg)), which varies between 90.1 and 94.4 (Table 1). Seven samples (out of the forty-one for which the olivine Mg# has been measured) have more Fe-rich olivines (Fo ≤ 89). Among these samples, 4 are very-coarse granular dunites from Olmani or from the rift axis localities (EL14, PEL11, PEL41, 89-772). The 3 other Fe-rich samples are: a harzburgite from Olmani with high orthopyroxene contents (>50%; 03TZ14K), a granular dunite from Lashaine (LS15), and a porphyroclastic harzburgite from Pello Hill (PEL1). There is no significant difference between olivine Mg# for samples from the in-axis and off-axis localities. Olivine always has NiO > 0.25 wt.% and low CaO (≤ 0.11 wt.%). Orthopyroxenes are enstatite, with Mg# > 90. Clinopyroxenes are Cr-bearing diopside (Cr_2O_3 comprised between 1.0 and 3.7 wt.%) with Mg# > 90, except for sample EL15 where Cr_2O_3 < 0.1 wt.% and lower Mg# are measured. Spinels have high MgO (10-17 wt%) and variable Cr# (atomic Cr/(Cr+Al)), ranging between 36 and 89.

We have been able to estimate equilibrium temperatures for only 9 of the 15 samples analyzed, because the others lacked clinopyroxene. Independently of their provenance or microstructure, all these samples have core equilibrium temperatures (calculated from core compositions in orthopyroxene and clinopyroxene) between 1000 and 1100°C ±50°C (Table 1). Rim equilibrium temperatures (calculated from rim compositions in orthopyroxene and clinopyroxene) tend to be slightly, but systematically lower (by 5-21°C), except for sample PEL22 from Pello Hill, where rim equilibrium temperature is lower than core equilibrium temperature by >100°C (960°C versus 1090°C). In a garnet harzburgite from Lashaine (LS11), rim and core equilibrium pressures of 3.3 GPa and 3.1 GPa were obtained, respectively.

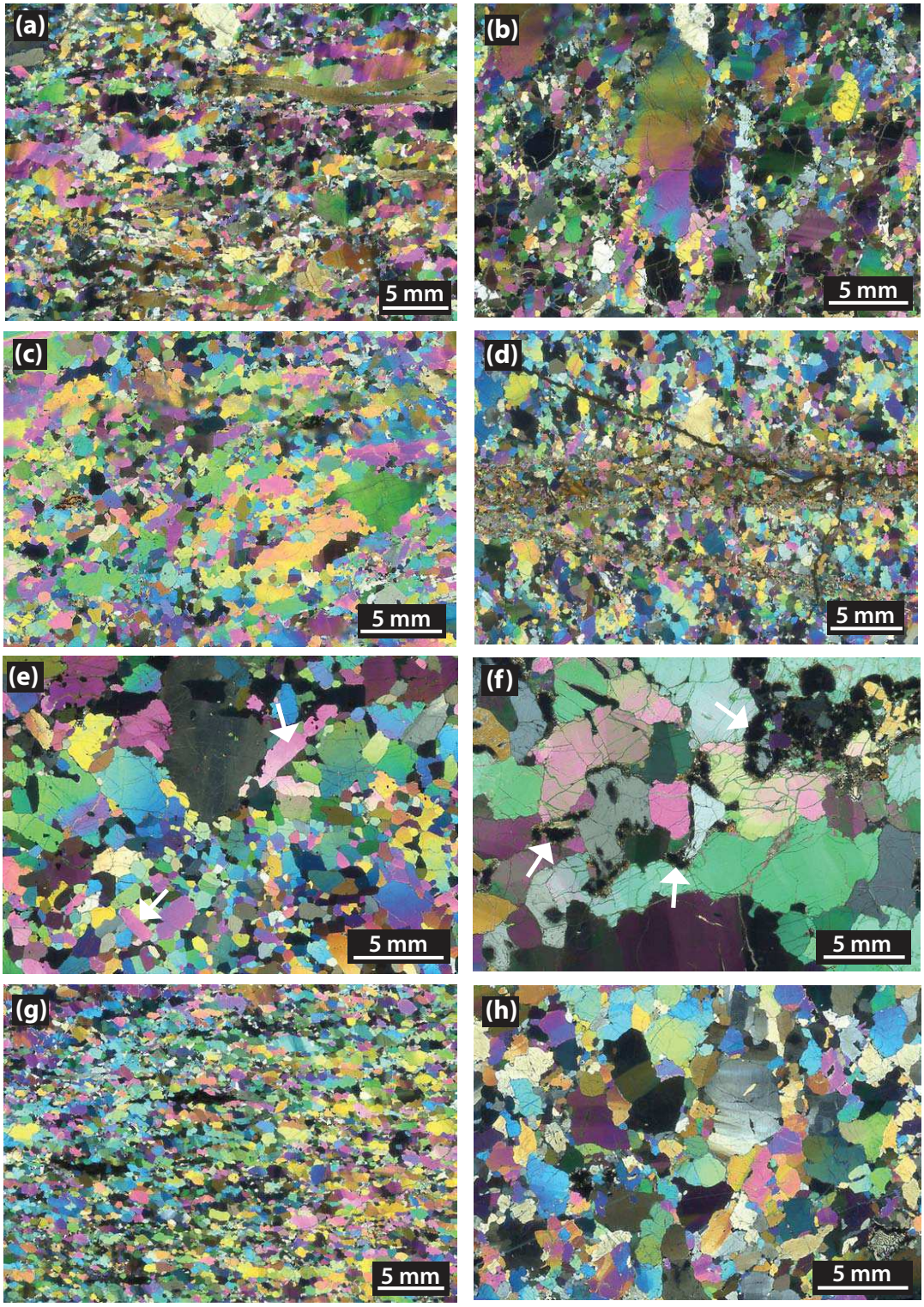

Figure 3: Photomicrographs in cross-polarized light showing typical microstructures for the studied xenoliths. (a) Mylonite PEL17B, showing highly elongated orthopyroxenes and olivines, with strong intracrystalline deformation (undulose extinction, subgrains, kinks) surrounded by a finer-grained matrix composed mainly of olivine. (b) Porphyroclastic peridotite PEL7, with large olivine porphyroclasts displaying closely-spaced subgrain boundaries, surrounded by small polygonal olivine neoblasts. (c) Porphyroclastic peridotite PEL1, showing large olivine porphyroclasts with widely-spaced subgrains and polygonal neoblasts devoid of

substructure. (d) Porphyroclastic peridotite EL15, displaying olivine grains with well-defined subgrain boundaries, as well as diffuse metasomatic veins that crosscut the foliation. (e) Coarse-granular dunite PEL11 showing large olivine grains with rare subgrains, frequent polygonal grain boundaries and triple junctions and, locally, subautomorphic olivine crystals devoid of any substructure (marked by arrows). (f) Very coarse-grained peridotite LS4A from Lashaine, showing large olivine grains with curvilinear boundaries and widely spaced subgrain boundaries and orthopyroxenes rimmed by garnet (arrows). (g) Porphyroclastic peridotite OL-NN4 from Olmani showing elongated olivine porphyroclasts with well-defined subgrain boundaries. (h) Very coarse-grained harzburgite 89-773 from Olmani, showing large olivines with curvilinear boundaries.

4.2 Microstructures

Because of their very different characteristics, the xenoliths microstructures will be described as a function of their provenance: the rift axis (Pello Hill and Eledoi) or the transverse volcanic belt (Lashaine and Olmani).

4.2.1 Rift axis samples

The xenoliths from volcanic localities within the rift axis display variable microstructures. Among the 27 studied xenoliths, 2 are mylonitic, 22 are porphyroclastic, and 3 are coarse-granular to tabular.

Mylonitic microstructures are only observed in 2 samples from Pello Hill (PEL15 and PEL17; Fig. 3a). These rocks are characterized by centimeter-sized orthopyroxenes, which are highly elongated (aspect ratios of up to 15:1), defining the lineation. These orthopyroxenes always display well-defined kink bands and undulose extinctions. They have indented grain boundaries, with olivine grains filling the embayments or even forming vein-like inclusions parallel to the orthopyroxene elongation (Fig. 4a). Exsolution in orthopyroxene is ubiquitous. Olivine is present as plurimillimetric porphyroclasts and as recrystallized grains with sizes ranging from 0.4 to 2 mm. It displays curvilinear boundaries, evolving sometimes to polygonal shapes. Subgrain boundaries in olivine are highly oblique to perpendicular to the grains elongation. The frequency and extent of deformation features in the porphyroclasts vary, however, between the 2 samples. In mylonite PEL17, subgrain boundaries are well developed and closely spaced. In mylonite PEL15, there are fewer subgrain boundaries. In both mylonites, the olivine neoblasts exhibit few subgrain boundaries and sometimes form 120° triple junctions.

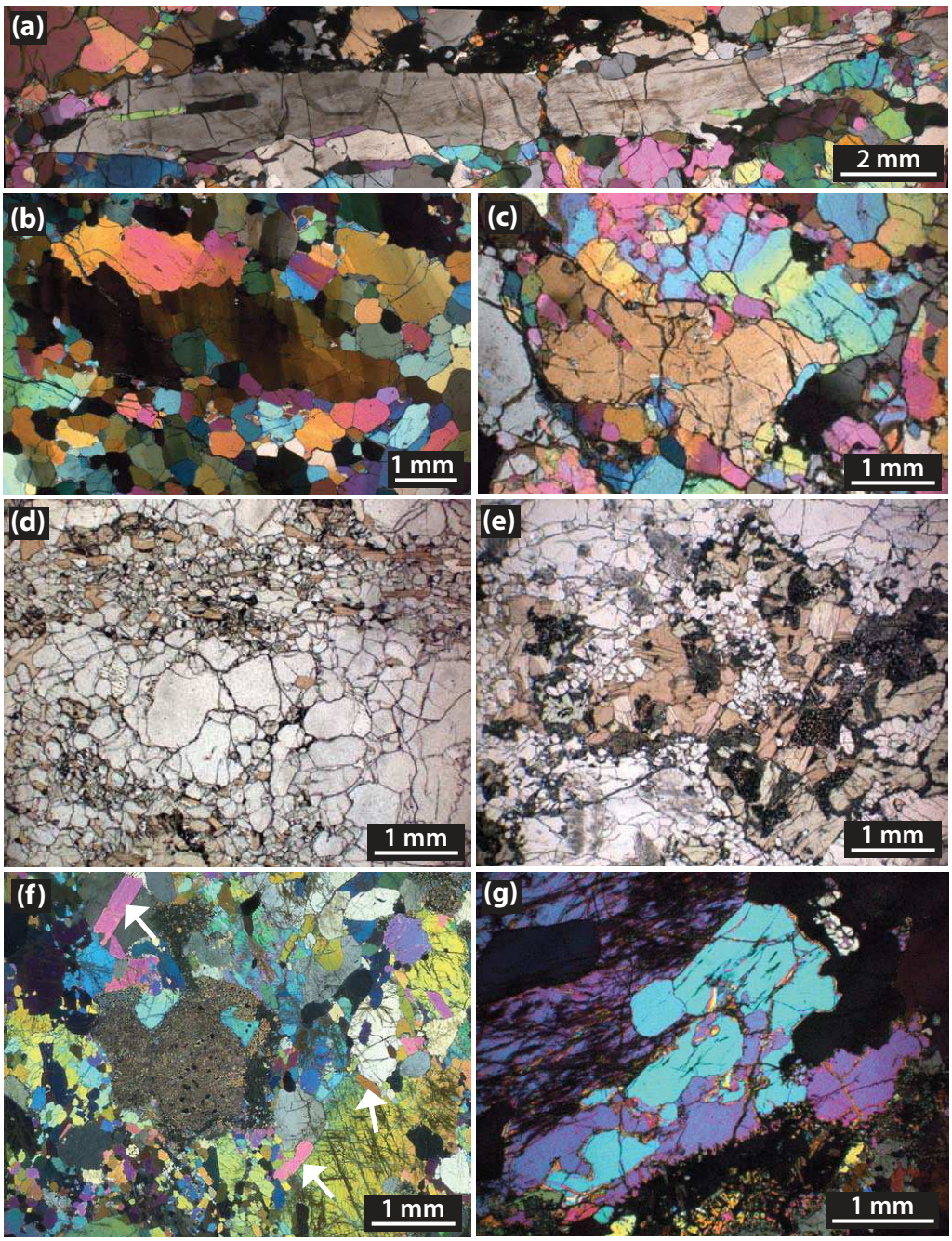

Figure 4: Photomicrographs in cross-polarized (a, b, c, f, and g) and plane-polarized light (d and e) of: (a) Highly elongated orthopyroxene in mylonite PEL15 from Pello Hill displaying embayments filled with olivine in crystalline continuity with the surrounding grains, as well as olivine inclusions elongated parallel to the orthopyroxene elongation and displaying subgrains. (b) Elongated olivine porphyroclasts with closely-spaced subgrain boundaries in peridotite PEL1 from Pello Hill. Small neoblasts forming triple junctions are also visible. (c) Orthopyroxene displaying inclusions and embayments filled with olivine in peridotite PEL7 from Pello Hill. (d) Diffuse veins composed of clinopyroxene, phlogopite, amphibole, spinel, and olivine in peridotite PEL39 from Pello Hill. The same phases are also present as interstitial grains between the veins. (e) Phlogopite, amphibole, clinopyroxene, and spinel "pockets" in peridotite PEL12 from Pello Hill. Note the smaller grain size and more polygonal shapes of olivine within these metasomatic pockets and veins. (f) Peridotite LS9 from Lashaine, characterized by coexistence of large olivine grains and of "recrystallized" zones composed of small

olivine neoblasts with polygonal shapes. Olivine tablets (arrows) growing on other grains are also visible. (g) Interpenetrating olivine-olivine grain boundaries, indicating active grain boundary migration in peridotite LS9 from Lashaine.

The *porphyroclastic peridotites* (Fig. 3b, c) are the most common textural type at Pello Hill; though less common, they are also present at Eledoi. They display plurimillimetric elongated olivine porphyroclasts (Fig. 3b), with common subgrain boundaries, undulose extinction, and sutured grain boundaries. Subgrain boundaries in olivine are dominantly at high angle to the foliation, but in many grains 2 orthogonal subgrain boundary families are observed (Fig. 4b). Small olivine neoblasts have fewer intracrystalline deformation features and tend to have more polygonal shapes, sometimes forming triple junctions. The frequency of the triple junctions in the recrystallized matrix and the subgrain boundaries spacing in porphyroclasts varies from sample to sample. For example, in sample PEL7, olivine porphyroclasts exhibit closely spaced subgrain boundaries and serrated grain boundaries (Fig. 4b), whereas olivine porphyroclasts in sample PEL1 display fewer subgrain boundaries and have polygonal grain boundaries (Fig. 3c). In the porphyroclastic peridotites from Eledoi, olivine porphyroclasts are rare, giving to the rock a more homogeneous microstructure. Interpenetrating olivine-olivine grain boundaries are common (Figs. 3b,c), suggesting grain boundary migration. In both sites, when present, orthopyroxene is anhedral, with intracrystalline deformation features, such as kink bands and undulose extinction. Exsolutions and corrosion embayments filled with olivine are common (Figs. 3b and 4c).

All *coarse-granular* to *tabular peridotites* are dunites (Fig. 3d,e). They exhibit coarse olivine grains (1-8 mm) with equant to tabular shapes. Olivine has curvilinear to polygonal boundaries and is often devoid of any substructure. 120° triple junctions are common. Six coarse-granular to tabular dunites (EL6, EL14, EL15, PEL39, PEL40 and PEL41) are crosscut by diffuse veins composed of millimeter-sized clinopyroxene, phlogopite, amphibole and spinel (Fig. 3d, 4d). Intracrystalline deformation features are very rarely observed in phlogopite and amphibole grains. The orthopyroxene crystals in contact with the vein are partially replaced by diopside.

In the porphyroclastic and mylonitic samples, the distribution of metasomatic minerals (phlogopite, amphibole, clinopyroxene, and spinel) is usually more diffuse. They form irregular pockets (Fig. 4e) or occur as small interstitial grains dispersed in the rock. When these minerals are dispersed in the rock, they may display subgrain boundaries. They are

usually associated with fine-grained olivines, forming “bands” with smaller grain sizes. In the pockets, spinel grows on clinopyroxene, pargasite or phlogopite (Fig. 4e).

4.2.2 Xenoliths from the transverse volcanic belt

The xenoliths from the two localities (Olmani and Lashaine) within the divergence exhibit different microstructures. We will thus describe them separately.

4.2.2.1 Lashaine

The xenoliths from Lashaine show mainly very coarse granular microstructures (Fig. 3f). Olivine grain size ranges from few millimeters to more than a centimeter. They have curvilinear boundaries and widely spaced subgrain boundaries. Interpenetrating grain boundaries are common. Orthopyroxene is usually smaller (1-8 mm) than olivine, with rare kink bands or undulose extinction. Exsolution in orthopyroxene is only observed in sample LS4. Lashaine is the only location where garnet peridotites (samples LS4, LS11, 89-680, and L1) were sampled. Garnet is present as irregularly-shaped crystals, several mm long, most often rimming orthopyroxene (marked by arrows in Fig. 3f). Kelyphitic rims are always present. In sample L1, garnet has been entirely replaced by kelyphite. Clinopyroxene is present as exsolutions in orthopyroxene or as very small interstitial crystals associated with pargasite and spinel. Olivine with interpenetrating boundaries is commonly observed (Figs. 3f and 4g), as well as orthopyroxene embayments filled with olivine. Peridotite LS9 displays slightly different characteristics: it contains recrystallized zones with finer-grained olivine showing curvilinear to polygonal boundaries (Fig. 4f). Olivine tablets free of any substructure form on other olivine crystals (Fig. 4f). Orthopyroxene often contains olivine inclusions.

Two samples have granular microstructures but smaller grain sizes: the coarse-granular harzburgite 89-680 and the granular dunite LS15. In harzburgite 89-680, olivine grain size ranges mainly between 1 and 4 mm. Olivine displays curvilinear to polygonal boundaries, and few subgrain boundaries. Orthopyroxene grain size varies between 0.5 and 2 mm. It has irregular shapes with curvilinear boundaries and may contain kink bands. Small interstitial clinopyroxene, phlogopite and amphibole grains are present. Dunite LS15 displays even smaller olivine grain sizes, ranging between 0.5 and 2 mm. Olivine has curvilinear, sometimes interpenetrating grain boundaries and a higher proportion of subgrain boundaries than the other samples from Lashaine.

4.2.2.2 Olmani

The peridotites from Olmani display microstructures intermediate between those described for peridotites from the rift-axis localities and from Lashaine. Among the 18 studied xenoliths, 5 are porphyroclastic, 4 are coarse-porphyroclastic, 4 are coarse-granular, and 5 are very coarse -granular.

The *porphyroclastic harzburgites* display elongated olivine porphyroclasts with millimetric grain sizes (Fig. 3g), which mark the foliation, and small olivine neoblasts (0.2-1 mm) with curvilinear to polygonal boundaries. The frequency of subgrain boundaries and the degree of polygonization of the grain boundaries vary from sample to sample. For instance, sample 03TZ14H shows interpenetrating olivine-olivine grain boundaries, whereas polygonal olivine grains characterize sample OL-NN4. Orthopyroxene occurs as small (<1mm), interstitial crystals displaying rare kink bands.

In *coarse-porphyroclastic harzburgites*, olivine grains are millimetric to centimetric and elongated. They commonly display closely spaced subgrain boundaries and interpenetrating grain boundaries. Small olivine grains rim the porphyroclasts. These neoblasts display curvilinear to polygonal grain boundaries. Orthopyroxene usually display irregular shapes, rare kink bands, and undulose extinction, as well as common exsolutions and corrosion embayments filled with olivine. Olivine crystals included in orthopyroxene grains are sometimes observed. In sample 03TZ14M, spinel-pyroxene symplectites are observed.

In *coarse-granular harzburgites*, olivine and orthopyroxene grain size varies between 0.5 and 3 mm. Two of these samples (OL3 and 03TZ14K) display very high orthopyroxene content (>50%). Olivine is characterized by curvilinear to polygonal boundaries and common subgrain boundaries. In 2 samples (03TZ14K and 03TZ14L), olivine is occasionally included in orthopyroxene. Orthopyroxene grains are anhedral. They display well-defined kink bands and undulose extinction, as well as exsolutions. In several orthopyroxene grains, corrosion embayments filled with olivine are present.

The *very coarse-granular peridotites* from Olmani are similar to the samples from Lashaine (Fig. 3h). They display millimetric to centimetric olivine grains. The density of subgrain boundaries and their spacing vary considerably from one sample to another. Interpenetrating olivine grain boundaries are always observed. Orthopyroxene is present in only 1 of these samples (89-773). In this sample, orthopyroxene has millimeter grain sizes, curvilinear boundaries, and displays well-defined kink bands.

4.3 Crystallographic preferred orientations (CPO)

As for the microstructures, we describe separately the CPOs of peridotites from the rift axis, Lashaine, and Olmani

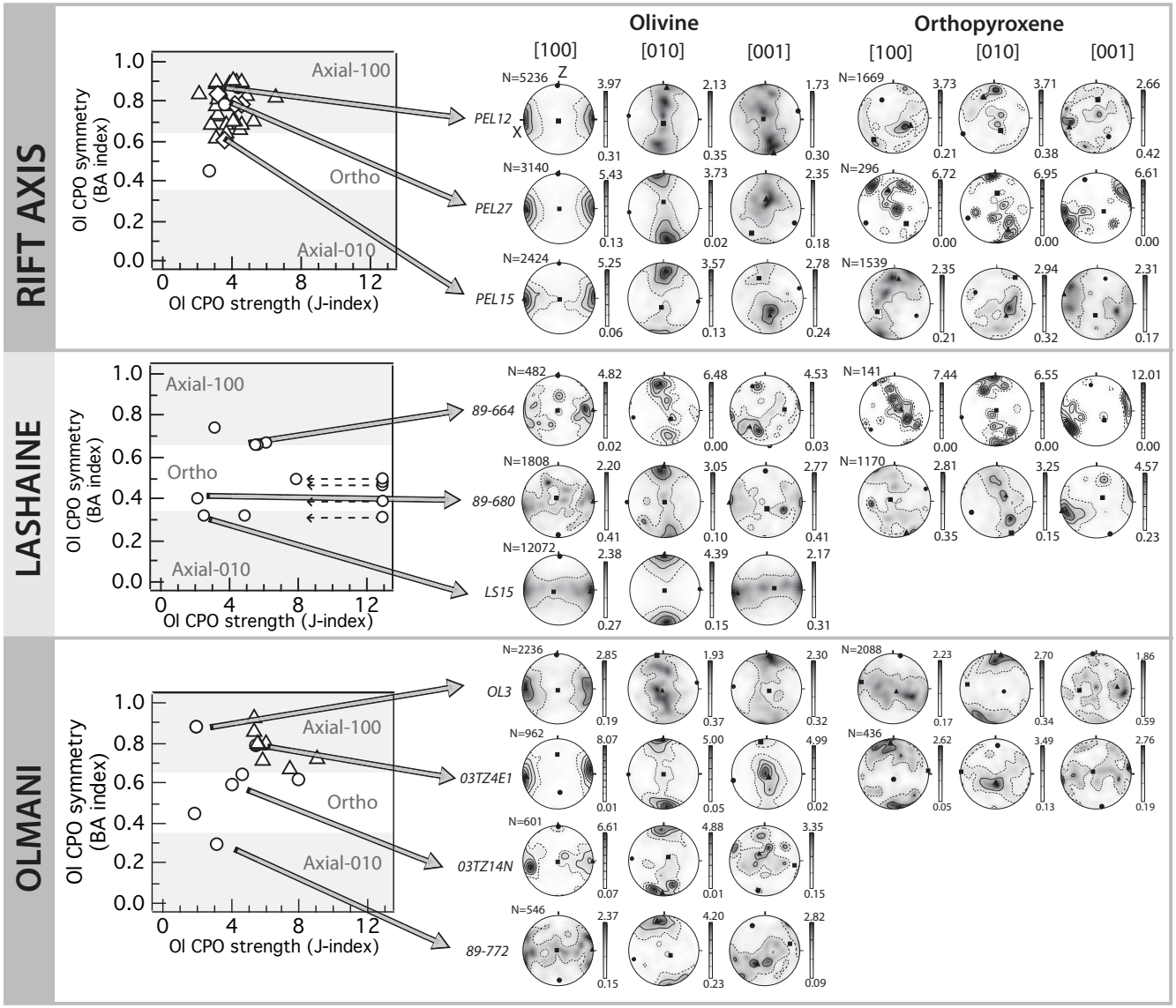

Figure 5: Olivine and orthopyroxene crystal preferred orientations (CPO): Olivine CPO strength (J-index) vs. symmetry (BA index) for all samples (granular, porphyroclastic and mylonitic microstructures symbolized by circles, squares, and diamonds, respectively) and pole figures of selected representative samples from the rift axis, Lashaine, and Olmani localities. Contours at 1 multiple of a uniform distribution. Dashed arrows indicate the samples in Lashaine where olivine J-index is overestimated because of the small number of indexed grains in coarse-grained peridotites.

4.3.1 Rift axis

Most rift-axis samples have low olivine CPO strength, with J-indexes varying mainly between 2-6 (Fig. 5). There is no correlation between the olivine CPO symmetry, its strength, and the microstructure. Peridotites from Pello Hill and Eledoi exhibit olivine CPO symmetries ranging from axial-[100] to orthorhombic (Fig. 5). Axial-[100] symmetry predominates. These patterns are characterized by a point concentration of [100], which in the mylonites and porphyroclastic peridotites is close to the lineation, and a girdle distribution of [010] and [001] normal to it. One sample has a clear orthorhombic olivine CPO, exhibiting a point concentration of the 3 crystallographic axes, with [100] showing the strongest concentration subparallel to the lineation. [010] is usually more concentrated than [001] and tends to align normal to the foliation. Most samples, like PEL27, display an intermediate pattern characterized by weak girdles of [010] and [001] normal to the maximum concentration of [100], with a concentration of [010] normal to the foliation plane and a concentration of [001] in the foliation plane parallel to the Y structural axis.

When present, orthopyroxene has more dispersed CPO, but correlated to the olivine CPO: the maximum concentration of [001] of orthopyroxene is parallel or slightly oblique to the olivine [100] maximum, except for one sample (PEL22). Orthorhombic CPO predominates, with [001] showing the strongest point concentration, which, in the mylonites and porphyroclastic peridotites, is subparallel to the lineation. In most samples, [100] axes are aligned normal to the foliation, but in some samples [010] is preferentially oriented perpendicular to the foliation.

Clinopyroxene crystals in the veins or as interstitial grains display a weak orthorhombic CPO pattern, with [001] axes showing the strongest point concentration, which is usually subparallel to the orthopyroxene [001] maximum and to the olivine [100] maximum. The clinopyroxene CPO is thus coherent with those of olivine and orthopyroxene. In 12 samples, [100] axes are perpendicular to the foliation plane. In 6 other samples, [010] tends to be preferentially oriented normal to the foliation.

4.3.2 Transverse volcanic belt

4.3.2.1 Lashaine

Olivine CPO strength of Lashaine samples is more variable than for the rift axis peridotites. J-index ranges between 2 and 8 for those samples where more than 100 grains could be measured (Fig. 5). However, in some very-coarse grained peridotites, the number of measured grains was <100, leading to a possible overestimation of the J-index (Ben Ismail and Mainprice, 1997). These values are marked by dashed arrows in Fig. 5. Olivine CPO in

Lashaine peridotites varies from axial-[100] to axial-[010] patterns, with a predominance of orthorhombic patterns (BA indexes vary between 0.3 and 0.74, Fig. 5). Three samples (LS9, LS15, and 89-680) display axial-[010] CPO, characterized by a point concentration of [010] and a girdle distribution of [100] and [001] normal to it. Two samples (L1A and L1B, LS4A and LS4B) display orthorhombic CPO. In 2 other samples (89-664 and LS11), CPOs with a pattern intermediate between orthorhombic and axial-[100] are observed. In these rocks, the CPO is generally weak, but a point concentration of [100] and incomplete girdles of [010] axes are observed.

Orthopyroxene CPOs are more dispersed than olivine CPOs. They are characterized by a weak point concentration of [001] axes parallel to [100] of olivine. In most samples, [100] are parallel to [010] of olivine.

4.3.2.2 Olmani

The peridotites from Olmani display olivine CPO with variable strength (J-indexes vary between 2 and 9; Fig. 5). They show mainly axial-[100] to orthorhombic olivine CPO patterns (Fig. 5). Porphyroclastic samples tend to exhibit axial-[100] patterns, that is, higher olivine BA indexes, as well as higher J-indexes than granular samples. A single coarse-granular sample (89-772) is characterized by axial-[010] pattern.

When present, orthopyroxene has a CPO correlated to the olivine one. ¬¬In three samples, weak axial-[010] patterns can be observed (see Figure 5, sample OL3). They are characterized by a girdle distribution of [100] and [001] in the foliation plane and point concentration of [010] normal to it. The other samples display weak orthorhombic CPO symmetry (Figure 5, sample 03TZ14E1).

4.4 Seismic properties

Average anisotropic seismic properties for rift-axis and off-axis samples are illustrated in Fig. 6. To a first order, all localities share common seismological characteristics. The P-waves propagation is fastest close to the olivine [100] maximum, which corresponds to the lineation in the samples where it has been identified, and slowest close to [010] maxima, then normal to the foliation. The slowest propagation directions of the slow S-wave (S2) are in the YZ structural plane. The fast split shear wave (S1) is polarized in a plane containing the main concentration of olivine [100] and the propagation direction. The highest Vp/Vs1 ratio is also parallel to the preferred orientation of olivine [100] and the lowest Vp/Vs1 is observed for waves propagating normal to this direction.

Changes in olivine CPO symmetry result in second order variations of the seismic anisotropy pattern. Within the rift axis and at Olmani, where axial-[100] and orthorhombic olivine CPOs predominate, P-waves velocities are slow and S-waves azimuthal anisotropy is high within the YZ plane. The fastest velocities of S2-waves are observed for directions close to the lineation. The slowest propagation of the S1-wave occurs for directions either close or normal to the lineation, while the fastest S1 propagation are expected for directions at 45° to the lineation.

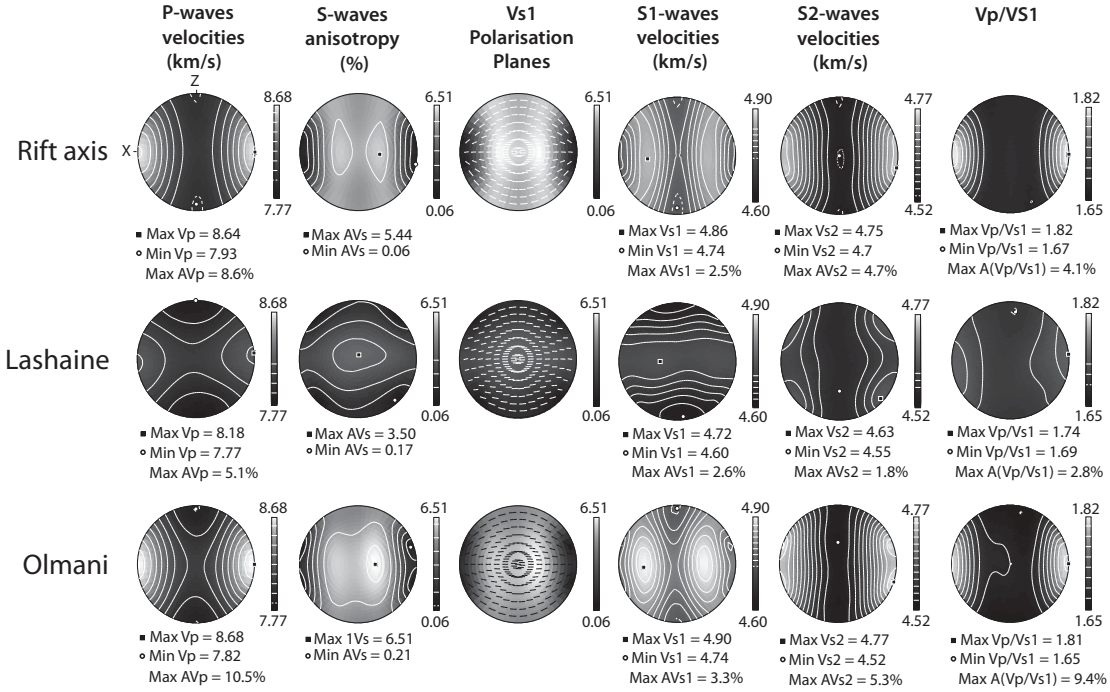

Figure 6: Calculated seismic properties of average samples for the rift axis, Lashaine, and Olmani localities. From left to right are displayed the 3-D distributions of P-wave velocities (V_p), S-wave polarization anisotropy (AV_s) and the orientation of fast shear wave polarization plane, S_1 wave velocities (VS_1), S_2 wave velocities, and Vp/VS_1 ratio. Black squares and white spots indicate maximum and minimum values, respectively.

At Lashaine, where axial-[010] to orthorhombic olivine CPOs dominate, slow P-waves velocities are found for propagation directions normal to the foliation plane. In contrast to the average properties computed for the rift axis, the S-waves polarization anisotropy is very low for propagation directions at high angle to the plane containing the concentrations of [100] and [001] (corresponding to the foliation when observed), with a minimum within the XZ plane at ~45° to the lineation. The maximum S-wave polarization anisotropy lies within the foliation at 90° to the lineation. The fastest propagation directions of S_1-wave are contained in the foliation plane, while the slowest directions are parallel to the Z structural

direction. Slow and fast S_2-waves propagation directions are observed in a plane normal to the lineation and in the XZ plane, at 45° to the lineation, respectively.

Seismic anisotropy intensities for individual samples are highly variable (Fig. 7, Table 1). Maximum P-waves anisotropies are comprised between 3.3 and 18.4%, while maximum S-waves polarization anisotropies range between 2.3 and 13.3 %. To a first order, both anisotropies display a weak positive correlation with olivine content (Fig. 7a-b). This is consistent with the observation that the presence of pyroxenes and garnet decreases the rock bulk anisotropy (Mainprice and Silver, 1993; Mainprice et al., 2000). Porphyroclastic peridotites, which have the strongest olivine CPO, tend to have the highest anisotropies, whereas granular peridotites yield the lowest anisotropies. Within a microstructural group, however, there is no systematic variation in anisotropy as a function of the provenance.

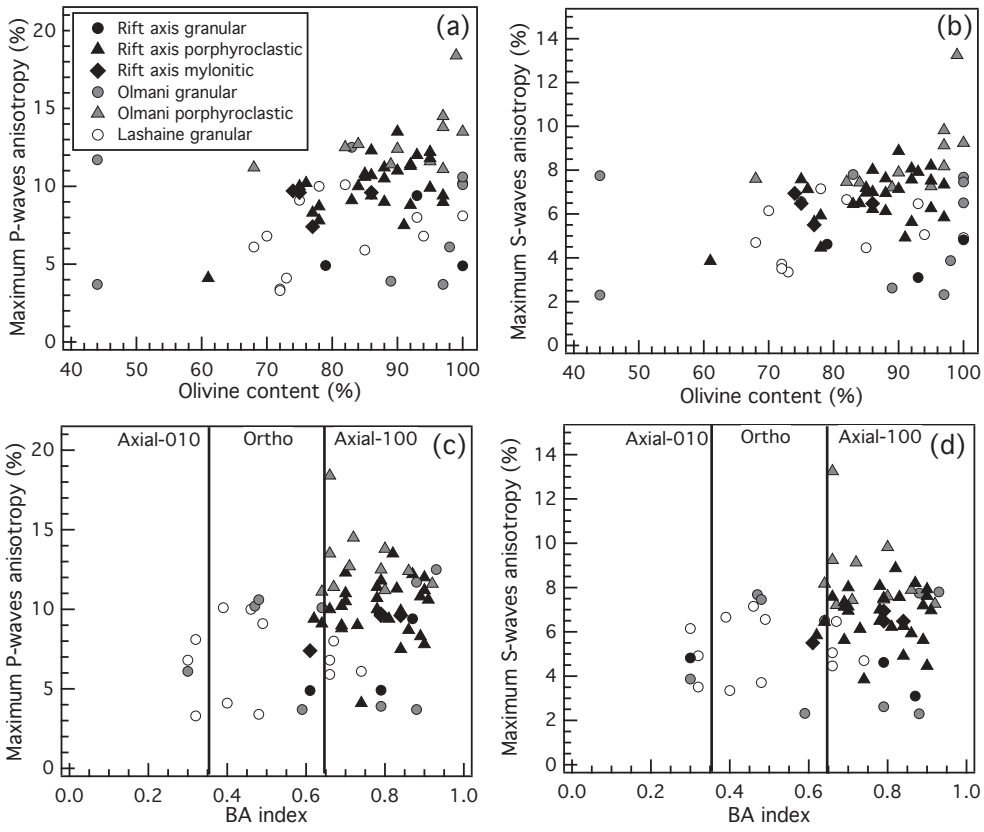

Figure 7: Dependence of the maximum P-wave anisotropy (AVp), and of the maximum S-wave polarization anisotropy (AVs) on the olivine content and the olivine CPO symmetry (BA index).

We observe no simple relationship between P- and S-waves anisotropy intensities and the olivine CPO symmetry (characterized by the BA index; Fig. 7 c, d). Most porphyroclastic peridotites, which have axial-[100] olivine CPO, are strongly anisotropic (Fig. 5), but their

large proportion of olivine and strong olivine CPO explain better their high anisotropy than the olivine CPO symmetry.

Crystallization of large volumes of metasomatic phases (>25% vol.) may considerably reduce P-, S_1- and S_2-waves velocities, and the maximum P- and S-waves anisotropy, as illustrated by Fig. 8, in which we compare the seismic properties of sample EL15 calculated by taking into account or not a phlogopite-bearing clinopyroxenite vein that crosscuts this sample. However, it has no effect on Vp/VS_1 and Vp/VS_2 ratios.

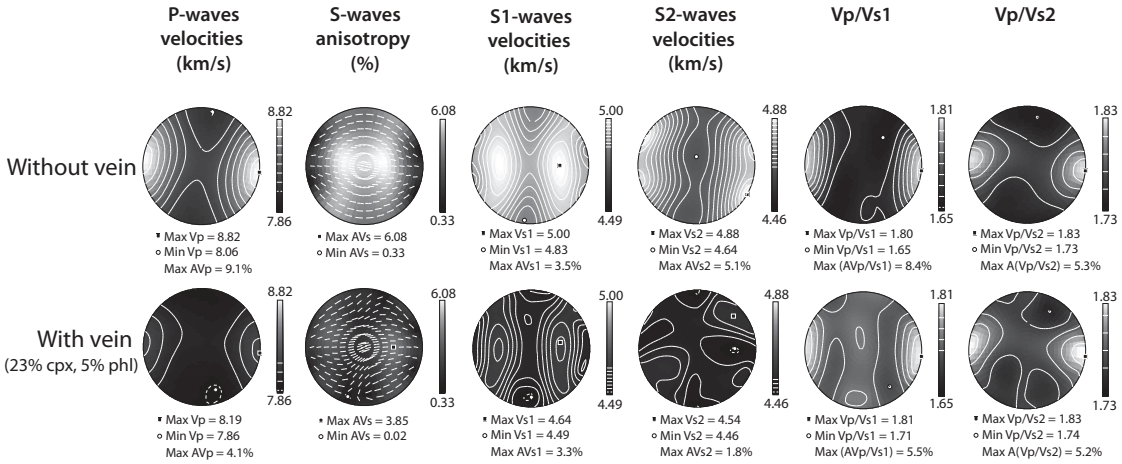

Figure 8: Effect of veins on the seismic properties of peridotite EL15 from Eledoi. From left to right are displayed the 3-D distributions of P-wave velocities (V_p), S-wave polarization anisotropy (AV_s) and the orientation of fast shear wave polarization plane, S_1 wave velocities (VS_1), S_2 wave velocities, and Vp/VS_1 and Vp/VS_2 ratios.

4.5 OH concentrations

4.5.1 Olivine

The olivine spectra of xenoliths from Pello Hill, Eledoi, Olmani, and Lashaine exhibit many absorption bands with highly variable intensities (Fig. 9a), suggesting H incorporation in a variety of point defects (Berry et al., 2005; Berry et al., 2007; Kovacs et al., 2010; Miller et al., 1987; Padron-Navarta et al., 2014). In a first group of samples (LS11, PEL41, 03TZ14J, EL6, PEL39), the absorption band at 3571 cm^{-1} displays the maximum O-H absorbance, while the intensity of the absorption bands at 3596 and 3525 cm^{-1} varies. Absorption bands between 3450 and 3200 cm^{-1} have minor peaks, except for the band at 3226 cm^{-1}, which can be more developed. In a second group of samples (EL15a, PEL17, PEL7, PEL15), absorption bands between 3450 and 3200 cm^{-1} present major peaks, with variable intensities. Finally, in a

third group of samples (PEL16, EL15b, 89-772, OL10, PEL40, PEL34), both absorption bands groups are observed.

4.5.2 Orthopyroxene and Garnet

Orthopyroxene spectra are more homogeneous (Fig. 9b) than those of olivine. They display up to seven absorption bands. The four major bands are found at 3600, 3544, 3517 and 3410 cm^{-1}. Their intensities are variable. Minor peaks are also present around 3473, 3324 and 3060 cm^{-1}.

Several millimeters long clear garnet grains were present in only one of the analyzed samples (harzburgite xenolith from Lashaine LS11). Their spectra are flat, indicating anhydrous garnet.

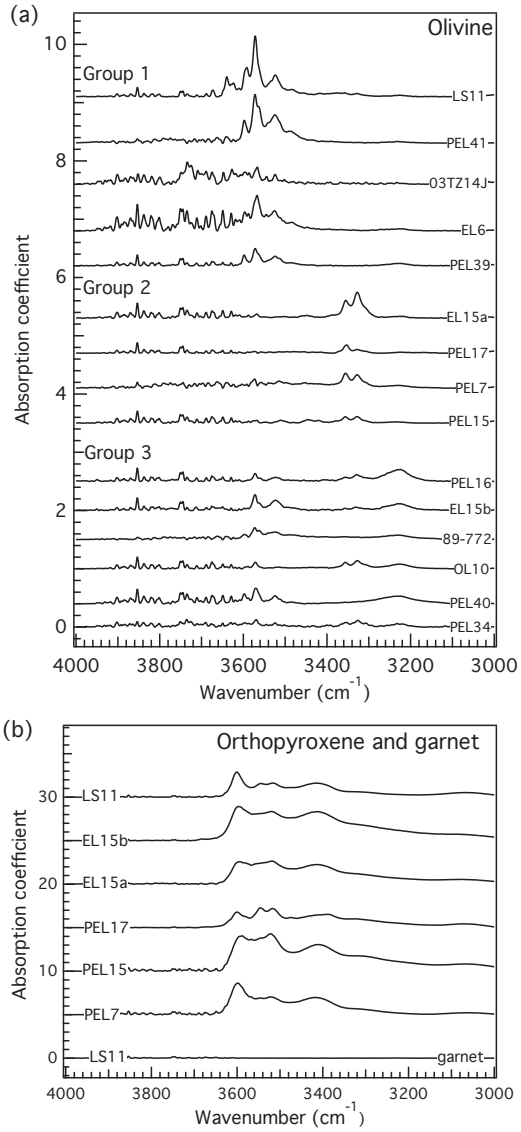

Figure 9: Representative unpolarized FT infrared spectra of nominally anhydrous minerals in xenoliths from Tanzania. (a) Olivine; (b) Orthopyroxene and garnet. All spectra are normalized to a sample thickness of 1 cm.

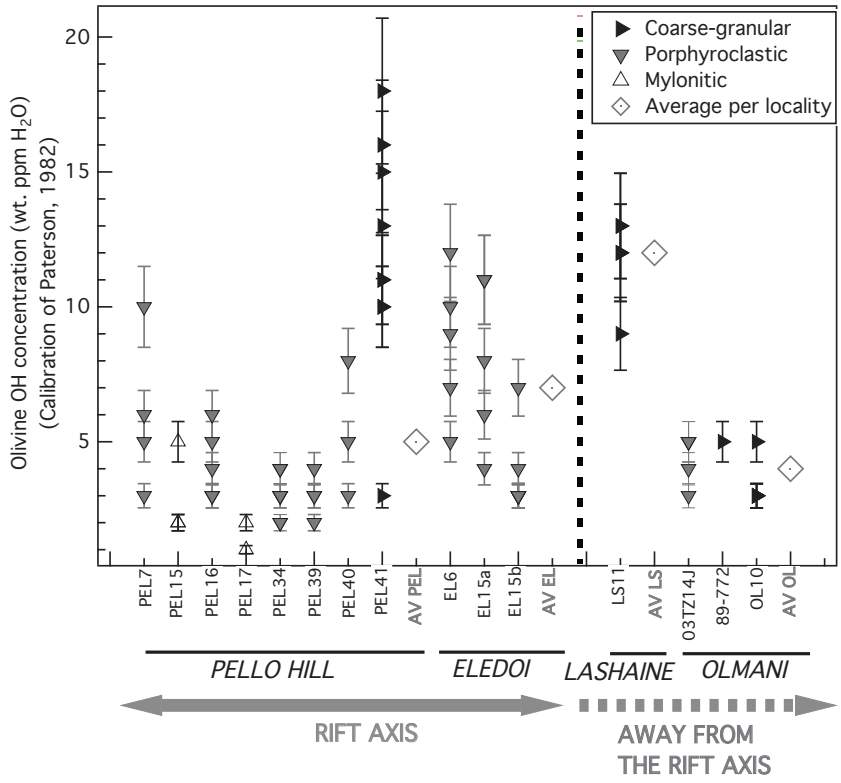

Figure 10: Representative unpolarized FT infrared spectra of nominally anhydrous minerals in xenoliths from Tanzania. (a) Olivine; (b) Orthopyroxene and garnet. All spectra are normalized to a sample thickness of 1 cm.

4.5.3 OH concentrations

Olivine OH concentrations are heterogeneous both between and within samples. They range between 2 and 12 wt. ppm H_2O (Table 2, Fig. 10 and 11) and are in the range of concentrations previously measured for spinel peridotites (Denis et al., 2013; Falus et al., 2008; Grant et al., 2007; Kurosawa et al., 1997; Li et al., 2008; Peslier, 2010; Peslier and Luhr, 2006; Soustelle et al., 2010; 2013; Yang et al., 2008). Olivines from Pello Hill xenoliths are more heterogeneous than those from Olmani and Eledoi. However, there is no systematic correlation between olivine OH concentrations and provenance (Fig. 10). The lowest olivine OH concentrations are found in mylonites, in agreement with data from previous studies (Baptiste et al., 2012; Falus et al., 2008). The highest average olivine OH concentrations (12 wt. ppm H_2O) are observed in dunite PEL41 from Pello Hill and harzburgite LS11 from Lashaine. Although both samples are coarse-granular, in the whole set of analyzed samples, there is no systematic correlation between olivine OH concentration and microstructure. There is also no correlation between the olivine OH concentration and Mg# (Fig. 11).

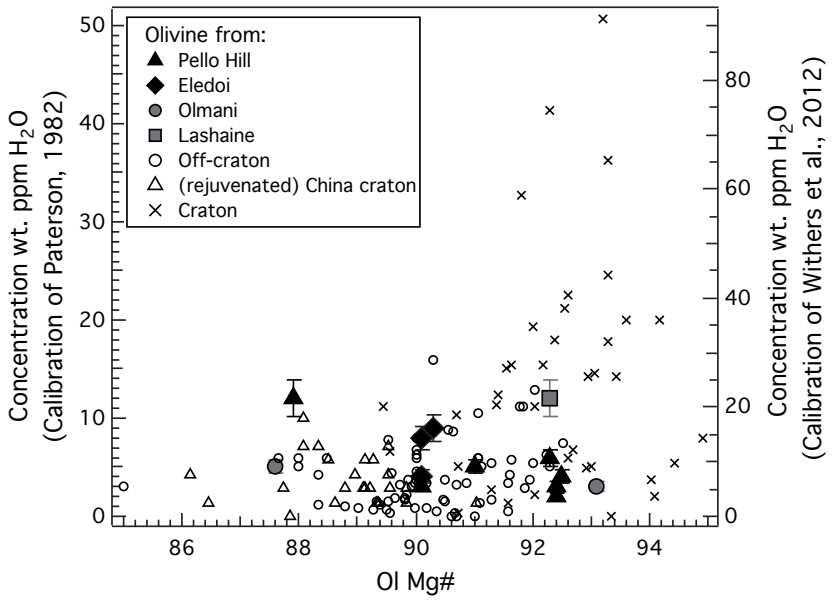

Figure 11: OH concentrations in wt. ppm H2O (calibration of Paterson, 1982) versus Mg# in olivine. For comparison, data obtained in previous studies on peridotite xenoliths from various localities are also shown (Baptiste et al., 2012; Demouchy et al., 2006; Denis et al., 2013; Falus et al., 2008; Grant et al., 2007; Kurosawa et al., 1997; Matsyuk et al., 1998; Matsyuk and Langer, 2004; Peslier and Luhr, 2006; Peslier et al., 2008; Peslier et al., 2010; Yang et al., 2008).

The homogeneity of OH concentrations in olivine was tested by profiles analyses with 50 to 150 μm step sizes along transect (850 to 3450 μm) on randomly oriented olivine grains in three samples: one mylonite from Pello Hill (PEL17), one garnet-bearing harzburgite from Lashaine (LS11), and one vein-bearing sample from Pello Hill (PEL41). These profiles indicate long homogeneous concentrations plateau within grains, incompatible with significant dehydration (Thoraval and Demouchy, 2014)

Average orthopyroxene OH concentrations range between 97 and 212 wt. ppm H2O (Table 2), being in the range of concentrations reported by previous studies (Falus et al., 2008; Peslier et al., 2002; Peslier, 2010). In rift axis samples, orthopyroxene OH concentrations are more heterogeneous, but there is no systematic correlation between orthopyroxene OH concentration and xenolith locality or microstructure. Indeed, the lowest orthopyroxene OH concentrations are measured in mylonite PEL17 and the highest, in mylonite PEL15. There is also no correlation between the olivine and orthopyroxene OH concentrations.

5. Discussion

5.1 Thermomechanical and metasomatic evolution of North Tanzanian Divergence peridotites

5.1.1 Rift Axis (Pello Hill and Eledoi)

The peridotites from the rift axis localities show a variety of microstructures, from mylonitic to porphyroclastic and coarse-granular. All exhibit evidence for plastic deformation and both dynamic and static recrystallization, but the deformation conditions and the extent of static recrystallization vary from one microstructure to another. The obliquity between the lineation and subgrain boundaries in olivine suggests simple shear deformation in both porphyroclastic peridotites and mylonites, but the higher elongation of orthopyroxenes and finer grain sizes imply deformation under higher stresses in the mylonites. The heterogeneity in microstructures may indicate a spatial or a temporal variation of deformation conditions and intensity within the mantle below Eledoi and Pello Hill.

In both mylonites and porphyroclastic peridotites, the frequency and spacing between subgrain boundaries in olivine porphyroclasts and the extent of grain boundary polygonization vary from sample to sample (Fig. 3a and b). These microstructural features support a deformation by dislocation creep followed by variable degree of annealing. The well-preserved intracrystalline deformation features in most porphyroclastic peridotites suggest, however, that the time span between the deformation and the extraction by the magma was too short to allow for complete annealing of the deformation microstructures. The recent character of the deformation is further supported by the rather high equilibration temperatures (1050-1100°C) recorded by these peridotites. The variable degree of annealing observed in these rocks may be explained by variable interaction with fluids or melts, by sampling of different depths, or by transient and spatially heterogeneous heating events.

Mylonites also record a temporal variation of deformation conditions. Highly stretched orthopyroxenes are a characteristic feature of the mylonites (Fig. 3a). Similar highly stretched orthopyroxenes have been described, in mylonitic peridotites from the Lanzo (Nicolas et al., 1972), Ronda (Tubìa et al., 2004; Soustelle et al., 2009), and Beni Bousera massifs (Frets et al., 2014), and were interpreted as the result of deformation under high stress at moderate temperatures (850-950°C estimated from thermobarometry in the peridotites and associated pyroxenites; Frets et al. 2014; Garrido et al. 2011). Closely spaced kinks in orthopyroxene also indicate deformation under high stress conditions. However, the stretched orthopyroxenes from the mylonites have indented shapes, with embayments filled by vein-like olivine crystals, which are often subparallel to the orthopyroxene elongation (Figure 4a).

In porphyroclastic peridotites, orthopyroxene embayments filled with olivine and olivine inclusions in orthopyroxene (Fig. 4c) are also present. These microstructures suggest reactions leading to consumption of orthopyroxene and crystallization of olivine. In both mylonites and porphyroclastic peridotites, the olivine crystals that replace orthopyroxene display ubiquituous undulose extinction and subgrain boundaries dominantly oriented normal to the crystals' elongation. This suggests that this reaction is synkinematic. Three processes may produce replacement of orthopyroxene by olivine: (1) incongruent melting of orthopyroxene (Kubo, 2002); (2) reaction between the peridotite and a Si-undersaturated melt (Kelemen et al., 1990, 1995), (3) percolation of aqueous fluids (Padrón-Navarta et al., 2010). The last process may occur at low temperatures (650-700°C), but implies very large volumes of aqueous fluids (Padrón-Navarta et al., 2010), which are plausible in a subduction zone, but not in a continental rift.

In summary, the recent deformation event recorded by the rift axis xenoliths started under high stress and probably low temperature. The deformation was later coupled with partial melting or reactive percolation of Si-undersaturated melts. Both processes imply high, near-solidus temperatures, which are at odds with the high stresses inferred in the mylonites from the stretching of orthopyroxenes. Moreover, the ubiquituous exsolutions seen in orthopyroxenes suggest significant cooling between this melt-assisted deformation and the extraction of the xenoliths. Together these observations imply transient and probably spatially heterogeneous temperature fields, marked by fast heating and cooling episodes, which probably accompanied deformation and reactive melt percolation. Interestingly, similar observations have been recently reported for peridotites samples from the boundary of the Middle Atlas (Marocco) in a context of progressive exhumation, leading to convergent interpretation (El Messbahi et al., in press).

Coarse-grained dunites (EL14, PEL11, and PEL41) contain more Fe-rich olivine in comparison to the other Tanzanian samples. In these rocks, subgrain boundaries are rare and triple junctions are common (Fig. 3e). They display, however, a clear crystallographic fabric. Altogether this suggests that efficient annealing followed deformation by dislocation creep. Dunite may form when a harzburgite interacts with Si-undersaturated melts (Berger, 1985; Berger and Vannier, 1984; Kelemen et al., 1990; Morgan and Liang, 2003). The coarse-grained dunites from Pello Hill and Eledoi contain olivines with significantly lower Mg# (84-88, while the average for the other microstructures in these localities is ~92, Table 1). Such a strong enrichment in Fe suggests interaction with very large volumes of melts. The coarse-grained dunites might represent melt channels or melt accumulation levels within the mantle

lithosphere (Berger, 1985; Berger and Vannier, 1984; Kelemen et al., 1995; Kelemen and Dick, 1995; Tommasi et al. 2004).

In mylonitic, porphyroclastic and coarse-granular peridotites, the well-defined olivine CPO indicates dislocation creep as the dominant deformation process. The olivine CPO patterns range from to orthorhombic. These olivine CPOs are consistent with deformation by simple or pure shear with dominant activation of (010)[100] or (0kl)[100] slip systems under high temperature, low pressure and anhydrous conditions (Tommasi et al., 1999; Tommasi et al., 2000). Axial-[100] CPO symmetry likely denotes a strain regime producing a well-defined stretching direction, such as transtension; Chatzaras and Kruckenberg (in press) have recently shown the correlation between axial-[100] CPO symmetry and prolate strain ellipsoids due to constructional deformation. Orthopyroxene CPOs indicate deformation by dislocation creep with activation of the [001](100) slip system. They are always correlated to the olivine CPO, indicating that both minerals underwent the same deformation event.

In addition to the olivine-forming reactive melt percolation, textural evidence for metasomatism by hydrous melts has also been identified in many peridotites from Pello Hill and Eledoi (see also Dawson and Smith, 1988, who first analyzed the composition of the veins from Pello Hill mantle xenoliths and concluded that they bear asthenospheric Nd and Sr isotopic signatures and imparted REE, K, Fe, Ti metasomatism on the surrounding peridotite). It encompasses: (1) veins with diffuse margins that comprise clinopyroxene, amphibole, phlogopite, and spinel that crosscut deformation microstructures (Fig. 3d), (2) irregularly-shaped pockets of clinopyroxene, amphibole, phlogopite, and spinel (Fig. 4e). In these minerals, deformation substructures are uncommon. However, clinopyroxene crystals in veins do exhibit a clear CPO that is coherent with the CPO of olivine and orthopyroxene from the surrounding peridotite. Two hypotheses may explain this observation. First, vein intrusion may be synkinematic, but this hypothesis is at odds with the orientation of the veins that crosscut the foliation and with the lack of plastic deformation of the metasomatic phases. Thus, we propose that the vein intrusion was post-kinematic and the minerals crystallized in a preferential orientation controlled by the orientation of the preexisting orthopyroxene.

5.1.2 Lashaine

Mantle xenoliths from Lashaine mainly display very coarse-grained microstructures characterized by millimeter- to centimeter-sized grains with curvilinear, interpenetrating boundaries and low densities of subgrain boundaries (Figure 3f, 4g). These observations point to efficient grain boundary migration. Together with the well-defined olivine and

orthopyroxene CPOs, they support deformation by dislocation creep at high temperature or effective annealing. In LS9, the frequent olivine-orthopyroxene interpenetrating boundaries suggest reaction with percolating melts. In addition, the olivine tablets growing on other crystals (Fig. 4f) have been previously interpreted as resulting from fast grain growth in presence of fluids (Drury and Van Roermund, 1989).

Among the studied samples, the xenoliths from Lashaine are the only ones containing garnet, implying that deeper parts of the Tanzanian lithosphere have been sampled. Garnet crystals in peridotites LS4 and LS11 display interstitial shapes and usually rim orthopyroxene. This morphology led Gibson et al. (2013) to interpret these pyrope garnets as the product of exsolution from orthopyroxene due to cooling.

Well-defined olivine and orthopyroxene CPOs in Lashaine peridotites indicate that dislocation creep was the main deformation process. Orthopyroxene CPOs are consistent with deformation by dislocation creep with dominant activation of [001](100), as usually observed in deformed mantle peridotites and pyroxenites (e.g., Frets et al. 2012, 2014; Vauchez et al., 2005). Olivine CPO patterns are dominantly orthorhombic to axial-[010] (Fig. 5). Axial-[010] olivine CPO symmetry, though less common than orthorhombic and axial-[100] symmetries (Tommasi et al., 2000), has been described in many xenoliths suites from continental and oceanic environments (e.g., Bascou et al., 2008; Tommasi et al. 2008; Vauchez et al., 2005; Zaffarana et al., 2014) and in peridotite massifs (e.g., Frets et al. 2014, Soustelle et al. 2010). It may result from similar activation of [100](010) and [001](010) slip systems as a result of changes in physical parameters (e.g., olivine water contents, pressure, differential stresses, presence of melt) during deformation or from a deformation regime characterized by an oblate strain ellipsoid (Chatzaras and Kruckenberg, in press) such as pure shear or transpression (Tommasi et al., 1999). A dispersion of olivine [100] axes has also been observed in rocks undergoing dynamic and static recrystallization (Falus et al., 2011; Tommasi et al., 2008). Experiments on olivine single crystals and polycrystals have shown that [001]-glide is favored at low temperature and high differential stresses (Demouchy et al., 2009; Demouchy et al., 2013; Demouchy et al., 2014; Durham and Goetze 1977; Phakey et al., 1972; Raleigh, 1968). However, this explanation is inconsistent with the very-coarse granular microstructures of Lashaine peridotites. The OH concentrations measured in olivine are too low (<20 wt. ppm H_2O) to induce the transition from dominant [100] to dominant [001] glide suggested by Jung et al. (2006). Transition from [100] to [001] glide have also been observed as a result of increasing pressure in deformation experiments at high confining pressure (Couvy et al., 2004; Jung et al., 2006; Raterron et al., 2009). Occurrence of axial-

[010] CPO in garnet-bearing harzburgite LS11 may suggest a change in dominant mechanism with increasing pressure, an interpretation similar to the one proposed by Vauchez et al. (2005) for the deepest Labait peridotites. However, this explanation cannot account for the common axial-[010] patterns in the Lashaine spinel peridotites. Deformation in presence of melt, accompanied by refertilization reactions, also results in development of axial-[010] olivine CPO (Le Roux et al., 2008; Higgie et al., 2012, 2014). Yet, there is no clear evidence for synkinematic refertilisation reactions in the studied peridotites. Thus axial-[010] olivine CPO in Lashaine peridotites probably results from either transpression or recrystallization. Transpression should also result in dispersion of orthopyroxene [001] axes in the foliation plane, but the small number of orthopyroxene crystals present in most samples does not allow corroborating or excluding this hypothesis. Evidence for static recrystallization and grain boundary migration is, on the other hand, widespread in these peridotites.

5.1.3 Olmani

Xenoliths from Olmani display microstructures and CPOs intermediate between those found in peridotites from rift-axis localities and from Lashaine (Fig. 3 and 7). Half of the Olmani samples display coarse-grained to very coarse-grained sizes, similar to the microstructures observed in Lashaine. The other half of Olmani samples exhibits coarse-porphyroclastic to porphyroclastic microstructures, with characteristics similar to those observed in rift axis peridotites. All textural types from Olmani show evidence for olivine crystallization at the expenses of orthopyroxene. Chemical evidence for interaction with carbonatites was identified in several of the studied peridotites (89-772, 89-774, 89-776, and 89-773) by Rudnick et al. (1993). These samples display coarse-granular microstructures, suggesting that the carbonatitic metasomatism is not directly related to the recent deformation (probably rift-related), recorded by the porphyroclastic microstructures.

The well-defined olivine CPOs measured in Olmani peridotites suggests that dislocation creep was the main deformation process. All three olivine CPO symmetries are observed. Interestingly, Olmani granular peridotites tend to display axial-[010] olivine CPO, similar to those of the granular peridotites from Lashaine, whereas porphyroclastic to coarse-porphyroclastic samples show dominantly axial-[100] patterns, similar to rift axis peridotites. Moreover, the weak annealing observed in the porphyroclastic peridotites suggests that deformation occurred shortly before extraction. The orthopyroxene CPO is consistent with deformation by dislocation creep with dominant activation of [001](100) and [001](010) slip

systems. Olivine and orthopyroxene CPOs are always correlated, implying that they record the same deformation event.

A variation in microstructures and olivine CPO patterns between the localities of Olmani and Lashaine was not expected, as both localities are within the Tanzanian Divergence and distant of less than 30km. This variation may be explained by: (1) younger eruption ages in Olmani than Lashaine, in which case Olmani peridotites would record the recent deformation associated with the rifting, (2) a bias in xenolith sampling, (3) Olmani and Lashaine sample lithospheric domains with different tectonic ages, or (4) heteregeneous deformation of the lithospheric mantle at the scale of few tens of km within the transverse volcanic belt. The eruption age of Olmani and Lashaine is poorly constrained. However, neighboring volcanic centers with similar morphologies have eruption ages between 2.5-1.56 Ma (Evans et al., 1971; Le Gall et al., 2008; MacIntyre et al., 1974; Wilkinson et al., 1986). Hypothesis (1) is therefore improbable. A bias in xenolith sampling (2) cannot be definitely excluded, but is unlikely, since in spite of the large number of xenoliths collected, Lashaine xenoliths have very homogeneous microstructures. The presence of lithospheric domains of different ages (3) within the Mozambique belt is possible. Indeed, Lashaine and Olmani are located in a domain of the Mozambique belt that is interpreted as a remnant of cratonic lithosphere reworked during the Neoproterozoic Orogeny (Mansur et al., 2014; Möller et al., 1998). Similarities between Lashaine and cratonic peridotites are numerous. Rudnick et al. (1994) first highlighted similarities in mineral compositions between Lashaine and the Kaapvaal craton peridotites. Minimum ages of 3.4 and 2.9 Ga were obtained from Re-Os studies of sulphides in mantle xenoliths from both Lashaine and Labait, a Quaternary volcano located on the eastern boundary of the Tanzanian craton (Fig. 1; Burton et al., 2000; Chesley et al., 1999). Comparison of the microstructures and the olivine CPOs of the Labait and Lashaine peridotites provides additional evidence for a common origin. Vauchez et al. (2005) described three textural types in the Labait peridotites, among which the garnet-free, coarse-grained peridotites display microstructures and olivine CPO very similar to those observed in the Lashaine peridotites. However, the similarities between Lashaine and Olmani coarse-granular peridotites make hypothesis (3) unlikely. Heterogeneous rift-related deformation within the volcanic belt is the most probable explanation to Lashaine and Olmani microstructural and CPO difference. Indeed, the deformation recorded by the Olmani porphyroclastic peridotites might be related to localized deformation in a strain transfer zone connecting the main rift to the Pangani Graben (Fig. 1) or to reactivation of the

neoproterozoic Aswa shear zone (e.g., Corti et al., 2007; Ruotoistenmäki, 2014 and references therein) in a transtensional regime that resulted in the opening of the Pangani Graben.

5.2 Hydration state of the Tanzanian lithosphere

Diffusion data from experimentation and dehydration profiles from basalt-borne peridotite xenoliths, both point out to a very fast hydrogen ionic diffusion in olivine at high temperature (Mackwell and Kohlstedt, 1990; Demouchy and Mackwell, 2006; Demouchy et al., 2006; Peslier and Luhr, 2006; Denis et al., 2013). However, the length and homogeneity of OH concentrations plateau in olivine along profiles in three samples demonstrates that the measured concentrations were not modified during xenolith extraction (Demouchy et al., 2006; Thoraval and Demouchy, 2014).

Average OH concentrations in olivine measured in the Tanzanian samples vary from very low to moderate (up to 12 wt. ppm H2O; Fig. 10, Table 2). Average orthopyroxene OH concentrations range between 97 and 212 wt. ppm H2O. In xenoliths from Pello Hill, the olivine OH concentrations are more heterogeneous than in those from Eledoi and Olmani. However, this difference might be related to the fact that we analyzed more samples from Pello Hill than from other localities. We also observe no clear relationship between the microstructure or the olivine CPO pattern and OH concentrations (Table 2, Fig. 10). We also do not observe significant differences in olivine OH concentrations between in- and off-axis samples (Fig. 10). The 2 samples that exhibit the highest OH concentrations in olivine, are a garnet-bearing harzburgite LS11 from Lashaine and a vein-bearing dunite PEL41 from Pello Hill. We discuss below the potential origin of these relatively higher OH concentrations.

The harzburgitic to dunitic compositions, and high olivine Mg# in most samples suggest extensive partial melting, which might be as old as 3.4 Ga, based on Os isotopic dating of sulphides in a garnet lherzolite from Lashaine (Burton et al., 2000). Since H behaves as an incompatible element during partial melting (Bolfan-Casanova, 2005; Dixon et al., 2002; Hirschmann et al., 2005), olivine with high Mg# should have the lowest OH concentrations. However, we observe no correlation between olivine Mg# and OH concentrations (Fig. 11), implying that the Tanzanian samples were potentially hydrated or rehydrated during later metasomatic events.

Geochemical studies have provided evidence for multiple metasomatic events in mantle xenoliths from the sampled localities. Carbonatite metasomatism led to enrichment in REE, increase in Mg#, and the crystallization of clinopyroxene and phosphate in Olmani xenoliths (Rudnick et al. 1993, 1994). However, this carbon-rich metasomatism should not

result in extensive hydration of Nominally Anhydrous Minerals (NAM) because a high CO2 fugacity will lower H2O fugacity in the system and thus minimize the hydration of NAMs (Dixon et al., 1995, Sokol et al., 2010). In Lashaine peridotites, an episode of metasomatism, which enriched the peridotites in K, Fe Ca, Ti, Rb and REE, was dated at ~2 Ga based on Re-Os isotope data on sulphides (Burton et al., 2000; Dawson, 2002). A more recent metasomatism led to addition of Si, K, Ti, Ca, Fe, Nb, and Ta (Dawson, 2002). Rudnick et al. (1994) suggested that the SiO2 enrichment in Lashaine garnet peridotites was caused by the interaction with silicic melts derived from partial melting of a subducting slab, during the major subduction on the eastern edge of the Kaapvaal craton around 2 Gy ago (Möller et al., 1995). Such a process may modify the trace element contents of NAMs and therefore allow for OH incorporation in olivine. It might therefore explain the relatively high OH concentration in olivine from garnet-bearing harzburgite LS11 (Fig. 10). Moreover, LS11 harzburgite is a garnet-bearing peridotite. Its deeper origin may also explain the higher OH concentration, since higher pressure implies higher water fugacity, favoring OH incorporation in olivine (Kohlstedt et al., 1996; Férot and Bolfan-Casanova, 2012).

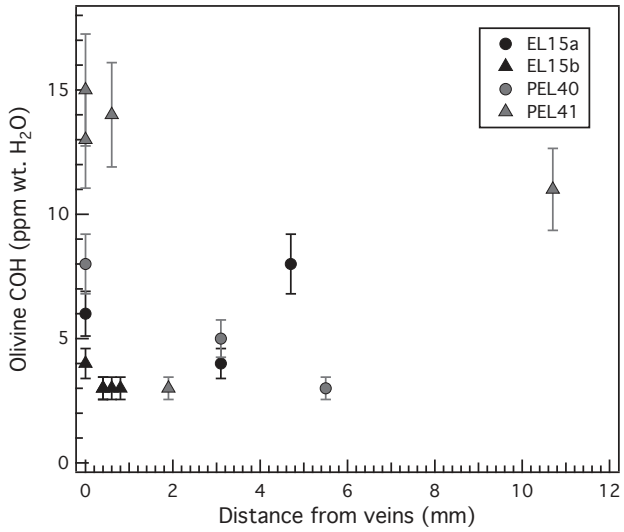

Figure 12: Olivine OH concentrations in wt. ppm H_2O, (calibration of Paterson, 1982) as a function of the distance from hydrous mineral-rich veins.

The presence of undeformed hydrous phases in veins or diffuse pockets (Fig. 3d, 4d,e) in xenoliths from all sites implies extensive post-kinematic metasomatism by hydrous fluids or melts. Indeed, the vein-bearing dunite PEL41 from Pello Hill shows the highest OH concentrations in olivine from all analyzed samples (Fig. 10). However, measurement of the OH concentration in olivine at different distances from the veins in dunite PEL41 shows no systematic increase in olivine OH concentrations in the vicinity of the vein (Fig. 12). Similar

measurements were performed for samples EL15 and PEL40. These data suggest that hydration of olivine is not related to the metasomatic event that formed the veins. The actual nature of the metasomatic agent and the timing of the hydration of olivine remain therefore undetermined.

5.3 Upper mantle deformation and seismic anisotropy in the North Tanzanian Divergence

Microstructures and CPOs analysis of the Tanzanian xenoliths show that the lithospheric mantle in the Northern Tanzanian Divergence is pervasively deformed. However, the strong heterogeneity in microstructures and olivine CPO suggests that this deformation was acquired during multiple tectonic events, probably separated by quiescence episodes, which allowed for annealing. The observed microstructural heterogeneity could also be explained by spatial variations in strain rate. The mylonitic to granular microstructures of the rift axis peridotites, despite rather high equilibrium temperatures, underwent limited annealing, which suggests that they were deformed shortly before extraction. Therefore, these samples likely record the deformation associated with the rift propagation in this region. Among the peridotites from the rift axis, the most common olivine CPO pattern is the axial-[100] pattern. This pattern implies that: (1) [100] is the dominant glide direction in olivine and (2) the active deformation regime has a well-defined stretching direction. Numerical models show that development of axial-[100] olivine CPO is characteristic of transtensional deformation regimes (Tommasi et al., 1999). High temperature (1200°C), high strain rate (<10-6 s-1) torsion experiments in dry olivine aggregates (Bystriky et al., 2000; Hansen et al. 2014) have shown, however, that [100]-axial CPO also forms during the initial stages of simple shear deformation, with a progressive transition from axial-[100] symmetry to orthorhombic symmetry for $\gamma>5$. The obliquity between subgrain boundaries and the foliation observed in the mylonites and porphyroclastic peridotites are consistent with a simple shear component of deformation. In addition, the extreme stretching of the pyroxenes in the mylonites (Fig. 3a, 4a) implies high finite strains. Altogether, these observations support that the deformation, which developed the mylonites and porphyroclastic peridotites in the mantle lithosphere beneath the southern part of the East-African rift, results from a transtensional strain regime with a strong simple shear component.

Comparison between the seismic properties of the studied xenoliths and seismological data may help to further constrain the deformation regime in the region (e.g., Vauchez et al., 2000). Anisotropy measurements in the Tanzania Divergence show fast SKS polarization directions parallel or slightly oblique to the rift axis (Albaric et al., 2014; Bagley and

Nyblade, 2013; Gao et al., 1997; Walker et al., 2004). Oblique fast polarization directions for teleseismic shear waves are expected for a rift formed by transtensional deformation of the lithosphere, which should result in axial-[100] olivine CPO patterns with a concentration of olivine [100] axes close to horizontal and slightly oblique to the rift axis (Vauchez et al., 2000). These data, together with the predominance of axial-[100] olivine CPO in the studied mantle xenoliths from Pello Hill and Eledoi, are in good agreement with the suggestion that the East African Rift was initiated by a transtensional reactivation of inherited crystallographic fabrics, as suggested by Tommasi and Vauchez (2001) and Tommasi et al. (2009) who showed, using numerical models, that a CPO-induced mechanical anisotropy in the mantle imposes deformation with a strong strike-slip component parallel to the reactivated mantle structure.

Away from the rift axis, the coarse-granular, highly annealed microstructures of the Lashaine peridotites probably record an older deformation event. The olivine CPO in these peridotites also differ markedly from those from the rift axis: axial-[010] to orthorhombic patterns predominate. The deformation microstructures and CPOs frozen in these peridotites might be related to the last major compressive event in the region: the formation of the Mozambique Belt during the Neoproterozoic East African Orogeny (e.g., Pinna et al., 1993). Considering the similarity in microstructure and composition between the xenoliths from Lashaine, Labait (Vauchez et al. 2005), and the Kaapvaal craton (Baptiste et al. 2012), it may also be hypothesized that the lithosphere beneath Lashaine is a remnant of a cratonic domain embedded and preserved in the Mozambique Belt, as suggested by Gibson et al. (2013) from the geochemical study of ultra-depleted garnets. In this case, the structures and CPO of Lashaine xenoliths might result from even older deformations, such as those recorded in the neighboring Tanzanian craton (e.g., Bagley and Nyblade, 2013; Walker et al., 2004). Although localized within the transverse volcanic belt, the Olmani mantle xenoliths show both types of microstructures and CPOs: rift-axis or Lashaine ones. This might result from localized deformation reworking an older lithosphere (similar to the Lashaine mantle, or affected by the Aswa transcurrent shear zone) leading to the development of a subordinate branch of the East African Rift southeast of Mount Kilimandjaro (see Fig. 1).

The present study shows that lithospheric mantle beneath the southern part of the East African Rift is anisotropic. Below the rift axis, calculated seismic anisotropy intensities (Fig. 7, Table 1) range between 3.3 and 18.4% for P-waves, and between 2.3 and 13.3 % for S-waves. The contribution of the mantle lithosphere cannot therefore be neglected in the interpretation of shear wave splitting data, even if the coherence of the large-scale seismic

anisotropy pattern has lead investigators to favor a sublithospheric flow interpretation (e.g., Bagley and Nyblade, 2013). Estimates of the crustal and lithospheric thicknesses in this region vary between 36-44 km and 100-150 km (Dugda et al., 2009; Julià et al., 2005), respectively. Upper mantle S-wave velocities of 4.6 km/s were measured in the region (Julià et al., 2005). Assuming that the rift formed by transtension, we expect the foliation to be near vertical and the lineation close to horizontal and slightly oblique to the rift axis (Vauchez et al., 2000). SKS-waves will then sample the maximum S-wave polarization anisotropy (Z direction in Fig. 6), leading to delay times around 0.65s for a 60 km-thick mantle, and of 1.2s for a 110 km-thick mantle. In the North Tanzanian Divergence, Walker et al. (2004) measured SKS delay times of 0.3-0.8s, while Bagley and Nyblade (2013) and Albaric et al. (2014) obtained mean delay times of 0.7 and 1.2s, respectively. Therefore, the anisotropy induced by olivine CPOs in the Tanzanian peridotites can explain the SKS delay times measured in the region. Within the main Ethiopian rift, SKS studies also report polarization directions subparallel to the rift trend and variable delay times (0.5-1.7s: Gashawbeza et al., 2004, 1-3 s: Kendall et al., 2005). However, SKS splitting delay times as high as those reported by Kendall et al. (2005) in the Afars, cannot be explained by the anisotropies recorded in Tanzanian xenoliths, in agreement with the interpretation that they reflect the presence of oriented melt pockets (Ayele et al., 2004; Bastow et al., 2010; Hammond, 2014; Kendall et al., 2005; Sicilia et al., 2008).

6. Conclusions

Xenoliths sampling the lithospheric mantle beneath the North Tanzanian Divergence in the East African Rift display a high variability in microstructures and olivine CPO depending on their location. Beneath the rift-axis and Olmani, within the volcanic transverse belt, the occurrence of mylonitic to porphyroclastic microstructures suggests recent deformation by dislocation creep. Variable microstructures and grain sizes in these rocks suggest lateral and/or vertical variation of the deformation conditions within the mantle, as well as variable degrees of annealing, that may be related to variable interaction with fluids or melts, or to different time spans between deformation and xenolith extraction. The presence of mylonites point to strain localization, but there is no evidence of dominant grain boundary sliding in any of the studied rocks: the ubiquitous dislocation-related intracrystalline deformation features in olivine and orthopyroxene and the strong axial-[100] olivine CPO point to dislocation creep with dominant activation of the [100](010) slip system. The mylonites also record evidence for marked changes in temperature, probably due to transient

heating events. Highly stretched orthopyroxene crystals in mylonites from rift axis localities suggest that the deformation initiated under high stress and probably low/moderate temperature conditions, but the evidence of synkinematic olivine crystallization at the expenses of orthopyroxene observed in both mylonitic and porphyroclastic peridotites from rift axis localities and Olmani indicate that deformation continued in the presence of melt, under near-solidus conditions. Finally, ubiquitous exsolutions in orthopyroxene in the mylonites suggest significant cooling between this melt-assisted deformation and the xenoliths extraction. Late, postkinematic metasomatism by hydrous melts is evidenced by the occurrence of veins crosscutting the microstructure, as well as the presence of interstitial clinopyroxene and phlogopite in rift axis peridotites.

In the volcanic transverse belt, the coarse-granular microstructures and well-defined CPOs that characterize the Lashaine and part of the Olmani peridotites likely result from an older deformation event. The well-defined axial-[010] to orthorhombic CPO patterns in these peridotites may be associated with the formation of the Mozambique Belt or with an even older event. Finally, the variability of microstructures and CPOs in Olmani peridotites, which are either Lashaine-like or rift-axis-like, may indicate a heterogeneous deformation within the volcanic transverse belt, probably related to localized deformation associated to the development of the Pangani Graben through transtensional reactivation of the Aswa shear zone (Fig. 1).

Tanzanian xenoliths are variably hydrated (OH contents in olivine vary between 2 and 18 ppm H2O wt., Paterson calibration), but olivine OH concentrations do not vary systematically neither between in- and off-axis samples, nor as a function of the microstructure or CPO patterns. Occurrence of OH in olivines with high Mg# implies hydration by metasomatism after partial melting. However, the lack of spatial correlation between OH contents in olivine and the veins containing hydrous phases, implies that the olivine hydration is not directly due to the vein-forming metasomatism.

Maximum P wave azimuthal anisotropy (AVp) ranges between 3.3 and 18.4% and the maximum S wave polarization anisotropy (AVs), between 2.3 and 13.2%. The change in olivine CPO symmetry from a locality to another results in a variation in the seismic anisotropy patterns. Comparison between olivine CPOs and polarization direction of the fast SKS wave is consistent with a rift formed by a transtensional deformation involving reactivation of inherited tectonic fabric.

Acknowledgments

Julien Baticle is thanked for analyzing several thin sections with the EBSD and Philippe Nonnotte for lending several mantle xenoliths from his collection. W. Behr and an anonymous reviewer are thanked for their constructive reviews. D. Mainprice provided the programs for treating the CPO data and calculating seismic properties. C. Nevado and D. Delmas prepared high-quality polished thin sections for FTIR and EBSD measurements. EBSD measurements were performed with the help of F. Barou at the EBSD-SEM national facility at Geosciences Montpellier. Electron microprobe analyses were carried out with the help of C. Merlet at the Service Microsonde Sud, Montpellier University. FTIR analyses were performed with the assistance of D. Maurin at the Lab. Colloids, Verre et Nanomateriaux, at Montpellier University, France.

References:

Abramson, E.H., Brown, J.M., Slutsky, L.J. and Zaug, J., 1997. The elastic constants of San Carlos olivine to 17 GPa. Journal of geophysical Research, 102(B6): 12,253-12,263.

Albaric, J., Déverchère, J., Perrot, J., Jakovlev, A. and Deschamps, A., 2014. Deep crustal earthquakes in North Tanzania, East Africa: Interplay between tectonic and magmatic processes in an incipient rift. Geochemistry Geophysics Geosystems, 15(2): 374-394.

Albaric, J., Perrot, J., Déverchère, J., Deschamps, A., Le Gall, B., Ferdinand, R.W., Petit, C., Tiberi, C., Sue, C. and Songo, M., 2010. Contrasted seismogenic and rheological behaviours from shallow and deep earthquake sequence in the North Tanzanian Divergence, East Africa. Journal of African Earth Sciences, 58(5): 799-811.

Ayele, A., Stuart, G.W., Kendall, J.-M., 2004. Insights into rifting from shear wave splitting and receiver functions: An example from Ethiopia. Geophys. J. Int. 157, 354-362.

Bagley, B. and Nyblade, A., 2013. Seismic anisotropy in eastern Africa, mantle flow, and the African superplume. Geophysical research letters, 40: 1500-1505.

Baptiste, V., Tommasi, A. and Demouchy, S., 2012. Deformation and hydration of the lithospheric mantle beneath the Kaapvaal craton, South Africa. Lithos, 149: 31-50.

Bascou, J., Delpech, G., Vauchez, A., Moine, B.N., Cottin, J.Y., Barruol, G., 2008. An integrated study of microstructural, geochemical, and seismic properties of the lithospheric mantle above the Kerguelen plume (Indian Ocean). Geochemistry Geophysics Geosystems, 9(4): 1-26.

Bastow, I.D., Pilidou, S., Kendall, J.-M. and Stuart, G.W., 2010. Melt-induced seismic anisotropy and magma assisted rifting in Ethiopia: Evidence from surface waves. Geochemistry Geophysics Geosystems, 11(6): Q0AB05.

Ben Ismaïl, W. and Mainprice, D., 1998. An olivine fabric database: an overview of upper mantle fabrics and seismic anisotropy. Tectonophysics, 296(1-2): 145-157.

Berger, E.T., 1985. Petrographic heterogeneities of the South Pacific mantle below the Austral archipelago: evidence and interpretation using ultramafic investigations. Bull. Soc. Geol. Fr., 1: 207-216.

Berger, E.T. and Vannier, M., 1984. Les dunites en enclaves dans les basaltes alcalins des îles océaniques: approche pétrologique. Bulletin de minéralogie, 107: 649-663.

Berry, A.J., Hermann, J., O'Neill, H.S.C. and Foran, G.J., 2005. Fingerprinting the water site in mantle olivine. Geology, 33(11): 869-872.

Berry, A.J., O'Neill, H.S.C., Hermann, J. and Scott, D.R., 2007. The infrared signature of water associated with trivalent cations in olivine. Earth and Planetary Science Letters, 261(1-2): 134-142.

Bezacier, L., Reynard, B., Bass, J.D., Wang, J. and Mainprice, D., 2010. Elasticity of glaucophane, seismic velocities and anisotropy of the subducted oceanic crust. Tectonophysics, 494(3-4): 201-210.

Bolfan-Casanova, N., 2005. Water in the Earth's mantle. Mineral Mag, 69(3): 229-257.

Brey, G.P. and Köhler, T., 1990. Geothermobarometry in Four-phase Lherzolites II. New Thermobarometers, and Practical Assessment of Existing Thermobarometers. Journal of Petrology, 31(6): 1353-1378.

Buck, W.R., 2006. The role of magma in the development of the Afro-Arabian Rift System. Geological Society, London, Special Publications 259, 43-54.

Bunge, H. J., 1982. *Texture analysis in materials sciences*, 593 pp., Buttleworth, London.

Burton, K.W. et al., 2000. The distribution and behaviour of rhenium and osmium amongst mantle minerals and the age of the lithospheric mantle beneath Tanzania. Earth and Planetary Science Letters, 183: 93-106.

Bystricky, M., Kunze, K., Burlini, L. and Burg, J.-P., 2000. High shear strain in olivine agreggates: rheological and seismic consequences. Science, 290: 1564-1567.

Cerling, T.E. and Powers, D.W., 1977. Paleorifting between the Gregory and the Ethiopian rifts. Geology, 5: 441-444.
Chai, M., Brown, J.M. and Slutsky, L.J., 1997a. The elastic constants of pyrope-grossular-almandine garnets to 20 GPa. Geophys. Res. Lett., 24(4): 523-526.
Chai, M., Brown, J.M. and Slutsky, L.J., 1997b. The elastic constants of an aluminous orthopyroxene to 12.5 GPa. Journal of geophysical Research, 102(B7): 14,779-14,785.
Chatzaras, V., Kruckenberg, S.C., in press. Effect of strain geometry on mantle fabric and olivine crystallographic texture. Geology.
Chesley, J.T., Rudnick, R.L. and Lee, C.-T., 1999. Re-Os systematics of mantle xenoliths from the East African Rift: age, structure, and history of the Tanzanian craton. Geochimica et Cosmochimica Acta, 63: 1203-1217.
Collins, M.D. and Brown, J.M., 1998. Elasticity of an upper mantle clinopyroxene. Physics and Chemistry of Minerals, 26: 7-13.
Corti, G., van Wijk, J., Cloetingh, S. and Morley, C.K., 2007. Tectonic inheritance and continental rift architecture: Numerical and analogue models of the East African Rift system. Tectonics, 26(TC6006).
Couvy, H. et al., 2004. Shear deformation experiments of forsterite at 11 GPa – 1400°C in the multianvil apparatus. Eur J Mineral, 16(6): 877-889.
Crossley, R. and Knight, R.M., 1981. Volcanism in the western part of the Rift valley in Southern Kenya. Bulletin of Volcanology, 44: 117-128.
Dawson, J.B., 2002. Metasomatism and partial melting in the upper-mantle peridotite xenoliths from the Lashaine Volcano, Northern Tanzania. Journal of Petrology, 43(9): 1749-1777.
Dawson, J.B. and Smith, J.V., 1988. Metasomatised and veined upper-mantle xenoliths from Pello Hill, Tanzania: evidence for anomalously-light mantle beneath the Tanzanian sector of the East African Rift Valley. Contributions to Mineralogy and Petrology, 100: 510-527.
Demouchy, S., Jacobsen, S.D., Gaillard, F. and Stern, C.R., 2006. Rapid magma ascent recorded by water diffusion profiles in mantle olivine. Geology, 34(6): 429-432.
Demouchy, S., Tommasi, A., Boffa-Ballaran, T. and Cordier, P., 2013. Low strength of Earth's uppermost mantle inferred from tri-axial deformation experiments on dry olivine crystals. Physics of the Earth and Planetary Interiors, 220(37-49).
Demouchy, S., Mussi, A., Barou, F., Tommasi, A. and Cordier, P., 2014. Viscoplasticity of polycrystalline olivine at high pressure and 900°C Tectonophysics, 623: 123-135.
Demouchy, S., Schneider, S.E., Mackwell, S.J., Zimmerman, M.E. and Kohlstedt, D.L., 2009. Experimental deformation of olivine single crystals at lithospheric temperatures. Geophys. Res. Lett., 36(4): 1-5.
Denis, C. M., Demouchy, S., & Shaw, C. S., 2013. Evidence of dehydration in peridotites from Eifel Volcanic Field and estimates of the rate of magma ascent. Journal of Volcanology and Geothermal Research, 258, 85-99.
Dijkstra, A.H., Drury, M.R., Vissers, R.L.M. and Newman, J., 2004. On the role of melt-rock reaction in mantle shear zone formation in the Othris Peridotite Massif (Greece). Journal of Structural Geology, 24: 1431-1450.
Dixon, J.E., Stolper, E.M. and Holloway, J.R., 1995. An experimental study of water and carbon dioxide solubilities in mid-ocean ridge basaltic liquids. Part I: Calibration and solubility models. Journal of Petrology, 36(6): 1607-1631.
Dixon, J.E., Leist, L., Langmuir, C. and Schilling, J.-G., 2002. Recycled dehydrated lithosphere observed in plume-influenced mid-ocean-ridge basalt. Nature, 420(6914): 385-389.

Drury, M.R., Van Roermund, H.L.M., 1989. Fluid Assisted Recrystallization in Upper Mantle Peridotite Xenoliths from Kimberlites. Journal of Petrology 30, 133-152.

Dugda, M.T., Nyblade, A. and Julià, J., 2007. Thin lithosphere beneath the Ethiopian Plateau revealed by a joint inversion of Rayleigh wave group velocities and receiver functions. Journal of geophysical Research, 112, B08305.

Dugda, M.T., Nyblade, A. and Julià, J., 2009. S-wave velocity structure of the crust and upper mantle beneath Kenya in comparison to Tanzania and Ethiopia: Implications for the formation of the East African and Ethiopian Plateaus. South African Journal of Geology, 112: 241-250.

Dunbar, J.A. and Sawyer, D.S., 1989. How preexisting weaknesses control the styles of continental breakup. Journal of geophysical Research, 94: 7278-7292.

Durham, W.B. and Goetze, C., 1977. Plastic flow of oriented single crystals of olivine 1. Mechanical data. J. Geophys. Res.(82): 5737–5754.

Evans, A.L., Fairhead, J.D. and Mitchell, J.G., 1971. Potassium-argon ages from the volcanic province of Northern Tanzania. Nature, 229: 19-20.

Fabriès, J., 1979. Spinel-olivine geothermometry in peridotites from ultramafic complexes. Contributions to Mineralogy and Petrology, 69: 329-336.

Falus, G., Tommasi, A., Ingrin, J. and Csaba, S., 2008. Deformation and seismic anisotropy of the lithospheric mantle in the southeastern Carpathians as inferred from the study of mantle xenoliths. Earth Planet. Sci. Lett., 272: 50-64, doi:10.1016/j.epsl.2008.04.035

Falus, G., Tommasi, A. and Soustelle, V., 2011. Effect of dynamic recrystallization on olivine crystal preferred orientations in mantle xenoliths deformed under varied stress conditions. Journal of Structural Geology, 33: 1528-1540.

Férot, A. and Bolfan-Casanova, N., 2012. Water storage capacity in olivine and pyroxene to 14 GPa: Implications for the water content of the Earth's upper mantle and nature of seismic discontinuities. Earth and Planetary Science Letters, 349-350: 218-230.

Frets, E., Tommasi, A., Garrido, C.J. & Padron-Navarta, J.A., Amri, I and Targuisti, K., 2012. Deformation processes and rheology of pyroxenites deformed under lithospheric mantle conditions. J. Struct. Geol., 39 : 138-157, doi :10.1016/j.jsg.2012.02.019

Frets, E.C., Tommasi, A., Garrido, C.J., Vauchez, A., Mainprice, D., Targuisti, K., Amri, I., 2014. The Beni Bousera Peridotite (Rift Belt, Morocco): an oblique-slip low angle shear zone thinning the subcontinental mantle lithosphere. Journal of Petrology, 55(2): 283-313.

Gao, S. et al., 1997. SKS splitting beneath continental rift zones. Journal of geophysical Research, 102(B10): 22781-22797.

Garrido, C.J., Gueydan, F., Booth-Rea, G., Précigout, J., Hidas, K., Padrón-Navarta, J.A., Marchesi, C., 2011. Garnet lherzolite and garnet-spinel mylonite in the Ronda peridotite: Vestiges of Oligocene backarc mantle lithospheric extension in the western Mediterranean. Geology, 39: 927-930.

Gashawbeza, E.M., Klemperer, S.L., Nyblade, A.A., Walker, K.T., Keranen, K.M., 2004. Shear-wave splitting in Ethiopia: Precambrian mantle anisotropy locally modified by Neogene rifting. Geophysical Research Letters, 31, 1-4.

Gibson, S.A., McMahon, S.C., Day, J.A., Dawson, J.B., 2013. Highly refractory lithospheric mantle beneath the Tanzanian Craton: Evidence from Lashaine pre-metasomatic garnet-bearing peridotites. Journal of Petrology 54, 1503-1546.

Grant, K., Ingrin, J., Lorand, J. and Dumas, P., 2007. Water partitioning between mantle minerals from peridotite xenoliths. Contributions to Mineralogy and Petrology, 154(1): 15-34.

Hammond, J.O.S., Kendall, J.-M., Wookey, J., Stuart, G.W., Keir, D., Ayele, A., 2014. Differentiating flow, melt, or fossil seismic anisotropy beneath Ethiopia. Geochemistry Geophysics Geosystems 15, 1878-1894.

Hansen, S., Zhao, Y., Zimmerman, M.E. and Kohlstedt, D.L., 2014. Protracted fabric evolution in olivine: implications for the relationship among strain, crystallographic fabric, and seismic anisotropy. Earth and Planetary Science Letters, 387: 157-168.

Hielscher, R. and Schaeben, H., 2008. A novel pole figure inversion method: specification of the MTEX algorithm. Journal of Applied Crystallography, 41: 1024-1037.

Higgie, K. and Tommasi, A., 2014. Deformation in a partially molten mantle: Contraints from plagioclase-lherzolites from Lanzo, western Alps. Tectonophysics, 615-616: 167-181.

Higgie, K. and Tommasi, A., 2012. Feedbacks between deformation and melt distribution in the crust-mantle transition zone of the Oman ophiolite. Earth and Planetary Science Letters, 359-360: 61-72.

Hirschmann, M.M., Aubaud, C. and Withers, A.C., 2005. Storage capacity of H2O in nominally anhydrous minerals in the upper mantle. Earth and Planetary Science Letters, 236(1-2): 186-181.

Hirth, G., Kohlstedt, D., 2013. Rheology of the Upper Mantle and the Mantle Wedge: A View from the Experimentalists, Inside the Subduction Factory. American Geophysical Union, pp. 83-105.

Julià, J., Ammon, C.J. and Nyblade, A., 2005. Evidence for mafic lower crust in Tanzania, East Africa, from joint inversion of receiver functions and Rayleigh wave dispersion velocities. Geophysical Journal International, 162: 555-569.

Jung, H., Katayama, I., Jiang, Z., Hiraga, T. and Karato, S., 2006. Effect of water and stress on the lattice-preferred orientation of olivine. Tectonophysics, 421(1-2): 1-22.

Kelemen, P.B., 1990. Reaction between ultramafic rock and fractionating basaltic magma I. Phase relations, the origin of calc-alkaline magma series, and the formation of discordant dunite. Journal of Petrology, 31(1): 51-98.

Kelemen, P.B. and Dick, H.J.B., 1995. Focused melt flow and localized deformation in the upper-mantle juxtaposition of replacive dunite and ductile shear zones in the josephine peridotite, SW oregon. Journal of geophysical Research, 100(B1): 423-438.

Kelemen, P.B., Shimizu, N. and Salters, V.J.M., 1995. Extraction of mid-ocean-ridge basalt from the upwelling mantle by focused flow of melt in dunite channels. Nature, 375: 747-753.

Kendall, J.-M., Stuart, G.W., Ebinger, C., Bastow, I.D. and Keir, D., 2005. Magma-assisted rifting in Ethiopia. Nature, 433: 146-148.

Kohlstedt, D.L. and Zimmerman, M.E., 1996. Rheology of partially molten mantle rocks. Annual Review of Earth and Planetary Sciences, 24(1): 41-62.

Kovacs, I., O'Neill, H.C.J., Hermann, J. and Hauri, E.H., 2010. Site-specific infrared O-H absorption coefficients for water substitution into olivine. American Mineralogist, 95: 292-299.

Kubo, K., 2002. Dunite formation processes in highly depleted peridotite: Case study of the Iwanaidake peridotite, Hokkaido, Japan. Journal of Petrology, 43(3): 423-448.

Kurosawa, M., Yurimoto, H. and Sueno, S., 1997. Patterns in the hydrogen and trace element compositions of mantle olivines. Physics and Chemistry of Minerals, 24(6): 385-395.

Lee, C.-T., 2001. The origin, evolution, and demise of continental lithospheric mantle: perspectives from Re-Os isotopes, geochemistry, petrology, and modeling. Harvard University, PhD Thesis.

Le Gall, B. et al., 2008. Rift propagation at craton margin. Distribution of faulting and volcanism in the North Tanzanian Divergence (East Africa) during Neogene times. Tectonophysics, 448: 1-19.

Le Roux, V., Tommasi, A., Vauchez, A., 2008. Feedback between deformation and melt percolation in an exhumed lithosphere-asthenosphere boundary. Earth Planet. Sci. Lett., 274: 401-413, doi: 10.1016/j.epsl.2008.07.053

Li, J., Kornprobst, J., Vielzeuf, D. and Fabriès, J., 1995. An improved experimental calibration of the olivine-spinel geothermometer. Chinese Journal of Geochemistry, 14(1): 68-77.

Li, Z.-X.A., Lee, C.-T.A., Peslier, A.H., Lenardic, A. and Mackwell, S.J., 2008. Water contents in mantle xenoliths from the Colorado Plateau and vicinity: Implications for the mantle rheology and hydration-induced thinning of continental lithosphere. J. Geophys. Res., 113(B9): B09210.

MacDonald, R., Rogers, N.W., Fitton, J.G., Black, S. and Smith, M., 2001. Plume-lithosphere interactions in the generation of the basalts of the Kenya Rift, East Africa. Journal of Petrology, 42: 877-900.

MacIntyre, R.M., Mitchell, J.G. and Dawson, J.B., 1974. Age of the fault movements in the Tanzanian sector of the East African rift system. Nature, 247: 354-356.

Mainprice, D., 1990. A FORTRAN program to calculate seismic anisotropy from the lattice preferred orientation of minerals. Comp. Geosci., 16: 385-393.

Mainprice, D. and Silver, P.G., 1993. Interpretation of SKS-waves using samples from the subcontinental lithosphere. Physics of the Earth and Planetary Interiors, 78(3-4): 257-280.

Mainprice, D., Hielscher, R. and Schaeben, H., 2011. Calculating anisotropic physical properties from texture data using the MTEX open source package. In: D.J. Prior, Rutter, E.H., Tatham, D. J. (Editor), Deformation Mechanisms, Rheology and Tectonics: Microstructures, Mechanics and Anisotropy. Geological Society, Special Publications, London, pp. 175-192.

Mainprice, D., Bachmann, F., Hielscher, R. and Schaeben, H., 2014. Descriptive tools for the analysis of texture projects with large datasets using MTEX - strength, symmetry and components. Geological Society of London Special Publication, In Field Experiment and Theory : In Honour of Ernest Rutter.

Mansur, A.T., Shukrani, M., Timpa, S., Rudnick, R.L., 2014. Granulite-facies xenoliths in rift basalts of Northern Tanzania: Age, Composition and origin of Archean lower crust. Journal of Petrology 55, 1243-1286.

Matsyuk, S.S. and Langer, K., 2004. Hydroxyl in olivines from mantle xenoliths in kimberlites of the Siberian platform. Contributions to Mineralogy and Petrology, 147(4): 413-437.

Matsyuk, S.S., Langer, K. and Hösch, A., 1998. Hydroxyl defects in garnets from mantle xenoliths in kimberlites of the Siberian platform. Contributions to Mineralogy and Petrology, 132(2): 163-179.

McKenzie, D., 1978. Some remarks on the development of sedimentary basins. Earth and Planetary Science Letters, 40: 25-32.

Miller, G.H., Rossman, G.R. and Harlow, G.E., 1987. The natural occurrence of hydroxide in olivine. Physics and Chemistry of Minerals, 14(5): 461-472.

Möller, A., Mezger, K. and Schenk, V., 1998. Crustal age domains and the evolution of the continental crust int he Mozambique Belt of Tanzania: Combined Sm-Nd, Rb-Sr, and Pb-Pb isotopic evidence. Journal of Petrology, 39: 749-783.

Möller, A., Appel, P., Mezger, K. and Schenk, V., 1995. Evidence for a 2 Ga subduction zone: eclogites in the Usagaran belt of Tanzania. Geology, 23: 1067-1070.

Morgan, Z.T. and Liang, Y., 2003. An experimental and numerical study of the kinetics of harzburgite reactive dissolution with applications to dunite dike formation. Earth and Planetary Science Letters, 214: 59-74.

Morley, C.K., Wescott, W.A., Stone, D.M., Harper, R.M., Wigger, S.T. and Karanga, F.M., 1992. Tectonic evolution of the northern Kenya rift. Journal of the geological society, London, 149: 333-348.

Nyblade, A.A. and Brazier, R.A., 2002. Precambrien lithospheric controls on the development of the East African rift system. Geology, 30(8): 755-758.

Nyblade, A., Birt, C., Langston, C.A., Owens, T.J. and Last, R.J., 1996. Seismic experiment reveals rifting of craton in Tanzania. Eos (Transactions American Geophysical Union), 77(51): 517-521.

Nicolas, A., Achauer, U. and Daignieres, M., 1994. Rift initiation by lithospheric rupture. Earth and Planetary Science Letters, 123: 281-298.

Nicolas, A., Bouchez, J.L., Boudier, F., 1972. Interprétation cinématique des déformations plastiques dans le massif de lherzolite de Lanzo (Alpes piémontaises) - Comparaison avec d'autres massifs. Tectonophysics 14, 143-171.

Padrón-Navarta, J.A., Hermann, J. and O'Neill, H., 2014. Site-specific hydrogen diffusion rates in Forsterite. Earth and Planetary Science Letters, 392: 100-112.

Padrón-Navarta, J.A., Tommasi, A., Garrido, C.J., López Sánchez-Vizcaíno, V., Gómez-Pugnaire, M.T., Jabaloy, A. and Vauchez, A., 2010. Fluid transfer into the wedge controlled by high-pressure hydrofracturing in the cold top-slab mantle. Earth and Planetary Science Letters, 297(1-2): 271-286.

Paterson, M.S., 1982. The determination of hydroxyl by infrared absorption in quartz, silicate glasses and similar materials. Bulletin de Minéralogie, 105(1): 20-29.

Peslier, A.H., 2010. A review of water contents of nominally anhydrous natural minerals in the mantles of Earth, Mars and the Moon. Journal of Volcanology and Geothermal Research, 197(1-4): 239-258.

Peslier, A.H. and Luhr, J.F., 2006. Hydrogen loss from olivines in mantle xenoliths from Simcoe (USA) and Mexico: Mafic alkalic magma ascent rates and water budget of the sub-continental lithosphere. Earth and Planetary Science Letters, 242(3-4): 302-319.

Peslier, A.H., Luhr, J.F. and Post, J., 2002. Low water contents in pyroxenes from spinel-peridotites of the oxidized, sub-arc mantle wedge. Earth and Planetary Science Letters, 201(1): 69-86.

Peslier, A.H., Woodland, A.B. and Wolff, J.A., 2008. Fast kimberlite ascent rates estimated from hydrogen diffusion profiles in xenolithic mantle olivines from southern Africa. Geochimica et Cosmochimica Acta, 72(11): 2711-2722.

Phakey, P., Dollinger, G. and Christie, J.M., 1972. Transmission electron microscopy of experimentally deformed olivine. Flow and Fracture of Rocks, Geophysical Monograph, 16: 117-138.

Pinna, P., Jourde, G., Calvez, J.Y., Mroz, J.P. and Marques, J.M., 1993. The Mozambique Belt in northern Mozambique: Neoproterozoic (1100-850 Ma) crustal growth and tectogenesis, and superimposed Pan-African (800-550 Ma) tectonism. Precambrian Research, 62: 1-59.

Raleigh, C.B., 1968. Mechanisms of plastic deformation of olivine. Journal of geophysical Research, 73(16): 5391-5406.

Raterron, P., Amiguet, E., Chen, J.H., Li, L. and Cordier, P., 2009. Experimental deformation of olivine single crystals at mantle pressures and temperatures. Physics of the Earth and Planetary Interiors, 172(1-2): 74-83.

Rudnick, R.L., McDonough, W.F. and Chappell, B.W., 1993. Carbonite metasomatism in the northern Tanzanian mantle: petrographic and geochemical characteristics. Earth and Planetary Science Letters, 114: 463-475.

Rudnick, R.L., McDonough, W.F. and Orpin, A., 1994. Northern Tanzanian peridotite xenoliths: a comparison with Kaapvaal peridotites and inferences of metasomatic

interactions, in: Kimberlites, Related Rocks and Mantle Xenoliths. In: Meyer, H.O.A. and Leonardos, O.H. (Editor), Proceedings of the 5th International Kimberlite Conference, pp. 336-353.

Ruotoistenmäki, T., 2014. Geophysical characteristics of Aswa shear, Nagasongola discontinuity and ring dyke complex in Uganda. Journal of African Earth Sciences, 93: 23-41.

Ryan, W.B.F., S.M. Carbotte, J.O. Coplan, S. O'Hara, A. Melkonian, R. Arko, R.A. Weissel, V. Ferrini, A. Goodwillie, F. Nitsche, J. Bonczkowski, and R. Zemsky, 2009. Global Multi-Resolution Topography synthesis. Geochemistry Geophysics Geosystems, 10, Q03014, doi:10.1029/2008GC002332.

Sachtleben, T. and Seck, H.A., 1981. Chemical control of Al-solubility in orthopyroxene and its implications on pyroxene geothermometry. Contributions to Mineralogy and Petrology, 78: 157-165.

Sicilia, D., Montagner, J.-P., Cara, M., Stutzmann, E., Debayle, E., Lépine, J.-C., Lévêque, J.-J., Beucler, E., Sebai, A., Roult, G., Ayele, A., Sholan, J.M., 2008. Upper mantle structure of shear-waves velocities and stratification of anisotropy in the Afar Hotspot region. Tectonophysics 462, 164-177.

Sokol, A.G., Palyanov, Y.N., Kupriyanov, I.N., Litasov, K.D. and Polovinka, M.P., 2010. Effect of oxygen fugacity on the H2O storage capacity of forsterite in the carbon-saturated systems. Geochimica et Cosmochimica Acta, 74: 4793-4806.

Soustelle, V., Tommasi, A., Demouchy, S., Franz, L., 2013. Melt-rock interactions, deformation, hydration and seismic properties in the sub-arc lithospheric mantle inferred from xenoliths from seamounts near Lihir, Papua New Guinea. Tectonophysics 608, 330–345.

Soustelle, V., Tommasi, A., Demouchy, S. and Ionov, D.A., 2010. Deformation and Fluid, a Rock Interaction in the Supra-subduction Mantle: Microstructures and Water Contents in Peridotite Xenoliths from the Avacha Volcano, Kamchatka. Journal of Petrology, 51(1-2): 363-394.

Soustelle, V., Tommasi, A., Bodinier, J.-L., Garrido, C.J. and Vauchez, A., 2009. Deformation and reactive melt transport in the mantle lithosphere above a large-scale partial melting domain: the Ronda peridotite massif, southern Spain. Journal of Petrology, 50(7): 1235-1266.

Thoraval, C., Demouchy, S., 2014. Numerical models of ionic diffusion in one and three dimensions: application to dehydration of mantle olivine. Phys Chem Minerals 41, 709–723.

Tommasi, A. and Vauchez, A., 2001. Continental rifting parallel to ancient collisional belts: an effect of the mechanical anisotropy of the lithospheric mantle. Earth and Planetary Science Letters, 185: 199-210.

Tommasi, A., Tikoff, B. and Vauchez, A., 1999. Upper mantle tectonics: three-dimensional deformation, olivine crystallographic fabrics and seismic properties. Earth and Planetary Science Letters, 168(1-2): 173-186.

Tommasi, A., Vauchez, A. and Ionov, D.A., 2008. Deformation, static recrystallisation, and reactive melt transport in shallow subcontinental mantle xenoliths (Tol Cenozoic volcanic field, SE Siberia). Earth and Planetary Science Letters, 272(1-2): 65-77.

Tommasi, A., Mainprice, D., Canova, G. and Chastel, Y., 2000. Viscoplastic self-consistent and equilibrium-based modeling of olivine lattice preferred orientations: Implications for the upper mantle seismic anisotropy. J. Geophys. Res., 105(B4): 7893-7908.

Tommasi, A., Godard, M., Coromina, G., Dautria, J.-M. and Barsczus, H., 2004. Seismic anisotropy and compositionally induced velocity anomalies in the lithosphere above

mantle plumes: a petrological and microstructural study of mantle xenoliths from French Polynesia. Earth and Planetary Science Letters, 227(3-4): 539-556.
Tommasi, A., Knoll, M., Vauchez, A., Signorelli, J., Thoraval, C. and Loge, R., 2009. Structural reactivation in plate tectonics controlled by olivine crystals anisotropy. Nature Geoscience, 2: 423-427.
Tubìa, J.M., Cuevas, J. and Esteban, J.J., 2004. Tectonic evidence in the Ronda peridotites, Spain, for mantle diapirism related to delamination. Geology, 32(11): 941-944.
Vauchez, A., Barruol, G. and Tommasi, A., 1997. Why do continents break-up parallel to ancient orogenic belts? Terra Nova, 9: 62-66.
Vauchez, A., Dineur, F. and Rudnick, R.L., 2005. Microstructure, texture and seismic anisotropy of the lithospheric mantle above a mantle plume: Insights from the Labait volcano xenoliths. Earth and Planetary Science Letters, 232(3-4): 295-314.
Vauchez, A., Tommasi, A. and Mainprice, D., 2012. Faults (shear zones) in the Earth's mantle. Tectonophysics, 558-559: 1-27.
Vauchez, A., Tommasi, A., Barruol, G. and Maumus, J., 2000. Upper mantle deformation and seismic anisotropy in continental rifts. Physics and Chemistry of the Earth, 25(2): 111-117.
Vollmer, F. W., 1990. An application of eigenvalue methods to structural domain analysis. Geol. Soc. Am. Bull., 102: 786-791.
Walker, K.T., Nyblade, A.A., Klemperer, S.L., Bokelmann, G.H.R. and Owens, T.J., 2004. On the relationship between extension and anisotropy: Constraints from shear wave splitting accross the East African Plateau. Journal of geophysical Research, 109(B08302): 1-21.
Wells, P.R.A., 1977. Pyroxene thermometry in simple and complex systems. Contributions to Mineralogy and Petrology, 62: 129-139.
Wernicke, B., 1981. Low angle normal faults in Bassin and Range province. Nappe tectonics in an extending orogen. Nature, 291: 645-648.
Wernicke, B., 1985. Uniform-sense normal simple shear of the continental lithosphere. Canadian Journal of Earth Sciences, 22: 108-125.
Wilkinson, P., Mitchell, J.G., Cattermole, P.J. and Downie, C., 1986. Volcanic chronology of the Meru-Kilimanjaro region, Northern Tanzania. Journal of the geological society, London, 143: 601-605.
Withers, A.C., Bureau, H., Raepsaet, C. and Hirschmann, M.M., 2012. Calibration of infrared spectroscopy by elastic recoil detection analysis of H in synthetic olivine. Chemical Geology, 334: 92-98.
Witt-Eickschen, G. and Seck, H.A., 1991. Solubility of Ca and Al in orthopyroxene from spinel peridotite: an improved version of an empirical geothermometer. Contributions to Mineralogy and Petrology, 106(4): 431-439.
Yang, X.-Z., Xia, Q.-K., Deloule, E., Dallai, L., Fan, Q.-C. and Feng, M., 2008. Water in minerals of the continental lithospheric mantle and overlying lower crust: A comparative study of peridotite and granulite xenoliths from the North China Craton. Chemical Geology, 256(1-2): 33-45.
Zaffarana, C., Tommasi, A., Vauchez, A. Grégoire, M., 2014. Microstructures and seismic properties of south Patagonian mantle xenoliths (Gobernador Gregores and Pali Aike). Tectonophysics, 621: 175-197, doi : 10.1016/j.tecto.2014.02.017
Zimmerman, M.E. and Kohlstedt, D.L., 2004. Rheological properties of partially molten lherzolite. Journal of Petrology, 45(2): 275-298.

Chapitre 6 : Déformation et anisotropie du manteau lithosphérique sous un rift mature

Le rift Est-Africain est l'un des principaux rifts actifs de la planète. Il offre la possibilité d'étudier le rifting à différents stades de maturité, de l'initiation jusqu'à l'accrétion océanique. Si des études ont apportées des contraintes importantes sur la déformation de surface et le magmatisme durant le rifting, ainsi que le rôle des panaches mantelliques (e.g. Biggs et al., 2011; Corti, 2008; Ebinger et al., 1993; Stewart et Rogers, 1996), peu de choses sont connues sur la manière dont le manteau accommode la déformation durant le rifting. La présence de magmas à petite échelle peut diminuer de façon significative la viscosité du manteau (Hirth and Kohlstedt, 2003; Kohlstedt and Zimmerman, 1996; Kohlstedt et al., 2000; Zimmerman and Kohlstedt, 2004). Or, la partie éthiopienne du rift Est Africain a été soumise à plusieurs épisodes magmatiques importants. La formation rapide du plateau magmatique Ethiopien il y a 30 Ma (Ebinger, 1993; Georges et al., 1998; Hofman et al., 1997) a précédé un second épisode volcanique et de début de l'extension au Miocène (Ebinger et al., 1993; Hendrie et al. 1994; Morley et al. 1992). Enfin, la région enregistre un dernier épisode volcanique Plio-Pléistocène, se traduisant sous la forme de cônes et de fissures volcaniques au cœur de la vallée du rift (Bonini et al., 2005; Ebinger et al., 1993; Furman, 2007; Shinjo et al., 2011).

Le travail présenté dans ce chapitre repose sur l'analyse de 25 xénolites mantelliques (20 péridotites, 5 pyroxénites) du rift Est-Africain au Sud de Mega, en bordure Sud du plateau éthiopien. Cette étude est basée sur la caractérisation des microstructures et des OPRs des xénolites éthiopiens, ainsi que le calcul de leurs propriétés sismiques. Elle vise à mieux comprendre les relations entre déformation et percolation de fluides et magmas durant le rifting.

Les péridotites du Sud de Mega présentent des microstructures homogènes, suggérant que ces roches n'enregistrent probablement pas de variations spatiales ou temporelles des conditions de déformation. Contrairement à ce qui a précédemment été rapporté par Bedini et al. (1997), nous n'observons pas de variations significatives des microstructures en fonction du type de métasomatisme. La variation de l'espacement entre sous-joints dans les

porphyroclastes d'olivine, ainsi que la polygonisation variable des néoblastes d'olivine, suggèrent une déformation suivie par un recuit variable. Les OPRs de l'olivine de type orthorhombique indiquent une déformation par fluage-dislocation avec activation du système de glissement [100] (010). La présence de clinopyroxène et d'orthopyroxène suggère une cristallisation secondaire, probablement associée à l'épisode métasomatique identifié par Bedini et al. (1997). Les OPRs mesurées dans l'orthopyroxène et parfois dans le clinopyroxène, ainsi que la cohérence généralement observée entre les OPRs de l'olivine et de l'orthopyroxène, indiquent un épisode métasomatique pré- à syn-cinématique.

L'anisotropie azimutale maximale des ondes P varie entre 3.1 et 12.3%, tandis que l'anisotropie de polarisation maximale des ondes S est comprise entre 2.9 et 8.3%. De telles anisotropies ne peuvent expliquer à elles seules les déphasages des ondes SKS mesurées au niveau du rift Ethiopien et du rift Kenyan. Les microstructures et les relations entre magmas et percolation dans les péridotites éthiopiennes sont différentes de celles observées dans les xénolites de la Divergence Nord-Tanzanienne ou du Nord Kenya. La comparaison de ces données indique que, bien que la percolation de magmas dans le manteau lithosphérique durant le rifting soit commune, son timing par rapport à la déformation varie.

Deformation and anisotropy of the lithospheric mantle beneath a mature rift: constraints from mantle xenoliths from Southern Mega, SE Ethiopia

Virginie Baptiste, Andréa Tommasi, and Alain Vauchez

Géosciences Montpellier, Université Montpellier 2 & CNRS, CC 60, Place E. Bataillon, 34095 Montpellier cedex 5, France.

Running title: Deformation of the lithospheric mantle beneath a mature rift

(*) corresponding author: virginie.baptiste@gm.univ-montp2.fr;
Phone: +33 467144912
Fax: +33 467143603

1. Introduction

The East African rift is great natural laboratory, which allows studying continental rifting at variable degree of maturity, from its initiation to oceanic accretion. Over the past years, studies have brought important constraints on surface deformation and magmatism during rifting, as well as on the role of mantle plumes (e.g. Biggs et al., 2011; Corti, 2008; Ebinger et al., 1993; Stewart et Rogers, 1996). Despite this, little is known about how the lithospheric mantle accommodate rifting deformation through time. Many studies point out the major role of magmas during rifting initiation and formation. Buck (2006), for instance, proposed that dyke intrusions might help initiating the deformation within the strong continental lithosphere. This hypothesis is supported by seismic anisotropy studies, which suggest the presence of oriented melt pockets in the crust and the mantle within the rift axis in Ethiopia and in Afar (Bastow et al., 2010; Hammond et al., 2014). At a larger scale, body-wave tomography images a broad and deep low velocity anomaly beneath the Ethiopian Plateau and the eastern branch of the rift system in Kenya and Tanzania, that have been proposed to be linked to the African Superplume (Nyblade, 2011). The presence of magma at a smaller scale may significantly decrease mantle viscosity (Hirth and Kohlstedt, 2003; Kohlstedt and Zimmerman, 1996; Kohlstedt et al., 2000; Zimmerman and Kohlstedt, 2004). Reaction with melts or fluids may as well reduce mantle strength through crystallization of weaker phases, grain size reduction, and phase mixing (e.g., Dijkstra et al. 2002; Soustelle et al. 2010).

In Ethiopia, the rapid formation of the magmatic Plateau during a plume-related peak volcanism at 30 Ma (Ebinger, 1993; Georges et al., 1998; Hofman et al., 1997) preceded continental extension initiation and a later volcanic episode in the Miocene (Ebinger et al., 1993; Hendrie et al. 1994; Morley et al. 1992). The Ethiopian branch of the East African Rift, the main Ethiopian rift, is therefore an ideal location to study the way the lithospheric mantle accommodated the rifting deformation in a mature rift and the role of magmatism in this process.

In the present study, we explore the relation between deformation and melt percolation in a suite of mantle xenoliths from the southern end of the main Ethiopian rift (South of Mega, Sidamo region). Based on their crystallographic preferred orientations and mineralogical compositions, we also estimate their seismic anisotropy and compare it to seismic anisotropy data performed in the area.

2. Geological background

2.1 Geological setting

The East African rift is one of the most active rifts on Earth. It extends over more than 4000 km, from the Afar triple junction to the Gulf of Mozambique, and splits into two branches around the Tanzanian craton. The Eastern branch and the main Ethiopian rift of the East African rift overlap in the Turkana Depression, a 300 km wide system of extensional basins (Shinjo et al., 2011), where the earliest traces of volcanic activity (45 Ma) in the East African rift system were found (Ebinger et al., 1993, Georges et al., 1998). Extension in the main Ethiopian rift started in South Ethiopia at ~25-20 Ma (Ebinger et al., 1993; Hoffman et al., 1997; Kieffer et al., 2004; Woldegabriel et al., 1991), through the thick Ethiopian plateau, which formed from a peak volcanic activity at 31-30 Ma. The region also records two later, lower volumes, volcanic episodes: one during the Miocene (19-11 Ma) dominated by alkaline basalts and trachytes, and another during the Plio-Pleistocene, occurring as fissural lavas and cinder cones within the rift axis (Bonini et al., 2005; Ebinger et al., 1993; Furman, 2007; Shinjo et al., 2011).

Seismic studies have investigated the structure of the Ethiopian rift. Joint inversion of Rayleigh wave group velocities and receiver functions indicate lithospheric thicknesses of 80-90 km beneath the Ethiopian Plateau (Dugda et al, 2007). In the lithospheric mantle, maximum S-waves velocities of 4.3 km/s and 4.1-4.2 km/s are measured beneath the Ethiopian Plateau and the main Ethiopian rift, respectively (Dugda et al, 2007). Based on 1D conductive thermal model, Dugda et al. (2007) suggested that a plume model could explain this structure, provided that the lithosphere was thinned by ~30-50 km, above a plume during the flood basalt volcanism at 30 Ma, and the warm material stayed beneath the lithosphere since then. Beneath the Ethiopian Plateau, body-wave tomographies also image a 500 km wide and 400 km thick anomaly at ~100-300 km depth, interpreted as the upper mantle continuation of the African Superplume (Bastow et al., 2008, Benoit et al., 2006). Within the main Ethiopian rift, SKS studies report coherent rift-parallel polarization of the fast S-wave (Gashawbeza et al., 2004; Kendall et al., 2005), but variable delay times (0.5-1.7s: Gashawbeza et al., 2004, 1-3 s: Kendall et al., 2005). Variations in splitting parameters and increasing amount of splitting above regions of recent volcanism support the idea of an anisotropic signal dominated by oriented melt pockets (Ayele et al., 2004; Kendall et al., 2005). However, beneath the Ethiopian plateau, the measured anisotropy may be related to a pre-existing fabric frozen in the lithosphere (Gashawbeza et al., 2004; Hammond et al., 2014). Surface waves and SKS studies report the presence of a ~100 km thick anisotropic upper

layer (Bastow et al., 2010; Hammond et al., 2010; Sicilia et al., 2008), possibly caused by a fossil fabric (Sicilia et al., 2008), which locally contains oriented melt pockets (Bastow et al., 2010; Hammond, 2014; Sicilia et al., 2008). A more recent SKS study shows the existence of two anisotropic layers (Hammond et al., 2014): an upper layer with variable polarization directions in the Ethiopian plateau and the main Ethiopian rift, and lower anisotropic layer with a consistent NE-SW orientation that could be attributed to flow from the African Superplume.

In the Sidamo region (South Mega, SE Ethiopia), on the southern border of the Ethiopian plateau and the southern end of the Ethiopian rift, lava flows and pyroclastic rocks with basanitic to nephelinitic compositions erupted in the late Pleistocene, carrying mantle xenoliths (Morten et al., 1992; Bedini et al., 1997). The present study focuses on twenty-five mantle xenoliths from this region (Fig. 1).

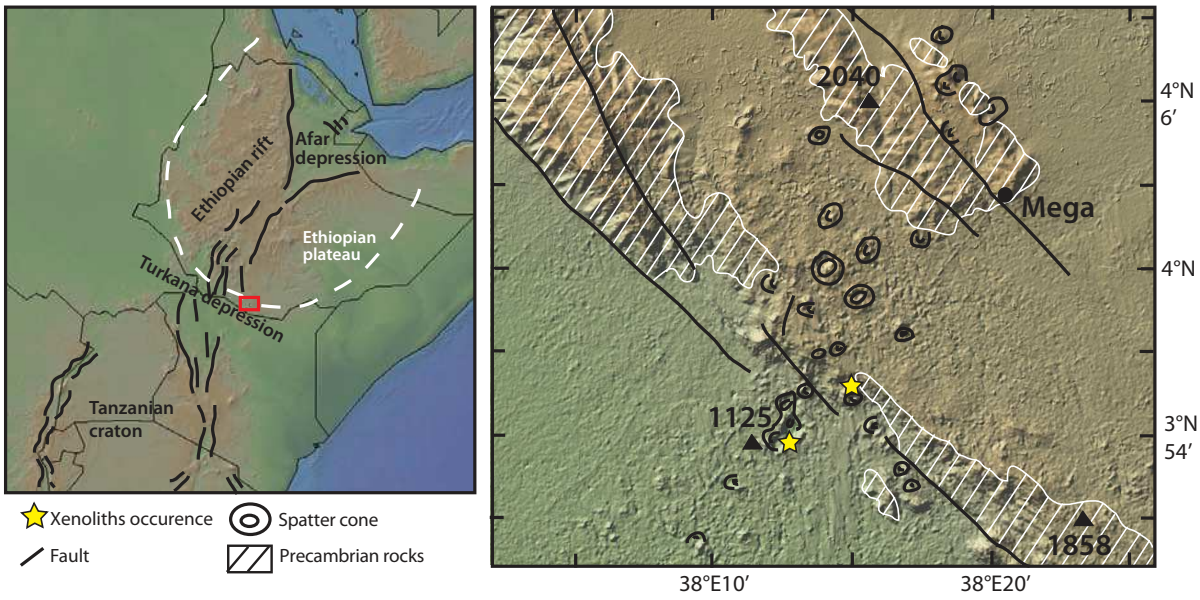

Fig. 1: Digital topographic map (http://www.geomapapp.org, topography data from Ryan et al., 2009) showing the East African rift and the xenolith localities studied here. Location of the Precambrien rocks, spatter cones, and faults near Mega were reported as in Morten et al. (1992).

2.2 Sample set: geochemical background

The geochemical composition of the studied mantle xenoliths has been previously studied in detail (Bedini, 1994; Bedini et al., 1997; Bedini et al., 1999; Lorand et al., 2003). Bedini et al. (1997) showed that beneath south Mega, the lithospheric mantle was infiltrated by asthenospheric magmas linked to a mantle plume. During their upward migration, these magmas reacted with the surrounding peridotite, which progressively modified their

composition, generating different types of metasomatism along the percolated column and through time (Bedini et al., 1997). Bedini et al. (1997) indeed identified two geochemical groups among the peridotites from south Mega: (1) The less recrystallized samples (or "deformed"), strongly enriched in LILE, with negative anomalies of the HFSE and sometimes apatite-bearing, (2) The more recrystallized samples (or "granular"), depleted or slightly enriched in LILE and devoided of significant HFSE anomaly. The geochemical characteristics of "deformed" peridotites were interpreted as the result of interaction with small fractions of LILE-enriched melts saturated in Ti-oxides, while "granular" peridotites are believed to have re-equilibrated with high fractions of basaltic melts (Bedini et al., 1997). In deformed peridotites, PGE abundances and sulphides modal compositions suggest interaction with volatile-rich small melt fractions (Lorand et al., 2003), while in granular peridotites, re-equilibration with OIB-like melts in high porosity zones at the bottom of the lithosphere is likely.

Because our observations and interpretations on sample microstructures are significantly different than that of Bedini et al. (1997), we will refer in the following to "deformed" peridotites as "metasomatism 1" (M1) peridotites and to granular peridotites as "metasomatism 2" (M2) peridotites.

3. Methods

3.1 Electron-backscattered diffraction (EBSD)

The crystallographic preferred orientations (CPO) of olivine, pyroxenes, garnet and spinel were measured at the SEM-EBSD facility at Geosciences Montpellier by indexation of electron back-scattered diffraction (EBSD) patterns produced by interaction of an incident electron beam with a carefully polished thin section tilted at 70° to the electron beam. Measurements were performed in a JEOL JSM 5600 scanning electron microscope using an acceleration voltage of 17 kV and a working distance of 23 mm. Maps covering almost entirely each thin section were obtained using steps between 100 and 30 μm, depending on grain size. Indexation rates ranged between 70 and 90% depending of the mineral. Orthopyroxene and clinopyroxene were seldom misindexed for one another. Careful post-acquisition data treatment by comparing EBSD maps and microscopic observations was performed to reduce inaccurate mineral determination and misindexation due to olivine pseudosymmetry. Grain sizes and modal compositions were also obtained from EBSD maps.

Crystal-preferred orientation data is displayed in pole figures, presented as lower hemisphere stereographic projections. To avoid over-representation of large grains, data were

reduced to one average crystallographic orientation per grain. When the foliation and lineation could be identified, the orientation of the main crystallographic directions: [100], [010] and [001] for olivine and pyroxenes, was plotted relatively to the principal axes of the deformation ellipsoid X, Y, and Z. Because the foliation and lineation could not be identified in coarse-grained samples, thin sections were cut in random orientations. To allow comparison between different samples, we rotated the CPO of randomly oriented samples into a common orientation, in which the maximum concentration of olivine [100] and [010] axes are parallel to the E–W and the N–S directions of the pole figure, respectively.

To better describe the olivine CPO symmetry, we calculated the dimensionless BA index (Mainprice et al., 2014) defined as:

$$BAindex = \frac{1}{2}\left(2-\left(\frac{P010}{G010+P010}\right)-\left(\frac{G100}{G100+P100}\right)\right) \quad (1)$$

Where P and G are indexes used to characterize the shape of the distribution (P for Point and G for Girdle; Vollmer, 1990) of the olivine principal axes ([100], [010] and [001]); these indexes were calculated from the eigenvalues of the normalized orientation matrix as P=λ1-λ3 and G=2(λ2-λ3), calculated using the MTEX texture analysis Matlab toolbox (Hielscher and Schaeben, 2008; Mainprice et al., 2011). The BA index allows a more precise classification of the olivine CPO symmetry into 3 types: axial-[010] (BA index<0.35), orthorhombic (0.35<BA index<0.65), and axial-[100] (BA index>0.65).

The strength of the fabric was quantified using the dimensionless J-index, which is the volume-averaged integral of squared orientation densities defined by:

$$J = \int f(g)^2 dg \quad (2)$$

where f(g) is the orientation distribution function (ODF) and $dg = d\varphi_1 d\varphi d\varphi_2 \sin\varphi\pi^2$. φ_1, φ, and φ_2 are the Euler angles, that define the rotations allowing for coincidence between the crystallographic and external reference frames. Natural peridotites classically show J-indexes between 2 and 20, with a peak at 8–10 (Ben Ismaïl and Mainprice, 1998; Tommasi et al., 2000). The J-index for each sample was calculated based on the mean orientation of each grain using the MTEX texture analysis Matlab toolbox.

3.2 Seismic properties

Seismic properties were calculated using the CPO of all major phases and their respective modal content estimated from EBSD maps (Mainprice, 1990). For olivine,

Table 1:

Sample	Thin section name	Rock type	Apatite-bearing samples	Texture	Metasomatism type from Bedini et al. (1997)	Temperature[a] (°C)	Ol Mg# (%)	Opx Mg# (%)	Reference for mg# and T data	Modal compositions[b] (%)					Olivine CPO type	Olivine J-index	Olivine BA index	Density ($g.cm^{-3}$)	Max AVp (%)	Max AVs pol (%)	Max AVS_1 (%)	Max AVS_2 (%)
										ol	opx	cpx	gt	sp								
ET32	ET32	Lz		CP	M2	1049	88.5	89.3	Bedini, 1994	46	36	16	0	2	ortho	3.8	0.39	3.3676	3.1	3.9	2.6	2.8
ET40	ET40	Lz		CP	M2	-	-	-	-	62	21	15	0	2	ortho	3.1	0.71	3.3752	4.3	3.7	1.8	2.9
ET41	ET41	Lz	x	CP	M1	-	-	-	-	78	14	7	0	1	ortho	3.9	0.42	3.3635	7.0	6.4	3.5	3.7
ET46	ET46	Lz	x	CP	M1	1009	90.9	91.8	Bedini, 1994	83	11	5	0	1	ortho	5.7	0.48	3.3656	10.5	6.6	3.8	5.8
ET48	ET48A	Lz		CP	M2	942	89.5	89.8	Bedini, 1994	52	26	20	0	2	ortho	3.0	0.75	3.3714	4.7	2.9	1.8	2.6
	ET48B	Lz		CP	M2					56	29	14	0	1	ortho	5.1	0.59	3.3542	5.4	4.9	2.5	2.9
ET49	ET49	Hz	x	CP	M1	954	91.2	92.0	Bedini, 1994	81	15	3	0	1	ortho	3.2	0.56	3.3642	6.8	4.9	2.4	3.5
ET53	ET53	Lz		CP	M2	969	90.2	90.9	Bedini, 1994	72	16	11	0	1	ortho	4.7	0.69	3.3614	7.8	5.3	2.2	4.9
ET54	ET54	Hz	x	CP	M1	901	91.5	92.2	Bedini, 1994	84	12	4	0	0	ortho	7.8	0.62	3.3480	12.3	8.0	4.5	5.9
ET63	ET63	Lz		CP	M2	-	-	-	-	46	24	26	0	4	ortho	3.9	0.34	3.4054	3.8	3.0	2.3	1.6
ET66	ET66A	Lz		CP*	M1	-	-	-	-	69	24	6	0	1	ortho	2.7	0.58	3.3439	5.6	3.6	1.6	3.4
	ET66B	Hz		CP*	M1	-	-	-	-	76	21	3	0	0	ortho	2.0	0.43	3.3695	4.9	3.5	1.6	2.4
ET69	ET69	Lz	x	CP	M1	863	90.7	91.3	Bedini, 1994	50	32	16	0	2	axial-[010] to ortho	4.9	0.45	3.3695	5.2	4.5	2.4	3.0
ET70	ET70A	Lz		CP	M2	-	-	-	-	61	14	23	0	2	ortho	4.0	0.56	3.3584	5.5	4.4	2.3	3.0
	ET70B	Lz		CP	M2	-	-	-	-	53	30	15	0	2	ortho	4.9	0.51	3.3708	3.3	3.3	2.7	2.1
ET73	ET73	Lz		CP	M2	-	-	-	-	61	19	17	0	3	axial-[010]	5.5	0.49	3.3930	5.8	4.3	2.4	3.4
ET74	ET74A	Lz		CP	M2	916	90.9	91.6	Bedini, 1994	61	14	23	0	2	ortho	3.1	0.43	3.3764	6.5	4.2	2.2	3.1
	ET74B	Lz		CP	M2					64	16	19	0	1	ortho	5.0	0.53	3.3592	8.6	5.4	2.1	4.2
ET76	ET76	Lz		CP	M2	933	89.5	90.3	Bedini, 1994	57	30	10	0	3	ortho	3.5	0.79	3.3895	5.2	4.0	1.6	3.4
ET82	ET82	Lz		CP	M2	-	-	-	-	62	20	17	0	1	axial-[010]	3.0	0.41	3.3578	4.1	3.7	2.4	2.7
ET83	ET83A	Hz	x	CP	M1	-	-	-	-	84	13	2	0	1	axial-[010] to ortho	5.7	0.58	3.3654	11.4	7.4	4.0	6.1
	ET83B	Hz	x	CP	M1	-	-	-	-	72	25	2	0	1	axial-[010] to ortho	5.0	0.45	3.3595	7.3	5.7	2.4	3.6
ET84	ET84A	Hz	x	CP*	M1	830	92.1	92.7	Bedini, 1994	86	11	3	0	0	axial-[100] to ortho	4.2	0.56	3.3488	7.4	5.4	2.1	4.3
	ET84B	Hz	x	CP*	M1					76	22	1	0	1	axial-[100] to ortho	4.8	0.68	3.3613	8.8	6.9	3.2	5.4
ET85	ET85A	Lz		CP	M1	-	-	-	-	85	10	5	0	0	ortho	6.4	0.49	3.3487	10.6	7.7	4.8	4.4
	ET85B	Lz		CP	M1	-	-	-	-	66	13	17	0	4	ortho	9.5	0.69	3.4133	6.4	5.7	3.6	3.6
ET-VB1	ET-VB1	Hz		CP*	-	-	-	-	-	79	17	3	0	1	ortho	7.2	0.39	3.3632	12.2	8.3	5.8	5.3
ET55	ET55A	Wb		CP	-	-	-	-	-	0	36	64	0	0	-	-	-	3.3194	6.9	4.2	4.2	3.6
	ET55B	Wb		CP	-	-	-	-	-	0	14	86	0	0	-	-	-	3.3241	-	-	10.6	12.3
ET64B	ET64B	Wb		G	-	-	-	-	-	0	44	54	0	2	-	-	-	3.3530	4.8	3.4	2.4	1.8
ET68	ET68	Cpx		CP	-	-	-	-	-	0	0	90	10	0	-	-	-	3.3753	12.8	9.8	8.5	8.5
ET77	ET77	Wb		CP	-	-	-	-	-	0	42	58	0	0	-	-	-	3.3182	6.5	4.9	4.0	3.5
ET81	ET81	Wb		G	-	-	-	-	-	0	36	53	10	1	-	-	-	3.3854	5.7	4.4	2.3	3.8

[a] Brey and Köhler (1990) thermometry;

[b] Modal compositions determined from EBSD maps;

* Samples bearing automorphic olivines;

Texture: CP= Coarse-porphyroclastic; G= Granular;

Metasomatism type from Bedini et al. (1997):M1= Deformed ; M2= Granular;

CPO types: ortho= orthorhombic, axial-[100], axial-[010], axial-[100] to orthorhombic, and axial-[010] to orthorhombic crystal-preferred orientations, see main text for details.

AVp: Vp azimuthal anisotropy; AVs: Vs azimuthal anisotropy; AVs_1: Fast Vs azimuthal anisotropy; AVs_2: Slow Vs azimuthal anisotropy; maximum values

orthopyroxene, clinopyroxene, garnet and spinel single-crystal elastic constant tensors at ambient conditions were used (Abramson et al., 1997; Chai et al., 1997a; Chai et al., 1997b; Collins and Brown, 1998; Hearmon, 1984). A Voigt-Reuss-Hill averaging was applied in all calculations. The seismic anisotropy parameters and the elastic constants of all samples are presented in Table 1 and online Supplementary Material 1, respectively.

3.3 Thermometry

The samples equilibrium temperature was calculated using the mineral compositions measured by Bedini (1994). The two pyroxenes Fe-Mg exchange geothermometer from Brey and Köhler (1990; uncertainty of ±50°C) was chosen. Since post-exsolution pyroxene compositions were used in the calculation, the equilibration temperatures are lower than the temperatures that would be obtained for "primary" pyroxene compositions. Primary equilibration temperatures were estimated by Bedini et al. (1997) for one peridotite of each group, by taking into account the volume of exsolutions in the orthopyroxene; they are of 1130°C (±10) and of 1210°C (±20) for a deformed and a granular peridotite, respectively.
However, the data on the exsolutions volume fraction and composition is not available for the other samples.

4. Results

4.1 Modal compositions and equilibrium temperatures

Because most of the xenoliths from Mega were entirely used during previous geochemical analysis (Bedini, 1994; Bedini et al., 1997; Bedini et al., 1999), we were able to obtain the thin sections of 25 xenoliths out of the originally larger sample set of Bedini (1994). In the present sample set, M1 peridotites are mainly harzburgites, while M2 peridotites are mainly lherzolites (Fig. 2 and Table 1). However, it has to be emphasized that the two groups included both harzburgites and lherzolites in the larger xenolith suite analysed by Bedini et al. (1997). In both M1 and M2 peridotites, orthopyroxene contents vary mainly between 10 and 35%. In M2 lherzolites, clinopyroxene content is highly variable, ranging between 10 and 26% (Table 1). In these rocks, the olivine content varies between 46 and 72%. In addition to these peridotites, we have also analyzed four websterites (three spinel-bearing and one garnet-bearing) and one garnet clinopyroxenite (Fig.2 and Table 1).
The M1 peridotites studied here display high olivine Mg# (Mg#: atomic Mg/(Fe+Mg)), ranging between 90.7 and 92.1% (Table 1). M2 peridotites tend to display lower olivine Mg#, varying between 88.5 and 90.9%. Equilibrium temperatures range between 830 and 1049°C

(Table 1). There is no systematic correlation between temperature and the geochemical group or the microstructure.

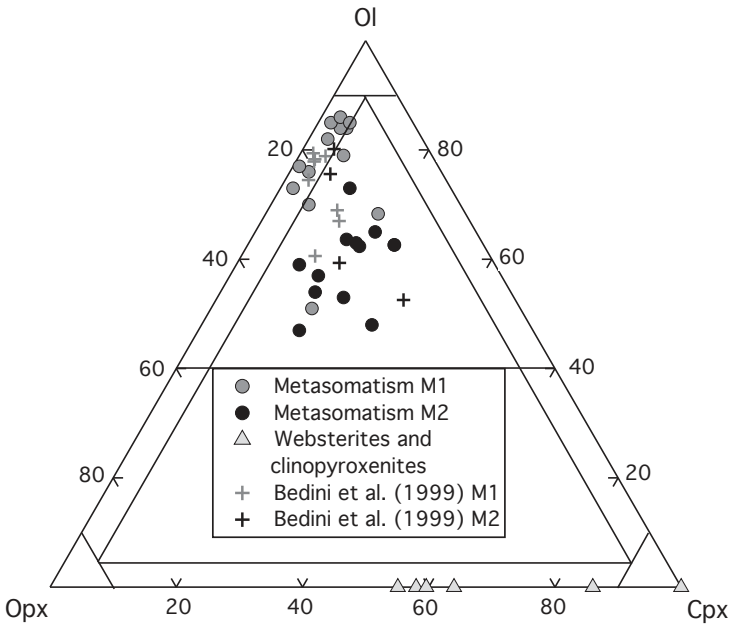

Fig. 2: Olivine:Orthopyroxene:Clinopyroxene modal ratios in the studied xenoliths as a function of the metasomatism type of Bedini et al. (1997) (M1= Deformed; M2= Granular), and rock type. Garnet and spinel were not considered for the construction of the ternary diagram; modal compositions derived from the EBSD maps were recalculated for a total of 100% of Olivine+Orthopyroxene+Clinopyroxene. Modal compositions in twelve samples from Mega reported by Bedini et al. (1999) are plotted for comparison.

4.2 Microstructures

The microstructural analysis of the peridotites from Mega reveals that there is no marked change in microstructures between M1 and M2 peridotites as previously reported by Bedini et al. (1997). Ethiopian peridotites have dominantly coarse-porphyroclastic microstructures (Fig. 3). They present plurimillimetric olivine porphyroclasts with well-defined subgrain boundaries. Smaller olivine neoblasts (~0.4- 3 mm) usually show fewer intracrystalline deformation features and tend to have more polygonal shapes, sometimes forming triple junctions. The subgrain boundary spacing and the frequency of triple junctions vary from a sample to another. For example, in sample ET48 (Fig. 3a), the subgrain boundaries in olivine porphyroclasts are closely-spaced and triple junctions are rare, whereas in sample ET53 (Fig. 3b), neoblasts commonly have polygonal boundaries, as well as some porphyroclasts.

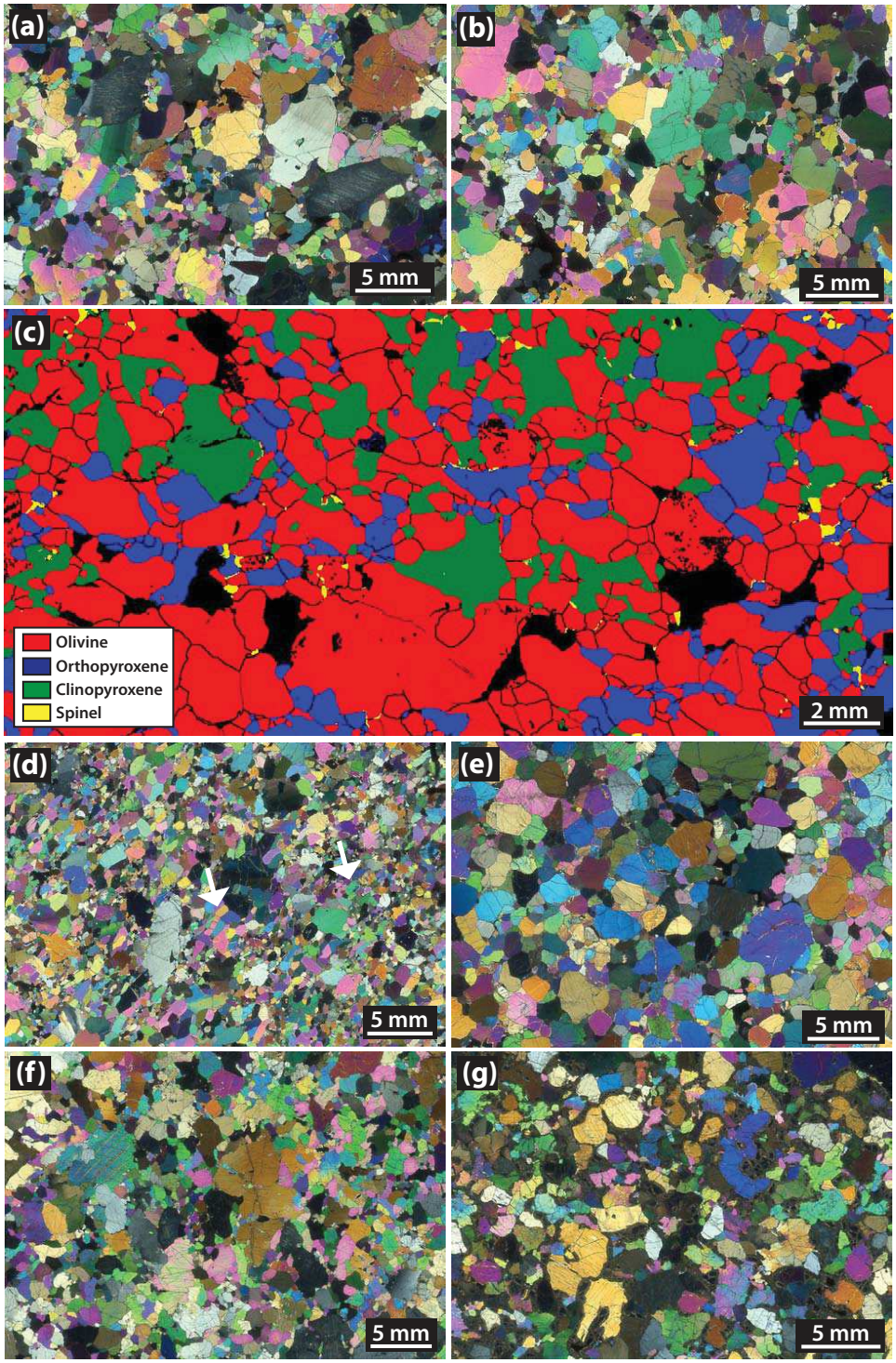

Fig. 3: Photomicrographs in plane-polarised light (a, b, d, e, f, g) and EBSD map (c) of: (a) coarse-porphyroclastic lherzolite ET48A, with large olivine porphyroclasts showing well- defined subgrain boundaries. Orthopyroxene porphyroclasts display kink bands and exsolutions. Olivine neoblasts free of internal deformation features are also present; (b) Coarse-porphyroclastic lherzolite ET53, showing olivine porphyroclasts and neoblasts that tends to have polygonal grain boundaries; (c) EBSD maps of the coarse-porphyroclastic lherzolite ET74B, where large orthopyroxene and clinopyroxene porphyroclasts are visible, as well as smaller, interstitial orthopyroxene and clinopyroxene grains; (d) Coarse- pophyroclastic lherzolite ET66A, where euhedral olivine tablets (arrows) can be found among the olivine neoblasts; (e) Granular websterite ET64 with plurimillimetric

orthopyroxene and clinopyroxene crystals with common polygonal grain boundaries; (f) Coarse-porphyroclastic websterite ET77, with large orthopyroxene and clinopyroxene crystals with well-defined undulose extinctions and exsolutions, as well as smaller pyroxene neoblasts devoid of intracrystalline deformation features; (g) Coarse-porphyroclastic websterite ET81, with interstitial garnet crystal partially kelyphitized.

In three samples (ET-VB1, ET66, and ET84), tabular olivines with polygonal boundaries and devoid of any intracrystalline deformation features can be observed (Fig. 3d). In five samples, olivine interpenetrating boundaries are present. Orthopyroxene porphyroclasts are plurimillimetric and anhedral (Fig. 3a-b). They often display intracrystalline deformation features, such as well-defined kink bands and undulose extinctions. In seventeen samples, they contain exsolutions. Large orthopyroxene crystals (~0.4-1cm) often contain olivine inclusions and interpenetrating olivine-orthopyroxene boundaries are common (Fig. 3a). Smaller orthopyroxene grains (0.7-3mm) are also present (Fig. 3c). They commonly display interstitial shapes and rarely contain subgrain boundaries. In most samples, isolated interstitial clinopyroxene grains (0.3-3mm) can be observed (Fig. 3c). Twelve samples show plurimillimetric and anhedral clinopyroxene porphyroclasts with rare subgrain boundaries. These grains often contain olivine inclusions. When present, spinel occurs as dark, irregularly shaped, millimetric to plurimillimetric grains. In sample ET85, plurimillimetric are concentrated in a smaller area and surrounded by very small olivine and clinopyroxene grains.

Websterites and clinopyroxenites microstructures range from granular (ET64, ET81) (Fig. 3e) to coarse-porphyroclastic (ET55, ET68, ET77; Fig. 3f). In the granular websterites, the plurimillimetric clinopyroxene and orthopyroxene crystals often display polygonal boundaries and exsolutions. In the porphyroclastic websterites, millimetric to centimetric anhedral porphyroclasts of clinopyroxene with exsolutions can be observed. They sometime exhibit undulose extinctions as well as kink bands. The millimetric neoblasts tend to display polygonal boundaries and are devoid of intracrystalline deformation features. In ET68 and ET81, garnet crystals are partially kelyphitized and millimetric to plurimillimetric (Fig. 3g). In ET81, it is present as small interstitial grains, while in ET68, it is enclosed both interstitial and enclosed within clinopyroxene.

4.3 Crystallographic preferred orientations

Peridotites from Ethiopia exhibit variable olivine CPO intensity, characterized by J-indexes ranging between 2.0 and 9.5, and dominantly orthorhombic patterns (Fig.4 and Table 1). There is no correlation between the olivine CPO symmetry and strength. There is also no

systematic variation in the olivine CPO among the two geochemical groups defined by Bedini et al. (1997)

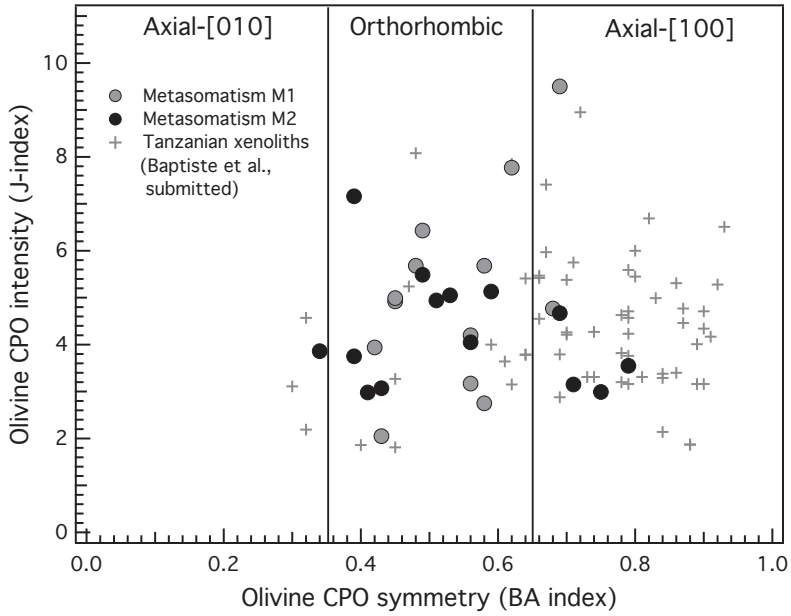

Fig. 4: Olivine CPO intensity (J-index) vs. symmetry (BA index) for all samples as a function of the metasomatism type.

The dominant olivine CPO patterns are characterized by point concentrations of the three crystallographic axis, with [100] usually showing the strongest concentration (Fig. 5). In two samples (ET73 and ET82), axial-[010] CPOs are observed. These patterns are characterized by a point concentration of [010] axes, and a girdle distribution of [100] and [001] normal to it. Sample ET83 shows an olivine CPO pattern intermediate between orthorhombic and axial-[010]. It is characterized by a point concentration of [010] and incomplete girdles of [100] and [001] axes. Finally, in sample ET84, a pattern intermediate between orthorhombic and axial-[100] is observed, with a point concentration of [100] axes and incomplete girdles of [010] and [001] axes.

Orthopyroxene CPO patterns are more dispersed than the olivine ones. They exhibit weak point concentrations of the three crystallographic axes. In most samples, orthopyroxene [100] and [001] maximum concentrations are parallel to olivine the [010] and [100] maximum concentrations, respectively. Clinopyroxene CPOs are still more dispersed than orthopyroxene CPOs. When a clinopyroxene CPO can be defined, it is correlated to the olivine and orthopyroxene CPOs, with clinopyroxene [001] being parallel to orthopyroxene [001] and olivine [100].

PERIDOTITES: Metasomatism 1

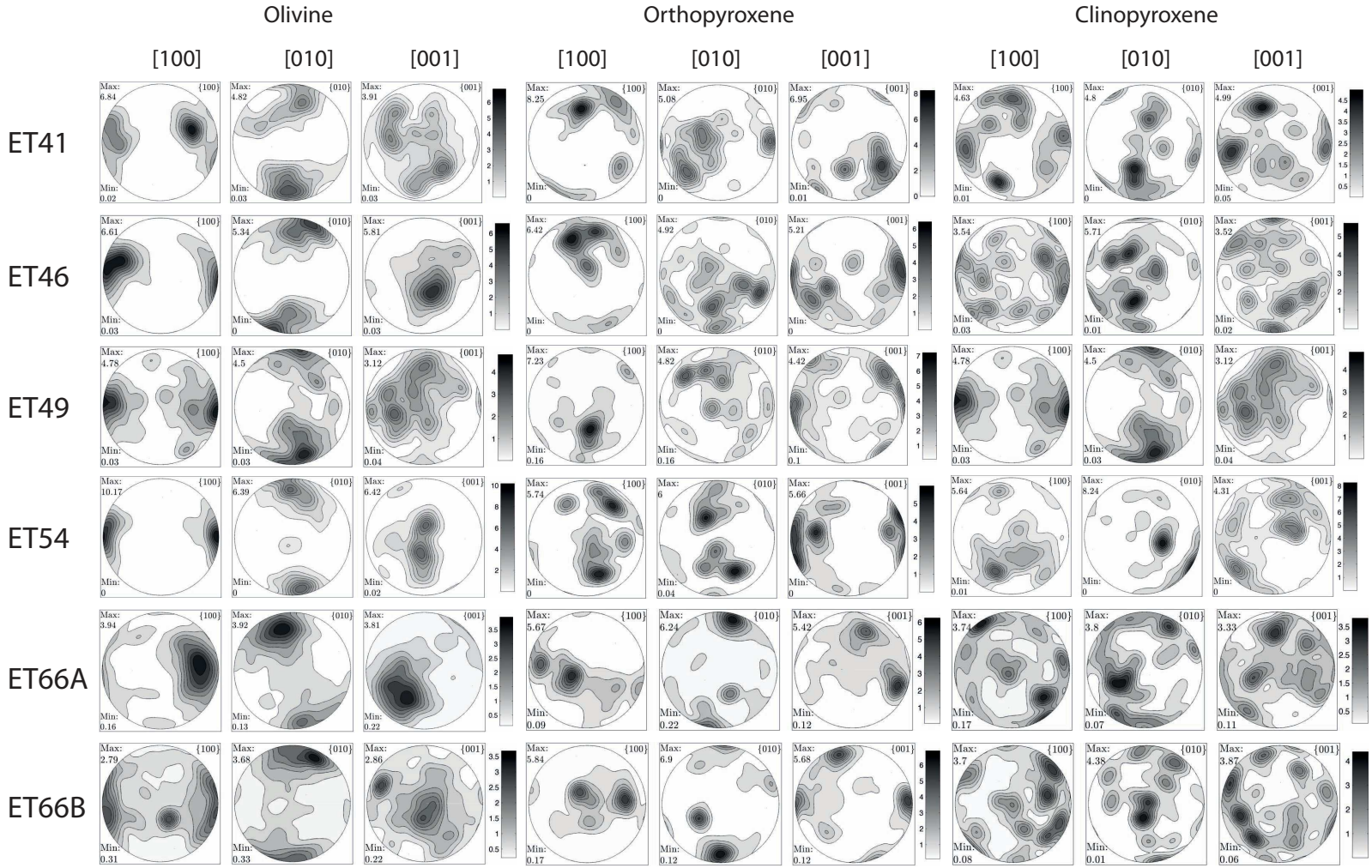

Fig. 5: Olivine, orthopyroxene, and clinopyroxene crystal preferred orientations (CPO) for all samples.

PERIDOTITES: Metasomatism 1

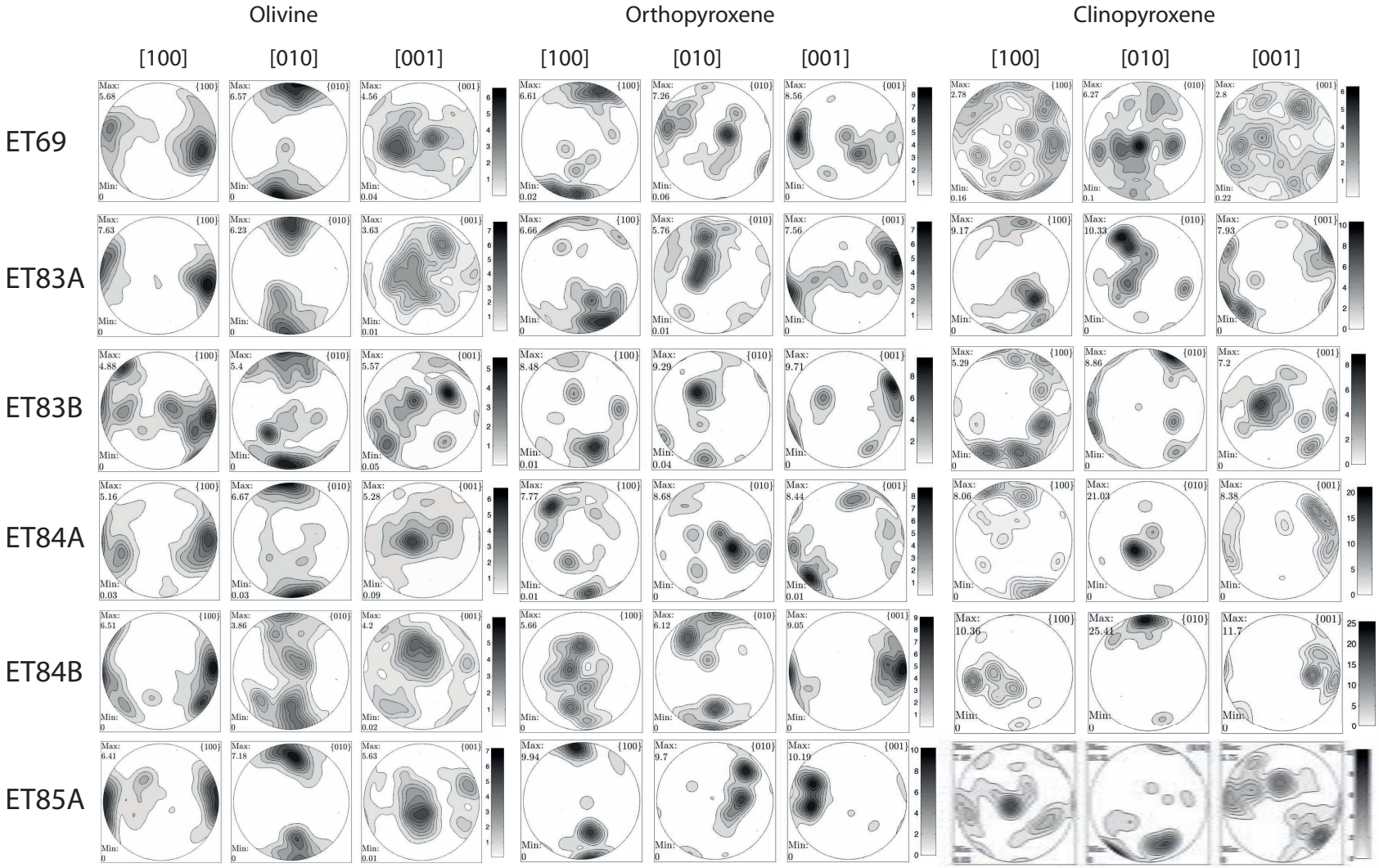

Fig. 5 (suite)

METASOMATISM 2

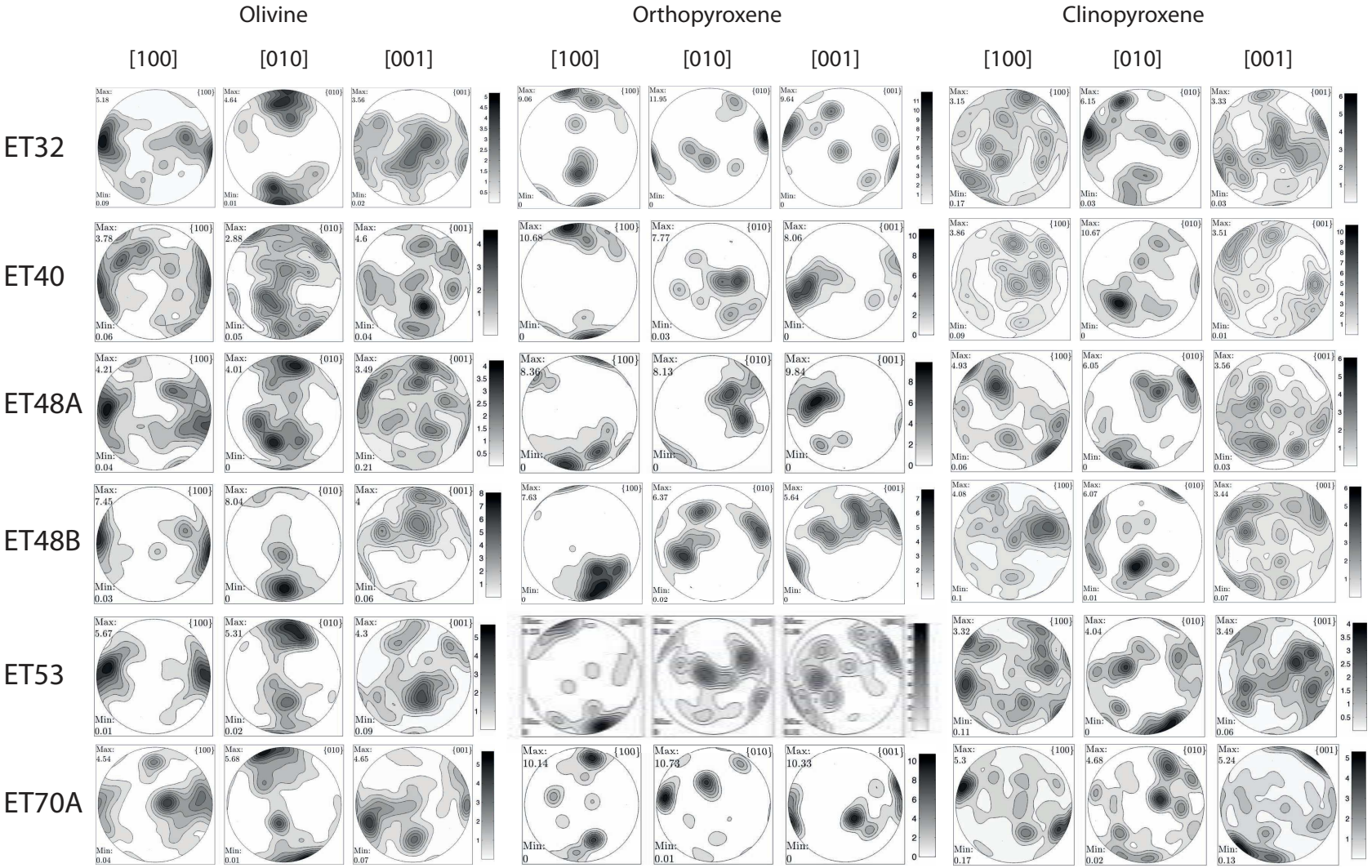

Fig. 5 (suite)

PERIDOTITES: Metasomatism 2

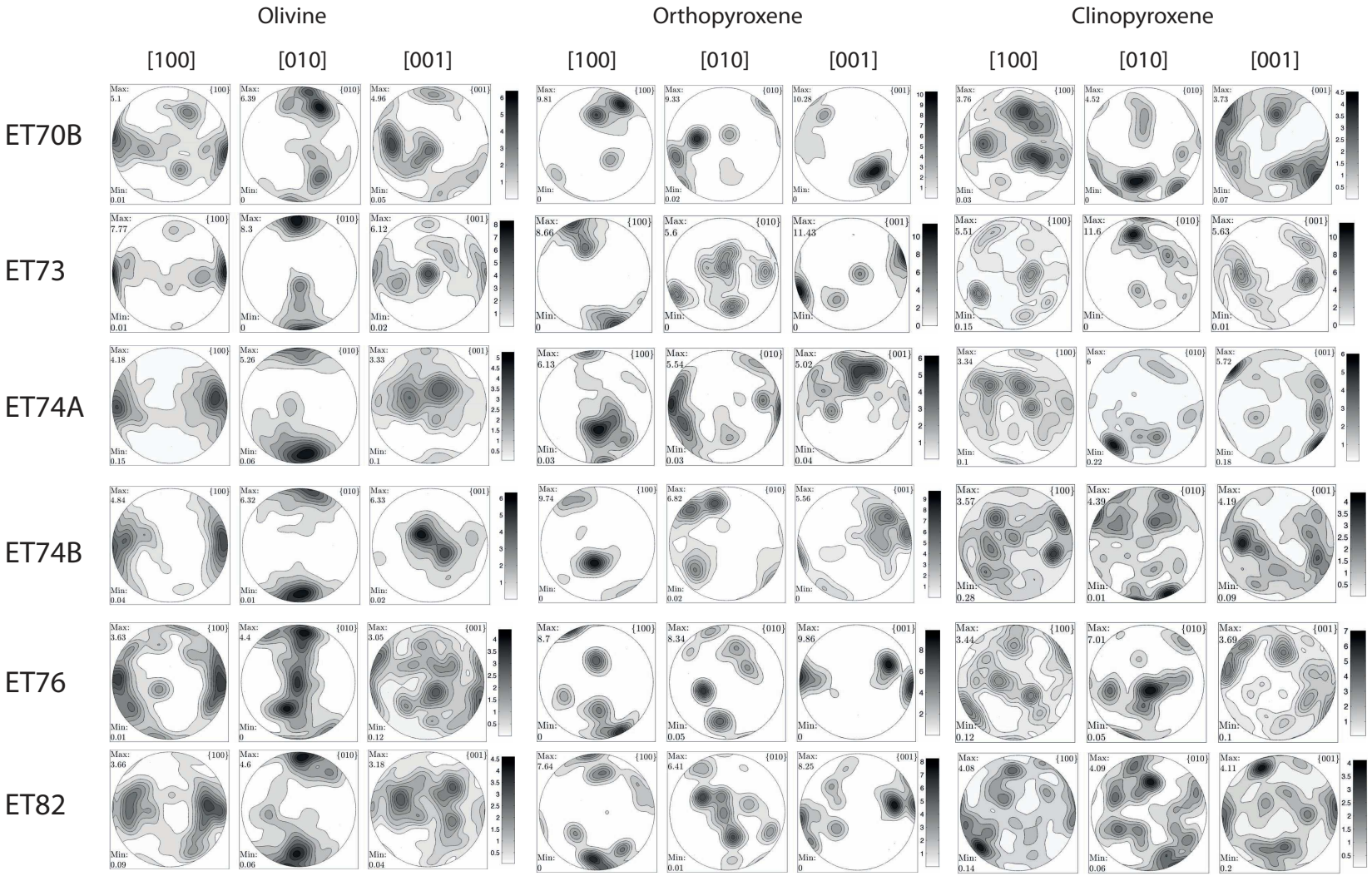

Fig. 5 (suite)

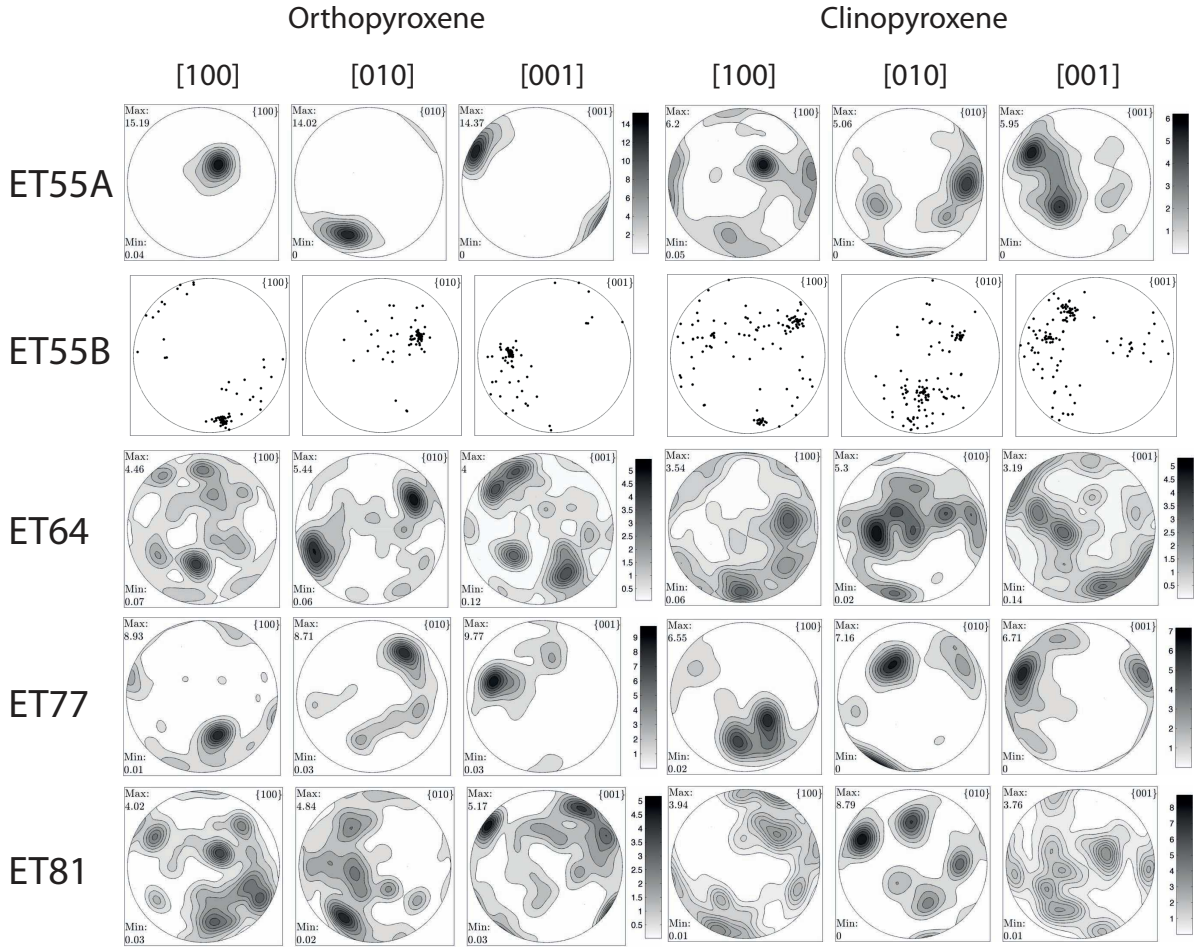
Orthopyroxene
Clinopyroxene
[100]
[010]
[001]
[100]
[010]
[001]
ET55A
ET55B
ET64
ET77
ET81

Fig. 5 (suite)

All pyroxenites show orthopyroxene and clinopyroxene CPO with a weak orthorhombic pattern. Only two samples (ET77 and ET81) have coherent orthopyroxene and clinopyroxene CPOs. In the thwo other websterites (ET55 and ET64), they are not correlated.

4.4 Seismic properties

All peridotites share a common seismic anisotropy pattern (Fig. 6). The P-waves propagation is the fastest close to the olivine [100] maximum and the slowest close to [010] maximum. S-waves azimuthal anisotropy is the highest close to the olivine [001] and the slowest for directions close to maximum concentration of olivine [100] axes. The slowest propagation of the S1-wave occurs for directions close to the olivine [010] maximum, while the fastest S1 propagation is in the plane containing the olivine [100] and [010] maxima, close to Y or at 45° to it. The slowest propagation directions of the slow S-wave (S_2) are in the plane containing the olivine [010] and [001] maxima. The fastest velocities of S2-waves are observed for directions close to the maximum concentration of olivine [100] axes. The highest Vp/Vs_1 ratio is also parallel to the olivine [100] maximum and the lowest Vp/Vs1 is observed for waves propagating normal to this direction.

Seismic anisotropy intensities for individual samples are highly variable (Fig. 7 and Table 1). Maximum P-waves anisotropies are comprised between 3.1 and 12.3%, while maximum S-waves polarization anisotropies range between 2.9 and 8.3 %. Both anisotropies show a positive correlation with olivine content (Fig. 7). Because pyroxenes and garnet are known to dilute the rock bulk anisotropy (Mainprice et al., 2000; Mainprice and Silver, 1993), the samples with higher olivine contents are generally more anisotropic.

Websterites and clinopyroxenites also show highly variable anisotropies. Maximum P-waves anisotropies range between 4.8 and 12.8%, while maximum S-waves polarization anisotropies are comprised between 4.2 and 9.8 %. In clinopyroxenite ET68 and websterite ET55, P-wave and VS_2 velocities are the fastest and Vp/Vs_1 ratios the highest parallel to the maximum concentration of clinopyroxene [001] axis and minimum at high angle to this direction, in a plane containing the [010] maximum. The S-waves polarization anisotropy pattern is more complex. S-waves polarization anisotropy tend to be maximum for directions close to the clinopyroxene [100] maximum concentration. In the other samples, P-wave and VS_2 velocities are fastest and Vp/Vs_1 ratios the highest parallel to the maximum concentration of orthopyroxene [001] axis and minimum at high angle to this direction, in a plane containing the orthopyroxene [100] maximum. S-waves polarization anisotropy maximum varies significantly from a sample to another.

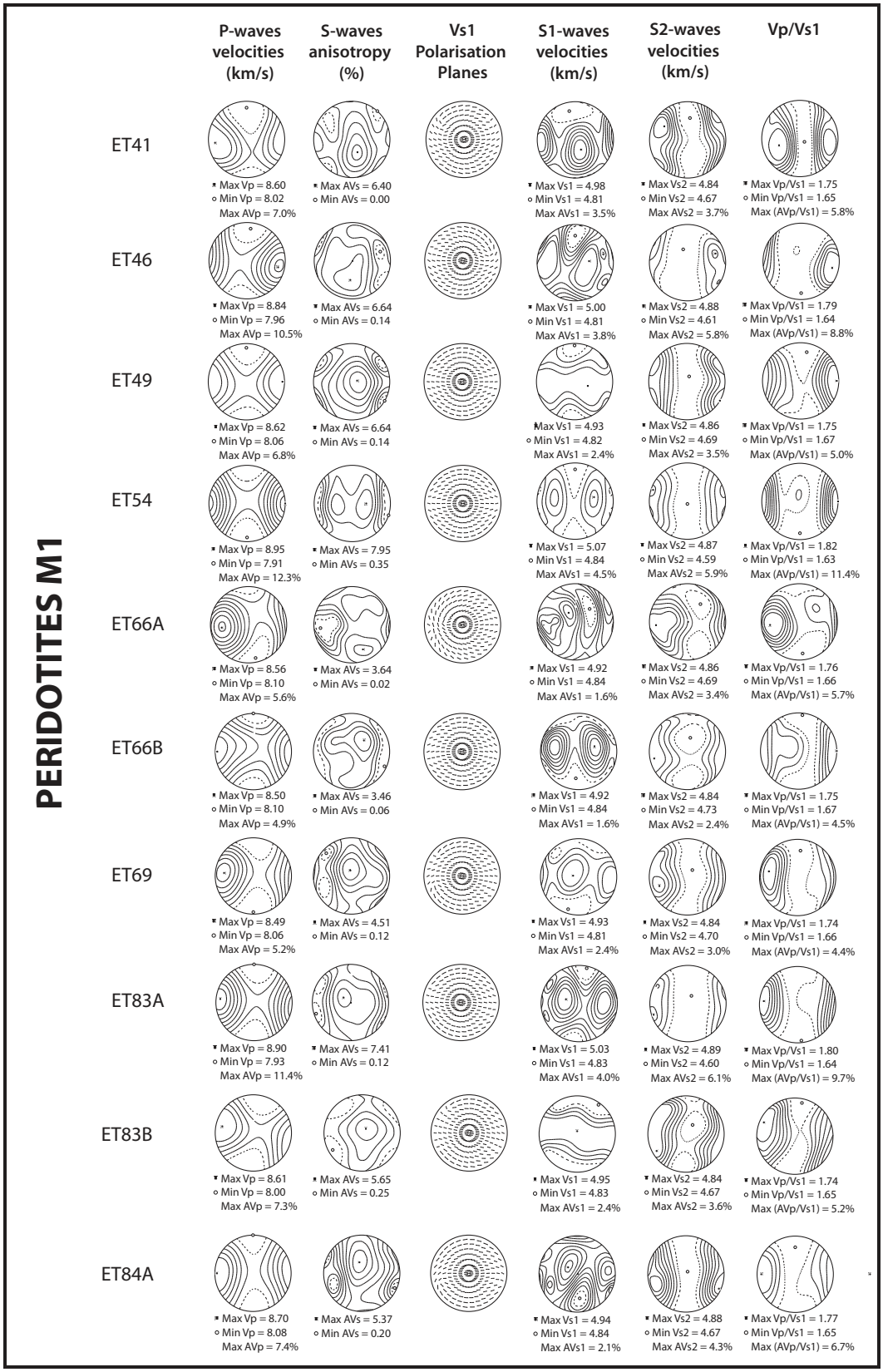

Fig. 6: Calculated seismic properties for all samples. From left to right are displayed the 3-D distributions of P-wave velocities (V_p), S-wave polarization anisotropy (AV_s) and the orientation of fast shear wave polarization plane, S_1 wave velocities (VS_1), S_2 wave velocities, Vp/VS_1 and Vp/VS_2 ratio. Black squares and white spots indicate maximum and minimum values, respectively.

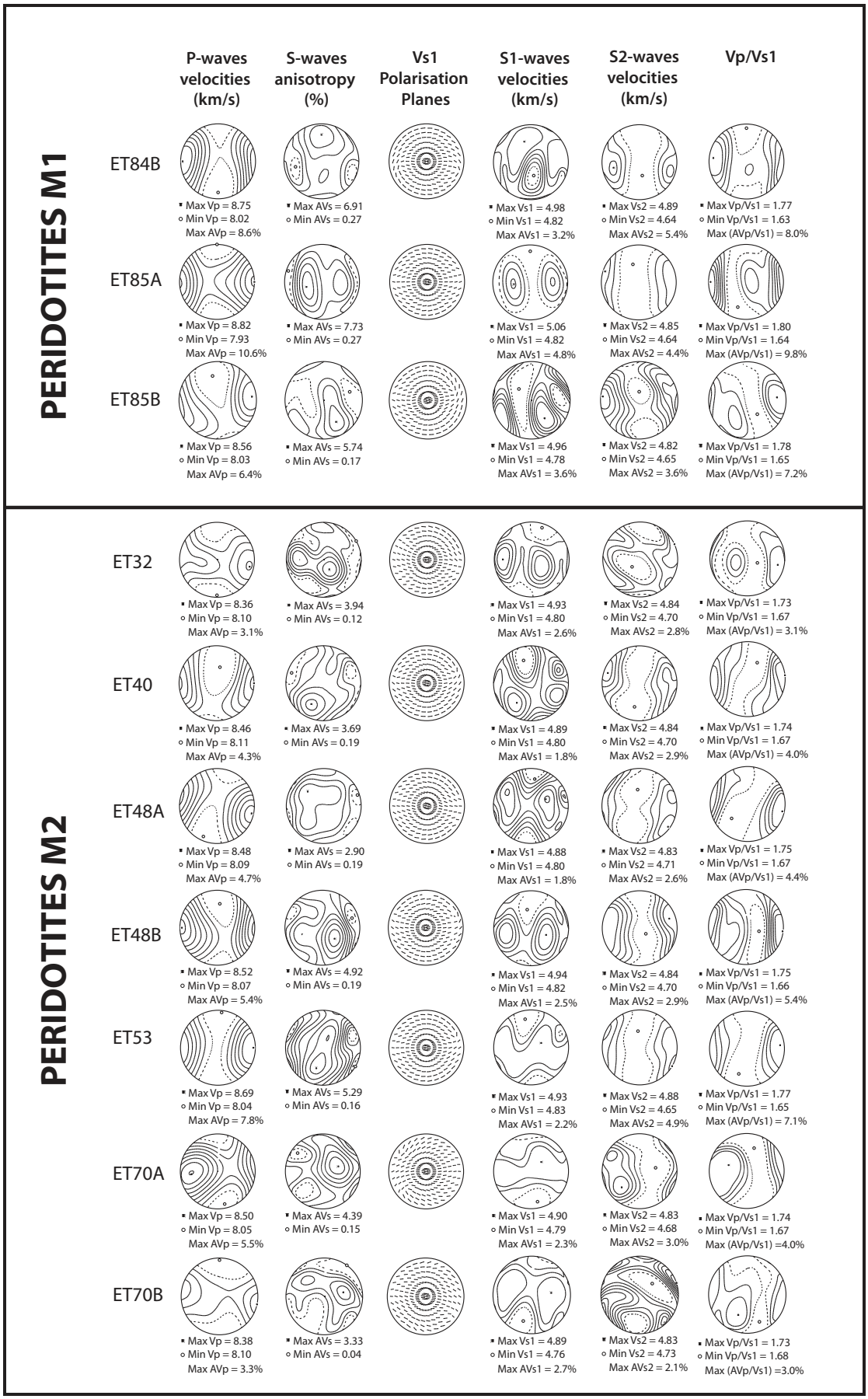
PERIDOTITES M1
P-waves velocities (km/s)
S-waves anisotropy (%)
Vs1 Polarisation Planes
S1-waves velocities (km/s)
S2-waves velocities (km/s)
Vp/Vs1
ET84B
▪ Max Vp = 8.75
◦ Min Vp = 8.02
Max AVp = 8.6%
▪ Max AVs = 6.91
◦ Min AVs = 0.27
▪ Max Vs1 = 4.98
◦ Min Vs1 = 4.82
Max AVs1 = 3.2%
▪ Max Vs2 = 4.89
◦ Min Vs2 = 4.64
Max AVs2 = 5.4%
▪ Max Vp/Vs1 = 1.77
◦ Min Vp/Vs1 = 1.63
Max (AVp/Vs1) = 8.0%
ET85A
▪ Max Vp = 8.82
◦ Min Vp = 7.93
Max AVp = 10.6%
▪ Max AVs = 7.73
◦ Min AVs = 0.27
▪ Max Vs1 = 5.06
◦ Min Vs1 = 4.82
Max AVs1 = 4.8%
▪ Max Vs2 = 4.85
◦ Min Vs2 = 4.64
Max AVs2 = 4.4%
▪ Max Vp/Vs1 = 1.80
◦ Min Vp/Vs1 = 1.64
Max (AVp/Vs1) = 9.8%
ET85B
▪ Max Vp = 8.56
◦ Min Vp = 8.03
Max AVp = 6.4%
▪ Max AVs = 5.74
◦ Min AVs = 0.17
▪ Max Vs1 = 4.96
◦ Min Vs1 = 4.78
Max AVs1 = 3.6%
▪ Max Vs2 = 4.82
◦ Min Vs2 = 4.65
Max AVs2 = 3.6%
▪ Max Vp/Vs1 = 1.78
◦ Min Vp/Vs1 = 1.65
Max (AVp/Vs1) = 7.2%
PERIDOTITES M2
ET32
▪ Max Vp = 8.36
◦ Min Vp = 8.10
Max AVp = 3.1%
▪ Max AVs = 3.94
◦ Min AVs = 0.12
▪ Max Vs1 = 4.93
◦ Min Vs1 = 4.80
Max AVs1 = 2.6%
▪ Max Vs2 = 4.84
◦ Min Vs2 = 4.70
Max AVs2 = 2.8%
▪ Max Vp/Vs1 = 1.73
◦ Min Vp/Vs1 = 1.67
Max (AVp/Vs1) = 3.1%
ET40
▪ Max Vp = 8.46
◦ Min Vp = 8.11
Max AVp = 4.3%
▪ Max AVs = 3.69
◦ Min AVs = 0.19
▪ Max Vs1 = 4.89
◦ Min Vs1 = 4.80
Max AVs1 = 1.8%
▪ Max Vs2 = 4.84
◦ Min Vs2 = 4.70
Max AVs2 = 2.9%
▪ Max Vp/Vs1 = 1.74
◦ Min Vp/Vs1 = 1.67
Max (AVp/Vs1) = 4.0%
ET48A
▪ Max Vp = 8.48
◦ Min Vp = 8.09
Max AVp = 4.7%
▪ Max AVs = 2.90
◦ Min AVs = 0.19
▪ Max Vs1 = 4.88
◦ Min Vs1 = 4.80
Max AVs1 = 1.8%
▪ Max Vs2 = 4.83
◦ Min Vs2 = 4.71
Max AVs2 = 2.6%
▪ Max Vp/Vs1 = 1.75
◦ Min Vp/Vs1 = 1.67
Max (AVp/Vs1) = 4.4%
ET48B
▪ Max Vp = 8.52
◦ Min Vp = 8.07
Max AVp = 5.4%
▪ Max AVs = 4.92
◦ Min AVs = 0.19
▪ Max Vs1 = 4.94
◦ Min Vs1 = 4.82
Max AVs1 = 2.5%
▪ Max Vs2 = 4.84
◦ Min Vs2 = 4.70
Max AVs2 = 2.9%
▪ Max Vp/Vs1 = 1.75
◦ Min Vp/Vs1 = 1.66
Max (AVp/Vs1) = 5.4%
ET53
▪ Max Vp = 8.69
◦ Min Vp = 8.04
Max AVp = 7.8%
▪ Max AVs = 5.29
◦ Min AVs = 0.16
▪ Max Vs1 = 4.93
◦ Min Vs1 = 4.83
Max AVs1 = 2.2%
▪ Max Vs2 = 4.88
◦ Min Vs2 = 4.65
Max AVs2 = 4.9%
▪ Max Vp/Vs1 = 1.77
◦ Min Vp/Vs1 = 1.65
Max (AVp/Vs1) = 7.1%
ET70A
▪ Max Vp = 8.50
◦ Min Vp = 8.05
Max AVp = 5.5%
▪ Max AVs = 4.39
◦ Min AVs = 0.15
▪ Max Vs1 = 4.90
◦ Min Vs1 = 4.79
Max AVs1 = 2.3%
▪ Max Vs2 = 4.83
◦ Min Vs2 = 4.68
Max AVs2 = 3.0%
▪ Max Vp/Vs1 = 1.74
◦ Min Vp/Vs1 = 1.67
Max (AVp/Vs1) =4.0%
ET70B
▪ Max Vp = 8.38
◦ Min Vp = 8.10
Max AVp = 3.3%
▪ Max AVs = 3.33
◦ Min AVs = 0.04
▪ Max Vs1 = 4.89
◦ Min Vs1 = 4.76
Max AVs1 = 2.7%
▪ Max Vs2 = 4.83
◦ Min Vs2 = 4.73
Max AVs2 = 2.1%
▪ Max Vp/Vs1 = 1.73
◦ Min Vp/Vs1 = 1.68
Max (AVp/Vs1) =3.0%

Fig. 6 (suite)

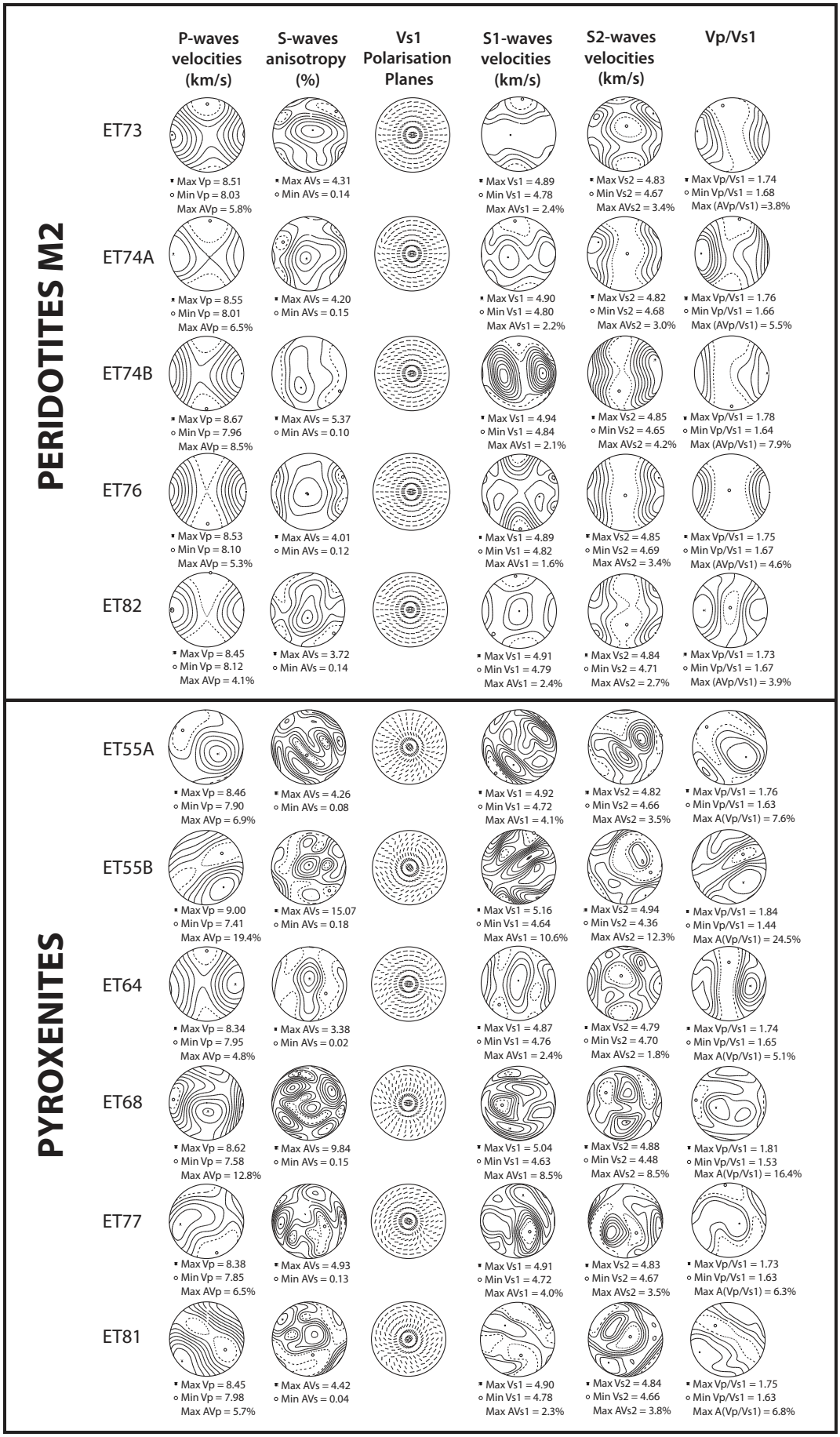
PERIDOTITES M2
PYROXENITES
P-waves velocities (km/s)
S-waves anisotropy (%)
Vs1 Polarisation Planes
S1-waves velocities (km/s)
S2-waves velocities (km/s)
Vp/Vs1
ET73
▪ Max Vp = 8.51
◦ Min Vp = 8.03
Max AVp = 5.8%
▪ Max AVs = 4.31
◦ Min AVs = 0.14
▪ Max Vs1 = 4.89
◦ Min Vs1 = 4.78
Max AVs1 = 2.4%
▪ Max Vs2 = 4.83
◦ Min Vs2 = 4.67
Max AVs2 = 3.4%
▪ Max Vp/Vs1 = 1.74
◦ Min Vp/Vs1 = 1.68
Max (AVp/Vs1) =3.8%
ET74A
▪ Max Vp = 8.55
◦ Min Vp = 8.01
Max AVp = 6.5%
▪ Max AVs = 4.20
◦ Min AVs = 0.15
▪ Max Vs1 = 4.90
◦ Min Vs1 = 4.80
Max AVs1 = 2.2%
▪ Max Vs2 = 4.82
◦ Min Vs2 = 4.68
Max AVs2 = 3.0%
▪ Max Vp/Vs1 = 1.76
◦ Min Vp/Vs1 = 1.66
Max (AVp/Vs1) = 5.5%
ET74B
▪ Max Vp = 8.67
◦ Min Vp = 7.96
Max AVp = 8.5%
▪ Max AVs = 5.37
◦ Min AVs = 0.10
▪ Max Vs1 = 4.94
◦ Min Vs1 = 4.84
Max AVs1 = 2.1%
▪ Max Vs2 = 4.85
◦ Min Vs2 = 4.65
Max AVs2 = 4.2%
▪ Max Vp/Vs1 = 1.78
◦ Min Vp/Vs1 = 1.64
Max (AVp/Vs1) = 7.9%
ET76
▪ Max Vp = 8.53
◦ Min Vp = 8.10
Max AVp = 5.3%
▪ Max AVs = 4.01
◦ Min AVs = 0.12
▪ Max Vs1 = 4.89
◦ Min Vs1 = 4.82
Max AVs1 = 1.6%
▪ Max Vs2 = 4.85
◦ Min Vs2 = 4.69
Max AVs2 = 3.4%
▪ Max Vp/Vs1 = 1.75
◦ Min Vp/Vs1 = 1.67
Max (AVp/Vs1) = 4.6%
ET82
▪ Max Vp = 8.45
◦ Min Vp = 8.12
Max AVp = 4.1%
▪ Max AVs = 3.72
◦ Min AVs = 0.14
▪ Max Vs1 = 4.91
◦ Min Vs1 = 4.79
Max AVs1 = 2.4%
▪ Max Vs2 = 4.84
◦ Min Vs2 = 4.71
Max AVs2 = 2.7%
▪ Max Vp/Vs1 = 1.73
◦ Min Vp/Vs1 = 1.67
Max (AVp/Vs1) = 3.9%
ET55A
▪ Max Vp = 8.46
◦ Min Vp = 7.90
Max AVp = 6.9%
▪ Max AVs = 4.26
◦ Min AVs = 0.08
▪ Max Vs1 = 4.92
◦ Min Vs1 = 4.72
Max AVs1 = 4.1%
▪ Max Vs2 = 4.82
◦ Min Vs2 = 4.66
Max AVs2 = 3.5%
▪ Max Vp/Vs1 = 1.76
◦ Min Vp/Vs1 = 1.63
Max A(Vp/Vs1) = 7.6%
ET55B
▪ Max Vp = 9.00
◦ Min Vp = 7.41
Max AVp = 19.4%
▪ Max AVs = 15.07
◦ Min AVs = 0.18
▪ Max Vs1 = 5.16
◦ Min Vs1 = 4.64
Max AVs1 = 10.6%
▪ Max Vs2 = 4.94
◦ Min Vs2 = 4.36
Max AVs2 = 12.3%
▪ Max Vp/Vs1 = 1.84
◦ Min Vp/Vs1 = 1.44
Max A(Vp/Vs1) = 24.5%
ET64
▪ Max Vp = 8.34
◦ Min Vp = 7.95
Max AVp = 4.8%
▪ Max AVs = 3.38
◦ Min AVs = 0.02
▪ Max Vs1 = 4.87
◦ Min Vs1 = 4.76
Max AVs1 = 2.4%
▪ Max Vs2 = 4.79
◦ Min Vs2 = 4.70
Max AVs2 = 1.8%
▪ Max Vp/Vs1 = 1.74
◦ Min Vp/Vs1 = 1.65
Max A(Vp/Vs1) = 5.1%
ET68
▪ Max Vp = 8.62
◦ Min Vp = 7.58
Max AVp = 12.8%
▪ Max AVs = 9.84
◦ Min AVs = 0.15
▪ Max Vs1 = 5.04
◦ Min Vs1 = 4.63
Max AVs1 = 8.5%
▪ Max Vs2 = 4.88
◦ Min Vs2 = 4.48
Max AVs2 = 8.5%
▪ Max Vp/Vs1 = 1.81
◦ Min Vp/Vs1 = 1.53
Max A(Vp/Vs1) = 16.4%
ET77
▪ Max Vp = 8.38
◦ Min Vp = 7.85
Max AVp = 6.5%
▪ Max AVs = 4.93
◦ Min AVs = 0.13
▪ Max Vs1 = 4.91
◦ Min Vs1 = 4.72
Max AVs1 = 4.0%
▪ Max Vs2 = 4.83
◦ Min Vs2 = 4.67
Max AVs2 = 3.5%
▪ Max Vp/Vs1 = 1.73
◦ Min Vp/Vs1 = 1.63
Max A(Vp/Vs1) = 6.3%
ET81
▪ Max Vp = 8.45
◦ Min Vp = 7.98
Max AVp = 5.7%
▪ Max AVs = 4.42
◦ Min AVs = 0.04
▪ Max Vs1 = 4.90
◦ Min Vs1 = 4.78
Max AVs1 = 2.3%
▪ Max Vs2 = 4.84
◦ Min Vs2 = 4.66
Max AVs2 = 3.8%
▪ Max Vp/Vs1 = 1.75
◦ Min Vp/Vs1 = 1.63
Max A(Vp/Vs1) = 6.8%

Fig. 6 (suite)

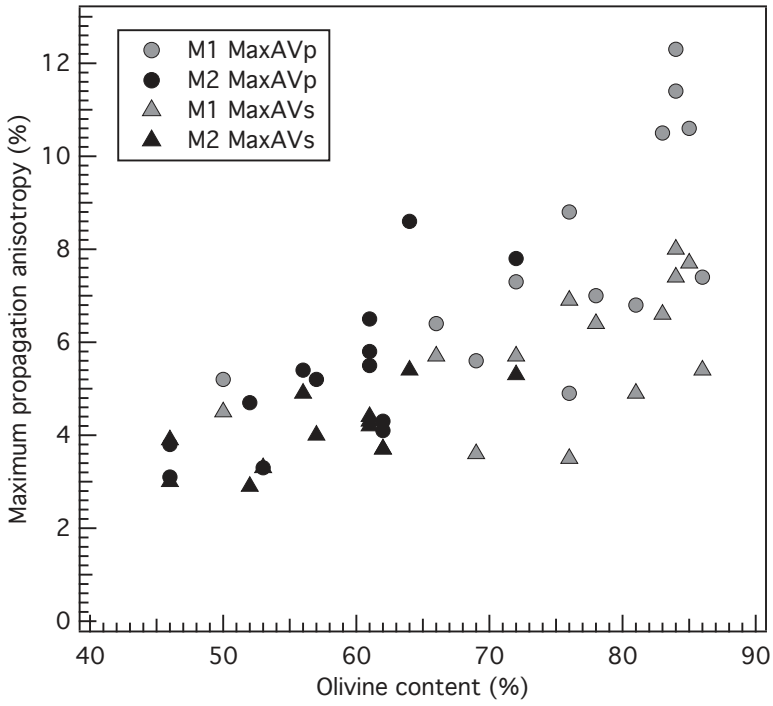

Fig. 7: Dependence of the maximum P- and S-waves anisotropy (AVp, AVs) on the olivine content.

5. Discussion

5.1 Deformation history of the mantle peridotites

All peridotites from south of Mega exhibit coarse-porphyroclastic microstructures, with evidence for plastic deformation by dislocation creep, followed by some static recrystallization. The homogeneity in microstructures and grain size suggest that these rocks record no major temporal or spatial variations of deformation conditions. However, the slight variations in subgrain boundaries spacing in olivine porphyroclasts and in grain boundary polygonization variable annealing degrees. The preservation of well-defined intracrystalline deformation features in olivine porphyroclasts suggests, however, that the time span between deformation and xenolith extraction was short enough to prevent complete annealing of the deformation microstructures. Common exsolutions in orthopyroxenes suggest post-kinematic cooling. Temperatures in the two samples devoid of exsolutions are high (959°C and 1009°C in ET53 and ET46, respectively). There is no clear correlation between temperature and microstructures or the geochemical group.

The well-defined olivine CPOs indicate that dislocation creep was the main deformation process. Most samples have orthorhombic olivine CPO patterns, coherent with deformation by pure or simple shear with dominant activation of (010)[100] slip system under

high temperature, low pressure and anhydrous conditions (e.g. Nicolas and Poirier, 1976; Tommasi et al., 1999, 2000). Orthopyroxene CPOs indicate deformation with dominant activation of the (100)[001] slip system. They are always correlated to the olivine CPO, implying that they record the same deformation event.

Textural evidence for metasomatism in these rocks encompasses: (1) small interstitial orthopyroxene grains, (2) small interstitial clinopyroxene grains, (3) the anhedral shapes of some larger pyroxenes, (4) common olivine inclusions in orthopyroxenes, (5) interpenetrating olivine and orthopyroxene grain boundaries. Observations (1), (3), and (4) suggest secondary crystallization of orthopyroxene, while observation (2) indicates secondary crystallization of clinopyroxene. Observation (5) may result from olivine crystallization at the expenses of orthopyroxene as a result of interaction with Si-undersaturated melts or from orthopyroxene crystallization at the expenses of olivine in response to reactions with Si-rich fluids or melts. Interstitial orthopyroxenes and clinopyroxenes sometimes display intracrystalline deformation features. Moreover, pyroxenes CPOs are usually coherent with the olivine one, suggesting that the metasomatic event(s) responsible for their crystallization was pre- to syn-kinematic. Based on geochemical analyses, Bedini et al. (1997) identified two distinct types of metasomatism among those rocks (see section 2.2 for more details). The geochemical characteristics of M1 peridotites were interpreted as the result of interaction with small fractions of LILE-enriched melts saturated in Ti-oxides, whereas M2 peridotites are believed to have re-equilibrated with high fractions of basaltic melts. Using numerical simulation of reactive porous flow at the transition between the lithospheric and the convective mantle, they demonstrated that the processes responsible for the two metasomatisms could be contemporary and linked to thermo-mechanical erosion of the lower lithosphere above a mantle plume. Despite the fact that they equilibrated with different melt fractions, we do not observe any significant variation of the peridotites' microstructures, contrary to what Bedini et al. (1997) pointed out, suggesting pre- or syn-kinematic rather than post-kinematic metasomatism. In their simulation, a series of distinct reactions occurs in a single melt percolation column. Melt-peridotite reactions at the top of the percolation column allow crystallization of clinopyroxene from the consumption orthopyroxene, whereas the two reactions at the bottom crystallize orthopyroxene at the expenses of olivine or olivine at the expense of orthopyroxene. While crystallization of orthopyroxene at the expense of olivine might be suggested by observation (4), we found no evidence for clinopyroxene crystallization at the expense of orthopyroxene in these rocks. The pyroxenites from southern Mega were interpreted by Bedini (1994) as magmatic conduits formed during the same

metasomatic event that originated in the two types of metasomatism identified in peridotites. The fact that some of these pyroxenites exhibit intracrystalline deformation features as well as

pyroxene CPOs reinforces the idea that deformation and metasomatism were at least simultaneous.

5.2 Anisotropy in the lithospheric mantle beneath the Ethiopian rift

Our results show that the lithospheric mantle beneath the southern part of the main Ethiopian rift is anisotropic. Calculated maximum seismic anisotropies range between 3.1 and 12.3% for P-waves, and between 2.9 and 8.3 % for S-waves. Estimates for crustal and lithospheric thickness beneath the Ethiopian rift from shear velocity models range between 25-35 km, and 70-80 km, respectively (Dugda et al., 2007). Upper mantle S-wave velocities measured in the region average 4.1-4.2 km/s (Dugda et al., 2007). Along the Main Ethiopian Rift, fast polarization directions slightly oblique to parallel to the rift axis are measured by SKS studies (Kendall et al., 2005). Such orientations are expected for a narrow rift formed as a result of transtension and would result in a near vertical foliation and a near horizontal lineation (Vauchez et al., 2000). In such a case, SKS-waves will then sample the maximum S-wave polarization anisotropy (Z structural direction), leading to delay times ranging between 0.3-0.9s for a 45 km-thick mantle. Higher SKS delay times of 1-3s were measured in the Main Ethiopian Rift, north of the area sampled by the present study (Kendall et al., 2005). In Northern Kenya, south of the study area, slightly lower SKS delay times of 0.8-2.4s have been measured (Gao et al., 1997). Therefore, the anisotropy calculated for the Ethiopian peridotites cannot explain alone the SKS delay times measured within the rift in neighboring regions. This result may indicate that the anisotropic signal is indeed dominated by oriented melt pockets (Ayele et al., 2004; Kendall et al., 2005).

5.3 Consequences for the deformation of the lithospheric mantle beneath a continental rift

The microstructures and the relations between magma percolation and deformation we observe in the xenoliths from Mega are different from those observed in other xenolith localities along the East African rift, in the North Tanzanian Divergence and the Masarbit volcanic field in Northern Kenya.

The apparent homogeneity of the microstructures and CPOs of the xenoliths from South Mega suggests that they were acquired during a single deformation event that occurred during the metasomatic event that led to the refertilisation of these rocks, probably the one

interpreted in geochemical studies as the result of interaction with a plume head (Bedini et al., 1997). In Ethiopia, the rapid formation of the magmatic Plateau during a plume-related peak volcanism at 30 Ma (Ebinger, 1993; Georges et al., 1998; Hofman et al., 1997) was followed in the Miocene by continental extension initiation and a volcanic episode also interpreted as plume-related (Ebinger et al., 1993; Hendrie et al. 1994; Morley et al. 1992). Therefore, we expect the deformation recorded by the xenoliths from South Mega to be rift-related. The relatively weak annealing of these samples and the high equilibrium temperatures of samples devoid of exsolutions in orthopyroxene suggest that they were deformed not long before extraction. Common exsolutions in orthopyroxenes suggest the region underwent a later cooling.

Previous studies have described the microstructures and CPOs in mantle xenoliths from other localities of the East African rift. In the Masarbit volcanic field in Northern Kenya (in the Anza Graben), the porphyroclastic to ultramylonitic microstructures suggest intense deformation and strain localisation. Based on thermobarometry and geochemistry measurements and textural analysis, Kaeser et al. (2006) suggested that these deformation was linked to the exhumation of subcontinental mantle lithosphere during the early stages of continental rifting. Deformation and decompression was then followed by a heating and melt infiltration event (Kaeser et al., 2006). In mylonites, olivine CPOs are coherent with deformation with activation of [001](010) slip system (Kaczmarek and Reddy, 2013). In the North Tanzanian Divergence, the microstructure of rift axis peridotites mainly ranges from mylonitic to porphyroclastic and shows evidence for melt-assisted deformation (Baptiste et al., submitted). Olivine CPOs range from axial-[100] to orthorhombic (Fig. 4; Baptiste et al., submitted). The microstructures of the xenoliths from Southern Mega are more homogeneous then these localities. Mylonites or fine-grained porphyroclastic structures, indicating deformation under high stress conditions are not observed. All these observations form various xenolith localities of the East African rift suggest that, although melt infiltration within the lithospheric mantle seems to be a common process along the East African Rift, its timing relative to the beginning of the deformation and the resulting microstructures vary from a region to another.

Conclusion

The peridotites from South Mega in the East African rift display homogeneous microstructures, suggesting that they probably do no record any spatial nor temporal variations of deformations conditions. We do not observe any significant change in

microstructures with the geochemical group, despite what was previously reported by Bedini et al. (1997). Slight variations in subgrain boundary spacing in olivine porphyroclasts and in polygonization among olivine neoblast however suggest that the deformation was followed by variable annealing. Exsolutions in pyroxenes indicate later cooling. The orthorhombic olivine CPOs indicate deformation by dislocation creep with dominant activation of the [100] (010) slip system. Evidence for interstitial orthopyroxene and clinopyroxene suggest secondary crystallisation, probably associated to a single metasomatic event identified by Bedini et al. (1997). The CPOs observed in orthopyroxene and sometimes in clinopyroxene, as well as the coherence between olivine and orthopyroxene CPOs in most pyroxenes indicate that metasomatism was pre- to syn-kinematic. Pyroxenites display granular to porphyroclastic microstructures and weaker CPO patterns, suggesting pre- to syn-kinematic metasomatism. Calculated maximum seismic anisotropies range between 3.1 and 12.3% for P-waves, and between 2.9 and 8.3 % for S-waves. These anisotropies cannot explain alone the SKS delay times measured in the main Ethiopian rift or in the Kenya rift. Variations in microstructures and relations between magma percolation and deformation in Ethiopian peridotites are different to what is observed in other xenoliths localities from the East African rift. This indicates that, although melt infiltration within the lithospheric mantle during rifting is commonly observed, its timing relative to deformation and the resulting microstructures varies.

Acknowledgements

D. Mainprice provided the programs for calculating seismic properties. C. Nevado and D. Delmas prepared high-quality polished thin sections for FTIR and EBSD measurements. EBSD analyses were performed with the help of F. Barou at the EBSD-SEM national facility at Geosciences Montpellier.

References:

Abramson, E.H., Brown, J.M., Slutsky, L.J., Zaug, J., 1997. The elastic constants of San Carlos olivine to 17 GPa. Journal of geophysical Research 102, 12,253-212,263.

Ayele, A., Stuart, G.W., Kendall, J.-M., 2004. Insights into rifting from shear wave splitting and receiver functions: An example from Ethiopia. Geophys. J. Int. 157, 354-362

Baptiste, V., Vauchez, A., Tommasi, A., Demouchy, S., Rudnick, R.L., 2014. Deformation, hydration, and anisotropy of the lithospheric mantle in an active rift: constraints from mantle xenoliths from the North Tanzanian Divergence of the East African Rift. Submitted to Tectonophysics.

Bastow, I.D., Pilidou, S., Kendall, J.-M., Stuart, G.W., 2010. Melt-induced seismic anisotropy and magma assisted rifting in Ethiopia: Evidence from surface waves. Geochem. Geophys. Geosyst. 11, Q0AB05.

Bastow, I.D., Nyblade, A., Stuart, G.W., Rooney, T.O., Benoit, M.H., 2008. Upper mantle seismic structure beneath the Ethiopian hot spot: Rifting at the edge of the African low-velocity anomaly. Geochem. Geophys. Geosyst. 9, 1-25.

Bedini, R.M., Bodinier, J.-L., 1999. Distribution of incompatible trace elements between the constituents of spinel peridotite xenolihts: ICP-MS data from the East African Rift. Geochimica et Cosmochimica Acta 63, 3883-3900.

Bedini, R.M., Bodinier, J.-L., Dautria, J.-M., Morten, L., 1997. Evolution of LILE-enriched small melt fractions in the lithospheric mantle: a case study from the East African Rift. Earth and Planetary Science Letters 153, 67-83.

Ben Ismaïl, W., Mainprice, D., 1998. An olivine fabric database: an overview of upper mantle fabrics and seismic anisotropy. Tectonophysics 296, 145-157.

Benoit, M.H., Nyblade, A.A., Pasyanos, M.E., 2006. Crustal thinning between the Ethiopian and East African plateaus from modeling Rayleigh wave dispersion. Geophysical research letters, 33, 1-5.

Bonini, M., Corti, G., Innocenti, F., Manetti, P., Mazzarini, F., Abebe, T., Pecskay, Z., 2005. Evolution of the Main Ethiopian rift in the frame of Afar and Kenya rifts propagation. Tectonics 24, 1-21.

Brey, G.P., Köhler, T., 1990. Geothermobarometry in Four-phase Lherzolites II. New Thermobarometers, and Practical Assessment of Existing Thermobarometers. Journal of Petrology 31, 1353-1378.

Buck, W.R., 2006. The role of magma in the development of the Afro-Arabian Rift System. Geological Society London Special Publications 259, 43-54.

Chai, M., Brown, J.M., Slutsky, L.J., 1997a. The elastic constants of an aluminous orthopyroxene to 12.5 GPa. Journal of geophysical Research 102, 14,779-714,785.

Chai, M., Brown, J.M., Slutsky, L.J., 1997b. The elastic constants of pyrope-grossular-almandine garnets to 20 GPa. Geophys. Res. Lett. 24, 523-526.

Collins, M.D., Brown, J.M., 1998. Elasticity of an upper mantle clinopyroxene. Physics and Chemistry of Minerals 26, 7-13.

Dijkstra, A.H., Drury, M.R., Vissers, R.L.M., Newman, J., 2002. On the role of melt-rock reaction in mantle shear zone formation in the Othris Peridotite Massif (Greece). Journal of Structural Geology 24, 1431-1450.

Dugda, M.T., Nyblade, A., Julià, J., 2007. Thin lithosphere beneath the Ethiopian Plateau revealed by a joint inversion of Rayleigh wave group velocities and receiver functions. Journal of geophysical Research 112.

Ebinger, C., Yemane, T., Woldegabriel, G., Aronson, J.L., Walter, R.C., 1993. Late Eocene: recent volcanism and faulting in the southern Main Ethiopian Rift. Journal of the geological society, London 150, 99-108.

Furman, T., 2007. Geochemistry of East African rift basalts: An overview. Journal of African Earth Sciences 48, 147-160.

Gao, S., Davis, P.M., Liu, H., Slack, O.D., Rigor, A.W., Zorin, Y.A., Mordvinova, V.V., Kozhevnikov, V.M., Logatchev, N.A., 1997. SKS splitting beneath continental rift zones. Journal of geophysical Research 102, 22781-22797.

Gashawbeza, E.M., Klemperer, S.L., Nyblade, A.A., Walker, K.T., Keranen, K.M., 2004. Shear-wave splitting in Ethiopia: Precambrian mantle anisotropy locally modified by Neogene rifting. Anglais 31, 1-4.

Georges, R., Rogers, N., Kelley, S., 1998. Earliest magmastim in Ethiopia: evidence for two mantle plumes in one flood basalt province. Geology 26, 923-926.

Hammond, J.O.S., Kendall, J.-M., Angus, D., Wookey, J., 2010. Interpreting spatial variations in anisotropy: insights into the Main Ethiopian Rift from SKS waveform modelling. Geophys. J. Int. 181, 1701-1712.

Hammond, J.O.S., Kendall, J.-M., Wookey, J., Stuart, G.W., Keir, D., Ayele, A., 2014. Differentiating flow, melt, or fossil seismic anisotropy beneath Ethiopia. Geochem. Geophys. Geosyst. 15, 1878-1894.

Hearmon, R.F.S., 1984. The elastic constants of crystals and other anisotropic materials. In K.H. Hellwege and A.M. Hellwege, Eds., Landolt-BörnsteinTables, III/18, 559. Springer Verlag, Berlin.

Hendrie, D.B., Kusznir, N.J., Morley, C.K., Ebinger, C., 1994. Cenozoic extension in northern Kenya: a quantitative model of rift basin development in the Turkana region. Tectonophysics 236, 409-438.

Hielscher, R., Schaeben, H., 2008. A novel pole figure inversion method: specification of the MTEX algorithm. Journal of Applied Crystallography 41, 1024-1037.

Hirth, G., Kohlstedt, D., 2003. Rheology of the upper mantle and the mantle wedge: a view from the experimentalists. Geophysical Monograph 138, 83-105.

Hofmann, C., Courtillot, V., Feraud, G., Rochette, P., Yirgu, G., Ketefo, E., Pik, R., 1997. Timing of the Ethiopian flood basalt event and implications for plume birth and global change. Nature 389, 338-341.

Kaczmarek, M.-A., Reddy, S.M., 2013. Mantle deformation during rifting: Constraints from quantitative microstructural analysis of olivine from the East African Rift (Marsabit, Kenya). Tectonophysics 608, 1122-1137.

Kaeser, B., Kalt, A., Pettke, T., 2006. Evolution of lithospheric mantle beneath the Marsabit volcanic flied (Northern Kenya): Constraints from textural, P-T and geochemical studies on xenoliths. Journal of Petrology 47, 2149-2184.

Kendall, J.-M., Stuart, G.W., Ebinger, C., Bastow, I.D., Keir, D., 2005. Magma-assisted rifting in Ethiopia. Nature 433, 146-148.

Kieffer, B., Arndt, N., Lapierre, H., Bastien, F., Bosch, D., Pecher, A., Yirgu, G., Ayalew, D., Weis, D., Jerram, D.A., Keller, F., Meugniot, C., 2004. Flood and shield basalts from Ethiopia: Magmas from the African Superswell. Journal of Petrology 45, 793-834.

Kohlstedt, D.L., Zimmerman, M.E., 1996. Rheology of partially molten mantle rocks. Annual Review of Earth and Planetary Sciences 24, 41-62.

Kohlstedt, D., Bai, Q., Wang, Z.-C., Mei, S., 2000. Rheology of Partially Molten Rocks, in: Bagdassarov, N., Laporte, D., Thompson, A. (Eds.), Physics and Chemistry of Partially Molten Rocks. Springer Netherlands, pp. 3-28.

Lorand, J.-P., Reisberg, L., Bedini, R.M., 2003. Platinum-group elements and melt percolations processes in Sidamo spinel peridotite xenoliths, Ethiopia, East African Rift. Chemical Geology 196, 57-75.

Mainprice, D., 1990. A FORTRAN program to calculate seismic anisotropy from the lattice preferred orientation of minerals. Comp. Geosci. 16, 385-393.

Mainprice, D., Hielscher, R., Schaeben, H., 2011. Calculating anisotropic physical properties from texture data using the MTEX open source package, in: Prior, D.J., Rutter, E.H., Tatham, D. J. (Ed.), Deformation Mechanisms, Rheology and Tectonics: Microstructures, Mechanics and Anisotropy. Geological Society, Special Publications, London, pp. 175-192.

Mainprice, D., Bachmann, F., Hielscher, R., Schaeben, H., 2014. Descriptive tools for the analysis of texture projects with large datasets using MTEX - strength, symmetry and components. Geological Society of London Special Publication In Field Experiment and Theory : In Honour of Ernest Rutter.

Morley, C.K., Wescott, W.A., Stone, D.M., Harper, R.M., Wigger, S.T., Karanga, F.M., 1992. Tectonic evolution of the northern Kenya rift. Journal of the geological society, London 149, 333-348.

Morten, L., De Francesco, A.M., Bonavia, F., Haileselassie, G., Bargossi, G.M., Bondi, M., 1992. A new mantle xenolith locality in southern Ethiopia. Mineralogical Magazine 56, 422-425.

Nyblade, A., 2011. The upper-mantle low-velocity anomaly beneath Ethiopia, Kenya, and Tanzania: Constraints on the origin of the African superswell in eastern Africa and plate versus plume models of mantle dynamics. The Geological Society of America Special Paper 478, 37-50.

Nicolas, A., Poirier, J.P., 1976. Crystalline plasticity and solid state flow in metamorphic rocks. Wiley, London.

Ryan, W.B.F., S.M. Carbotte, J.O. Coplan, S. O'Hara, A. Melkonian, R. Arko, R.A. Weissel, V. Ferrini, A. Goodwillie, F. Nitsche, J. Bonczkowski, and R. Zemsky, 2009. Global Multi-Resolution Topography synthesis. Geochemistry Geophysics Geosystems, 10, Q03014, doi:10.1029/2008GC002332.

Shinjo, R., Chekol, T., Meshesha, D., Itaya, T., Tatsumi, Y., 2011. Geochemistry and geochronology of the mafic lavas from the southeastern Ethiopian rift (the East African Rift System): assessment of models on magma sources, plume-lithosphere interaction and plume evolution. Contributions to Mineralogy and Petrology 162, 209-230.

Sicilia, D., Montagner, J.-P., Cara, M., Stutzmann, E., Debayle, E., Lépine, J.-C., Lévêque, J.-J., Beucler, E., Sebai, A., Roult, G., Ayele, A., Sholan, J.M., 2008. Upper mantle structure of shear-waves velocities and stratification of anisotropy in the Afar Hotspot region. Tectonophysics 462, 164-177.

Soustelle, V., Tommasi, A., Demouchy, S., Ionov, D.A., 2010. Deformation and Fluid, a Rock Interaction in the Supra-subduction Mantle: Microstructures and Water Contents in Peridotite Xenoliths from the Avacha Volcano, Kamchatka. Journal of Petrology 51, 363-394.

Tommasi, A., Tikoff, B., Vauchez, A., 1999. Upper mantle tectonics: three-dimensional deformation, olivine crystallographic fabrics and seismic properties. Earth and Planetary Science Letters 168, 173-186.

Tommasi, A., Mainprice, D., Canova, G., Chastel, Y., 2000. Viscoplastic self-consistent and equilibrium-based modeling of olivine lattice preferred orientations: Implications for the upper mantle seismic anisotropy. J. Geophys. Res. 105, 7893-7908.

Vauchez, A., Tommasi, A., Barruol, G., Maumus, J., 2000. Upper mantle deformation and seismic anisotropy in continental rifts. Physics and Chemistry of the Earth 25, 111-117.

Vollmer, F.W., 1990. An application of eigenvalue methods to structural domain analysis. Geological Society of America Bulletin 102, 786-791.

Woldegabriel, G., Yemane, T., Suwa, G., White, T., Asfaw, B., 1991. Age of volcanism and rifting in the Burji-Soyama Area, Amaro Horst, Southern Main Ethiopian Rift: geochronological and biochronologic data. Journal of African Earth Sciences 13, 437-447.

Zimmerman, M.E., Kohlstedt, D.L., 2004. Rheological properties of partially molten lherzolite. Journal of Petrology 45, 275-298.

Chapitre 7 : Discussion, Conclusion et Perspectives

7.1. Discussion

Ce travail apporte des informations sur les caractéristiques du manteau subcontinental sous le craton du Kaapvaal et sous le rift Est-Africain. Il apporte également des contraintes supplémentaires sur le rôle de l'hydratation, de la percolation de fluides et de magmas, de l'anisotropie mécanique et des hétérogénéités rhéologiques sur le comportement géodynamique du manteau subcontinental. Les paramètres seront donc traités successivement dans la discussion suivante après avoir donné un récapitulatif des différentes caractéristiques des péridotites du craton du Kaapvaal et du rift Est-Africain.

7.1.1. Récapitulatif des caractéristiques du manteau subcontinental sous le Kaapvaal et le rift Est-Africain

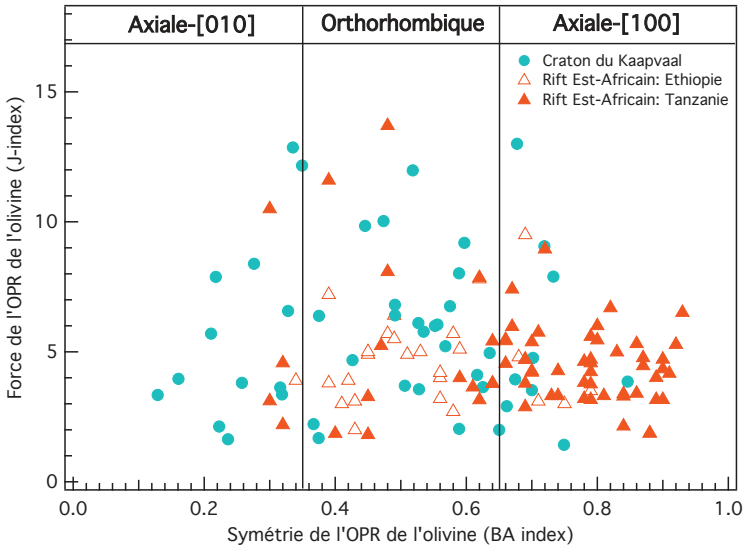

Figure 7.1: Variation de la force de la fabrique de l'olivine (J-index) en fonction de sa symétrie (BA index) dans les échantillons du craton du Kaapvaal, de la Divergence Nord-Tanzanienne et du SE de l'Ethiopie.

La comparaison entre les péridotites du craton du Kaapvaal et ceux du rift Est-Africain révèle une variation des microstructures et des OPRs de l'olivine ainsi que des teneurs en hydrogène dans l'olivine du manteau subcontinental (Tableau 3 et Figures 7.1 et 7.2). Les échantillons étudiés dans ces trois localités sont majoritairement des harzburgites.

Les péridotites du Kaapvaal montrent principalement des textures granulaires à gros grains fortement recuites, suggérant un épisode de déformation suivi par une longue période de quiescence. Les OPRs de l'olivine sont majoritairement orthorhombiques, mais des

axiales-[100] et des axiales-[010] ont été aussi mesurées (Tableau 3, Figure 7.1). Les péridotites cratoniques montrent également une plus large gamme de J-index de l'olivine que dans les rifts. Les teneurs en hydrogène dans l'olivine tendent également à être plus importantes que dans les échantillons de la Divergence Nord Tanzanienne, probablement du fait d'une plus grande solubilité de l'hydrogène dans l'olivine à plus grande profondeur (Figure 7.2).

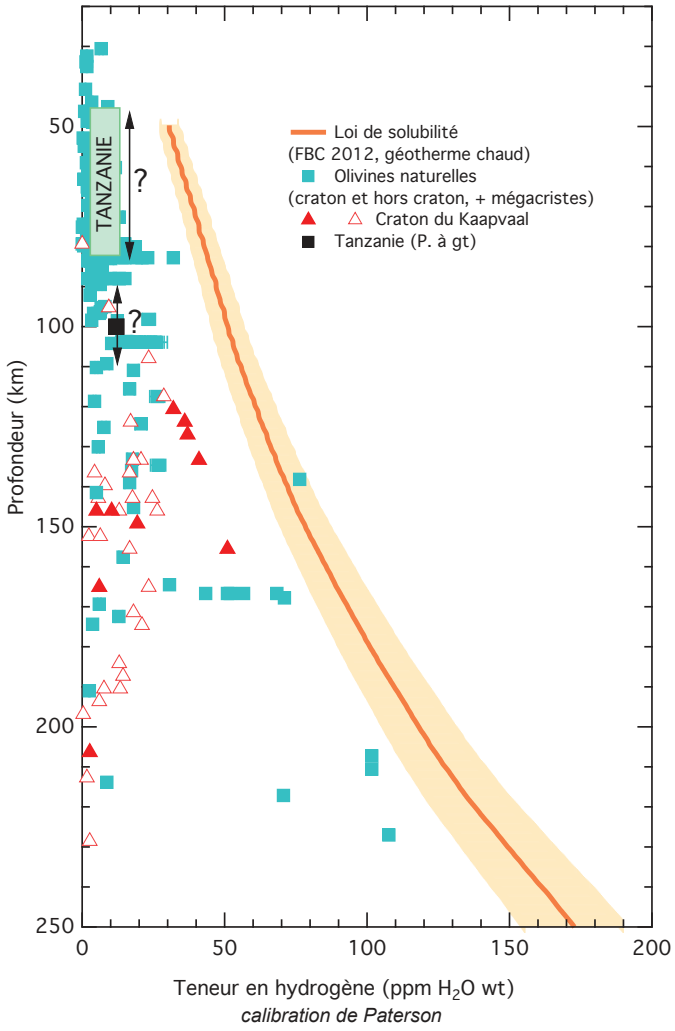

Figure 7.2 : Teneur en hydrogène dans l'olivine en fonction de la profondeur d'équilibre dans les xénolites du craton du Kaapvaal (triangles rouges : Baptiste et al., 2012 ; triangles blancs, Peslier et al., 2010) et dans les xénolites tanzaniens (représenté par un champ vert couvrant la profondeur d'équilibre du spinelle). Pour comparaison, les teneurs en hydrogène dans l'olivine de péridotites d'autres contextes et des mégacrystes d'olivine dans les kimberlites sont également représentés (Bell et al., 2004 ; Demouchy et al., 2006 ; Denis et al., 2013, Base de données de Peslier, 2010). La ligne en pointillés représente la solubilité l'hydrogène dans l'olivine de Férot et Bolfan-Casanova (2012) pour un géotherme océanique.

Tableau 3: Récapitulatif des caractéristiques des péridotites du craton du Kaapvaal et du Rift Est-Africain

	CRATON DU KAAPVAAL		RIFT EST AFRICAIN			
	Péridotites à gros grains (76%)	**Mylonites (24%)**	**Axe du rift (51%)**	**TANZANIE Lashaine (13%)**	**Olmani (36%)**	**ETHIOPIE**
Type de roche	- 84% Harzburgites à spinelle et/ou à grenat - 16% Lherzolites à spinelle et/ou grenat	- 50% Harzburgites à grenat - 50% Lherzolites à grenat	- 74% Harzburgites à spinelle - 19% Dunites à spinelle - 7% Lherzolites à spinelle	- 71% Harzburgites à spinelle ou grenat - 29% Lherzolites à spinelle	- 82% Harzburgites à spinelle - 18% Dunites à spinelle	- 75% Harzburgites à spinelle - 25% Lherzolites à spinelle
Microstructures	- 81% Granulaires à gros grains - 19% Porphyroclastiques à gros grains	- 42% Mosaïques - 42% Mosaïques fluidales - 17% Mylonites	- 81% Porphyroclastiques - 7% Mylonites - 12% Granulaires à gros grains	- Granulaires à gros grains	- 24% Porphyroclastiques à gros grains - 18% Porphyroclastiques - 59% Granulaires à gros grains	- Porphyroclastiques à gros grains.
OPR de l'olivine	- 60% Orthorhombique - 22% Axial-[010] - 19% Axial-[100]	- 67% Orthorhombique - 33% Bimodale	- 56% Axial-[100] - 26% Orthorhombique - 18 % Intermédiaire Axial-[100]/Ortho	- 43% Axial-[010] - 29% Orthorhombique - 29% Intermédiaire Axial-[010]/ Ortho	- 47% Intermédiaire Axial-[100]/ Ortho - 35% Axial-[100] - 12% Orthorhombique	- 75% Orthorhombique - 10% Intermédiaire Axial-[010]/ Ortho - 10% Axial-[010] - 5% Intermédiaire Axial-[100]/ Ortho
J-index de l'olivine	1,5-13,0	1,8-4,6	2,1-6,7	2,1-6,0	1,8-9,0	2,0-9,5
Teneurs en H (ppm wt. H_2O)	3-50	-	2-12	12	3-5	-

Il existe aussi des variations des caractéristiques de la déformation le long du rift Est-Africain. Dans l'axe du rift, les échantillons ont majoritairement des textures porphyroclastiques et plus rarement mylonitiques, suggérant une localisation de la déformation. Les OPRs de l'olivine de type axial-[100] y sont majoritaires. A Lashaine, les échantillons montrent des textures granulaires à gros grains et des OPRs de l'olivine orthorhombique à axiales-[010]. Enfin, Olmani présente des textures et des OPRs intermédiaires. En Ethiopie, les péridotites montrent principalement des textures porphyroclastiques à gros grains et les OPRs de l'olivine de type orthorhombique dominent. Les gammes de J-index de l'olivine calculés dans les péridotites de Tanzanie et d'Ethiopie sont toutefois semblables.

7.1.2. Rôle de l'état d'hydratation

Le rôle de l'état d'hydratation a dans un premier temps pu être exploré au travers de l'étude des xénolites du craton du Kaapvaal (Baptiste et al., 2012). Cette étude nous révèle des teneurs en hydrogène dans l'olivine très variables (3-50 wt. ppm H_2O, calibration de Paterson (1982)). Les teneurs maximales ont toutefois tendance à augmenter jusqu'à 150 km de profondeur, atteignant alors jusqu'à 50 wt. ppm H_2O. A contrario, les échantillons les plus profonds sont presque secs (<10 wt. ppm H_2O ; Baptiste et al., 2012). Ces résultats confirment les variations des teneurs en hydrogène dans l'olivine précédemment mesurées dans des péridotites du Kaapvaal par Peslier et al. (2010), mais différent de ceux obtenus dans les xenolites du craton Sibérien, où les valeurs maximales sont observées dans les échantillons de la base de la racine (Doucet et al., 2014). Les résultats expérimentaux sur la diffusion de l'hydrogène d'un liquide kimberlitique à la forstérite indiquent que la présence de CO_2 dans les kimberlites pourrait diminuer la fugacité en eau, au point de ne pouvoir hydrater l'olivine lors du transport des xénolites vers la surface (Baptiste et al., en prep pour Am. Min.). Ces résultats suggèrent donc que les fortes teneurs en hydrogène dans l'olivine mesurées dans les péridotites du craton du Kaapvaal ont bien été acquises durant un épisode métasomatique en profondeur (>3 GPa). Ces teneurs en hydrogène seraient donc représentatives de la composition du manteau subcratonique au moment de l'extraction des xénolites, du Jurassique supérieur au Crétacé. Pourtant, cet état d'hydratation n'a pas à ce jour entraîné la remobilisation du craton, comme le montre les études sismiques qui détectent une racine atteignant au moins 200 km (Chevrot et Zhao, 2007 ; Fishwick, 2010 ; James et al., 2001 ; Li et Burke, 2006 ; Priestley, 1999 ; Priestley et al., 2006).

Il est donc nécessaire de s'interroger sur le volume affecté par de telles teneurs en

hydrogène dans l'olivine. Les récents modèles de conductivité de Fullea et al. (2011) indiquent qu'une variation verticale d'une composition hydratée à une composition anhydre est nécessaire afin d'expliquer les réponses magnétotelluriques mesurées au niveau du craton du Kaapvaal par Evans et al. (2011). La cohérence entre la variation requise par les modèles de Fullea et al. (2011) et la variation des teneurs en hydrogène dans l'olivine des péridotites du Kaapvaal pourrait indiquer qu'elles sont bien représentatives de l'ensemble de la racine cratonique. Il est aussi possible que les études magnétotelluriques aient moyenné une distribution hétérogène des teneurs en hydrogène à échelle kilométrique. Si c'est en effet le cas, cela implique qu'il existe des domaines riches en hydrogène connectés au sein de la racine mantellique du craton du Kaapvaal, et que ces domaines occupent un volume significatif. L'existence de tels domaines est cohérente avec l'hypothèse de Griffin et al. (2009), qui, en comparant les données de tomographie régionales et globales et la position des diatrèmes kimberlitiques, proposèrent que les xénolites du Kaapvaal n'échantillonneraient que les marges de blocs lithosphériques, aux vitesses sismiques plus faibles. En se basant sur l'hypothèse que les variations des vitesses sismiques sont le reflet d'une variation de composition, Griffin et al. (2009) suggérèrent ainsi que les kimberlites échantillonneraient préférentiellement un matériel métasomatisé.

Que ces teneurs en hydrogène élevées dans l'olivine soient présentes dans l'ensemble de la racine ou dans des domaines distincts, elles devraient avoir entraîné une déstabilisation du craton du Kaapvaal depuis l'extraction des xénolites au Jurassique et au Crétacé. En effet, des récents modèles numériques (Liao et al., 2013) suggèrent que la présence d'une couche peu résistante (liée au métasomatisme et/ou à l'hydratation) au cœur de la racine cratonique favoriserait la déformation dans le manteau et la croûte qui se trouve au-dessus, et ainsi la déstabilisation du craton. Des modèles numériques suggèrent que la stabilité des cratons pourrait être favorisée par la présence de matériel peu résistant autour du craton, telles que des chaines collisionnelles Néoprotérozoïques ou plus récentes (Lenardic et al., 2003). Cette hypothèse n'explique toutefois pas comment une racine hydratée ou partiellement hydratée a pu échapper à une remobilisation liée à la convection mantellique. Ainsi, pour expliquer la longévité du craton du Kaapvaal malgré son état d'hydratation, Peslier et al. (2010) ont suggéré que la présence d'une couche sèche, et donc plus résistante à la base de la racine, pourrait avoir permis sa préservation. Cependant, des modèles numériques sont nécessaires afin de tester la plausibilité de cette hypothèse et tous les cratons ne présentent pas des péridotites de racine profonde pauvre en hydrogène (Doucet et al., 2014). Enfin, l'impact de l'eau sur la résistance du manteau pourrait avoir été surestimé, comme le suggère des

expériences récentes de détermination du coefficient de diffusion du Si dans la forstérite par Fei et al. (2013).

Les analyses par spectroscopie infra-rouge sur les xénolites mantelliques de la Divergence Nord Tanzanienne (Rift Est Africain) révèlent des teneurs en hydrogène dans l'olivine aussi variables, mais comprises entre 2 et 12 wt. ppm H_2O. Le timing de l'incorporation d'hydrogène dans les xénolites de la Divergence Nord Tanzanienne reste difficile à contraindre (Baptiste et al., soumis à *Tectonophysics*). L'absence de profils de diffusion dans l'olivine suggère que ces concentrations ont été acquises avant l'extraction des xénolites. De plus, l'absence de variation systématique des teneurs en hydrogène dans l'olivine à l'approche des veines riches en minéraux hydratés indiquent que le métasomatique tardif à l'origine de leur formation n'est pas responsable de l'hydratation mesurée. Il est impossible de déterminer la chronologie relative entre la déformation liée au rifting et l'acquisition de ces teneurs en hydrogène à partir de nos données. Si le manteau Tanzanien était en effet hydraté avant le début de la déformation associée au rifting, l'importante interaction avec des magmas pendant la déformation (Baptiste et al., soumis à *Tectonophysics*) pourrait en avoir modifié la composition, puisque les taux de diffusion de l'hydrogène dans l'olivine sont très rapides à haute température (T> 1000 °C, Demouchy et Mackwell, 2006 ; Demouchy et al., 2006). Les teneurs en hydrogène mesurées pourraient donc ne pas être représentatives de l'état d'hydratation précédant le rifting. Si, a contrario, ces teneurs ont été acquises durant un épisode métasomatique syn-déformation, l'absence de corrélation entre teneurs en hydrogène et microstructures pourrait indiquer qu'il ne représente pas un mécanisme déterminant lors de la localisation de la déformation dans les péridotites tanzaniennes.

Dans les xénolites du craton du Kaapvaal comme dans les xénolites de la Divergence Nord Tanzanienne, il n'existe pas de corrélation claire entre microstructures et teneurs en hydrogène dans l'olivine. Si dans ces localités, les mylonites montrent les plus faibles teneurs en eau, le faible nombre de mesures (2 échantillons) empêche d'affirmer qu'il s'agit d'un trait systématique.

Enfin, les données expérimentales de Jung et al. (2006) prédisent une transition du système de glissement [100](010) à [100](001) de l'olivine pour des teneurs en hydrogène supérieures à ~15 wt. ppm H_2O. Pourtant, même dans les échantillons porphyroclastiques à gros grains du Kaapvaal pour lesquels la foliation est identifiable, un tel changement de plan de glissement n'est pas observé malgré des teneurs en hydrogène supérieures à cette valeur.

7.1.3. Rôle de la percolation de fluides et magmas

Les études réalisées sur des xénolites du rift Est-Africain (Tanzanie et Ethiopie) dans le cadre de cette thèse indiquent que le manteau subcontinental sous un craton ou sous un rift est soumis de manière fréquente à de la percolation réactive de fluides ou de magmas qui modifient sa composition minéralogique mais aussi parfois ses microstructures et probablement son comportement mécanique.

Les xénolites mantelliques du craton du Kaapvaal enregistrent de multiples épisodes métasomatiques. De ces épisodes résulte une forte hétérogénéité de compositions à petite échelle qui ne peut être détectée par les études sismologiques (Baptiste et Tommasi, 2014). Les teneurs élevées en orthopyroxène ont ainsi été attribuées à un métasomatisme lié à des fluides ou magmas riches en Si (Bell et al., 2005 ; Kelemen et al., 1998 ; Wasch et al., 2009) pré- à syn-cinématique (Baptiste et al., 2012). Un enrichissement en clinopyroxène et phlogopite post-cinématique (Baptiste et al., 2012) a été relié à un métasomatisme par des fluides ou magmas riches en K (Bell et al., 2005 ; Grégoire et al., 2003 ; Griffin et al., 2003). Que ces hétérogénéités de composition soient présentes uniquement en bordure de blocs (Griffin et al., 2009) ou représentatives de l'ensemble du manteau cratonique, elles devraient avoir généré des contrastes de viscosité au sein de la racine. En effet, une refertilisation locale et progressive de la racine à partir de sa base est un des processus proposés comme pouvant amener à l'érosion thermomécanique du manteau cratonique (Foley et al., 2008 ; Lee et al., 2011). Toutefois, le craton du Kaapvaal est resté stable malgré cela depuis le Jurassique-Crétacé.

Que ce soit en Tanzanie ou au SE de l'Ethiopie, la percolation de magmas dans le manteau lithosphérique semble être un processus indissociable du rifting. L'analyse des microstructures des xénolites de la Divergence Tanzanienne suggère en effet que la déformation a été accompagnée de réactions magma-roche sous des conditions proches du solidus. Ces réactions ont eu pour effet de modifier la composition, mais aussi les microstructures des péridotites mylonitiques et porphyroclastiques (Baptiste et al., soumis à *Tectonophysics*). En effet, elle entraîne une dunification des harzburgites en cristallisant de l'olivine à la place de l'orthopyroxène, mais également une fragmentation plus efficace des porphyroclastes d'orthopyroxène durant la déformation.

D'autre part, l'hétérogénéité de microstructures et des OPRs de l'olivine suggère que la déformation a été acquise durant plusieurs épisodes tectoniques, probablement séparés par des périodes d'accalmie, permettant le recuit de ces roches. L'analyse des microstructures des

xénolites tanzaniens indique également des variations locales et transitoires de température. Ces variations sont certainement associées à la percolation réactive et épisodique de magmas, qui pourrait être à l'origine du caractère lui-même hétérogène et épisodique de la déformation. Outre l'effet des variations de température associées à l'injection de magmas, une déformation en présence de magmas tend aussi à créer une anisotropie de viscosité au sein de la roche, en ségrégant le magma en bandes distinctes (Holtzman et al., 2003a, b).

Enfin, les xénolites tanzaniens enregistrent un épisode métasomatique plus tardif, à l'origine de la cristallisation de minéraux hydratés (amphibole, phlogopite) sous forme de veines recoupant la microstructure, ou sous forme d'amas plus diffus. Or, cet ajout de phases moins résistantes ne se traduit pas par une variation des microstructures de déformation des péridotites, suggérant que la percolation de magmas/fluides hydratés n'est pas toujours accompagnée d'une localisation de la déformation.

Au SE de l'Ethiopie, les données géochimiques de Bedini et al. (1997) sur les xénolites éthiopiens révèlent deux métasomatismes, interprétés comme le résultat d'un unique épisode de percolation magmatique, lié à des interactions entre un panache et la base de la lithosphère. Cet épisode a entraîné une modification de la composition modale de ces échantillons, permettant par exemple de cristalliser du clinopyroxène à partir de l'orthopyroxène, ou de l'orthopyroxène à partir de l'olivine, selon la position au sein de la colonne de percolation. Ces réactions se traduisent par la présence de cristaux interstitiels d'orthopyroxène et de clinopyroxène dans les xénolites éthiopiens. La présence de sous-joints dans ces cristaux et d'OPRs dans les pyroxènes suggèrent un métasomatisme pré- à syn-déformation (Baptiste et al., in prep). Les microstructures suggèrent également une déformation à haute température puis un refroidissement à l'origine de la formation d'exsolutions dans les pyroxènes. Ces observations suggèrent tout comme en Tanzanie une percolation transitoire de magmas. L'homogénéité apparente des microstructures et des OPRs de la majorité des xénolites éthiopiens semble indiquer qu'ils sont le résultat d'un épisode de déformation commun.

Que ce soit sous le craton du Kaapvaal ou le rift Est-Africain, l'injection de magmas/fluides responsables de la cristallisation de phases hydratées n'est pas accompagnée par une modification des microstructures et semble se faire de manière statique. Les magmas impliqués dans la déformation au cœur du rift Est-Africain ont une composition différente : en Tanzanie, il s'agit de magmas sous-saturés en Si entraînant une dunitisation progressive des harzburgites, alors qu'en Ethiopie, ils correspondent à des magmas de types OIB (Ocean

Island Basalt) entraînant une dunitisation de la roche à la base de la colonne de percolation et une refertilisation à son sommet (Bedini et al., 1997).

7.1.4. Rôle des hétérogénéités rhéologiques et de l'anisotropie mécanique

La présence d'hétérogénéités rhéologiques de grande échelle a été mise en avant comme un mécanisme pouvant favoriser la localisation de la déformation et contrôler la localisation d'un rift (Vauchez et al. 1997). Du fait de leur épaisseur, leur composition, mais aussi leur géotherme, les cratons peuvent induire une concentration de contraintes à leurs frontières (Tommasi et Vauchez, 1997 ; Tommasi et al., 1995). Le rift Est-Africain se scinde ainsi en deux branches de part et d'autre du craton Tanzanien. Au niveau de la Divergence Nord Tanzanienne, le rift Est-Africain s'interrompt pour se diviser en deux branches, à l'Est, le bassin d'Eyasi, et à l'Ouest, le graben de Pangani. L'étude des xénolites mantelliques tanzaniens révèle que sous Lashaine, au sein de la chaîne volcanique transverse, le manteau lithosphérique présente des microstructures et des OPRs différentes de celles des localités situées dans l'axe du rift. Nous (Baptiste et al., submitted to *Tectonophysics*) suggérons qu'elles pourraient être liées à la formation de la chaîne Mozambique ou à un domaine cratonique préservé dans la chaîne Mozambique, compte-tenu des similitudes entre les xénolites de Lashaine et les xénolites cratoniques du Labait et du Kaapvaal. En effet, les deux localités de la chaîne volcanique transverse étudiées se situent au niveau d'un domaine interprété comme un reste de craton repris lors de l'orogénèse Néoprotérozoïque (Mansur et al., 2014 ; Möller et al., 1998). La présence d'un tel domaine pourrait expliquer le fait que la branche est du REA se scinde en deux rifts au niveau de la Divergence Nord Tanzanienne (Graben de Pangani à l'Est et Basin d'Eyasi à l'Ouest, voir Chapitre 5 Figure 1).

Des modèles numériques suggèrent que le démarrage de rift contrôlé par la réactivation d'OPRs fossilisées dans d'anciens orogènes débute en transtension et est ensuite suivie par une déformation en extension normale (Tommasi et al., 2009). Or, les OPRs de l'olivine de type axial-[100] majoritairement mesurées dans les péridotites de Tanzanie sont cohérentes avec une déformation en transtension. Ces résultats sont cohérents avec les directions de polarisation rapides parallèles à obliques à l'axe du rift mesurées par les ondes SKS en Tanzanie, et devraient produire des OPRs de type axial-[100] (Vauchez et al., 2000) telles que celles mesurées dans les péridotites de l'axe du rift. L'analyse des OPRs de Lashaine suggère la présence d'OPRs fossilisées avant le début du rifting, qui pourraient avoir généré une anisotropie mécanique au sein du manteau lithosphérique. Dans les xénolites d'Ethiopie, les

OPRs de l'olivine de type orthorhombique sont majoritaires. Ces OPRs symmétriques pourraient suggérer une déformation en extension normale dans cette partie du rift Est-Africain plus mature.

Le calcul des propriétés sismiques des xénolites du craton du Kaapvaal apporte des contraintes supplémentaires sur la structure de la racine et des éléments de discussion sur la manière dont elle s'est formée. A partir du calcul de propriétés moyennes dans des sections de 20km, nous avons pu évaluer l'anisotropie qui devrait être mesurée par les ondes SKS, Rayleigh et Love (Baptiste et Tommasi, 2014). Une foliation et une linéation plongeante dans l'ensemble de la racine peuvent expliquer les faibles déphasages et les directions de polarisation cohérentes des ondes SKS sur l'ensemble du craton, ainsi que les faibles anisotropies azimutales des ondes de surface avec S_H plus rapide que S_V. Des foliations et linéations plongeantes à 45° au cœur de la lithosphère cratonique pourrait s'être développées si la racine a été formée par imbrication de panneaux plongeants. Dans un tel cas, des directions de polarisation perpendiculaires aux principales sutures devraient être mesurées par les ondes SKS, qui montrent au contraire des directions parallèles (Silver et al., 2001). Les faibles déphasages mesurés par les ondes SKS au niveau du craton du Kaapvaal pourrait également être produits par des variations verticales d'anisotropie. Un contraste d'impédance suffisant pour expliquer la discontinuité sismique à ~150km mesurée par les fonctions récepteurs des ondes S (Hansen et al., 2009 ; Savage et Silver, 2008 ; Wittlinger et Farra, 2007) peut être généré par un changement d'anisotropie. Une variation verticale d'anisotropie sismique avec une direction d'écoulement horizontale dominante dans le manteau lithosphérique du Kaapvaal pourrait avoir été produite si la racine s'est formée par l'injection épisodique de petits diapirs (de Smet, 1998, 1999). Toutefois, un tel modèle ne pourrait expliquer les directions de polarisation de l'onde rapide cohérentes sous l'ensemble de la racine mesurée par les ondes SKS (Silver et al., 2001).

7.2. Conclusion et Perspectives

L'étude des xénolites mantelliques du craton du Kaapvaal et du rift Est Africain révèle que le manteau lithosphérique subcontinental évolue par une succession d'épisodes de déformation, où le mécanisme de fluage par dislocation domine, et de percolation réactive de fluides et/ou de magmas. Il existe toutefois des différences notables dans les microstructures et les OPRs de l'olivine dans le manteau lithosphérique entre le craton et le rift, mais également le long du rift lui-même. De même, les teneurs en hydrogène mesurées dans l'olivine varient significativement d'un contexte à un autre.

L'étude des péridotites du craton du Kaapvaal révèle une racine aux compositions hétérogènes. En effet, les multiples épisodes métasomatiques subis par le craton entrainent des variations de compositions modales à une échelle probablement trop petite pour être détectée par les études sismologiques. Les teneurs en hydrogène dans l'olivine sont également variables, mais tendent à augmenter jusqu'à 150 km, atteignant alors jusqu'à 50 ppm wt. H_2O (calibration de Paterson, 1982). Les échantillons les plus profonds sont quant à eux presque secs (<5 ppm wt. H_2O). Nos expériences sur la diffusion de l'hydrogène d'un liquide kimberlitique riche en volatiles vers de la forstérite montrent que la présence de CO_2 dans les kimberlites pourrait diminuer la fugacité en eau, au point d'inhiber complétement l'hydratation de l'olivine. Ces résultats expérimentaux suggèrent que les teneurs en hydrogène dans l'olivine des péridotites du craton du Kaapvaal ont été acquises durant un épisode métasomatique dans le manteau lithosphérique et non pendant leur extraction par les kimberlites. Les données magnétotelluriques du Kaapvaal sont mieux expliquées par des modèles comprenant une variation verticale des teneurs en hydrogène dans l'olivine similaire à celle mesurée. Ces résultats peuvent être expliqués si les teneurs en hydrogène mesurées sont représentatives de l'ensemble de la racine ou encore de domaines interconnectés riches en hydrogène. L'acquisition de ces compositions n'a toutefois pas été suivie d'une remobilisation de la racine cratonique. En effet, les textures granulaires à gros grains très recuites, ainsi que des OPRs dans l'olivine et les pyroxènes bien développées dans les péridotites cratoniques ne témoignent que d'un épisode de déformation ancien, suivi par une longue période de quiescence. Ces résultats suggèrent que l'incorporation d'hydrogène dans le manteau pourrait ne pas avoir un effet sur sa viscosité aussi important que précédemment envisagé, comme semblent l'indiquer des expériences récentes de détermination du coefficient de diffusion du Si dans la forstérite par Fei et al. (2013) à 8 GPa et 1600-1800 K. Ces conditions expérimentales n'étant pas représentatives des conditions lithosphériques, il

serait intéressant de tester la reproductibilité de ce résultat à plus basse pression et température. De plus, les analyses par IRTF sur des péridotites du craton de Sibérie révèlent des teneurs en hydrogène dans l'olivine importantes, augmentant de manière progressive jusqu'à 6 GPa contrairement à ce que nous avons mesuré dans les péridotites du craton du Kaapvaal (Doucet et al., 2014). Il serait donc nécessaire d'étendre le type d'étude réalisé dans le Kaapvaal à d'autres cratons, afin de s'affranchir de particularités locales et de tirer des enseignements généraux sur les processus responsables de leur stabilité. Enfin, le calcul des propriétés sismiques des péridotites du Kaapvaal révèle que les anisotropies générées par les OPRs de ces échantillons sont suffisantes pour expliquer les anisotropies mesurées par les ondes SKS ainsi que par les ondes de surface.

L'étude des péridotites de la Divergence Nord-Tanzanienne a révélé une forte hétérogénéité latérale et temporelle de la déformation au sein du rift. Il existe en effet des variations significatives de microstructures et d'OPR de l'olivine entre les péridotites provenant de localités dans l'axe du rift et celles de la chaîne volcanique transverse (Lashaine et Olmani). A Lashaine, les microstructures granulaires à gros grains et les OPRs de type orthorhombique et axial-[010] peuvent être expliquées par une déformation en transpression liée à la formation de la chaîne Mozambique, ou par la présence d'une relique d'un domaine cratonique à l'intérieur de la chaîne Mozambique. Dans l'axe du rift, les microstructures porphyroclastiques et mylonitiques suggèrent une déformation plus récente, accompagnée de réactions magma-roche sous des conditions proches du solidus, suivie d'un recuit variable. L'hétérogénéité des microstructures des échantillons du rift suggère de multiples épisodes de déformation localisée, probablement liés à l'injection percolation épisodique de magmas, espacés de périodes d'accalmie.

A contrario, les péridotites du Sud-Est de l'Ethiopie présentent des microstructures porphyroclastiques à gros grains moins recristallisées et plus homogènes qu'en Tanzanie. Les microstructures et les OPRs principalement de type orthorhombique sont cohérentes avec une déformation syn- à post-métasomatisme. Il serait donc intéressant de vérifier si la déformation dans le manteau lithosphérique sous la partie éthiopienne du Rift Est-Africain est homogène latéralement et temporellement en échantillonnant d'autres localités. Si c'est effectivement le cas, cette homogénéité pourrait être liée à une percolation de magmas plus homogène à l'aplomb d'un panache. En effet, une distribution homogène de magmas dans un volume important tend à promouvoir une déformation homogène (e.g. Vauchez et al., 2007). De même, cela pourrait alors suggérer que l'homogénéité est une caractéristique de la

déformation sous un rift mature, tandis que la déformation en début de rifting se fait de manière plus hétérogène, du fait d'une percolation de magmas plus localisée.

Enfin, les OPRs de l'olivine de type axial-[100] majoritaires dans les péridotites de l'axe du rift peuvent être produites par une déformation en transtension. Ces résultats sont cohérents avec les directions de polarisation de l'onde S rapide parallèles à obliques à l'axe du rift mesurées par les ondes SKS en Tanzanie, et devraient produire des OPRs de type axial-[100] (Vauchez et al., 2000), telles que celles mesurées dans les échantillons étudiés. Contrairement à ce qui est obtenu en Tanzanie, les anisotropies de polarisation des ondes S calculées pour les péridotites éthiopiennes sont insuffisantes pour expliquer à elles seules les déphasages des ondes SKS dans cette partie du rift. Cela pourrait ainsi suggérer que les anisotropies estimées en utilisant les ondes SKS dans le rift éthiopien sont effectivement liées à la présence de poches de magmas orientées sous le rift (Ayele et al., 2004; Kendall et al., 2005).

Références (Hors articles)

Adams, A., Nyblade, A., Weeraratne, D., 2012. Upper mantle shear wave velocity structure beneath the East African plateau: evidence for a deep, plateauwide low velocity anomaly. Geophys. J. Int. 189, 123-142.

Allsopp, H.L., Bristow, J.W., Skinner, E.M.W., 1985. The Rb-Sr geochronology of the Colossus kimberlite pipe, Zimbabwe. Transactions of the Geological Society of South Africa 88, 245-248.

Arndt, N.T., Coltice, N., Helmstaedt, H., Grégoire, M., 2009. Origin of Archean subcontinentatl lithospheric mantle: Some petrological constraints Lithos 109, 61-71.

Ayele, A., Stuart, G.W., Kendall, J.-M., 2004. Insights into rifting from shear wave splitting and receiver functions: An example from Ethiopia. Geophys. J. Int. 157, 354-362.

Baptiste, V., Tommasi, A., 2014. Petrophysical constraints on the seismic properties of the Kaapvaal craton mantle root. Solid Earth 5, 45-63.

Baptiste, V., Tommasi, A., Demouchy, S., 2012. Deformation and hydration of the lithospheric mantle beneath the Kaapvaal craton, South Africa. Lithos 149, 31-50.

Baptiste, V., Vauchez, A., Tommasi, A., Demouchy, S., Rudnick, R.L., 2014. Deformation, hydration, and anisotropy of the lithospheric mantle in an active rift: constraints from mantle xenoliths from the North Tanzanian Divergence of the East African Rift. Submitted to Tectonophysics.

Bedini, R.M., Bodinier, J.-L., Dautria, J.-M., Morten, L., 1997. Evolution of LILE-enriched small melt fractions in the lithospheric mantle: a case study from the East African Rift. Earth and Planetary Science Letters 153, 67-83.

Begg, G.C., Griffin, W.L., Natapov, L.M., O'Reilly, S.Y., Grand, S.P., O'Neill, C.J., Hronsky, J.M.A., Poudjom Djomani, Y., Swain, C.J., Deen, T., Bowden, P., 2009. The lithospheric architecture of Africa: Seismic tomography, mantle petrology, and tectonic evolution. Geosphere 5, 23-50.

Béjina, F., Jaoul, O., Liebermann, R.C., 1999. Activation volume of Si diffusion in San Carlos olivine: Implications for upper mantle rheology. Journal of Geophysical Research: Solid Earth 104, 25529-25542.

Bell, D., Grégoire, M., Grove, T., Chatterjee, N., Carlson, R., Buseck, P., 2005. Silica and volatile-element metasomatism of Archean mantle: a xenolith-scale example from the Kaapvaal Craton. Contributions to Mineralogy and Petrology 150, 251-267.

Bell, D.R., Rossman, G.R., Maldener, J., Endisch, D., Rauch, F., 2003. Hydroxide in olivine: A quantitative determination of the absolute amount and calibration of the IR spectrum. J. Geophys. Res. 108, ECV8.1-ECV8.9.

Bell, D.R., Rossman, G.R., Moore, R.O., 2004. Abundance and Partitioning of OH in a High-pressure Magmatic System: Megacrysts from the Monastery Kimberlite, South Africa. Journal of Petrology 45, 1539-1564.

Benoit, M.H., Nyblade, A.A., Pasyanos, M.E., 2006. Crustal thinning between the Ethiopian and East African plateaus from modeling Rayleigh wave dispersion. Geophysical research letters 33, 1-5.

Beran, A., Putnis, A., 1983. A Model of the OH positions in olivine, derived from Infrared-spectroscopic investigations. Physics and Chemistry of Minerals 9, 57-60.

Beran, A., Zemman, J., 1969. Üder OH-gruppen in Olivin. Österreich Akademie des Wissenschaften 3, 73-74.

Bercovici, D., Ricard, Y., 2012. Mechanisms for the generation of plate tectonics by two-phase grain damage and pinning. Physics of the Earth and Planetary Interiors 202-203, 27-55.

Biggs, J., Bastow, I.D., Keir, D., Lewi, E., 2011. Pulses of deformation reveal frequently recurring shallow magmatic activity beneath the Main Ethiopian Rift. Geochem. Geophys. Geosyst. 12, 1-11.

Bolfan-Casanova, N., 2005. Water in the Earth's mantle. Mineral Mag 69, 229-257.

Bonini, M., Corti, G., Innocenti, F., Manetti, P., Mazzarini, F., Abebe, T., Pecskay, Z., 2005. Evolution of the Main Ethiopian Rift in the frame of Afar and Kenya rifts propagation. Tectonics 24, 1-21.

Borch, R.S., Green II, H.W., 1989. Deformation of peridotite at high pressure in a new molten salt cell: comparison of traditional and homologous temperature treatments. Physics of the Earth and Planetary Interiors 55, 269-276.

Boullier, A.M., Gueguen, Y., 1975. SP-Mylonites: Origin of some mylonites by superplastic flow. Contributions to Mineralogy and Petrology 50, 93-104.

Boyd, F.R., Mertzman, S.A., 1987. Composition and structure of the Kaapvaal lithosphere, in: Mysen, B.O. (Ed.), Magmatic Processes: Physiochemical Principles, B.O. ed. Geochemical Society Special Publications, Washington, DC, pp. 13-24.

Buck, W.R., 2006. The role of magma in the development of the Afro-Arabian Rift System. Geological Society London Special Publications 259, 43-54.

Carlson, R.W., Irving, A.J., Schulze, D.J., Hearn Jr, B.C., 2004. Timing of Precambrian melt depletion and Phanerozoic refertilization events in the lithospheric mantle of the Wyoming Craton and adjacent Central Plains Orogen. Lithos 77, 453-472.

Cerling, T.E., Powers, D.W., 1977. Paleorifting between the Gregory and the Ethiopian rifts. Geology 5, 441-444.

Chen, L., Tao, W., Zhao, L., Zheng, T., 2008. Distinct lateral variation of lithospheric thickness in the Northeastern North China Craton. Earth and Planetary Science Letters 267, 56-68.

Chevrot, S., Zhao, L., 2007. Multiscale finite-frequency Rayleigh wave tomography of the Kaapvaal craton. Geophys. J. Int. 169, 201-215.

Chopra, P.N., Paterson, M.S., 1984. The role of water in the deformation of dunite. Journal of Geophysical Research 86, 7861-7876.

Corti, G., 2008. Control of rift obliquity on the evolution and segmentation of the main Ethiopian rift. Nature 11, 258-262.

Crossley, R., Knight, R.M., 1981. Volcanism in the western part of the Rift valley in Southern Kenya. Bulletin of Volcanology 44, 117-128.

Daines, M.J., Kohlstedt, D.L., 1997. Indluence of deformation on melt topology in peridotites. Journal of geophysical Research 102, 10257-10271.

Dawson, J.B., 1992. Neogene tectonics and volcanicity in the North Tanzania sector of the Gregory Rift Valley: contrasts with the Kenya sector. Tectonophysics 204, 81-92.

Denis, C.M.M., Demouchy, S., Shaw, C.S.J., 2013. Evidence of dehydration in peridotites from Eifel Volcanic Field and estimates of the rate of magma ascent. Journal of Volcanology and Geothermal Research 258, 85-99.

de Smet, J.H., van den Berg, A.P., Vlaar, N.J., 1998. Stability and growth of continental shields in mantle convection models including melt production. Tectonophysics 296, 15-29.

de Smet, J.H., van den Berg, A.P., Vlaar, N.J., 1999. The evolution of continental roots in numerical thermo-chemical mantle convection models including differentiation by partial melting. Lithos 48, 153-170.

de Smet, J.H., Van den Berg, A.P., Vlaar, N.J., 2000. Early formation and long-term stability of continents resulting from decompression melting in a convecting mantle. Tectonophysics 322, 19-33.

de Wit, M.J., Roering, C., Hart, R.G., Armstrong, R.A., de Ronde, C.E.G., Green, R.W.E., Tredoux, M., Pederby, E., Hart, R.A., 1992. Formation of an Archean Continent. Nature 357, 553-562.
Debayle, E., Kennett, B., Priestley, K., 2005. Global azimuthal seismic anisotropy and the unique plate-motion deformation of Australia. Nature 433, 509-512.
Demouchy, S., Jacobsen, S.D., Gaillard, F., Stern, C.R., 2006. Rapid magma ascent recorded by water diffusion profiles in mantle olivine. Geology 34, 429-432.
Demouchy, S., Mackwell, S., 2006. Mechanisms of hydrogen incorporation and diffusion in iron-bearing olivine. Physics and Chemistry of Minerals 33, 347-355.
Demouchy, S., Tommasi, A., Barou, F., Mainprice, D., Cordier, P., 2012. Deformation of olivine in torsion under hydrous conditions. Physics of the Earth and Planetary Interiors 202-203, 56-70.
Dixon, J.E., Leist, L., Langmuir, C., Schilling, J.-G., 2002. Recycled dehydrated lithosphere observed in plume-influenced mid-ocean-ridge basalt. Nature 420, 385-389.
Doin, M.-P., Fleitout, L., Christensen, U., 1997. Mantle convection and stability of depleted and undepleted continental lithosphere. J. Geophys. Res. 102, 2771-2787.
Doucet, L.S., Peslier, A.H., Ionov, D.A., Brandon, A.D., Golovin, A.V., Goncharov, A.G., Ashchepkov, I.V., 2014. High water contents in the Siberian cratonic mantle linked to metasomatism: An FTIR study of Udachnaya peridotite xenoliths. Geochimica et Cosmochimica Acta 137, 159-187.
Dunbar, J.A., Sawyer, D.S., 1989. How preexisting weaknesses control the styles of continental breakup. Journal of geophysical Research 94, 7278-7292.
Eaton, D.W., Darbyshire, F., Evans, R.L., Grütter, H., Jones, A.G., Yuan, X., 2009. The elusive lithosphere-asthenosphere boundary (LAB) beneath cratons. Lithos 109, 1-22.
Ebinger, C., Yemane, T., Woldegabriel, G., Aronson, J.L., Walter, R.C., 1993. Late Eocene: recent volcanism and faulting in the southern Main Ethiopian Rift. Journal of the geological society, London 150, 99-108.
Eggler, D.H., Furlong, K.P., 1991. Destruction of subcratonic mantle keel: the Wyoming province, 5th Kimberlite Conf. Ext. Abs, pp. 85-87.
Evans, R.L., Jones, A.G., Garcia, X., Muller, M., Hamilton, M., Evans, S., Fourie, C.J.S., Spratt, J., Webb, S., Jelsma, H., Hutchins, D., 2011. Electrical lithosphere beneath the Kaapvaal craton, southern Africa. J. Geophys. Res. 116, B04105.
Farla, R.J.M., Karato, S.-i., Cai, Z., 2013. Role of orthopyroxene in rheological weakening of the lithosphere via dynamic recrystallization. Proceedings of the National Academy of Sciences 110, 16355-16360.
Fei, H., Wiedenbeck, M., Yamazaki, D., Katsura, T., 2013. Small effect of water on upper-mantle rheology based on silicon self-diffusion coefficients. Nature 498, 213-215.
Férot, A., Bolfan-Casanova, N., 2012. Water storage capacity in olivine and pyroxene to 14 GPa: Implications for the water content of the Earth's upper mantle and nature of seismic discontinuities. Earth and Planetary Science Letters 349-350, 218-230.
Fishwick, S., 2010. Surface wave tomography: Imaging of the lithosphere-asthenosphere boundary beneath central and southern Africa? Lithos 120, 63-73.
Foley, S.F., 2008. Rejuvenation and erosion of the cratonic lithosphere. Nature geoscience 1, 503-510.
Fouch, M.J., James, D.E., VanDecar, J.C., van der Lee, S., 2004. Mantle seismic strucutre beneath the Kaapvaal and Zimbabwe Cratons. South African Journal of Geology 107, 33-44.
Fullea, J., Muller, M.R., Jones, A.G., 2011. Electrical conductivity of continental lithospheric mantle from integrated geophysical and petrological modeling: Application to the

Kaapvaal Craton and Rehoboth Terrane, southern Africa. Journal of geophysical Research 116, 32 pp.
Furman, T., 2007. Geochemistry of East African rift basalts: An overview. Journal of African Earth Sciences 48, 147-160.
Gaetani, G.A., Grove, T.L., 1998. The influence of water on melting of mantle peridotite. Contributions to Mineralogy and Petrology 131, 323-346.
Gao, S., Rudnick, R.L., Carlson, R.W., McDonough, W.F., Liu, Y.-S., 2002. Re-Os evidence for replacement of ancient mantle lithosphere beneath the North China craton. Earth and Planetary Science Letters 198, 307-322.
Georges, R., Rogers, N., Kelley, S., 1998. Earliest magmastim in Ethiopia: evidence for two mantle plumes in one flood basalt province. Geology 26, 923-926.
Gibson, S.A., McMahon, S.C., Day, J.A., Dawson, J.B., 2013. Highly refractory lithospheric mantle beneath the Tanzanian Craton: Evidence from Lashaine Pre-metasomatic garnet-bearing peridotites. Journal of Petrology.
Grégoire, M., Bell, D.R., Le Roex, A.P., 2003. Garnet Lherzolites from the Kaapvaal Craton (South Africa): Trace Element Evidence for a Metasomatic History. Journal of Petrology 44, 629-657.
Griffin, W.L., Graham, S., O'Reilly, S.Y., Pearson, N.J., 2004. Lithosphere evolution beneath the Kaapvaal Craton: Re-Os systematics of sulfides in mantle-derived peridotites. Chemical Geology 208, 89-118.
Griffin, W.L., O'Reilly, S.Y., 2007. The earliest subcontinental mantle, in: M. Van Kranendonk, H.S.a.V.B. (Ed.), Earth's Oldest Rocks. Elsevier, Amsterdam, pp. 1013-1035.
Griffin, W.L., O'Reilly, S.Y., Abe, N., Aulbach, S., Davies, R.M., Pearson, N.J., Doyle, B.J., Kivi, K., 2003a. The origin and evolution of Archean lithospheric mantle. Precambrian Research 127, 19-41.
Griffin, W.L., O'Reilly, S.Y., Afonso, J.C., Begg, G.C., 2009. The Composition and Evolution of Lithospheric Mantle: a Re-evaluation and its Tectonic Implications. Journal of Petrology 50, 1185-1204.
Griffin, W.L., O'Reilly, S.Y., Natapov, L.M., Ryan, C.G., 2003b. The evolution of lithospheric mantle beneath the Kalahari Craton and its margins. Lithos 71, 215-241.
Hansen, S.E., Nyblade, A.A., Julià, J., 2009. Estimates of crustal and lithospheric thickness in sub-saharan Africa from S-wave receiver functions. South African Journal of Geology 112, 229-240.
Hendrie, D.B., Kusznir, N.J., Morley, C.K., Ebinger, C., 1994. Cenozoic extension in northern Kenya: a quantitative model of rift basin development in the Turkana region. Tectonophysics 236, 409-438.
Herwegh, M., Berger, A., Ebert, A., Brodhag, S., 2008. Discrimination of annealed and dynamic fabrics: consequence for strain localization and deformation episodes of large-scale shear zones. Earth and Planetary Science Letters 276.
Higgie, K., Tommasi, A., 2012. Feedbacks between deformation and melt distribution in the crust-mantle transition zone of the Oman ophiolite. Earth and Planetary Science Letters 359-360, 61-72.
Hiraga, T., Tachibana, C., Ohashi, N., Sano, S., 2010. Grain growth systematics for forsterite ± enstatite aggregates: Effect of lithology on grain size in the upper mantle. Earth and Planetary Science Letters 291, 10-20.
Hirschmann, M.M., Aubaud, C., Withers, A.C., 2005. Storage capacity of H2O in nominally anhydrous minerals in the upper mantle. Earth and Planetary Science Letters 236, 186-181.

Hirth, G., Kohlstedt, D., 2003. Rheology of the upper mantle and the mantle wedge: a view from the experimentalists. Geophysical Monograph 138, 83-105.
Hirth, G., Kohlstedt, D.L., 1995a. Experimental constraints on the dynamics of the partially molten upper mantle .2. Deformation in the dislocation creep regime. Journal of Geophysical Research-Solid Earth 100, 15441-15449.
Hirth, G., Kohlstedt, D.L., 1995b. Experimental constraints on the dynamics of the partially molten upper mantle: Deformation in the diffusion creep regime Journal of Geophysical Research-Solid Earth 100, 1981-2001.
Hirth, G., Kohlstedt, D.L., 1996. Water in the oceanic upper mantle: Implications for rheology, melt extraction, and the evolution of the lithosphere. Earth and Planetary Science Letters 144, 93-108.
Hofmann, C., Courtillot, V., Feraud, G., Rochette, P., Yirgu, G., Ketefo, E., Pik, R., 1997. Timing of the Ethiopian flood basalt event and implications for plume birth and global change. Nature 389, 338-341.
Holtzman, B.K., Groebner, N.J., Zimmerman, M.E., Ginsberg, S.B., Kohlstedt, D.L., 2003a. Stress-driven melt segregation in partially molten rocks. Geochem. Geophys. Geosyst. 4, 1-26.
Holtzman, B.K., Kohlstedt, D.L., Zimmerman, M.E., Heidelbach, F., Hiraga, T., Hustoff, J., 2003b. Melt segregation and strain partitioning: implications for seismic anisotropy and mantle flow. Science 301, 1227-1230.
Huismans, R.S., Cloetingh, S., Podladchikov, Y.Y., 2001. Transition from passive to active rifting : relative importance of asthenospheric doming and passive extension of the lithosphere. Journal of geophysical Research 106, 11271-11291.
Jacobsen, S.D., Jiang, F., Mao, Z., Duffy, T.S., Smyth, J.R., Holl, C.M., Frost, D.J., 2008. Effects of hydration on the elastic properties of olivine. Geophys. Res. Lett. 35, L14303.
James, D.E., Boyd, F.R., Schutt, D., Bell, D.R., Carlson, R.W., 2004. Xenolith constraints on seismic velocities in the upper mantle beneath southern Africa. Geochem. Geophys. Geosyst. 5, Q01002.
James, D.E., Fouch, M.J., Vandecar, J.C., Van der Lee, S., 2001. Tectospheric structure beneath southern Africa : The Kaapvaal Project: Formation and evolutions of cratons. Anglais 28, 2485-2488.
Jordan, T.H., 1978. Composition and development of continental tectosphere. Nature 274, 544-548.
Jung, H., Katayama, I., Jiang, Z., Hiraga, T., Karato, S., 2006. Effect of water and stress on the lattice-preferred orientation of olivine. Tectonophysics 421, 1-22.
Kampunzu, A.B., Bonhomme, M.G., Kanika, M., 1998. Geochronology of volcanic rocks and evolution of the Cenozoic western branch of the East African rift system. Journal of African Earth Sciences 26, 441-461.
Karato, S., 1990. The role of hydrogen in the electrical conductivity of the upper mantle. Nature 347, 272-273.
Karato, S., Ogawa, M., 1982. High-pressure recovery of olivine: implications for creep mechanisms and creep activation volume. Physics of the Earth and Planetary Interiors 28, 102-117.
Karato, S.-I., Jung, H., 2003. Effects of pressure on high-temperature dislocation creep in olivine. Philosophical Magazine 83, 401-414.
Karato, S.-i., Rubie, D.C., 1997. Toward an experimental study of deep mantle rheology: A new multianvil sample assembly for deformation studies under high pressures and temperatures. Journal of Geophysical Research: Solid Earth 102, 20111-20122.

Karato, S.-I., Rubie, D.C., Yan, H., 1993. Dislocation recovery in olivine under deep upper mantle conditions: Implications for creep and diffusion. Journal of Geophysical Research: Solid Earth 98, 9761-9768.
Karato, S.I., Paterson, M.S., Fitzgerald, J.D., 1986. Rheology of synthetic olivine aggregates - Influence of grain-size and water. Journal of geophysical Research-Solid Earth and Planets 91, 8151-8176.
Kelemen, P.B., Hart, S.R., Bernstein, S., 1998. Silica enrichment in the continental upper mantle via melt/rock reaction. Earth and Planetary Science Letters 164, 387-406.
Kendall, J.-M., Stuart, G.W., Ebinger, C., Bastow, I.D., Keir, D., 2005. Magma-assisted rifting in Ethiopia. Nature 433, 146-148.
Kohlstedt, D., Bai, Q., Wang, Z.-C., Mei, S., 2000. Rheology of Partially Molten Rocks, in: Bagdassarov, N., Laporte, D., Thompson, A. (Eds.), Physics and Chemistry of Partially Molten Rocks. Springer Netherlands, pp. 3-28.
Kohlstedt, D.L., Keppler, H., Rubie, D.C., 1996. Solubility of water in the alpha, beta, and Y phases of (Mg, Fe)2SiO4. Reviews in Mineralogy & Geochemistry 123, 345-357.
Kohlstedt, D.L., Nichols, H.P.K., Hornack, P., 1980. The effect of pressure on the rate of dislocation recovery in olivine. Journal of Geophysical Research: Solid Earth 85, 3122-3130.
Kohlstedt, D.L., Zimmerman, M.E., 1996. Rheology of partially molten mantle rocks. Annual Review of Earth and Planetary Sciences 24, 41-62.
Kourim, F., Bodinier, J.-L., Alard, O., Bendaoud, A., Vauchez, A., Dautria, J.-M., 2014. Nature and evolution of the lithospheric mantle beneath the Hoggar swell (Algeria): a record from mantle xenoliths. Journal of Petrology In press.
Kramers, J.D., Smith, C.B., 1983. A feasibility study of U-Pb and Pb-Pb dating of kimberlites using groundmass mineral fractions and whole-rock samples. Chemical Geology 41, 23-38.
Langdon, T.G., 1994. A unified approach to grain boundary sliding in creep and superplasticity. Acta Metallurgica et Materialia 42, 2437-2443.
Lee, C.-T.A., Luffi, P., Chin, E.J., 2011. Building and Destroying Continental Mantle. Annual Review of Earth and Planetary Sciences 39, 59-90.
Lenardic, A., Moresi, L.-N., 1999. Some thoughts on the stability of cratonic lithosphere: Effects of buoyancy and viscosity. Journal of Geophysical research 104, 12,747-712,758.
Lenardic, A., Moresi, L.N., Muhlhaus, H., 2003. Longevity and stability of cratonic lithosphere: Insights from numerical simulations of coupled mantle convection and continental tectonics. Journal of Geophysical Research-Solid Earth 108, 15.
Li, A., Burke, K., 2006. Upper mantle structure of southern Africa from Rayleigh wave tomography. Journal of geophysical Research 111.
Liao, J., Gerya, T., Wang, Q., 2013. Layered structure of the lithospheric mantle changes dynamics of craton extension. Anglais 40, 5861-5866.
Mackwell, S.J., Kohlstedt, D.L., Paterson, M.S., 1985. The role of water in the deformation of olivine single-crystals. Journal of Geophysical Research-Solid Earth and Planets 90, 1319-1333.
Mansur, A.T., Shukrani, M., Timpa, S., Rudnick, R.L., 2014. Granulite-facies xenoliths in rift basalts of Northern Tanzania: Age, Composition and origin of Archean lower crust. Journal of Petrology in press.
Mainprice, D., 1990. A FORTRAN program to calculate seismic anisotropy from the lattice preferred orientation of minerals. Comp. Geosci. 16, 385-393.

Mainprice, D., Barruol, G., Ben Ismaïl, W., 2000. The seismic anisotropy of the Earth's mantle: from single crystal to polycrystal, in: S. Karato, A.M.F., R.C. Libermann, G. Masters and L. Stixrude (Ed.), AGU Geophysical Monograph 117, pp. 237-264.

Mainprice, D., Humbert, M., 1994. Methods of calculating petrophysical properties from lattice preferred orientation data. Surveys in Geophysics 15, 575-592.

Mainprice, D., Silver, P.G., 1993. Interpretation of SKS-waves using samples from the subcontinental lithosphere. Physics of the Earth and Planetary Interiors 78, 257-280.

McKenzie, D., 1978. Some remarks on the development of sedimentary basins. Earth and Planetary Science Letters 40, 25-32.

Mehl, L., Hirth, G., 2008. Plagioclase preferred orientation in layered mylonites: evaluation of flow laws for thr lower crust. Journal of geophysical Research 113, 1-19.

Mei, S., Bai, W., Hiraga, T., Kohlstedt, D.L., 2002. Influence of melt on the creep behavior of olivine-basalt aggregates under hydrous conditions. Earth and Planetary Science Letters 201, 491-507.

Mei, S., Kohlstedt, D.L., 2000a. Influence of water on plastic deformation of olivine aggregates 1. Diffusion creep regime. J. Geophys. Res. 105, 21457-21469.

Mei, S., Kohlstedt, D.L., 2000b. Influence of water on plastic deformation of olivine aggregates 2. Dislocation creep regime. J. Geophys. Res. 105, 21471-21481.

Menzies, M.A., Fan, W., Zhang, M., 1993. Palaeozoic and Cenozoic lithoprobes and the loss of >120 km of Archaean lithosphere, Sino-Korean craton, China. Geological Society, London, Special Publications 76, 71-81.

Miller, G.H., Rossman, G.R., Harlow, G.E., 1987. The natural occurrence of hydroxide in olivine. Physics and Chemistry of Minerals 14, 461-472.

Mitchell, R.H., 1986. Kimberlites: Mineralogy, Geochemistry, and Petrology. Plenum Press, New York.

Möller, A., Mezger, K., Schenk, V., 1998. Crustal age domains and the evolution of the continental crust int he Mozambique Belt of Tanzania: Combined Sm-Nd, Rb-Sr, and Pb-Pb isotopic evidence. Journal of Petrology 39, 749-783.

Morency, C., Doin, M.-P., Dumoulin, C., 2002. Convective destabilization of a thickened continental lithosphere. Earth and Planetary Science Letters 202, 303-320.

Morley, C.K., Wescott, W.A., Stone, D.M., Harper, R.M., Wigger, S.T., Karanga, F.M., 1992. Tectonic evolution of the northern Kenya rift. Journal of the geological society, London 149, 333-348.

Neves, S.P., Tommasi, A., Vauchez, A., Hassani, R., 2008. Intraplate continental deformation: Influence of a heat-producing layer in the lithospheric mantle. Earth and Planetary Science Letters 274, 392-400.

Nicolas, A., Achauer, U., Daignieres, M., 1994. Rift initiation by lithospheric rupture. Earth and Planetary Science Letters 123, 281-298.

Nicolas, A., Christensen, N.I., 1987. Formation of Anisotropy in Upper Mantle Peridotites - A Review, Composition, Structure and Dynamics of the Lithosphere-Asthenosphere System. American Geophysical Union, pp. 111-123.

Nicolas, A., Poirier, J.P., 1976. Crystalline plasticity and solid state flow in metamorphic rocks.

Nixon, P.H., Rogers, N.W., Gibson, I.L., Grey, A., 1981. Depleted and fertile mantle xenoliths from southern african kimberlites. Ann. Rev. Earth Planet. Sci., 285-309.

Nyblade, A.A., Brazier, R.A., 2002. Precambrien lithospheric controls on the development of the East African rift system. Geology 30, 755-758.

Paterson, M.S., 1982. The determination of hydroxyl by infrared absorption in quartz, silicate glasses and similar materials. Bulletin de Minéralogie 105, 20-29.

Pearson, D.G., Carlson, R.W., Shirey, S.B., Boyd, F.R., Nixon, P.H., 1995. Stabilisation of Archaean lithospheric mantle: A Re-Os isotope study of peridotite xenoliths from the Kaapvaal craton. Earth and Planetary Science Letters 134, 341-357.

Pearson, D.G., Wittig, N., 2008. Formation of Archaean continental lithosphere and its diamonds: the root of the problem. Journal of the Geological Society 165, 895-914.

Peslier, A.H., 2010. A review of water contents of nominally anhydrous natural minerals in the mantles of Earth, Mars and the Moon. Journal of Volcanology and Geothermal Research 197, 239-258.

Peslier, A.H., Woodland, A.B., Bell, D.R., Lazarov, M., 2010. Olivine water contents in the continental lithosphere and the longevity of cratons. Nature 467, 78–81.

Petit, C., Déverchère, J., 2006. Structure and evolution of the Baikal rift: A synthesis. Geochemistry, Geophysics, Geosystems 7, Q11016.

Phillips, D., Machin, K.J., Kiviets, G.B., Fourie, L.F., Roberts, M.A., Skinner, E.M.W., 1998. A petrographic and 40Ar/39Ar geochronological study of the Voorspoed kimberlite, South Africa: Implications for the origin of Group II kimberlite magmatism. Special Issue, South African Journal of Geology 101, 299-306.

Pollack, H.N., 1986. Cratonization and thermal evolution of the mantle. Earth and Planetary Science Letters 80, 175-182.

Priestley, K., 1999. Velocity structure of the continental upper mantle: evidence from southern Africa. Lithos 48, 45-56.

Priestley, K., McKenzie, D., Debayle, E., 2006. The state of the upper mantle beneath southern Africa. Tectonophysics 416, 101-112.

Priestley, K., Tilmann, F., 2009. Relationship between the upper mantle high velocity seismic lid and the continental lithosphere. Lithos 109, 112-124.

Richardson, S.H., Shirey, S.B., Harris, J.W., Carlson, R.W., 2001. Archean subduction recorded by Re-Os isotopes in eclogitic sulfides inclusions in Kimberley diamonds. Earth and Planetary Science Letters 191, 257-266.

Riley, T.R., Leat, P.T., Curtis, M.L., Millar, I.L., Duncan, R.A., Fazel, A., 2005. Early, A Middle Jurassic Dolerite Dykes from Western Dronning Maud Land (Antarctica): Identifying Mantle Sources in the Karoo Large Igneous Province. Journal of Petrology 46, 1489-1524.

Ritsema, J., Nyblade, A.A., Owens, T.J., Langston, C.A., Vandecar, J.C., 1998. Upper mantle seismic velocity structure beneath Tanzania, east Africa: Implications for the stability of cratonic lithosphere. J. Geophys. Res. 103, 21,201-221,213.

Ritsema, J., van Heijst, H., 2000. New seismic model of the upper mantle beneath Africa. Geology 28, 63-66.

Ross, J.V., Ave'lallemant, H.G., Carter, N.L., 1979. Activation volume for creep in the upper mantle. Science 203, 261-263.

Rutter, E., Brodie, K., 1988. The role of tectonic grain size reduction in the rheological stratification of the lithosphere. Geol. Rundsch. 77, 295-307.

Savage, B., Silver, P.G., 2008. Evidence for a compositional boundary within the lithospheric mantle beneath the Kalahari craton from S receiver functions. Earth and Planetary Science Letters 272, 600-609.

Schmidt, S.M., Boland, J.N., Paterson, M.S., 1977. Superplastic flow in finegrained limestone. Tectonophysics 43, 257-291.

Schulze, D.J., 1989. Constraints on the abundance of eclogite in the upper mantle. Journal of Geophysical Research: Solid Earth 94, 4205-4212.

Scoates, J.S., Friedman, R.M., 2008. Precise age of the platiniferous merensky reef, Bushveld complex, South Africa, by The U-Pb zircon chemical abrasion ID-TIMS technique Economic Geology 103, 465-471.

Shinjo, R., Chekol, T., Meshesha, D., Itaya, T., Tatsumi, Y., 2011. Geochemistry and geochronology of the mafic lavas from the southeastern Ethiopian rift (the East African Rift System): assessment of models on magma sources, plume-lithosphere interaction and plume evolution. Contributions to Mineralogy and Petrology 162, 209-230.
Shirey, S.B., Harris, J.W., Richardson, S.H., Fouch, M.J., James, D.E., Cartigny, P., Deines, P., Viljoen, F., 2002. Diamond Genesis, Seismic Structure, and Evolution of the Kaapvaal-Zimbabwe Craton. Science 297, 1683-1686.
Silver, P.G., Gao, S.S., Liu, K.H., Group, a.t.K.S., 2001. Mantle deformation beneath southern Africa. Geophys. Res. Lett. 28, 2493-2496.
Simon, N.S.C., Carlson, R.W., Pearson, D.G., Davies, G.R., 2007. The Origin and Evolution of the Kaapvaal Cratonic Lithospheric Mantle. Journal of Petrology 48, 589-625.
Simon, N.S.C., Irvine, G.J., Davies, G.R., Pearson, D.G., Carlson, R.W., 2003. The origin of garnet and clinopyroxene in "depleted" Kaapvaal peridotites. Lithos 71, 289-322.
Smith, C.S., 1948. Grains, phases and interfaces an interpretation of microstructures. Trans. AIME 175, 15-51.
Stewart, K., Rogers, N., 1996. Mantle plume and lithosphere contributions to basalts from southern Ethiopia. Earth and Planetary Science Letters 139, 195-211.
Solomatov, V.S., El-Khozondar, R., Tikare, V., 2002. Grain size in the lower mantle: constraints from numerical modeling of grain growth in two-phase systems. Physics of the Earth and Planetary Interiors 129, 265-282.
Tang, Y.-J., Zhang, H.-F., Ying, J.-F., Zhang, J., Liu, X.-M., 2008. Refertilization of ancient lithospheric mantle beneath the central North China Craton: evidence from petrology and geochemistry of peridotite xenoliths. Lithos 101, 435-452.
Tommasi, A., Knoll, M., Vauchez, A., Signorelli, J., Thoraval, C., Loge, R., 2009. Structural reactivation in plate tectonics controlled by olivine crystals anisotropy. Nature Geoscience 2, 423-427.
Tommasi, A., Vauchez, A., 1997. Complex tectono-metamorphic patterns in continental collision zones: The role of intraplate rheological heterogeneities. Tectonophysics 279, 327-350.
Tommasi, A., Vauchez, A., 2001. Continental rifting parallel to ancient collisional belts: an effect of the mechanical anisotropy of the lithospheric mantle. Earth and Planetary Science Letters 185, 199-210.
Tommasi, A., Vauchez, A., Daudre, B., 1995. Initiation and propagation of shear zones in a heterogeneous continental lithosphere. Journal of geophysical Research 100, 22,083-022,101.
Vauchez, A., Barruol, G., Tommasi, A., 1997. Why do continents break-up parallel to ancient orogenic belts? Terra Nova 9, 62-66.
Vauchez, A., Egydio-Silva, M., Babinski, M., Tommasi, A., Uhlein, A., Liu, D., 2007. Deformation of a pervasively molten middle crust: insights from the neoproterozoic Ribeira-Araçuai orogen (SE Brazil). Terra Nova 19, 278-286.
Vauchez, A., Tommasi, A., Barruol, G., Maumus, J., 2000. Upper mantle deformation and seismic anisotropy in continental rifts. Physics and Chemistry of the Earth 25, 111-117.
Vauchez, A., Tommasi, A., Mainprice, D., 2012. Faults (shear zones) in the Earth's mantle. Tectonophysics 558-559, 1-27.
Vinnik, L., 1977. Detection of waves converted from P to SV in the mantle. Physics of the Earth and Planetary Interiors 15.
Vinnik, L., Green, R.W.E., Nicolaysen, L.O., 1995. Recent deformation of the deep continental root beneath southern Africa. Nature 375, 50-52.
Wang, Z., Zhao, Y., Kohlstedt, D., 2010. Dislocation creep accommodated by grain boundary sliding in dunite. Journal of Earth Science 21, 541-554.

Wasch, L.J., van der Zwan, F.M., Nebel, O., Morel, M.L.A., Hellebrand, E.W.G., Pearson, D.G., Davies, G.R., 2009. An alternative model for silica enrichment in the Kaapvaal subcontinental lithospheric mantle. Geochimica et Cosmochimica Acta 73, 6894-6917.

Wernicke, B., 1981. Low angle normal faults in Bassin and Range province. Nappe tectonics in an extending orogen. Nature 291, 645-648.

Wernicke, B., 1985. Uniform-sense normal simple shear of the continental lithosphere. Canadian Journal of Earth Sciences 22, 108-125.

Wittlinger, G., Farra, V., 2007. Converted waves reveal a thick and layered tectosphere beneath the Kalahari super-craton. Earth and Planetary Science Letters 254, 404-415.

Wolfenden, E., Ebinger, C., Yirgu, G., Deino, A., Ayalew, D., 2004. Evolution of the northern Main Ethiopian Rift: Birth of a triple junction. Earth and Planetary Science Letters 224, 213-228.

Yuan, H., Romanowicz, B., 2010. Lithospheric layering in the North American craton. Nature 466, 1063-1069.

Zhao, Y.-H., Ginsberg, S.B., Kohlstedt, D.L., 2004. Solubility of hydrogen in olivine: dependence on temperature and iron content. Contributions to Mineralogy and Petrology 147, 155-161.

Zimmerman, M.E., Kohlstedt, D.L., 2004. Rheological properties of partially molten lherzolite. Journal of Petrology 45, 275-298.

Résumé :

Les travaux réalisés durant cette thèse apportent de nouvelles contraintes sur les relations entre déformation, hydratation et percolation de fluides et/ou de magmas dans le manteau subcontinental sous un craton et sous un rift, et leurs implications sur son comportement rhéologique. Il repose sur l'analyse des microstructures, des OPRs et des teneurs en hydrogène de xénolites mantelliques du craton du Kaapvaal, et sur deux séries de xénolites provenant de différentes localités le long du rift Est-Africain (Divergence Nord Tanzanienne et SE de l'Ethiopie).

Les microstructures granulaires à gros grains et les OPRs bien définies des péridotites du craton du Kaapvaal sont cohérentes avec un épisode de déformation suivi d'une longue période de quiescence. Les OPRs de l'olivine sont majoritairement à symétrie orthorhombique, mais des symmétries axiale-[100] et axiale-[010] sont aussi mesurées. Les péridotites cratoniques enregistrent de multiples épisodes métasomatiques, ayant entraîné une hétérogénéité de compositions à petite échelle ne pouvant être détectée par les études sismiques. Les teneurs en hydrogène mesurées dans l'olivine sont variables, mais ont tendance à augmenter jusqu'à 150 km de profondeur, atteignant alors jusqu'à 50 ppm wt. H_2O. En dessous de cette profondeur, les échantillons montrent des teneurs en hydrogène très faibles. Les expériences réalisées en piston-cylindre sur la diffusion de l'hydrogène issue d'un liquide kimberlitique vers de la forstérite suggèrent que la fugacité en eau pourrait fortement être diminuée par la présence de CO_2, empêchant l'hydratation de l'olivine durant extraction des xénolites par les kimberlites. Ces résultats expérimentaux suggèrent que les teneurs en hydrogène dans l'olivine des péridotites du craton du Kaapvaal ont été acquises durant un épisode métasomatique en profondeur et non pendant leur extraction par les kimberlites. Ces teneurs n'ont toutefois pas à ce jour entraîné de remobilisation de la racine cratonique. Enfin, le calcul des propriétés sismiques des péridotites cratoniques révèle que les anisotropies générées par les OPRs de ces échantillons sont suffisantes pour expliquer les anisotropies mesurées par les ondes SKS et les ondes de surface.

Les xénolites de la Divergence Nord-Tanzanienne, montrent des variations significatives de microstructures et d'OPR de l'olivine entre les péridotites des localités dans l'axe du rift et celles de la chaîne volcanique transverse (Lashaine et Olmani). A Lashaine, les microstructures granulaires à gros grains et les OPRs de type orthorhombique et axial-[010] peuvent être expliquée par une déformation en transpression liée à la formation de la chaîne Mozambique ou par la présence d'une relique d'un domaine cratonique à l'intérieur de la chaîne Mozambique. Dans l'axe du rift, les microstructures porphyroclastiques à mylonitiques suggèrent une déformation plus récente, accompagnée de réactions magma-roche sous des conditions proches du solidus, suivie d'un recuit variable. L'hétérogénéité des microstructures enregistrées par les échantillons du rift suggère de multiples épisodes de déformation localisée, probablement liés à l'injection percolation épisodique de magmas, espacés de périodes d'accalmie. Les OPRs de l'olivine de type axial-[100] et l'orientation des directions de polarisation des ondes SKS suggère que le rift s'est formé en régime de transtension

Les péridotites du Sud-Est de l'Ethiopie présentent des microstructures porphyroclastiques à gros grains moins recristallisées qu'en Tanzanie. Les microstructures et les OPRs principalement de type orthorhombique suggèrent une déformation syn- à post-métasomatisme. Les anisotropies de polarisation des ondes S calculées pour ces échantillons sont insuffisantes pour expliquer à elles seules les déphasages des ondes SKS dans cette partie du rift.

MOTS CLÉS : Péridotite, déformation, OPR, teneurs en hydrogène, craton, rift, propriétés sismiques, percolation réactive.